The microstructure of confined and thin polymer films

Von der Fakultät für Mathematik, Informatik und Naturwissenschaften der Rheinisch-Westfälischen Technischen Hochschule Aachen zur Erlangung des akademischen Grades einer Doktorin der Naturwissenschaften genehmigte Dissertation

vorgelegt von

Diplom-Physikerin

Milena Lippmann, geb. Dimitrova Mihaylova

aus Kazanlak, Bulgarien

Berichter: Universitätsprofessor Dr. Thomas Brückel Universitätsprofessor Dr. Walter Richtering

Tag der mündlichen Prüfung: 27.10.2005

Diese Dissertation ist auf den Internetseiten der Hochschulbibliothek online verfügbar. На Илияна

Contents

1	Introduction				
2	Soft matter thin films				
	2.1	Dynar	mics of polymer thin films	9	
		2.1.1	General remarks	S	
		2.1.2	Height-height correlation function in the Liquid and Fractal model.	10	
	2.2	Prope	rties of confined liquids and confined polymer films	13	
3	Sca	ttering	g theory	19	
		Reflec	tivity theory	19	
		3.1.1	Fresnel's formulae	19	
		3.1.2	Multiple interfaces	21	
		3.1.3	Roughness	23	
		3.1.4	The critical angle at the confined reflectivity curves	26	
	v		e scattering theory	26	
		3.2.1	Born approximation	26	
		3.2.2	Distorted–Wave Born approximation	28	
4	Polymer thin films				
	4.1 Experimental setup		imental setup	31	
		4.1.1	Description of the beamline and the sample environment	31	
		4.1.2	Scattering geometry	33	
		4.1.3	Diffractometer resolution	35	
		4.1.4	Polymer samples under study	35	
	4.2 Results and Discussions		s and Discussions	38	
		4.2.1	Reflectivity measurements	38	
		4.2.2	The Liquid and the Fractal models	44	
		4.2.3	Diffuse scattering data depending on the temperature and the film thickness	53	
		4.2.4	Hydrophilic and hydrophobic substrates	55	
			J T T T T T T T T T T T T T T T T T T T		

4 CONTENTS

5	Confined liquids and polymer films						
	5.1 Experimental setup for X-ray scattering from confined liquid and polym						
		films.	61				
		5.1.1 The experimental cell	61				
		5.1.2 The beamline	63				
		5.1.3 Preparation of the confined films	65				
		5.1.4 Preparation of the wafer surface	69				
		5.1.5 The accuracy in the parallel alignment of the substrates	69				
		5.1.6 The procedure of the sample confining	70				
	5.2						
		5.2.1 Structure and properties of carbon tetrachloride (CCl ₄) and Oc-					
		tamethylcyclotetrasiloxane (OMCTS)	71				
		5.2.2 Self–assemble diblock copolymer systems	72				
	5.3 Results and discussions						
		5.3.1 Confined liquids	75				
		5.3.2 Confined polymers	79				
6	Con	Conclusions and Outlook					
\mathbf{R}	efere	nces	86				
\mathbf{A}	Res	ults after refinement of the scattering data.	95				
		Results from refinements of reflectivity curves	96				
	A.2	The Liquid and the Fractal models refinements	99				
	11.2	A.2.1 Samples studied at 150°C	99				
		A.2.1.1 Hydrophilic samples	99				
		A.2.1.2 Hydrophobic samples	134				
		A.2.2 Samples studied at 230°C	163				
		A.2.2 Samples studied at 250 C	163				
		A.2.2.2 Hydrophobic samples	198				
В	Lists						
	B.1	List of tables	228				
	B.2	List of figures	230				

Chapter 1

Introduction

Polymer molecules are sequences of identical units (monomers). The simplest example is the chain of polyethylene, which consists of $-CH_2-$ monomers. Depending on the number of monomers, the polymers can have molecular weights in the range of a few kg/mol to thousands of kg/mol. In principle, polymers with molecular chains showing a regular chemical structure, can crystallize, but due to the entanglements between the chains, these structures are normally not completely crystalline¹. They consist of crystals embedded in a 'matrix' of amorphous chains. In contrast, the polymers with non-regular chemical structures do not build crystalline phases. The bulk of these polymers is always completely amorphous.

An important parameter for the description of the amorphous structure is the radius of gyration R_g . If there is no special interaction between the molecules and the monomers, it is supposed that the volume occupied by a single amorphous polymer chain has the form of a sphere with the radius R_g . In thin films the amorphous phase is strongly affected by the substrate. Investigations show that R_g in direction perpendicular to the surface is significantly smaller than in the parallel plane [1, 2]. Moreover, it is supposed that the molecular movements in the perpendicular direction are relatively constrained due to the interaction with the substrate. The effect is called confinement of the polymer chain by the substrate. The confinement effects are responsible for all phenomena observed at the interface.

Polymers find wide application in biology and medical research. They can simulate the properties of some bio-composites, which are included into the cell structure of all living organisms. The lipids as basic structural elements of bio-membranes are a typical example [3, 4]. The application of polymers as building materials of membranes have pushed forward the investigation of polymer thin films and multilayers. Depending on the chemical structure some of the polymers deposited on a substrate can be assembled into nanosystems with special functionality [5]. In some cases the objects created on the surface can be manipulated by external forces or by temperature. Such nanosystems are probably useful in the future developments of micro- and nanotechnology. Moreover, polymers are

¹Exceptions are those polymers with very short chains in the order of a few kg/mol

of big importance in microelectronic and coating industry [6, 7]. Thus, the investigation of polymer films becomes important also from a commercial point of view. Since the chemical structure of the polymers is related to the physical properties, chemical industry always tries to develop new methods for the synthesis of polymers with growing complexity of the chemical structure and new interesting physical properties.

The application of polymer films is in most cases related to the structure and properties of the film surface, and the surface properties are mainly influenced by the dynamics of the chains, i.e. molecular movements and relaxation. On the other hand the dynamics of the polymer chains are determined by the film thickness, molecular mass of the polymer, temperature and the polymer–substrate interaction. Therefore, the investigation of the surface structure in dependence of all those parameters can elucidate the relation between the microscopic molecular motions and the macroscopic surface properties.

Conventional simple techniques for investigations of the surface structure are microscopic methods, i.e. Atom Force Microscopes (AFM), Scanning Tunneling Microscopy (STM) or High–Resolution Transmission Electron Microscopy (TEM). With the development of high–flux neutron and X–ray sources, surface scattering methods also became feasible techniques for surface structure studies. The interpretation of the results obtained from scattering methods is more complicated. Nevertheless, their advantage is founded in the provision of relevant statistic information, averaged over langer areas in comparison with the microscopic techniques. Additionally, scattering methods do not require special sample preparations and allow the investigation of buried interfaces. In most cases they are non destructive for the samples.

As mentioned above, an important part of the film properties, especially the dynamics of thin films, is influenced by the interplay between film and substrate. Thus, it seems useful in the context of basic research, to put some attention on the investigation of the interface. The processes at the interface are emphasized in extremely thin films which can be created by confining the fluids between substrates at a distance of the order of molecular dimensions. The confinement effects observed in polymers films are more pronounced in the case of liquids due to the smaller molecule sizes and ability to create ultra thin films on the substrate surface [8, 9]. Therefore, the investigation of confined liquid films appears to be extremely attractive in order to improve our knowledge of soft matter behaviour at the interface.

The larger dimension of the polymer molecules do not allow investigations of ultra thin confined films. Nevertheless, the confinement of polymers is also interesting for the fundamental research and technology. An example are the studies concerning basic questions appearing in polymer crystallization theory [10]. The process of polymer crystallization is far from being fully understood. For instance, the crystallization theory cannot predict such important parameters like the degree of crystallization and the thickness of the crystalliamela. Therefore, experiments, which allow a control of the crystallization process are very important. The management of the crystallization process would give a possibility to extract a certain crystallization step and observe it on a larger time scale. Self–assembling diblock copolymers are a proper model system for these investigations. This type of polymers allows (to some extent) to control the nucleation and the chain folding by varying

the length of the blocks. The combination of such samples with experiments at restricted geometries gives promising results [11].

The Surface Force Apparatus (SFA), AFM and Friction Force Microscopes (FFM) are the mostly used techniques for the investigation of confined fluids. A detailed description of these techniques and their advantages and disadvantages follows in the next section. There are only few works, where scattering methods were used, and due to the experimental difficulties a successful setup for scattering experiments on confined films with thicknesses of about a few hundreds of Angstroms is still not available. The development of an experimental setup that can confine liquid ultra thin films and simultaneously allows X–ray reflectivity and diffuse scattering measurements is extremelly challenging. An attempt was performed in the frame of this work.

The thesis is organized as follows: After a short overview of previous literature data and results, the reflectivity theory is summarized. The experimental part is divided into two sections: The first deals with the **time averaged dynamics of supported polymer thin films** and the second with **confined liquid and polymer films**.

In the first part the influence of thermally induced fluctuations on the polymer surface stucture depending on the film thickness, the molecular mass and the temperature is studied. The surface structure is probed by X–ray reflectivity and diffuse scattering measurements. In the second part a new setup for confined soft matter films is introduced. It was tested with liquid films of carbon tetrachloride (CCl₄) and octamethylcyclotetrasiloxane (OM-STS). Additionally, results of test experiments on confined polymers are presented. These experiments are based on ideas proposed by *Prof. W. de Jeu*, (FOM Institute AMOLF, Amsterdam), who works on problems related to the crystallization of self–assemble diblock copolymers.

Chapter 2

Soft matter thin films

2.1 Dynamics of polymer thin films.

2.1.1 General remarks

The glass transition temperature, T_g , is the borderline between hard and soft matter. Above the glass transition the mechanical moduli (storage moduli) of the polymers drastically decrease down to the order of MPa, whereas the hard materials have mechanical moduli of the order of GPa. The decrease of the mechanical moduli above T_q is associated with an increase of the viscose properties, and the polymers can start to flow. This peculiar mechanical behaviour is called viscoelastisity. Depending on the temperature with respect to T_q , the polymer material can be in some intermediate state between solid and the liquid. The strong viscoelastic mechanical properties of the polymers and the similarity of the diffuse scattering data (the transverse scans) obtained from polymer films with those observed from liquid films, initiated a discussion about the models that should be used for the description of the surface structure influenced by the dynamics of polymer films. Basically two ideas are favoured in literature: the first regards polymer films as viscose liquids and describes the surface structure as a result of the propagation of thermally induced capillary waves [12, 13]. The second assumption considers the structure as strongly influenced by the elastic properties. Thus, there is no evidence for capillary waves on the surface [14]. Consequently, in the present work the diffuse scattering data are refined using two different models: the Liquid and the Fractal model. The first is based on the theory of capillary waves and the second model assumes solid (unmovable) surfaces. The goal of the investigation is to compare the models for samples with different molecular masses and temperatures up to 230°C. Earlier studies were limited to only one molecular mass and temperatures up to 180°C. Since both temperature and the molecular mass are parameters that strongly influence the polymer viscosity, it is expected that a study in a wider range may explain disagreements observed in the previous works.

The film thickness and the interaction between the polymer and the substrate seems to play an important role in the dynamics of the polymer surface. It has been reported that polymers, which do not interact with the substrates, indeed exhibit surface capillary waves [15, 16]. Therefore, it is expected that thinner supported films will show less mobile surfaces than thicker ones. Similar effects have already been observed for thin liquid films [17].

The interaction between the polymer film and the substrate can also be manipulated using either hydrophobic or hydrophilic substrates. The presence of oxides on hydrophilic substrates forces the creation of hydrogen bonds between the polymer and the substrate atoms. Thus, it leads to a stronger connection of the polymer film to the surface compared to films, which are only bonded via van–der–Waals interactions. The comparison of both types of substrates in the present study should give an estimate for the hydrophobisites effects on the polymer/substrate interaction.

2.1.2 Height-height correlation function in the Liquid and Fractal model.

A fundamental part of the capillary wave theory used in the **Liquid model** is related to the surface hydrodynamic properties of liquids [18, 19, 20, 21]. Due to entropy reasons, at temperatures higher than 0 K thermal fluctuations (capillary waves) appear on the liquid surface. These fluctuations can be associated with a sum of propagating plane waves with different amplitudes A_j , wave vectors k_j , and phases φ_j , where the indices j indicate the number of the surface mode. The nature of these modes is determined by the competition between surface capillary effects and the internal bulk viscosity. A complete statistical picture of the surface wave spectrum in space and time can be derived from the dynamical power spectral density (PDS), $\tilde{C}(\vec{q}_{\parallel}, \omega)$. The PDS of the thermally fluctuating liquid surface is given by [19]

$$\widetilde{C}(\vec{q}_{\parallel},\omega) = 2k_B T \frac{\chi_{zz}^{"}(\vec{q}_{\parallel},\omega)}{\omega}, \tag{2.1}$$

where \vec{q}_{\parallel} is the wave vector in the surface plane, k_B is the Boltzmann constant, T is the temperature and $\chi''_{zz}(\vec{q}_{\parallel},\omega)$ is the imaginary part of the dynamic susceptibility, $\chi_{zz}(\vec{q}_{\parallel},\omega)$. The dynamic susceptibility is defined as the ratio of the vertical surface displacement u_z , and the internal pressure P_z , acting vertically on the liquid surface $(\chi_{zz}(\vec{q}_{\parallel},\omega) = u_z/P_z)$. Following the work of $J\ddot{a}ckle$ [19] the susceptibility of a thin liquid film has the form:

$$\chi_{zz}(\vec{q}_{\parallel},\omega) = \frac{q_{\parallel}^2 \cdot d/\rho}{\left[\left(g + \frac{A_{eff}}{2\pi\rho d^4}\right)q_{\parallel} + \frac{\gamma}{\rho}q_{\parallel}^3\right] \tanh(q_{\parallel}d) - \frac{6}{5}\omega - \frac{3\eta}{d^2\rho} \cdot i\omega},\tag{2.2}$$

where γ is the surface tension of the liquid, A_{eff} is the effective Hamaker constant which describes the interaction between the film and the substrate, d is the film thickness, ρ is the density of the liquid, g is the gravitational constant and η the viscosity.

If it is supposed that the investigated films have much smaller relaxation times compared to the measuring time, then the surface can be regarded as quasi–static within the measuring time. In this case the quasi–static PDS $\widetilde{C}(\vec{q}_{\parallel})$ is deduced by integrating the dynamical PSD $\widetilde{C}(\vec{q}_{\parallel},\omega)$ over all ω :

$$\widetilde{C}(\vec{q}_{\parallel}) = \int_{-\infty}^{+\infty} \widetilde{C}(\vec{q}_{\parallel}, \omega) \frac{d\omega}{2\pi} = k_B T \chi_{zz}(\vec{q}_{\parallel}, 0).$$
(2.3)

Using Eq. 2.2 for the $\widetilde{C}(\vec{q}_{\parallel})$ one obtains

$$\widetilde{C}(\vec{q}_{\parallel}) = \frac{k_B T}{4\pi^2 \gamma} \cdot \left[q_{\parallel}^2 + \left(\frac{g\rho}{\gamma} + \frac{A_{eff}}{2\pi\gamma d^4} \right) \right]^{-1} = \frac{k_B T}{4\pi^2 \gamma} \cdot \frac{1}{q_{\parallel}^2 + q_{Lc}^2},\tag{2.4}$$

where

$$q_{l,c}^2 = \frac{g\rho}{\gamma} + \frac{1}{d^4} \frac{A_{eff}}{2\pi\gamma}.$$
 (2.5)

is the wave number cut-off. The assumption that the surface is quasi-static allows the integration over ω , and it decouples the PSD from the viscosity. $q_{l,c}$ is the low limit of the wave vectors of the waves propagating on the film surface $(k_j > q_{l,c})$, and therefore it is called lower cutoff. $q_{l,c}$ depends on the gravitational cutoff, q_g , and the van-der-Waals cutoff, q_{vdW} , in the following way:

$$q_{l,c}^2 = q_q^2 + q_{vdW}^2. (2.6)$$

Here

$$q_{vdW}^2 = \frac{1}{d^4} \frac{A_{eff}}{2\pi\gamma} \tag{2.7}$$

and

$$q_g^2 = \frac{g\rho}{\gamma} \tag{2.8}$$

On the other hand the Wiener–Khinchin theorem guarantees that the PDS is the Fourier–transform of the height–height correlation function, $C(\vec{R})$. The height–height correlation function, which is also known as autocorrelation function, for a single interface is defined as

$$C(\vec{R}) = \frac{1}{S} \int_{S} z(\vec{r}_{\parallel}) z(\vec{r}_{\parallel} + \vec{R}) d\vec{r}_{\parallel}$$

$$= \left\langle z(\vec{r}_{\parallel}) z(\vec{r}_{\parallel} + \vec{R}) \right\rangle_{\vec{r}_{\parallel}}$$
(2.9)

Here, $z(\vec{r}_{\parallel})$ is the contour function of the interface depending on the lateral vector $\vec{r}_{\parallel} = (x, y)$ and S is the area of the interface. The function $C(\vec{R})$ determines the correlation

between two points of distance $\vec{R} = (X, Y)$. The height-height correlation function represents the structure of the interface. The intensity of the diffuse scattering coming from the surface depends on this function. The Fourier back transform of Eq. 2.4 is given by

$$C(R) = \frac{B}{2} K_0(q_{l,c}R), \tag{2.10}$$

where $B = \frac{k_B T}{\pi \gamma}$ and $K_0(q_{l,c}R)$ is the modified Bessel function of the second kind and of order zero [22]. Since the $q_{l,c}$ is small, the Eq. 2.10 can be approximated for small $q_{l,c}R$, and one obtains

$$C(R) \simeq -\frac{B}{2} \left[\ln(\frac{q_{l,c}R}{2}) + \gamma_E \right],$$
 (2.11)

where γ_E is Euler's constant [22].

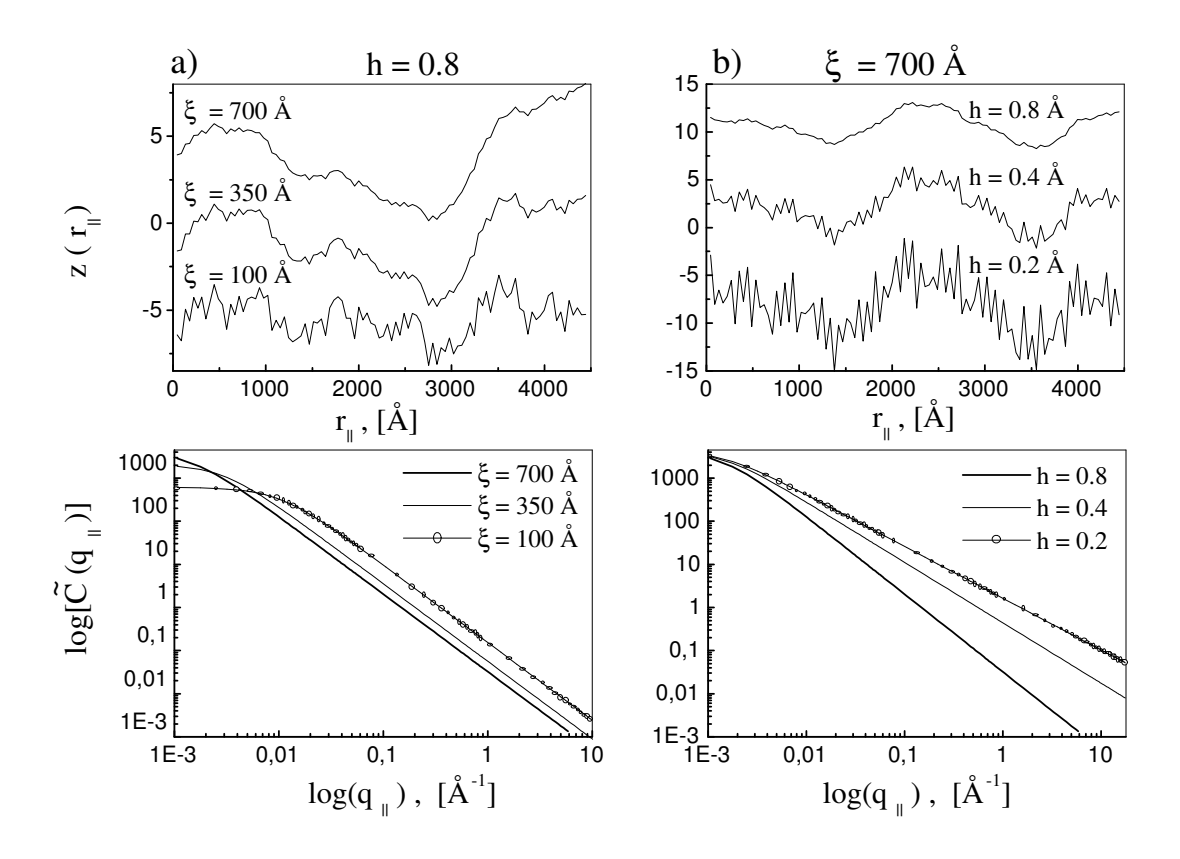


Figure 2.1: a) The effect of different correlation lengths on the contour function and on $\widetilde{C}(\vec{q}_{\parallel})$ for h=0.8. b) The effect of different Hurst parameters on $z(r_{\parallel})$ and the PSD for $\xi=700$ Å. The roughness σ is in all cases assumed to be 6.1 Å.

In contrast to the first model the **Fractal model** considers solid surfaces. The microstructure of many surfaces obtained by molecular beam epitaxy or by vapour deposition techniques shows so–called self–affine fractal scaling, i.e. in–plane the structure of the surface looks similar on different length scales (fractal structure), but perpendicular to the surface the structure scales differently compared to the lateral dimensions (self–affine structure). Usually, for a description of the self–affine surfaces the correlation function proposed by $Sinha\ et\ al.\ [23]$ is used

$$C(R) = \sigma^2 \exp\left\{-\frac{R^{2h}}{\xi^{2h}}\right\} \tag{2.12}$$

with the roughness σ , the correlation length (cutoff) ξ and the Hurst parameter h. For $R \ll \xi$ the surface is self-affine rough, whereas for $R \gg \xi$ the surface appears to be smooth. The Hurst parameter is restricted to the range 0 < h < 1 and defines the fractal dimension of the interface. Small values of h correspond to extremely jagged surfaces, whereas values close to unity lead to interfaces with smooth hills and valleys.

The contour function, $z(\vec{r}_{\parallel})$ can be calculated by

$$z(\vec{r}_{\parallel}) = \int_{-\infty}^{+\infty} \sqrt{\widetilde{C}(\vec{q}_{\parallel})} \exp^{i(\vec{r}_{\parallel} \cdot \vec{q}_{\parallel} + \varphi_{rnm})} dq_{\parallel}, \qquad (2.13)$$

where φ_{rnm} are the phases of \vec{q}_{\parallel} . Standard scattering methods do not provide information about the phases; therefore these have to be randomly generated. The phases give an individuality of the surface, but do not influence the correlation distance in the plane. The integral in Eq. 2.13 is numerically calculated and the results are presented in **Fig. 2.1a** and **b**. For the calculations, $\widetilde{C}(\vec{q}_{\parallel})$ is taken to be [24]:

$$\widetilde{C}(\vec{q}_{\parallel}) = \frac{\xi^2 \sigma^2}{\left(1 + q_{\parallel}^2 \xi^2\right)^{1+h}}.$$
(2.14)

Since $C(\vec{q}_{\parallel})$ does not depend on the direction of the wave vectors in the plane but only on their length, the contour function is also dependent only on the length of the space vector in the plane, r_{\parallel} . In order to be able to compare the effects only from the correlation length, identical sets of the wave vector phases are used for the calculation of the contour curves in **Fig. 2.1a**. The contour curves in **Fig. 2.1b** are calculated with another phase set, and they present the effect of the Hurst parameter.

2.2 Properties of confined liquids and confined polymer films.

In the past a detailed investigation of the tribology (friction and lubrication) phenomena of confined liquids started with the development of techniques for measuring the friction force in a sliding contact. The experiments were carried out by sensitive microscopes as Surface Force Apparatus, Atom Force Microscopes and Friction Force Microscopes. Additionally, scanning tunneling microscopy (STM) and quartz micro-balance techniques were applied [25, 26]. Those techniques and the computer simulations are able to give some understanding of the problem, but they also raise new questions. Dynamic and structure studies of the matter confined in a volume comparable with molecular size appear as a further challenge.

The works can be classified according to the geometry of the confined volume and the fluids under investigation. The latter can be divided into experiments with 'simple' liquids [27, 28], complex fluids and colloides [29, 30, 31, 32]. From the geometry point of view, in a significant number of experiments materials were confined in porous media (zeolites, membranes, silica gels, polymer networks), e.g. [33]. Most of those experiments were directed to study the dynamics of the fluid in a confined volume, and some of them were connected with the problems concerning organization of a complex fluid in vesicles and membranes. Other experiments were performed in a so-called parallel-plate geometry (or single slit-pore, sometimes used in the computer simulation literature). Here, the fluid is confined between two parallel flat substrates. The parallel-plate geometry provides a simple model for the computer simulations, and it is strongly exploited in theoretical investigations.

The experiments presented in this work were carried out in parallel–plate geometry. The 'simple' fluids CCl₄ and Octamethylcyclotetrasiloxane were used. Moreover, measurements with self–organized co–polymers have been performed. The purpose of the experiments was to study the structure changes depending on the gap size, if the fluid is confined in a distance comparable with the molecular dimension. A look at the structural properties was taken by probing the samples by X–ray reflectivity measurements. Since a significant part of this work was dedicated to the development of an appropriate experimental setup, a small overview of similar techniques follows below.

The most often used device for confinement of fluids in parallel–plate geometry is the Surface Force Apparatus (SFA). A construction scheme is shown in **Fig. 2.2a** [35, 36]. The distance between the substrates is controlled via an interferometer with an accuracy of 10 Å. The gap between the substrates is calculated by comparing the initial interference image obtained at closed gap with no liquid between the substrates and the image observed during the experiment. Since the measurement is relative, one should take into account that the first image is observed at completely closed gap, i.e. dust between the substrates has to be carefully avoided. Otherwise, the presence of impurity particles can affect the measurements considerably [37].

A modification of the SFA by *Israelachvili and co-workers* for in–situ experiments at a synchrotron (e.g. [38]) is called X–ray surface force apparatus (XSFA). Self–aligned liquid crystals have been taken as samples, because the signal from ultra thin layers is usually very small, if the radiation is homogeneously scattered. In contrast, the structure of a self–aligned crystal leads to an amplification for certain orientations.

Cosgrove and co-workers [39] have published a description of a setup constructed with similar ideas as the setup presented in the present work. Their device has been designed

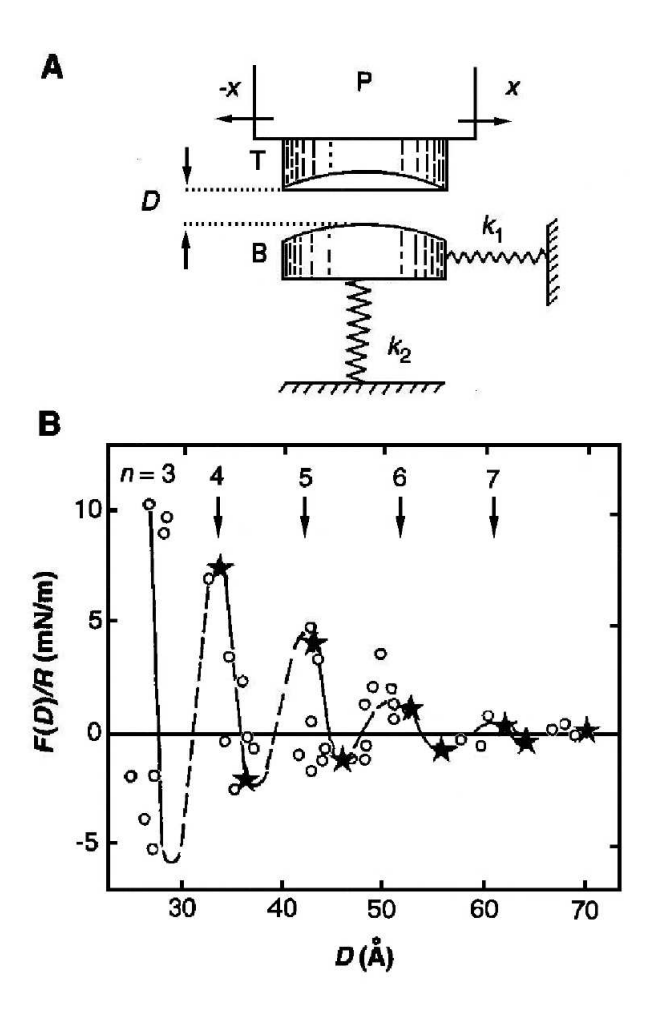


Figure 2.2: a) Scheme of the surface force balance. T and B are the upper and the lower substrates, respectively. The spring $\mathbf{k1}$ enables the lateral force to be measured, $\mathbf{k2}$ – the normal force depends on the gap size \mathbf{D} . b) The normal force $\mathbf{F}(\mathbf{D})/\mathbf{R}$ in dependence of the gap size ($\mathbf{R} \approx 1$ cm is the mean curvature of the mica cylinders). The data are for OMCTS. The data with the stars are taken from [28]. The number of monolayers corresponding to each force maximum is indicated. The figure was taken from [34]. Further explanations are given in the text.

for neutron reflectivity measurements, i.e. it is characterized by large dimensions of the cell and of the confined area. The authors reported that the accuracy in the measurement of the gap size is 1Å. Nevertheless, the presented results are not convincing, because the authors did not indicate the thickness of their films. Additionally, the large confined area of the quartz wafers (discs with 10 cm in diameter) raises suspicion that the roughness of these wafers was about 1Å.

A discussion of results from SFA experiments and computer simulations follows later in this work, because those experiments are more compatible with results presented here than the

experiments in porous media or the investigations of the confinement effect provided by the surface potential on ultra thin films. The application of pressure on the confined volume distinguishes the SFA experiments from the other ones. The pressure squeezes the fluid out of the gap, so that the dependence of the structure upon the gap size can be observed during the measurement. The geometry in the SFA experiment is not parallel—plate type, but it could be assumed that the fluids are constrained in almost parallel substrates because of the very small confined areas.

The existing X-ray surface force technique still cannot provide reasonable data of the structure of fluids confined in the range of a few hundreds of Å. Thus, those works are also not taken into consideration in the discussion here.

The computer simulations predict that the fluids in a confined geometry (the gap size should not be larger than a few times the molecular size) tend to organize in layers. Such tendency is also observed, if fluids are absorbed on solid surfaces [40] (simulations), [9] (experimental). Here, the normal force between the substrates (the solvation force) exhibits decaying oscillations with increasing gap sizes. The periodicity of these oscillations is equal to or a little bit less than the molecular diameters (e.g. [41]). The existence of an oscillatory force was first experimentally proved by *Horn and Israelachvili* [27]. The sample under investigation was OMCTS. They obtained a curve similar to that presented in **Fig. 2.2** b.

In the case of chain molecules, the oscillations are damped faster with increasing molecular weight. If the molecular mass enormously increases, as it is in the case of polymers, the solvation force does not show oscillations. A long range repulsive force was observed, which increases enormously at distances comparable to the molecular size [42, 43]. It has been found that the layering effect decays within 2 to 3 segmental layers (The data are taken from computer simulations presented by *Bitsanis and Hadziioannou* [44] and *Baschnagel and Binder* [30]. Here, one segment has the meaning of one monomer).

The confined ultra thin films exhibit two different responses to the shear: liquid–like, where the film responses to the deformation by flow and solid–like response, where the critical shear is needed to activate sliding. For 'simple' liquids the solid–like response appears approximately at gap sizes, where the oscillations in the normal force become visible. Klein and Kumacheva [34] have explained the effect by assuming freezing of the molecule motions, accomplished by ordering in crystal structures, if the gap size becomes as small as a few molecular layers. They called the phenomena 'confined–induced phase transition' (or 'confinement–induced solidification' by other authors). The other hypothesis is that in the solid–like regime, the film starts to exhibit order–disorder transitions in thermally fluctuating mode – 'stratification–induced order–disorder phase transitions' [45, 46].

For polymers the situation is more complex, since the viscosity of polymers is much higher. Consequently, the measured values at SFA experiments are the effective dynamic ones but not the equilibrium ones [47], as it is supposed in the computer simulations. Probably, this is the reason why, in contrast to the experiment, the computer simulations do not show a solid like transition, e.g. [44, 47]. In the latter reference the authors concluded that the polymer thin films, qualitatively, have the same behavior as 'simple' liquids, but the solid—like response occurs at significantly larger distances. The authors reported further

that the film thickness at the confined-induced phase transition does not depend on the molecular weight. The work of van Alsten and Granick [47] is not a manifest of the common accepted model. The model emerging from the literature survey does not include the idea of solid-like transition. Most of the authors support the asumption that the polymer molecules close to the substrate have strongly restricted motions in normal direction, but the molecules further from the interfacial region (in the middle of the gap) have motions similar to those in the bulk [42, 44].

Almost all authors observed a sluggishness of the dynamics with decreasing gap size for both 'simple' liquids and polymers in confined geometry [48, 30, 34, 47]. The observations are done on the basis of viscosity measurements [34], and increase of the relaxation times [47] at the gap size, where the confined-induced phase transition was observed. The recent works of Mukhopadhyay et al. [48] and Braun and Peyrard [49] shed more light on the questions concerning the dynamic and structure of highly confined systems. In these works, the translation diffusion coefficient was measured from the edges towards the centre of the contact in the SFA. The authors observed an exponential decay of the diffusion coefficient in the neighborhood of the center region, but the deduced activation volume for diffusion is larger than the bulk value. Mukhopadhyay et al. [48] concluded that even after the confined-induced phase transition, diffusion appears to involve cooperative rearrangements of many molecules. Furthermore, the shape of the recorded curve at the closest point to the centre suggests that the confined structure is heterogeneous¹. Braun and Peyrard [49] assume on the basis of their computer simulation and experimental results from Klein and Kumacheva and Mukhopadhyay et al. that the solid phase (the phase observed after confined-induced phase transition) is not a perfect crystal state. Instead, the structure of that phase is modulated by the shape of the confining surfaces, so that well-ordered domains are separated from regions with lower density, where the diffusion of particles is possible. The influence of the confining surfaces on the confined-induced phase structure has also been discussed in the following works [37, 50].

With respect to the results specified above, scattering experiments should give a clear answer, how the structure of the matter after the confined-induced phase transition really looks like. Moreover, they can provide information about the still open question, how the confined fluids organizes in-plane. In one of the earlier works of *Schoen et al.* it was predicted that the fluid 'freezes in an fcc-like structure'. The authors simulated a system of rare-gas atoms confined between parallel fcc (100) planes consisting of rigidly fixed atoms of the same type. The packing in a crystal lattice was also supposed by other authors [51, 36]. The local symmetry observed in liquid lead on a Si surface [8] and the heterogeneities suggested by *Mukhopadhyay et al.* [48] prove that fluid molecules tend to organize themselves in-plane.

The scattering experiments performed up to now used large gap sizes [38, 39], far away from the region where confined effects are observed by the SFA measurements. Recently, Seeck

¹Citation: 'The scale of heterogeneity must have been impressively large, if one considers that these heterogeneities do not average out despite the long averaging time and the fact that the laser beam spot (350 nm) exceeded the size of the diffusing molecules so much'.

and co-workers [51] succeeded in measuring the reflectivity curves of ultra thin OMCTS film confined between Si wafers. The observed film thickness was less than 25 Å. According to the SFA data, the measurements were performed beyond the confined-induced phase transition. The authors suggested a scheme of structure evolution in dependence of the pressure similar to that supposed in the Monte Carlo simulation by Diestler et al. [52]. Despite of the fact that the first work on ultra thin films probed by X-rays already appeared, the experimental difficulties obstruct the scattering methods to become routine methods for the investigation of ultra thin confined films. The experiments need a well-collimated, narrow and high-intense beam. According to that, neutrons seem to be not a proper choice for the investigation of 'simple' liquid confined films. Taking into account that the confined effects of polymers appear at larger gap sizes, neutron measurements could be more practical here, because they allow the variation of the scattering contrast along the polymer chain.

The confined experiments put a strong requirement on the substrates as well. They have to be molecularly clean and smooth in the range of at least a few square millimeters. It turned out that this requirement is a real challenge for the crystal industry.

Chapter 3

Scattering theory

In this work scattering methods are used for the investigation of confined soft matter and thin films. In the following the used methods are theoretically introduced.

3.1 Reflectivity theory

3.1.1 Fresnel's formulae

Assuming that there are no charges and currents in the medium, it follows from Maxwell's equations, that the electric field \vec{E} at point \vec{r} is given by

$$\nabla^{2}\vec{E}(\vec{r},\omega) - k^{2}\epsilon(\vec{r},\omega)\mu(\vec{r},\omega)\vec{E}(\vec{r},\omega) + \left[\nabla \ln \mu(\vec{r},\omega)\right] \times \nabla \times \vec{E}(\vec{r},\omega) + \left[\vec{E}(\vec{r},\omega) \cdot \nabla \ln \epsilon(\vec{r},\omega)\right] = 0 \quad (3.1)$$

where ω is the angular frequency, $k = 2\pi/\lambda$, λ is the wavelength in the vacuum and μ and ϵ are the magnetic permeability and dielectric constant of the material, respectively [53]. In general, μ and ϵ depend on the spacial coordinate \vec{r} and the angular frequency ω . If μ and ϵ are constant, the equation above simplifies to the so-called Helmholtz equation

$$\left(\nabla^2 + k^2 n^2\right) \vec{E}(\vec{r}, \omega) = 0, \tag{3.2}$$

where $n = \sqrt{\mu \epsilon}$ is the refractive index of the medium. The refractive index may also be expressed by:

$$n = 1 - \delta + i\beta. \tag{3.3}$$

Here, δ and β are the dispersion and the absorption of the medium, respectively. For a homogeneous medium and far away from absorption edges, δ und β can be approximated by

$$\delta = \frac{\lambda^2}{2\pi} r_e \rho$$

$$\beta = \frac{\lambda}{4\pi} \mu, \tag{3.4}$$

where r_e is the classical electron radius $e^2/4\pi\epsilon_0mc^2=2.814\times 10^{-5}$ Å and ρ is the electron density. δ is of the order of 10^{-6} for X–rays; thus the real part of the refractive index for X–rays is slightly smaller than one. β is usually one or two orders of magnitude smaller than δ for X–rays.

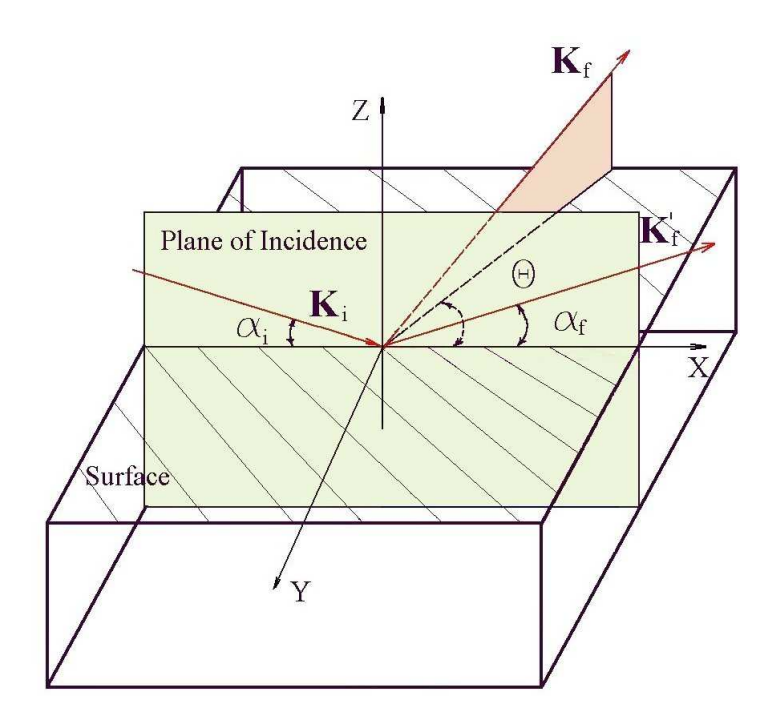


Figure 3.1: Scattering geometry. $\mathbf{K_i}$ is the wave vector of the incomming beam, $\mathbf{K_f}$ and $\mathbf{K'_f}$ are the wave vectors of the scattered and specular reflected waves, respectively. The intensity of the specular reflected wave is recorded, when the angle α_f is kept equal to the angel α_i (with $\Theta = 0$).

The simplest solution of the Helmholtz equation is a harmonic plane wave ¹

$$E(\vec{r}) = \vec{E}_0 \exp[i(\vec{k} \cdot \vec{r})]. \tag{3.5}$$

Here, the wave vector, \vec{k} can be expressed by $k\vec{s}$, where \vec{s} is the unit vector in direction of the wave propagation. If a plane wave impinges a boundary between two homogeneous media with refractive indices n_1 and n_2 , it splits into transmitted and reflected waves. The relation between the incoming wave and the transmitted and reflected waves is given by

$$\vec{E}_r = \mathbf{R}\vec{E}_i \tag{3.6}$$

$$\vec{E}_t = \mathbf{T}\vec{E}_i \tag{3.7}$$

¹The time dependence is not displayed here, since it is of no interest for the description of the experiments.

where \vec{E}_i is the electric field vector of the incoming wave and \vec{E}_r and \vec{E}_t are the vectors of the reflected and the transmitted fields, respectively. In general, the so called Fresnel transmission and reflection coefficients, \mathbf{T} and \mathbf{R} are matrices. They depend on the polarization of the incoming and reflected beams. In the used experimental setup the radiation is mainly s-polarized (i.e. the incoming beam is linearly polarized with the electric field vector in Y direction, see $\mathbf{Fig. 3.1}$). Additionally, in the current experiment, the reflected and transmitted waves have the same polarization. Therefore, only the diagonal elements of \mathbf{T} and \mathbf{R} , i.e. t_{yy} and t_{yy} , are different from zero. With respect to the boundary conditions that the tangential components of the electric and magnetic fields have to be continuous at the surface, for t_{yy} and t_{yy} the following equations are obtained [53].

$$t_{yy} = t = \frac{2k_{i,z}}{k_{i,z} + k_{t,z}}$$

$$r_{yy} = r = \frac{k_{i,z} - k_{t,z}}{k_{i,z} + k_{t,z}}.$$
(3.8)

Here $k_{i,z}$ and $k_{t,z}$ are the z-component of the incoming and transmitted waves, respectively.

$$k_{i,z} = k \sin \alpha_i \tag{3.9}$$

$$k_{t,z} = nk \sin \alpha_t = k\sqrt{n^2 - \cos^2 \alpha_i}, \tag{3.10}$$

where α_i is the incoming angle (see Fig. 3.1). Here, n denotes the ratio n_2/n_1 . Supposing that the first medium is vacuum, $n_1 = 1$ and $n = n_2$.

The angle where the expression in the square root in Eq. 3.10 becomes zero, is called critical angle $\alpha_{i,c}$. Using Eqs. 3.10, 3.3 and 3.4 for $\alpha_{i,c}$ the following useful approximation is obtained:

$$\alpha_{i,c} \approx \sqrt{2\delta} = \lambda \sqrt{\frac{r_e \rho}{\pi}}$$
 (3.11)

The intensities of the reflected wave, I_r and of the transmitted wave, I_t , are proportional to $|\mathbf{R}|^2$ and $|\mathbf{T}|^2$, respectively. These intensities as a function of the incoming angle, α_i , normalized to the critical angle, $\alpha_{i,c}$, are presented in **Fig. 3.2**. The figure shows that in the case, where the absorption is zero, the reflectivity is a constant and equal to one, i.e. the incoming wave is totally reflected until α_i becomes equal to $\alpha_{i,c}$. For larger incoming angles the intensity decreases dramatically, and at large angles it is proportional to $1/q_z^4$. Here, $\vec{q} = \vec{k_f} - \vec{k_i}$ is the wavevector transfer, where k_i and k_f are the wave vectors of the incoming and the reflected waves $(q_z = 4\pi \sin(\alpha_i)/\lambda)$.

3.1.2 Multiple interfaces

The considerations above only took reflections from a single surface into account, but for practical applications layer systems are more important. The general case covers a system of N-1 layers on a substrate (**Fig. 3.3**). The vacuum is usually treated as the first layer

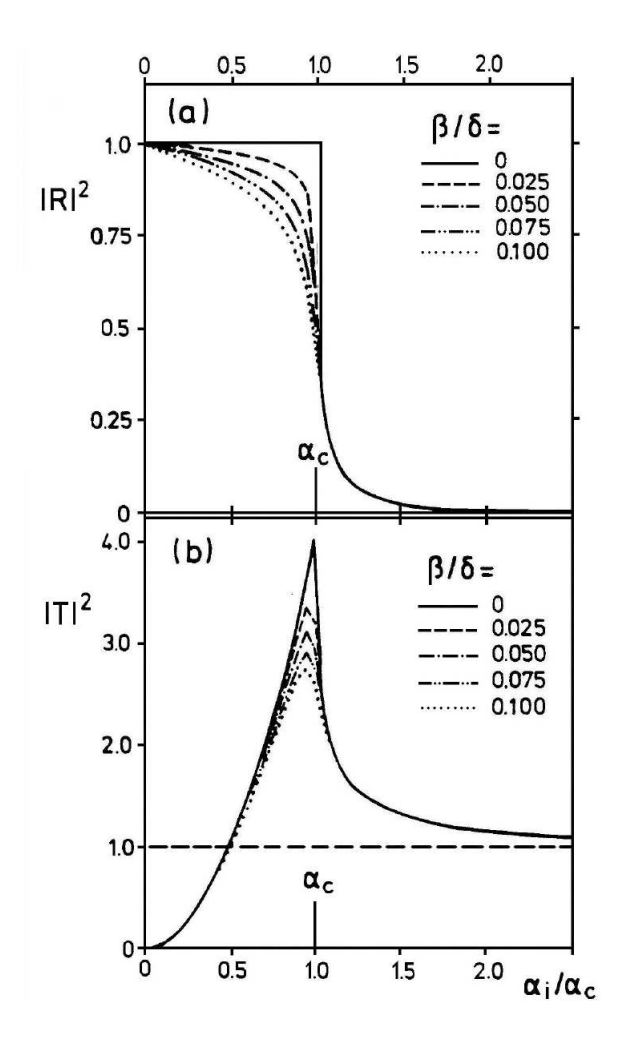


Figure 3.2: Intensities of the reflected and transmitted waves as a function of the incoming angle α_i normalized to $\alpha_{i,c}$. The presented curves are calculated for different absorptions β [54].

and the substrate as layer N+1. The zero point of the z-axis is at the first interface (layer 1/layer 2), and all other layers are positioned at negative z values. The amplitude of the incoming beam T_1 is normalized to one. Using Parratt's formalism [55], a recursive expression for the ratio of the reflected wave to the incoming wave, R_j/T_j , in the layer j, can be obtained

$$X_{j} = \frac{R_{j}}{T_{j}} = \exp(-2ik_{z,j}z_{j}) \frac{r_{j,j+1} + X_{j+1} \exp(2ik_{z,j+1}z_{j})}{1 + r_{j,j+1}X_{j+1} \exp(2ik_{z,j+1}z_{j})},$$
(3.12)

where

$$r_{j,j+1} = \frac{k_{z,j} - k_{z,j+1}}{k_{z,j} + k_{z,j+1}}$$
(3.13)

is the Fresnel coeffcient of the j-th interface with $k_{z,j} = k(n_j^2 - \cos^2 \alpha_i)^{1/2}$ and X_j is the ratio of R_j to T_j in layer j. Usually, the substrate is much thicker than the penetration depth of the X-rays, and the reflection from the bottom of the substrate is thus neglected. In other words, $R_{N+1} = X_{N+1} = 0$. Taking into account that the incident wave is normalized to one $(T_1 = 1)$, the speculary reflected intensity from the first layer R_1 can be obtained by Eq. 3.12 after N iterations.

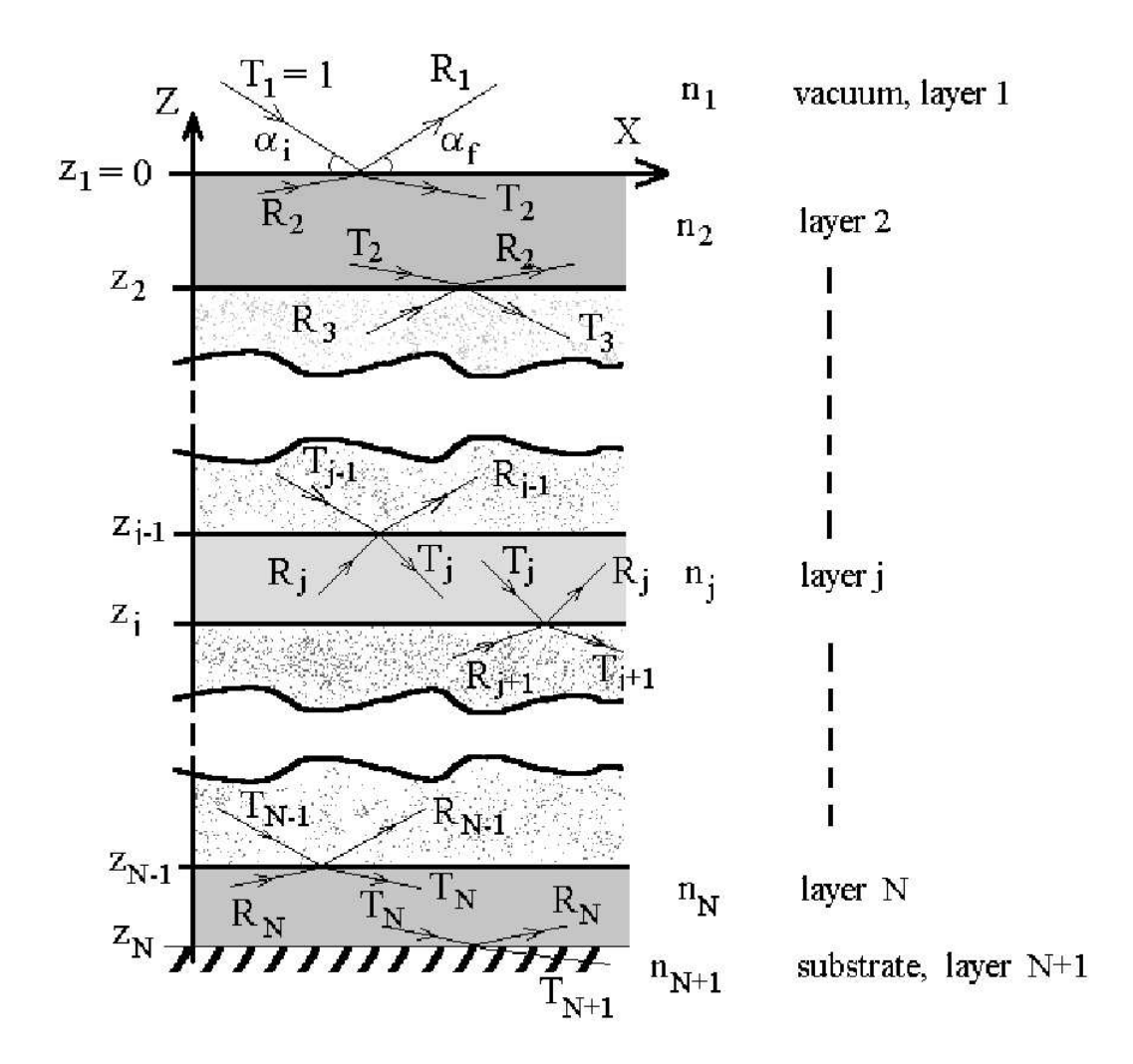


Figure 3.3: Multiple layer system. The vacuum is treated as the first layer and the substrate as layer N + 1.

3.1.3 Roughness

The equations for the reflected and transmitted intensity in the previous two sections were derived assuming that the refractive indices n_j do not depend on the spatial coordinates

and the wavelength within a layer ($\mu = \text{const.}$ and $\epsilon = \text{const.}$). Constant values of μ and ϵ allow to simplify Eq. 3.1 to the Helmholtz equation (Eq. 3.2), which can be solved analytically. On the other hand, taking μ and ϵ independently from the spatial coordinates, the information about the structure of the interface is lost, and the real rough interface is approximated by a sharp one.

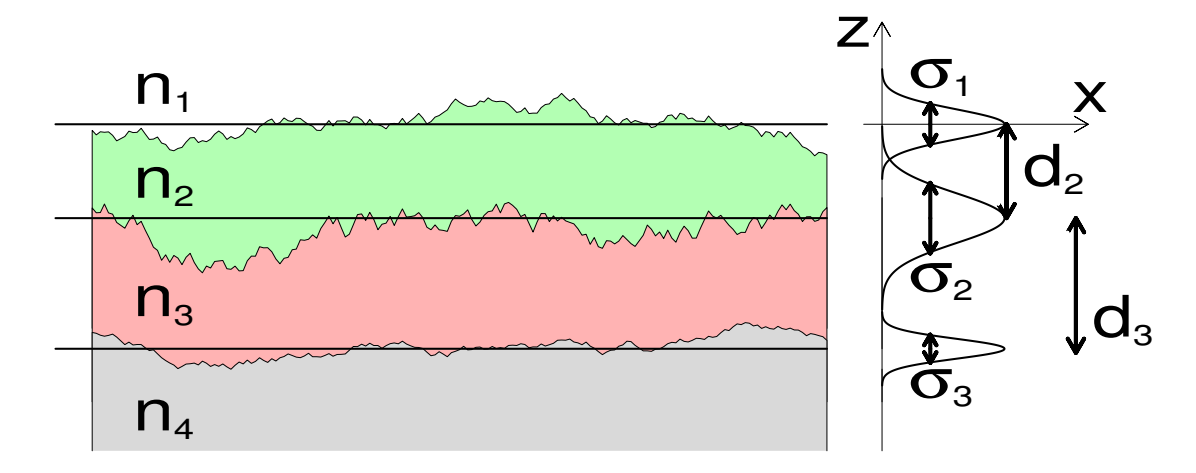


Figure 3.4: Two layers with refractive indices n_2 and n_3 . The vacuum is treated as the first layer with refractive index n_1 and the substrate as last layer with refractive index n_4 . σ_1 , σ_2 , and σ_3 are the thicknesses of the interfaces between the layers.

The expressions for the real rough surface can be obtained from the ideal case as shown below. Since the specular reflectivity is of interest (**Fig. 3.1**), the wavevector transfer has only a z-component. Hence, it can be assumed that the refractive index profile is only a function of the z-component. For instance, an error function refractive index profile can be taken for the description of a rough interface between the layers j and j + 1:

$$n_j(z) = \frac{n_j + n_{j+1}}{2} - \frac{n_j - n_{j+1}}{2} \operatorname{erf}\left(\frac{z - z_j}{\sqrt{2}\sigma_j}\right),$$
 (3.14)

where

$$\operatorname{erf}(z) = \frac{2}{\sqrt{\pi}} \int_{0}^{z} \exp(-t^{2}) dt$$
 (3.15)

and σ_j is the measure of the surface roughness (see **Fig. 3.4**). Then, for rough interfaces Eq. 3.12 changes to [56, 57]:

$$X_{j} = \frac{R_{j}}{T_{i}} = \exp(-2ik_{z,j}z_{j}) \frac{\tilde{r}_{j,j+1} + X_{j+1} \exp(2ik_{z,j+1}z_{j})}{1 + \tilde{r}_{i,j+1}X_{j+1} \exp(2ik_{z,j+1}z_{j})},$$
(3.16)

with modified reflection coefficients

$$\tilde{r}_{j,j+1} = r_{j,j+1} \exp(-2k_{z,j}k_{z,j+1}\sigma_j^2). \tag{3.17}$$

If the interface follows a hyperbolic tangent profile

$$n_j(z) = \frac{n_j + n_{j+1}}{2} - \frac{n_j - n_{j+1}}{2} \tanh\left(\frac{\pi}{2\sqrt{3}} \frac{z - z_j}{\sigma_j}\right),$$
 (3.18)

one obtains for $\tilde{r}_{j,j+1}$

$$\tilde{r}_{j,j+1} = \frac{\sinh\left[\sqrt{3}\sigma_j(k_{z,j} - k_{z,j+1})\right]}{\sinh\left[\sqrt{3}\sigma_j(k_{z,j} + k_{z,j+1})\right]}.$$
(3.19)

Eq. 3.16 can be applied, if the layers in the system are thick compared to the the roughness of the interfaces $(\sigma_j \ll d_j)$. Otherwise, the "effective—density model" must be used [56]. Here, the profiles at the interfaces are determined by functions $Y_i(z)$ given by

$$Y_j(z) = \tanh\left(z\frac{\pi}{2\sqrt{3}\sigma_j}\right) \tag{3.20}$$

or by

$$Y_j(z) = \operatorname{erf}\left(\frac{z}{\sqrt{2}\sigma_j}\right).$$
 (3.21)

 $Y_j(z)$ goes to ± 1 , if $z \to \pm \infty$. Using the functions $Y_j(z)$ the fraction of the material j, $W_j(z)$, at position z can be defined as

$$W_{j}(z) = \begin{cases} \frac{1}{2} \left[1 + Y_{j}(z - z_{j}) \right] & \text{for } z \leq \zeta_{j} \\ \frac{1}{2} \left[1 - Y_{j}(z - z_{j-1}) \right] & \text{for } z > \zeta_{j}. \end{cases}$$
(3.22)

Here, the coordinate ζ_j denotes the depth, where the upper and lower profiles of the interface j are connected continuously,

$$\zeta_j = \frac{\sigma_j z_{j-1} + \sigma_{j-1} z_j}{\sigma_j + \sigma_{j-1}}.$$
(3.23)

At the substrate (j = N + 1), z_{N+1} goes to $-\infty$, σ_{N+1} is equal to zero and ζ_{N+1} goes to $-\infty$. At the first interface (j = 1) $z_0 \to +\infty$ and $\sigma_0 = 0$, $\zeta_1 \to +\infty$. With Eq. 3.22 the whole dispersion profile can be defined by

$$\delta(z) = \frac{\sum_{j=1}^{N+1} \delta_j W_j(z)}{\sum_{j=1}^{N+1} W_j(z)},$$
(3.24)

where δ_j is the nominal dispersions in the layer j. For $\sigma_j \ll d_j$ the refractive index profile is approximated by a system consisting of N independent rough layers. Thus, the reflectivity of this profile can be calculating by Eq. 3.16 with corresponding modified reflection coefficients, $\tilde{r}_{j,j+1}$. For $\sigma_j \geq d_j$ Eq. 3.24 splits the refractive index profile into a large number of very thin and completely smooth sublayers. Then, Eq. 3.12 can be used to calculate the reflectivity. However, in this case, the refined parameters δ_j , σ_j and $d_j = z_{j-1} - z_j$ have not the same definition as above. Here, δ_j is the effective dispersion at depth z, σ_j defines the width of the intermediate region between layers j and j+1, and d_j gives the distance between the inflection points of $W_j(z)$.

3.1.4 The critical angle at the confined reflectivity curves

In Fig. 3.5 the scattering geometry used for the measurements of the confined films reflectivity curves is presented. The beam comes from the left side and its width and the detector aperture were set to 0.2 mm in the vertical. The gap size at the confined condition is of the order of hundreds of Angstroms. Hence, the intensity of the radiation going directly into the gap (through the liquid) is about five orders of magnitude less than the radiation which penetrates the wafer. Therefore, if both wafers are parallel, the beam runs mainly as shown in Fig. 3.5, and determines also the main part of the signal measured by the detector. In this case, according to Snell's law, the effect of the critical angle at the liquid (polymer)/substrate interface will not be seen in the reflectivity curves, since both wafers have the same refractive index.

3.2 Diffuse scattering theory

3.2.1 Born approximation

Eq. 3.1 presented in the beginning of the previous section cannot be solved generally. Using an approximation that μ and ϵ are constants, the Helmholtz equation is obtained. In a more general case, μ and ϵ depend on the spatial coordinate \vec{r} , but they are effectively constant over distances of the order of the wavelength $\lambda = 2\pi/k$. Then, the last two terms on the left side of Eq. 3.1 can be neglected and one obtains

$$\nabla^2 \vec{E}(\vec{r}, \omega) - k^2 n^2(\vec{r}, \omega) \vec{E}(\vec{r}, \omega) = 0. \tag{3.25}$$

Eq. 3.25 can be solved using Green's function theory [53], and its solution is

$$\vec{E}(\vec{r},\omega) = \vec{E}_0(\vec{r},\omega) + \int F(\vec{r'},\omega) \vec{E}(\vec{r'},\omega) \frac{e^{ik|\vec{r}-\vec{r'}|}}{|\vec{r}-\vec{r'}|} d^3r', \tag{3.26}$$

where the integral has to cover the sample volume and $\vec{E}_0(\vec{r},\omega)$ is the electric field vector of the incident wave. The function $F(\vec{r},\omega)$ is called the scattering potential of the medium and it is defined as:

$$F(\vec{r},\omega) = \frac{k^2}{4\pi} [n^2(\vec{r},\omega) - 1]. \tag{3.27}$$

Eq. 3.26 is a sum of the incident and the scattered field, and the integral describing the scattered wave again depends on $\vec{E}(\vec{r},\omega)$. Assuming weak coupling between incident and scattered radiation, in the integral $\vec{E}(\vec{r})$ can be replaced by the incident field $\vec{E}_0(\vec{r})$, and one obtains a first-order approximation of the solution².

$$\vec{E}(\vec{r}) = \vec{E}_0(\vec{r}) + \int F(\vec{r'}) \vec{E}_0(\vec{r'}) \frac{e^{ik|\vec{r}-r'|}}{|\vec{r}-\vec{r'}|} d^3r'$$
(3.28)

 $^{^{2}\}omega$ dependence in the equations further below will no longer be displayed, because it is of no interest for further calculations here.

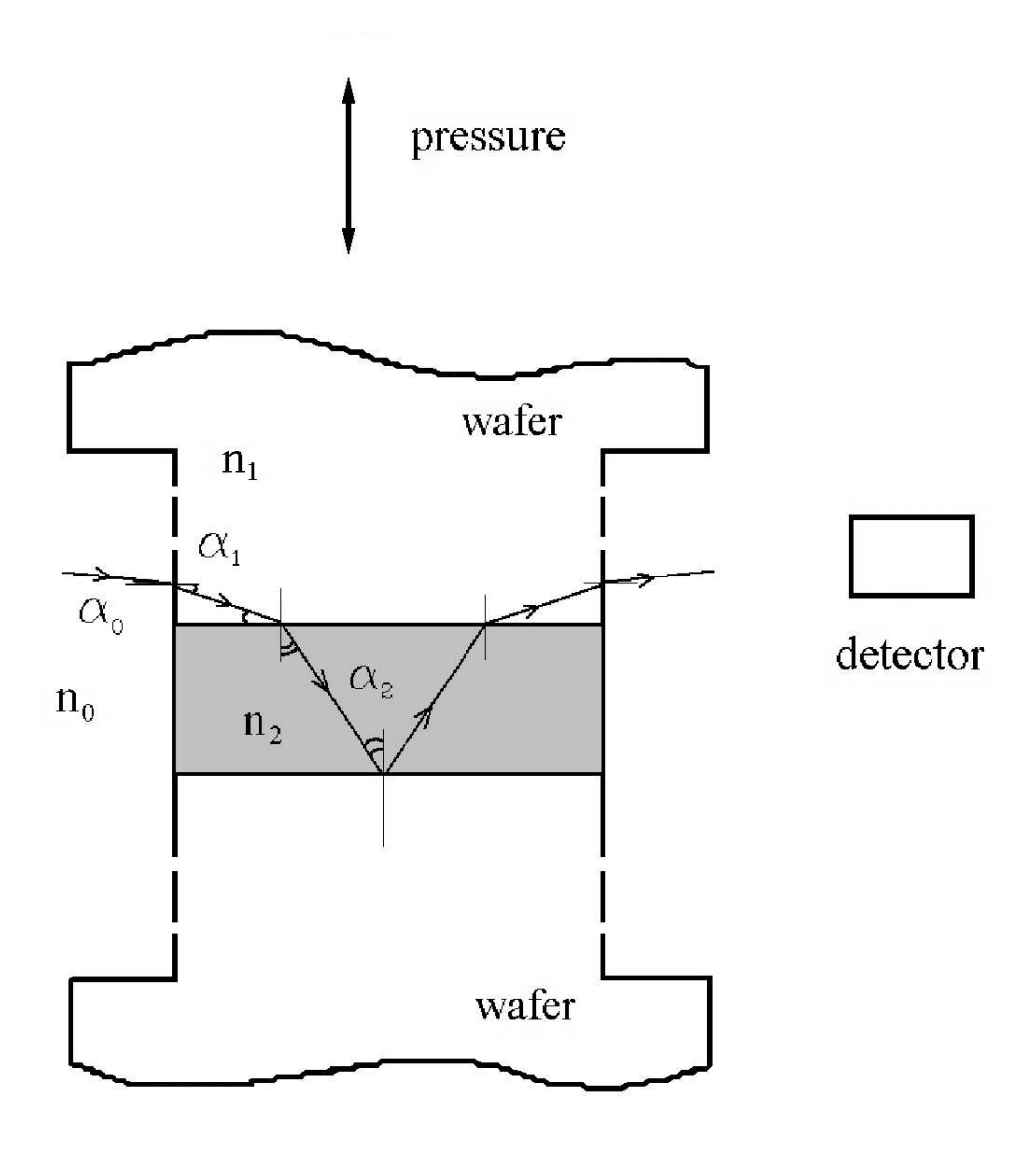


Figure 3.5: Scattering geometry used for the measurements of the confined films reflectivity curves.

This approximation is known as the (first-order) Born approximation. The Born approximation can be used, if the intensity of the scattered wave is small in comparison with the intensity of the incident wave. The calculations of the scattered intensity in terms of the first-order Born approximation is also known as kinematical scattering theory.

For large \vec{r} the following approximation can be applied [53]:

$$\frac{e^{i\vec{k}|\vec{r}-\vec{r'}|}}{\left|\vec{r}-\vec{r'}\right|} \approx \frac{e^{i\vec{k}\cdot\vec{r}}}{\left|\vec{r}\right|}e^{-i\vec{k}\cdot\vec{r'}},\tag{3.29}$$

and if the E_0 is replaced by the $e^{i(\vec{k_0}\cdot\vec{r})}$, Eq. 3.28 can be written in the form

$$\vec{E}(\vec{r}) = \vec{E}_0(\vec{r}) + A(\vec{k}, \vec{k_0}) \frac{e^{i\vec{k}\cdot\vec{r}}}{|\vec{r}|},$$
(3.30)

where

$$A(\vec{k}, \vec{k_0}) = \int F(\vec{r'}) e^{i(\vec{k} - \vec{k_0}) \cdot \vec{r'}} d^3 r'$$
(3.31)

is the scattering amplitude. The structure factor, S(q) (where $q = \vec{k} - \vec{k}_0$) is equal to $|A|^2$ and it is proportional to the scattered intensity.

It can be shown [23] that in the first-order Born approximation the diffuse scattered intensity, I_{diff} , from a single film/air interface is given by

$$I_{diff}(q_x, q_z) = \frac{(\Delta \rho)^2}{q_z^2} \exp(-q_z^2 \sigma^2) \int \left[\exp\left\{ q_z^2 C(X) \right\} - 1 \right] \exp(-iq_x X) dX, \tag{3.32}$$

where C(X) is the height-height correlation function which describes the structure of the interface. Eq. 3.32 is in accordance with the experimental conditions, i.e. wide-open slits in Y direction (see **Fig. 3.1**), which means that the recorded intensity is already averaged over q_y . In the case of a liquid/air interface the logarithmic correlation function given by Eq. 2.11 has to be used. Inserting Eq. 2.11 into Eq. 3.32, and for q_x being much larger than the diffractometer resolution in X direction ³, the scattered intensity can be approximated by a power law [56]

$$I_{diff}(q_x, q_z) \sim q_x^{\eta(q_z)-1},$$
 (3.33)

where

$$\eta(q_z) = \frac{k_B T}{2\pi\gamma} q_z^2 \tag{3.34}$$

The shape of I_{diff} as a function of q_x at fixed q_z is shown in **Fig. 3.6**. For thinner films, q_{vdW} is much larger than q_g and $q_{l,c} = q_{vdW}$ (see Eqs. 2.7 and 2.8). Here, $q_{l,c}$ appears as a 'kink' in the presented curve. If the film is thick, q_{vdW} becomes very small and the lower cutoff is in principal determined by q_g . Thus, $q_{l,c}$ moves to smaller q_x values. Generally, the diffractometer resolution in X direction exceeds q_g and the 'kink' merges with the specular peak and disappears from the curve.

3.2.2 Distorted-Wave Born approximation

In the vicinity of the critical angle the scattered intensity is no longer small compared to the incident intensity, and the Born approximation can not be applied. The multiple scattering effects are taken into account in the so-called Distorted-Wave Born approximation. Here, the scattering potential is presented as

$$V(\vec{r}) = V_0 + \delta V(\vec{r}), \tag{3.35}$$

³For the diffractometer resolution see Section 4.1

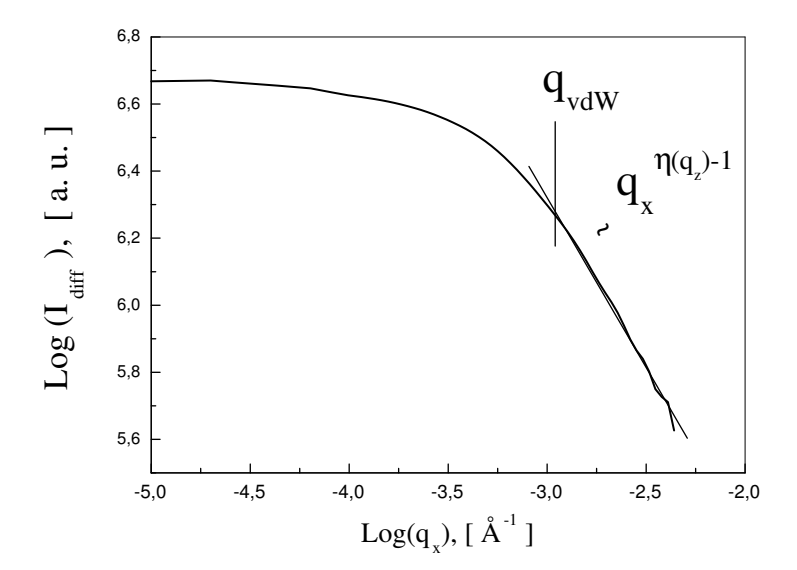


Figure 3.6: The dependence of I_{diff} as a function of q_x at $q_z = 0.25 \text{ Å}^{-1}$ for film with thickness 160 Å at 150°C. The curve was calculated at $\gamma = 0.030 \text{ N/m}$

where V_0 corresponds to the scattering potential in the case of sharp-interface systems and $\delta V(\vec{r})$ is a small perturbation representing the nano-scale structure in $V(\vec{r})$. The first-order approximation of the solution in terms of the Distorted-Wave Born approximation is obtained by replacing the scattering potential $F(\vec{r})$ in Eq. 3.26 by $V(\vec{r})$ and $\vec{E}(\vec{r}')$ by the solution of the Helmholtz equation for the transmitted wave given in Eq. 3.7. The strict calculations of the scattered intensity in terms of the distorted-wave Born approximation is presented in e.g. Sinha et al. [23] and Vineyard [58]. As a final result, for a single interface the diffuse scattered intensity is given by

$$I_{diff} \approx |\mathbf{T}(\alpha_{\mathbf{i}})|^2 S(\vec{q}) |\mathbf{T}(\alpha_{\mathbf{f}})|^2,$$
 (3.36)

where **T** is the transformation matrix from Eq. 3.7, α_i and α_f are the incident and reflection angles, respectively.

The diffuse scattered intensity in terms of the distorted—wave Born approximation for multiple layer systems is more complicated. It was calculated by *Holy and Baumbach* [59]

$$I_{diff}(\vec{q}) = \frac{\mathcal{G}k^2}{8\pi^2} \sum_{j,k=1}^{N} (n_j^2 - n_{j+1}^2) (n_k^2 - n_{k+1}^2)^*$$

$$\times \sum_{m,n=0}^{3} \widetilde{G}_j^m \widetilde{G}_k^{n*} \exp\left\{-\frac{1}{2} \left[(q_{z,j}^m \sigma_j)^2 + (q_{z,k}^{n*} \sigma_k)^2 \right] \right\} S_{jk}^{mn}(\vec{q})$$
 (3.37)

where \mathcal{G} is the illuminated area, and the scattering function $S_{jk}^{mn}(\vec{q})$ is given by

$$G_{j}^{0} = T_{i;j+1}T_{f;j+1} q_{j}^{0} = \vec{k}_{i;j+1} + \vec{k}_{f;j+1}$$

$$G_{j}^{1} = T_{i;j+1}R_{f;j+1} q_{j}^{1} = \vec{k}_{i;j+1} - \vec{k}_{f;j+1}$$

$$G_{j}^{2} = R_{i;j+1}T_{f;j+1} q_{j}^{2} = -q_{j}^{1}$$

$$G_{j}^{3} = R_{i;j+1}R_{f;j+1} q_{j}^{2} = -q_{j}^{0}$$

Table 3.1: The possible analytic continuations, G_j^m , and the perpendicular wave vector transfers, $q_{z,j}^m$.

$$S_{jk}^{mn}(\vec{q}) = \frac{1}{q_{z,j}^m q_{z,k}^{n*}} \int \left(\exp\left\{ q_{z,j}^m q_{z,k}^{n*} C_{jk}(\vec{R}) \right\} - 1 \right) \exp(-i\vec{q}_{\parallel}\vec{R}) dR$$
 (3.38)

 $q_{z,j}^m$ and $q_{z,k}^n$ are the perpendicular wave vector transfers inside the layers j and k, respectively. The quantities \widetilde{G}_j^m can be obtained by

$$\widetilde{G}_j^m = G_j^m \exp(-iq_{z,j}^m z_j). \tag{3.39}$$

The wave vector transfers $q_{z,j}^m$ and G_j^m are given explicitly in **Table 3.1**. The upper indices m or n indicate one of the combinations given in the **Table 3.1**. $C_{jj}(\vec{R})$ in Eq. 3.38 is the height-height correlation function of the j interface. C_{jk} , with $j \neq k$, are the so-called cross-correlation functions. They account for the vertical roughness correlation between the interfaces. In the present data refinement it is supposed that no correlation between the interfaces exists $(C_{jk} = 0, \text{ for } j \neq k)$.

Chapter 4

Polymer thin films

4.1 Experimental setup

4.1.1 Description of the beamline and the sample environment

Most of the measurements have been carried out at beamline W1 (DESY/Hasylab, Hamburg). Synchrotron radiation with a wavelength $\lambda = 1.1808$ Å(E = 10.5 keV) has been used. A scheme of the beamline is shown in **Fig. 4.1**.

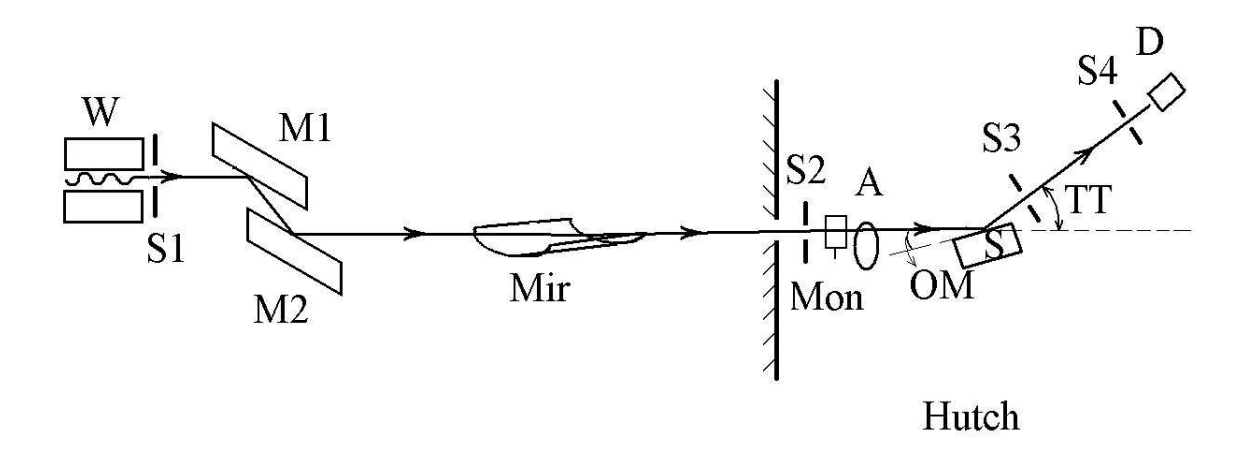


Figure 4.1: Scheme of the beamline W1. The length of the beamline is about 40 m. Further details are given in the text.

'White' synchrotron radiation is produced by a wiggler with a critical energy $E_{crit} = 8.4$ keV (denoted in the figure with **W**). The beam is collimated by the the first slit (**S1**) and monochromatized by a Si(111) double crystal monochromator denoted with **M1** and **M2**. The monochromatic beam hits a toroidal mirror (**Mir**), which suppresses higher harmonic radiation and focusses the beam to the sample position. Then, the beam enters the hutch, where it is additionally collimated by a second slit system (**S2**), monitored by an ionization

chamber (Mon), and filtered by attenuators mounted on a wheel (A). Finally it hits the sample S. The scattered radiation is recorded with a NaI scintillation detector D. Between the sample and the detector two guard slits (S3 and S4) serve to reduce the background and to define the resolution. The beam size that illuminates the sample is defined by the aperture of S2, and usually it was 2 mm in the horizontal and 0.2 mm in the vertical direction. The slits S3 and S4 have been aligned with the same opening.



Figure 4.2: The sample-cell. The cell has a diameter of about 100 mm and a height of 150 mm. The windows were made of kapton foil.

The reflectivity and diffuse scattering curves of each sample were measured in the temperature range 50°C to 230°C during heating and cooling runs, respectively. The cooling was carried out by switching the heater off until the desired temperature was reached. In order to avoid oxidation and dewetting of the samples during the heating, the sample chamber was evacuated down to 10^{-5} mbar. The sample–cell used for the measurements is presented in Fig. 4.2. Two different sample heaters¹ have been used which are shown in Fig. 4.3a and b. The maximum temperature that can be reached with heater (a) is 220°C. The device was replaced by heater (b) at a later date, which reaches a maximum temperature of 600°C. Heater (b) provides a more uniform temperature distribution within the sample, because the sample is heated from all sides. The temperature was mesaured using a Pt100 temperature sensor and controlled via a Lakeshore temperature controler model type 340 or 330.

¹The heaters have been designed by the author.

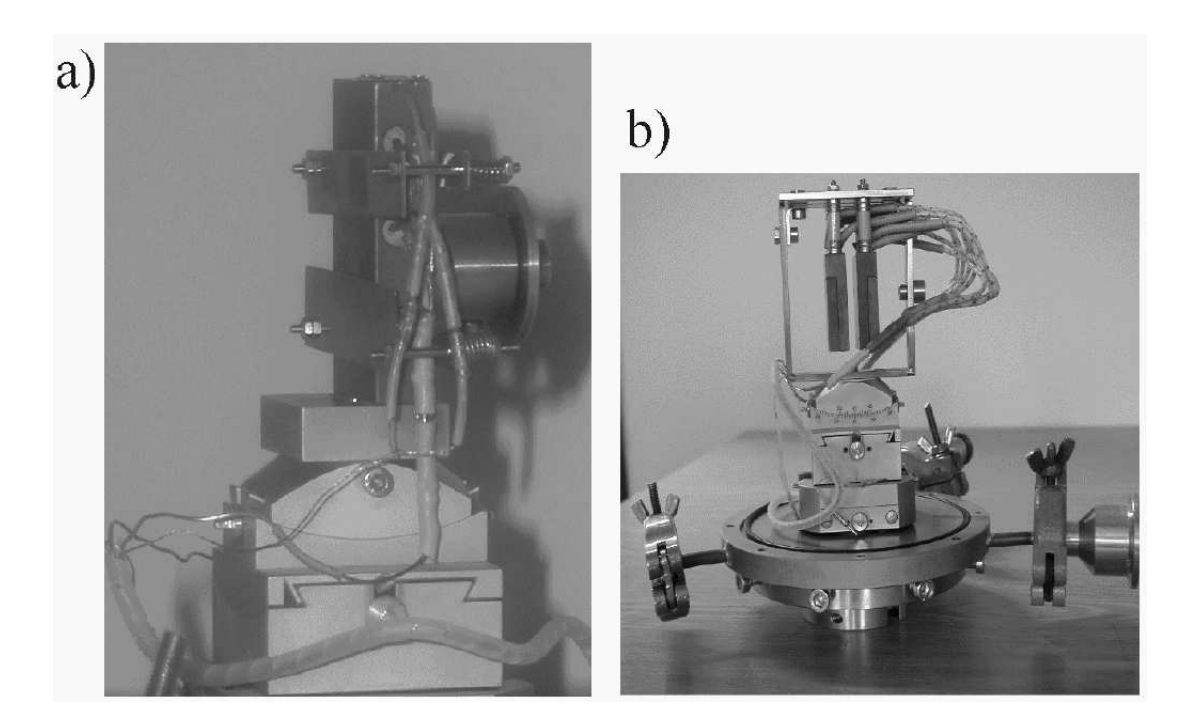


Figure 4.3: The sample-heaters. **a)** The heater with a maximum temperature of 220°C. **b)** This heater can be used up to a maximum temperature of 600°C. The sample is placed in the gap between the heat plates and it is fixed to one of the plate sufaces.

4.1.2 Scattering geometry

In **Fig. 3.1** a sketch of a sample under investigation was depicted. The coordinate system is related to the surface of the sample. The z-axis is perpendicular to the sample surface. The incoming and the specular reflected beams define the plane of incidence. The plane of incidence coincides with the (x, z)-plane. Thus, the wave vector transfer defined as

$$\vec{q} = \mathbf{K_f} - \mathbf{K_i},\tag{4.1}$$

has the coordinates

$$q_x = \frac{2\pi}{\lambda} (\cos \alpha_f \cos \Theta - \cos \alpha_i)$$

$$q_y = \frac{2\pi}{\lambda} (\cos \alpha_f \sin \Theta)$$

$$q_z = \frac{2\pi}{\lambda} (\sin \alpha_f + \sin \alpha_i)$$
(4.2)

If the angle α_i is kept equal to the angle α_f , and angle $\Theta = 0$ (**Fig. 3.1**), the reflectivity curve is measured. According to Eqs. 4.2, the reflectivity curve corresponds in reciprocal space to a q_z - scan at $q_x = 0$ (**Fig. 4.4**). In **Fig. 4.1** the angle **OM** is identical to the

incoming angle α_i and the angle $\mathbf{TT} = \alpha_i + \alpha_f$. Then, the reflectivity curves are recorded by simultaneously scanning angles \mathbf{OM} and \mathbf{TT} , where \mathbf{TT} is kept equal to $\mathbf{2OM}$.

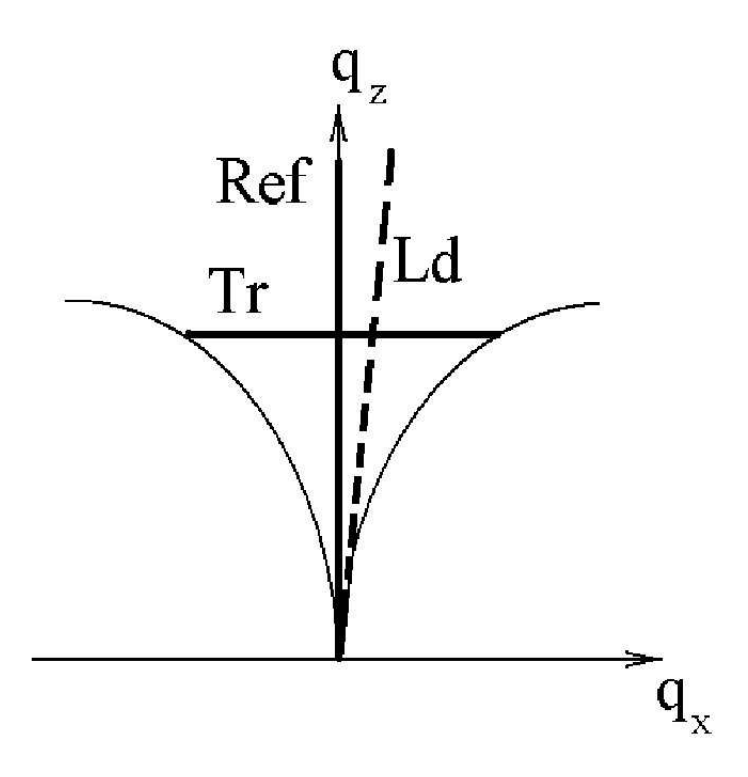


Figure 4.4: Scans in the reciprocal (q_x, q_z) plane. The regions below the thin solid wings are inaccessible for the in-plane scattering (angle $\Theta = 0$), because the beam or the detector are below the surface. Ref: reflectivity scan, Tr: transverse scan (rocking curves), Ld: longitudinal diffuse scan.

The scan, where the angle α_f has a small offset, δ , with respect to the angle α_i , is called longitudinal diffuse scan. In reciprocal space the longitudinal diffuse curve corresponds to the curve denoted with **Ld** in **Fig. 4.4**. The scan is performed again by simultaneously scanning angles **OM** and **TT**, where **OM** = $\alpha_i + \delta$ and **TT** = $2\alpha_i$.

The transverse scans in reciprocal space are q_x scans at almost fixed q_z (see the curve **Tr** in **Fig. 4.4**). The scans are recorded at fixed **TT** and scanning of **OM** from 0 to the value of **TT**.

Since the FWHM of the primary beam is about 0.02° , the offset δ of the longitudinal diffuse scattering curves is 0.05° . Thus, the longitudinal diffuse scattering curves are used to approximate the diffuse scattering under the reflectivity curves. According to the power law of the intensity dependence given in Eq. 3.33, the transverse scans were performed at different values of **TT**. For most of the samples, the values of **TT** were 3.77° , 2.69° , 2.15° and 1.61° . In reciprocal space these angles correspond to q_z equal to 0.35 Å^{-1} , 0.25 Å^{-1} , 0.25 Å^{-1} , respectively.

4.1.3 Diffractometer resolution

The diffractometer resolution can be calculated using the error propagation law (Gauss) applied to Eqs. 4.2. Assuming that α_i and α_f are small angles, and angle $\Theta = 0$ (in–plane scattering, $q_y = 0$), one obtains

$$\delta_{q_x}^2 = \left(\frac{\Delta\lambda}{\lambda}\right)^2 q_x^2 + k^2 (\alpha_i^2 \Delta \alpha_i^2 + \alpha_f^2 \Delta \alpha_f^2)$$

$$\delta_{q_z}^2 = \left(\frac{\Delta\lambda}{\lambda}\right)^2 q_z^2 + k^2 (\Delta \alpha_i^2 + \Delta \alpha_f^2), \tag{4.3}$$

where δ_{q_x} and δ_{q_z} are the resolutions parallel and perpendicular to the surface, $k=2\pi/\lambda$, $\Delta\alpha_i$ and $\Delta\alpha_f$ are the angular divergence and the acceptance of the incoming and outgoing radiation. For most surface X-ray experiments the monochromaticity of the radiation does not affect the resolution significantly. Assuming an energy resolution of 1 eV or better at 10 KeV $\Delta\lambda/\lambda = \Delta E/E$ is less than 10^{-4} , so that the first terms in eqs. 4.3 are orders of magnitude less than the second terms. An estimation of these is rather difficult, because $\Delta\alpha_i$ and $\Delta\alpha_f$ are determined by the distances between the beamline components, slit sizes and optical elements (here $\Delta\alpha_i$ depends on the monochromator and the mirror). In some synchrotron experiments the value of $\Delta\alpha_i$ can be significantly smaller than $\Delta\alpha_f$. Nevertheless, in order to simplify the estimation, it is supposed here that $\Delta\alpha_i = \Delta\alpha_f = \Delta\alpha$. Then, using $\sin\alpha_i \approx \alpha_i$ and $\sin\alpha_f \approx \alpha_f$ at small angles, and Eq. 4.2 one obtains

$$\delta_{q_x} \approx q_z \Delta \alpha \sqrt{1 - \frac{2\alpha_i \alpha_f}{(\alpha_i + \alpha_f)^2}}$$

$$\delta_{q_z} \approx 2k \Delta \alpha, \tag{4.4}$$

which is λ independent. The function under the square root in Eq. 4.4 can adopt values between 0 and 0.5. Hence,

$$\delta_{q_x} \le q_z \Delta \alpha \sqrt{\frac{1}{2}} \tag{4.5}$$

 $\Delta \alpha$ can be easily measured by determining the width of the primary beam without a sample. Since angle $\mathbf{TT} = \alpha_i + \alpha_f$ (Fig. 4.1), the FWHM of the primary beam is $\Delta \mathbf{TT} = 2\Delta \alpha_i$. Having $\Delta \mathbf{TT} = 0.018$, Eqs. 4.4 and 4.5 one obtains for δ_{q_x} and δ_{q_z} 10^{-4} and 10^{-3} Å⁻¹, respectively. Hence, the maximum length scale that can be measured in x-direction is $\approx 2\pi/\delta_{q_x} \approx 10^5$ Å, and in z-direction it is $\approx 2\pi/\delta_{q_z} \approx 10^4$ Å. The minimum length scales in both directions are determined by the maximum wave vector transfer, which is restricted either by the rapid decrease of the measured intensity with increasing of q_z or by the scattering geometry.

4.1.4 Polymer samples under study

Since polystyrene (PS) has a high glass transition temperature and builds stable films, PS spin-coated films on hydrophobic and hydrophilic Si substrates were studied. The glass

Sample Number	Type of the	Thickness of the	Molecular mass
	Si substrate	polymer layer [Å]	M_w [kg/mol]
n26	non-hydrophobic	200	650
n46	non-hydrophobic	400	650
n86	non-hydrophobic	800	650
n16	non-hydrophobic	1700	650
n36	non-hydrophobic	3000	650
h26	hydrophbic	200	650
h46	hydrophbic	400	650
h86	hydrophbic	800	650
h16	hydrophbic	1700	650
h36	hydrophbic	3000	650
n21	non-hydrophobic	200	123
n41	non-hydrophobic	400	123
n81	non-hydrophobic	800	123
n11	non-hydrophobic	1700	123
n31	non-hydrophobic	3000	123
h21	hydrophbic	200	123
h41	hydrophbic	400	123
h81	hydrophbic	800	123
h11	hydrophbic	1700	123
h31	hydrophbic	3000	123
n23	non-hydrophobic	200	30
n43	non-hydrophobic	400	30
n83	non-hydrophobic	800	30
n13	non-hydrophobic	1700	30
n33	non-hydrophobic	3000	30
h23	hydrophobic	200	30
h43	hydrophobic	400	30
h83	hydrophobic	800	30
h13	hydrophobic	1700	30
h33	hydrophobic	3000	30

Table 4.1: List of the studied samples. The molecular weights are measured by the supplier.

transition temperature of PS is about 100° C. Hence, it allows measurements below and above the glass transition without experimental complications². The melting temperature of the polymer is 200° C.

The polymer films were prepared from toluene solution of PS by spincoating onto Si wafers with native SiO_x layer (hyrophilic substrates, also called non–hydrophobic in the **Tab.**

 $^{^2}$ For comparison, the glass transition temperatures of polyethylene and polypropylene are about -20°C and -3.2°C, respectively [60].

4.1) and onto hydrogen–passivated Si surfaces (hydrophobic substrates). The thicknesses of the films can be estimated from the concentration of the polymer in the solution. After spincoating the samples were annealed in vacuum at 150°C for 12 h and slowly cooled down to room temperature.

Before the spin coating, the substrates were cleaned in an ultrasonic bath in a solution of a ceton, methanol and toluene for 5 min. Then, the samples were immersed in a solution of $\rm H_2O_2:H_2SO_4,\,v:v=1:3$ (pirhania etch) for 5 min and rinsed with destilled water several times. Pirhania solution removes organic contaminations but does not etch the native SiO_x layer. The hydrophobic surfaces were obtained by an additional treatment of the Si wafers with 10% water solution of HF for 10 s and rinsing with destilled water.

Polystyrene with molecular weights, $M_w = 650$, 123 and 30 kg/mol were used. The polymers were purchased from Pressurechemical Co.(USA) and they have molecular weight distributions, M_w/M_n of 1.06, 1.08, 1.06, respectively.

The monomer of the polystyrene is presented in **Fig. 4.5**. Depending on the steric orientation of the benzene ring there are three types of polystyrene: isotactic (i–PS), syndiotactic (s–PS) and atactic (a–PS, also called amorphous PS). The first two types have regular orientations of the benzene rings along the chain, and they are able to crystallize [61]. In contrast, the a–PS has no regular steric orientation and does not crystallize. Since a–PS was used here, it is not expected that the polymer has created a regular structure after spincoating on the wafers.

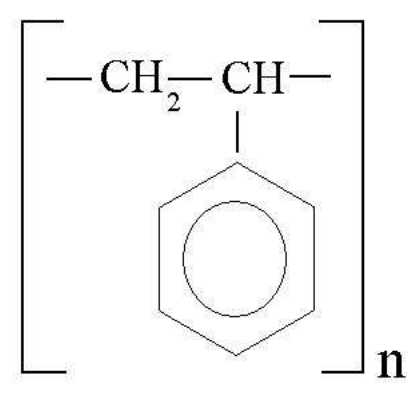


Figure 4.5: The monomer of the polystyrene.

A full list of the investigated samples³ is shown in **Tab. 4.1**. The sample notations are created from the first letter of the substrate type (<u>hydrophobic</u>, <u>non-hydrophobic</u>), the first number of the nominal film thickness⁴ ($\underline{2}00$, $\underline{4}00$, $\underline{8}00$, $\underline{1}700$, $\underline{3}000$) and the molecular mass ($\underline{6}50$, $\underline{1}23$, $\underline{3}0$).

³The samples have been prepared by Dr. Hyunjung Kim (APS, Argone).

⁴The film thickness depends on the polymer concentration in the solution. The values in **Tab. 4.1** are estimated in accordance with the polymer concentration in the solution.

The radii of gyration, R_g , of the PS with molecular masses 650, 123 and 30 kg/mol are 418, 183 and 86 Å, respectively. They are estimated by the equation for the end-to-end distance of the freely joined chain [62], $R_g^2 = \frac{Nl_0^2}{6}$, where N is the number of the monomers in the molecule and l_0 is the persistence length, which was assumed to be 10Å.

4.2 Results and Discussions

4.2.1 Reflectivity measurements.

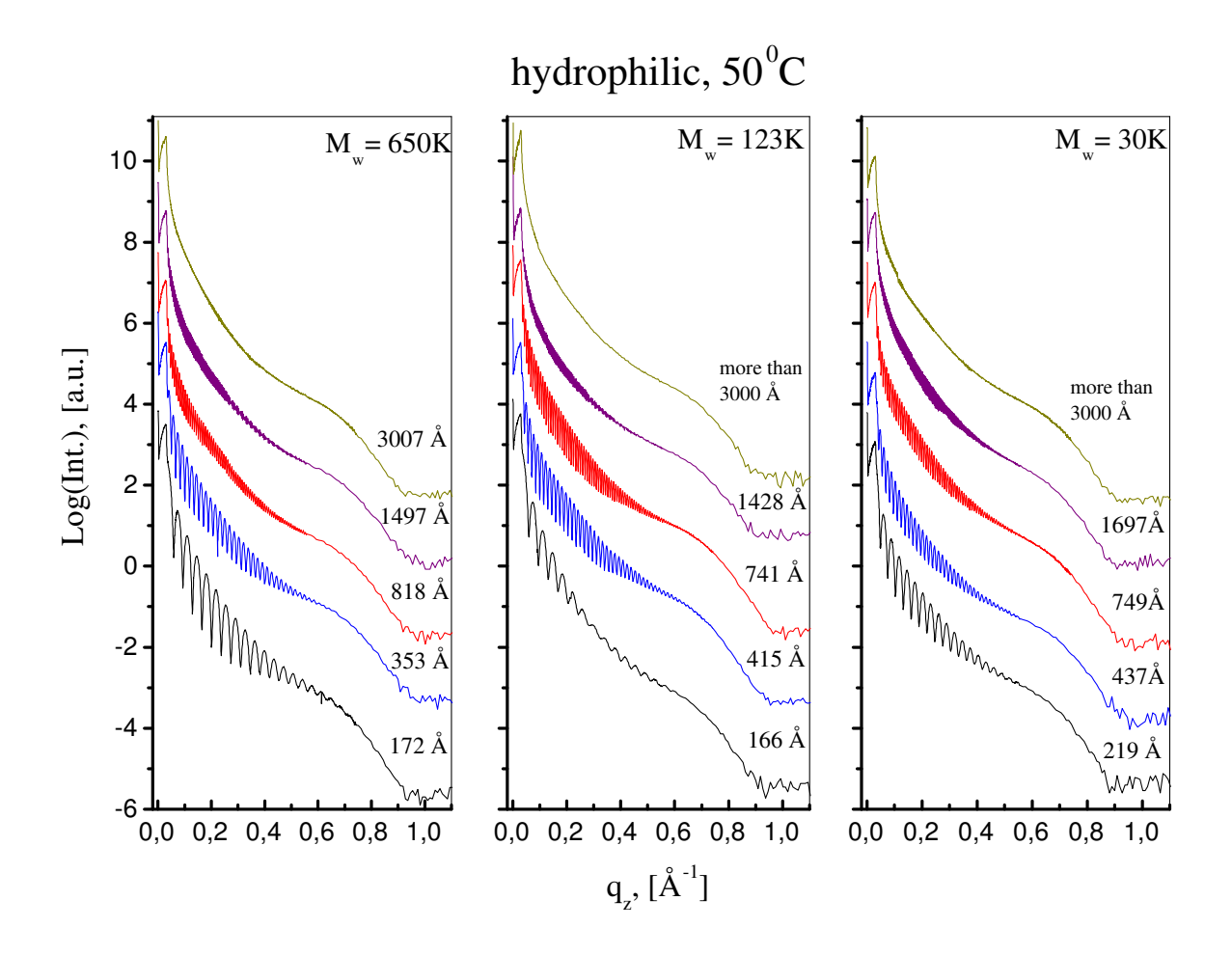


Figure 4.6: The reflectivity curves of all hydrophilic samples at 50°C. The film thicknesses in the figures are results taken from the data evaluation.

The reflectivity curves of all samples, which were measured at 50°C, are presented in **Fig.** 4.6 and **Fig.** 4.7. All curves are superpositions of 'fast' and 'slow' oscillations with q_z . The fast oscillation is determined by the thickness of the polymer film. The slow oscillation stems from a thin layer between the polymer film and the Si substrate. With

respect to these observations, the data evaluation was done with a model consisting of the silicon substrate, layer 1 describing the thin layer, and layer 2 assigned to the polymer film. For the refinement, Parratt's equation, Eq. 3.16, has been used. The roughness of the interfaces was mainly described with the error function profile (Eq. 3.17). An example of the dispersion profile together with the reflectivity curve of sample **n26** and the fit are shown in **Fig. 4.8**. Tables with values calculated from the refinement parameters are given in the appendix (**Tabs. A.1 and A.2**).

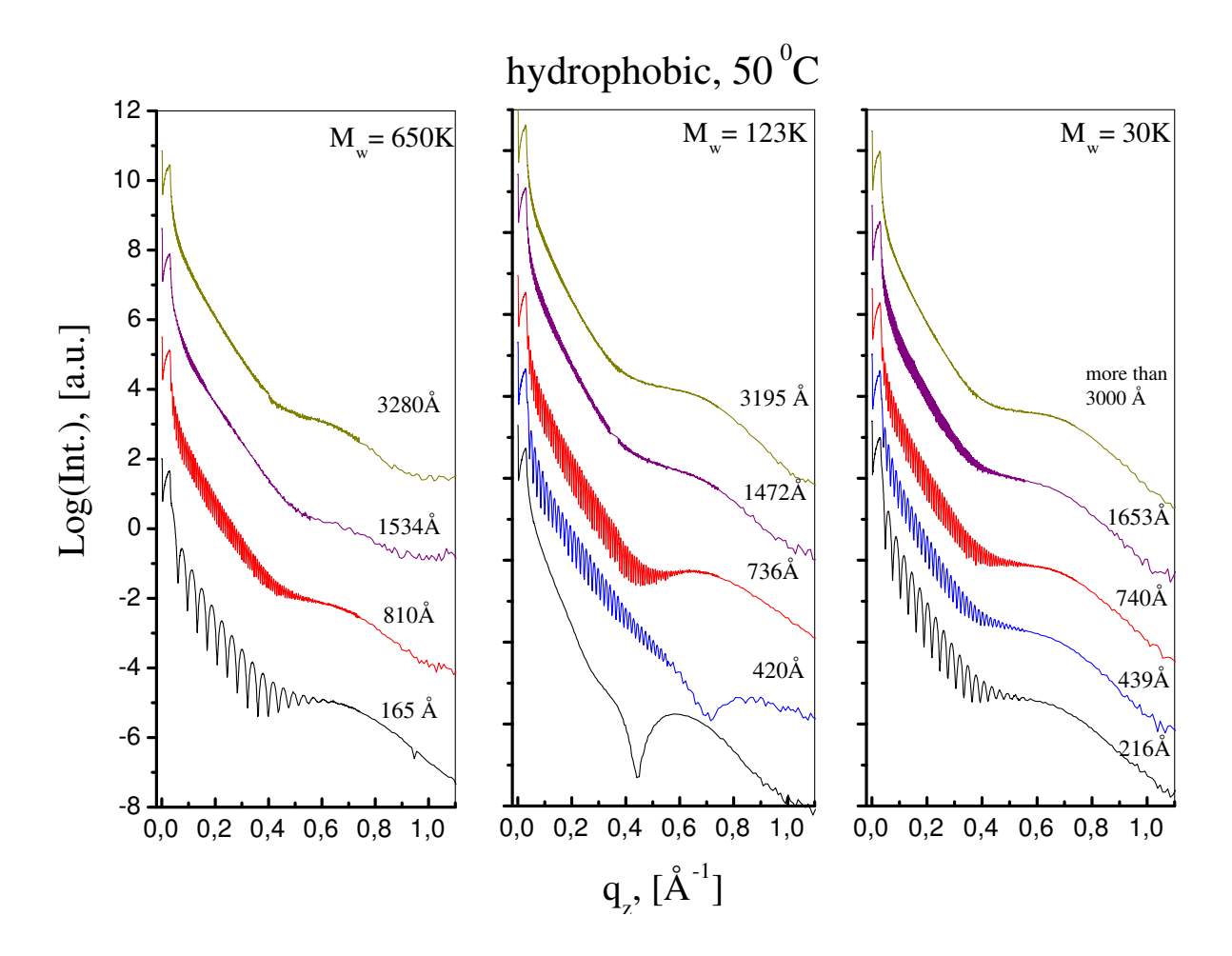


Figure 4.7: The reflectivity curves of all hydrophobic samples at 50°C. The film thicknesses in the figures are results taken from the data evaluation.

The reflectivity curve of sample **h21** does not show fast oscillations. Probably the film was extremely rough or the polymer did not cover the whole wafer for some reason (**Fig. 4.7**). This sample was excluded from the analysis of polymer thin film behavior. The curves of samples **h33**, **n13** and **n33** also do not show fast oscillations. Here, it is supposed that the polymer film was quite thick, which results in oscillations on the reflectivity curve with a very high frequency, so that they can not be resolved by the diffractometer.

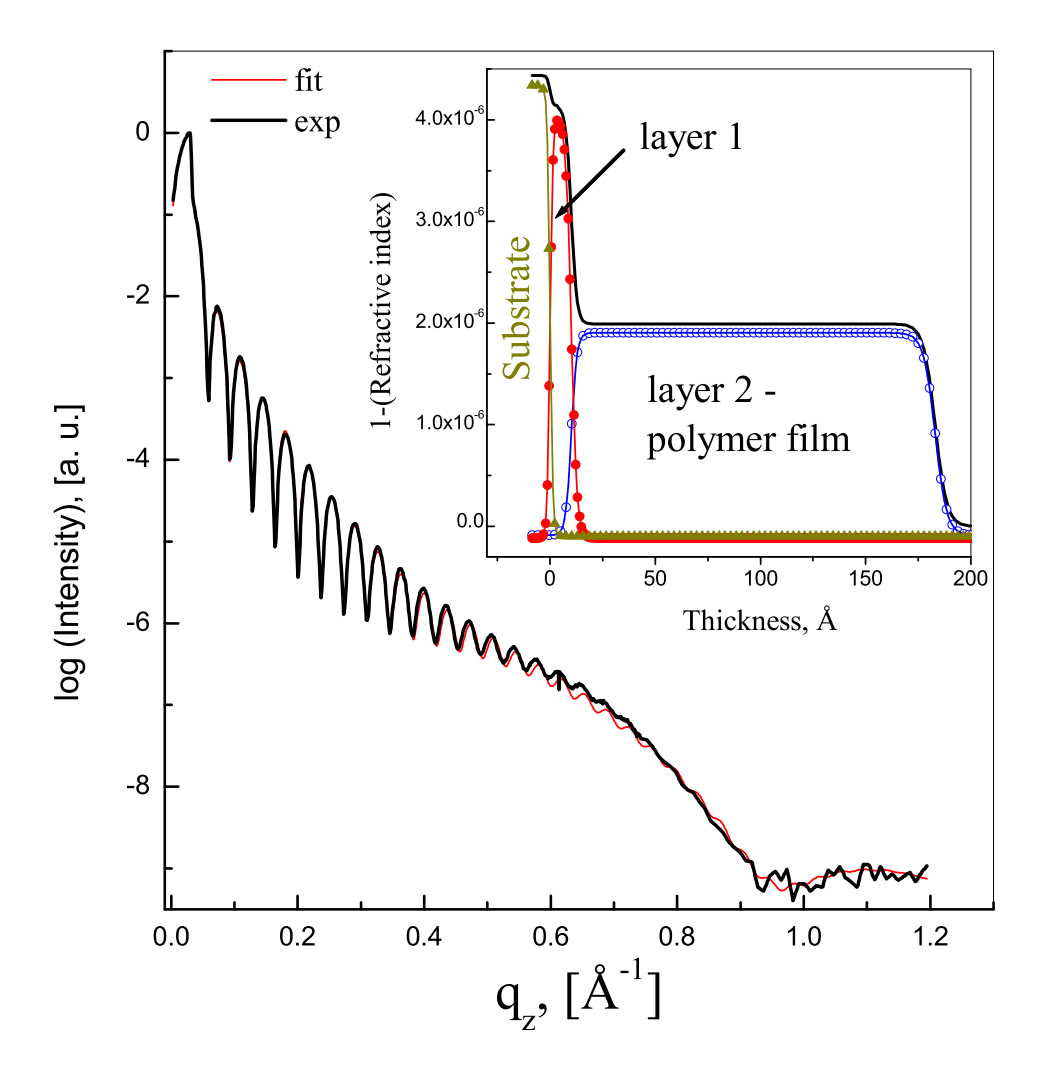


Figure 4.8: The reflectivity curve of sample **n26** together with a fit. In the inset the calculated dispersion profile and the curves assigned to the layers and the substrate are shown. For clarity the curve of the profile is shifted with respect to the curves of the layers and the substrate.

The high intense synchrotron radiation allows measurements of the reflectivity curve within a comparatively large range in reciprocal space. It could happen that the tail of the reflectivity curve is affected also from the scattered intensity coming from the structure factor of the polymer film. By means of grazing–incidence diffraction [58, 54] the structure factor of the polymer film for sample **h81** and **h36** have been measured. The curves are presented in **Fig. 4.9**. The scattered intensity is normalized against the monitor counts, and the background is subtracted. The curves are measured at incoming angle, α_i , equal to the outgoing angle, α_f , equal to 0.15°. The scattering curve obtained from an HF–etched Si wafer measured at the same grazing conditions as the samples is taken as background. The critical angles of the polymer and the Si substrate are 0.12° and 0.17°, respectively (see

the inset of **Fig. 4.9**). The incoming angle was chosen thus that the radiation penetrates the polymer film but not the Si substrate. It can be seen in **Fig. 4.9** that the structure factor appears at about 0.6 Å⁻¹, and its intensity is strongly dependent on the polymer film thickness. The structure factor of sample **h81** (with thickness 736 Å) is already hardly visible.

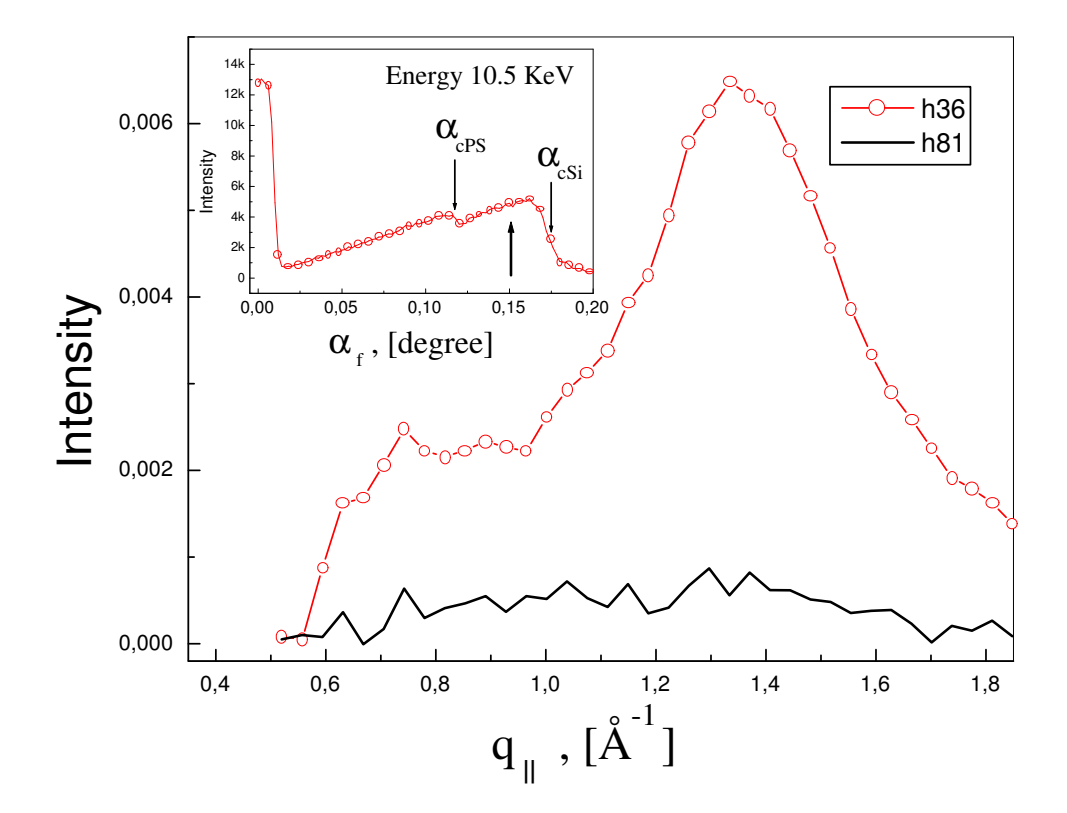


Figure 4.9: The polymer structure factor of the samples h36 and h81 measured by grazing—incidence diffraction at $\alpha_i = \alpha_f = 0.15^{\circ}$. In the inset, the beginning of the reflectivity cuve of sample h36 is presented. On the curve, the critical angles α_{cPS} and α_{cSi} of the polymer and of the Si substrate are denoted.

The results from grazing-incidence diffraction suggest that the humps observed in the tail of the longitudinal diffuse scattering curve are due to scattering from the polymer structure factor (**Fig. 4.10**). The ratio of the speculary reflected intensity, I_{ref} , to the intensity of the longitudinal diffuse scattering curves, I_{ld} , at q_z equal to 0.7 Å⁻¹, is about 0.04 for sample **h36**. Since this estimation is valid for one of the thickest samples, it can be expected that for the other samples the ratio is even less. Because of the negligible small contribution of the polymer scattering to the intensity of the reflectivity curve, a special correction was not applied to the data before the refinement.

The properties of the polymer film and layer 1 (the dispersion, the roughness and the thickness) at different temperatures are the results obtained after refinement of the reflec-

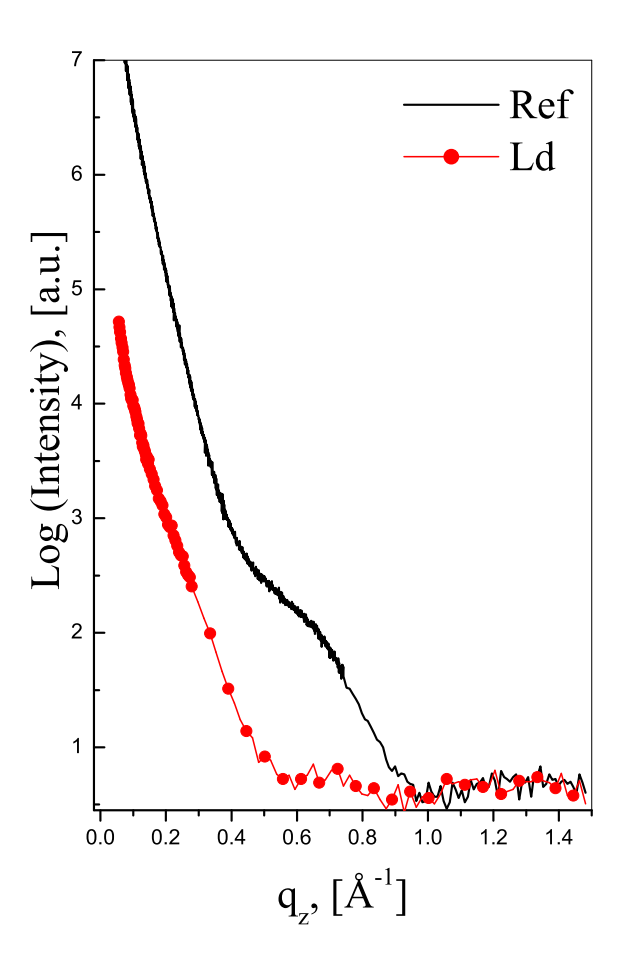


Figure 4.10: The longitudinal diffuse scattering curve and the tail of the reflectivity for samples **h36**.

tivity curves. The dispersion, δ_{Si} , and the roughness, σ_{Si} , of the substrate are not refined. During all fits they were kept equal to $4.43 \cdot 10^{-6}$ and 1.2 Å, respectively. The average value obtained for the dispersion of the polymer film, δ_{PS} , is $(1.8 \pm 0.3) \cdot 10^{-6}$. The roughness of the polymer film, σ_{PS} , does not significantly depend on the thickness of the studied films. The result coincides with the results presented in [14], where a strong increase of the polymer film roughness was observed for films with thicknesses less than 200 Å. For larger films the roughness has been about 7 Å and has remained constant within the error limits [14]. The observed independence of the roughness of the film thickness and of the type of the substrate allows to take the average of σ_{PS} 's for all available poylmer films at a given temperature.

The obtained temperature dependence of the polymer film roughness is shown in **Fig. 4.11** (open symbols). The roughness increases during the heating run (up to 230°C), and it slightly decreases during the cooling procedure. Nevertheless, at 50°C after the cooling, it is considerably larger than the roughness in the beginning of the heating run. Since the

quality of the polymer film becomes worse at higher temperatures (the oscillations on the reflectivity curve vanish at smaller q_z), the error bars in the cooling runs are larger.

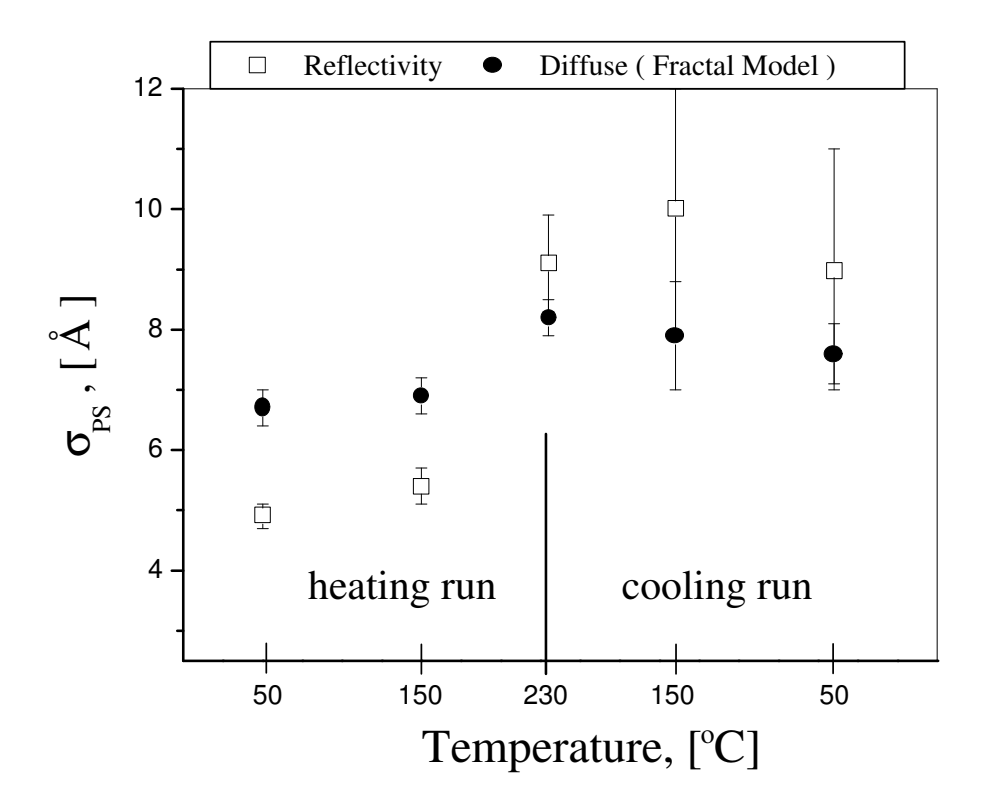


Figure 4.11: The roughness of the polymer film versus the temperature. The figure shows also results from refinement of diffuse scattering curves, which are explained in detail later in the text.

The thicknesses of the polymer films are not significantly dependent on the temperature. They increase by a factor of 1.1 during the heating run and slightly recover at the end of the cooling run (**Tab. A.3** in the appendix). The increase of the polymer film thickness with the temperature is related to the temperature change of the polymer chain conformation. The thin covering (the layer 1) on the hydrophilic substrates is the native SiO_x usually observed on Si wafers. The layer 1 on the hydrophobic substrates is obtained after treating the wafer with HF water solution. The properties of both coverings are compared in **Tab. 4.2**.

From the table, it can be seen that the hydrophobic layer is thinner and has less dispersion than the hydrophilic. The curves in $\mathbf{Fig.}$ 4.6 and $\mathbf{Fig.}$ 4.7 show that in contrast to the hydrophobic layer the SiO_{x} layer has uniform properties for all samples, which also results in smaller errors of the SiO_{x} layer dispersion (Tab. 4.2). The hydrophilic samples also reveal higher stability with increasing temperature. Only two hydrophilic samples show modifications with temperature (Fig. 4.12a). Possible reasons for this behaviour can be either the polymer films themselves or an increase of the SiO_{x} layer roughness.

	hydrophobic	hydrophilic
thickness, d , [Å]	8.4 ± 0.1	10.1 ± 0.1
roughness, σ , [Å]	2.6 ± 0.1	2.5 ± 0.1
dispersion, δ	3.70 ± 0.05	4.08 ± 0.01

Table 4.2: The layer 1 parameters for the hydrophobic and hydrophilic substrates. The values in the table are calculated by taking the mean values of the results from the reflectivity data at all temperatures for hydrophobic and hydrophilic samples, respectively.

In contrast, almost all reflectivity curves of the hydrophobic samples change their shapes during the heating and cooling runs. The most pronounced cases are shown in Fig. 4.12b. Nevertheless, a significant relation between the temperature and one of the hydrophobic layer parameter could not be established. All parameters describing the properties of layer 1 and those of the polymer film are fitted simultaneously. Thus the effects resulting from the polymer film influence the properties of layer 1, and a reliable distinction of a temperature dependence is hardly to obtain. Moreover, the investigation of the hydrophobic substrate properties in dependence on the preparation, storage parameters and the temperature is out of the frame of the current study. Therefore, the three fit parameters thickness, roughness and dispersion for layer 1 have been averaged over all hydrophobic samples and all temperatures (Tab. 4.2). The same has been carried out for the hydrophilic samples. Additionaly, the hydophobic layer thickness depends on the storage time of the samples. The samples are measured within a time interval of one year. The sample **h41** is the first considered hydrophobic sample, and it was measured about half a year before the other samples of the same series. The thickness (4.62 Å) of its hydrophobic layer is about two times less than the average hydrophobic layer thickness given in **Tab. 4.2** (compare also the reflectivity curves in Fig. 4.7 and Fig. 4.12b). The hydrophobic layer thickness of sample **h41** at different temperatures is not included in the calculation of the mean value of the thickness shown in **Tab.** 4.2.

The unexpected temperature and storage time dependences of the hydrophobic layer provokes further experiments, and it is discussed in section 4.2.4. The results obtained from the reflectivity curve refinements are used for the refinement of the diffuse scattering data.

4.2.2 The Liquid and the Fractal models.

In Fig. 4.13 and Fig. 4.14 the transverse (diffuse–scattering) curves of all available samples are presented. The curves were recorded at q_z equal⁵ to 0.2 Å⁻¹ for temperatures 50°C and 150°C. In Fig. 4.13, kinks similar to that predicted by the capillary wave theory are observed for samples with molecular weight, $M_w = 650$ kg/mol, as well as for the

 $^{^5}q_z=0.2 \text{ Å}^{-1}$ was chosen, because the transverse curves of samples **n81** and **h81** were measured at q_z values, where the first minimum and maximum appear on the reflectivity curve, i.e. near $q_z=0.17 \text{ Å}^{-1}$ and $q_z=0.26 \text{ Å}^{-1}$. Data at $q_z=0.15 \text{ Å}^{-1}$ and $q_z=0.35 \text{ Å}^{-1}$ for those samples were not taken.

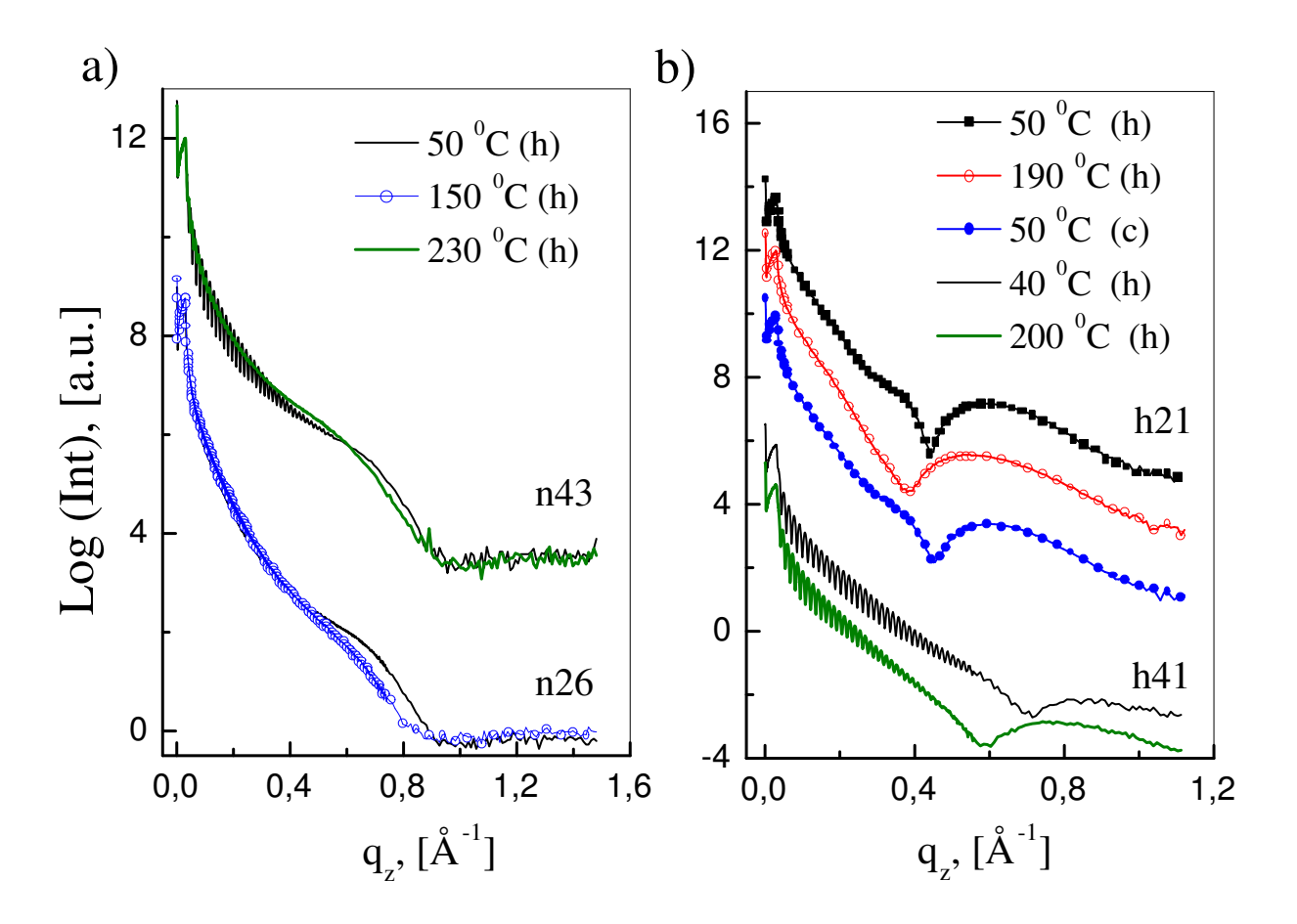


Figure 4.12: a) The hydrophilic samples which show some modifications in the reflectivity curves with the temperature. b) The most pronounced changes observed for hydrophobic samples with temperature. Sample $\mathbf{h21}$ is a very good example, since the polymer film is dewetted and the superposition effect of the polymer film and layer 1 features is not so strong. The letters \mathbf{h} and \mathbf{c} in the figure legendes denote heating and cooling runs, respectively.

samples with $M_w = 123$ kg/mol and film thickness less than 800 Å. From the series with molecular weight 30 kg/mol only the sample with film thickness of 200 Å shows kinks. Comparing the hydrophobic and hydrophilic samples in **Fig. 4.13** and **Fig. 4.14** it becomes clear that the appearance of the kinks does not depend on the substrate type. The kinks in the transverse scans can be, in principle, related to the liquid–like properties of the polymer film. Since atomic–force microscopy observations were not carried out, it can be argued here that the kinks are a manifest of the droplet structure created after the dewetting of the polymer film⁶ [63, 64, 65]. The dewetting investigations of PS thin films show that the films are comparatively stable [14, 63]. Dewetting is observed after annealing of films with thicknesses of about $R_q/3$ or if the PS has a low molecular weight

⁶The dewetting is the process, where the integrity of the film breaks up and it decays into randomly distributed droplets and holes.

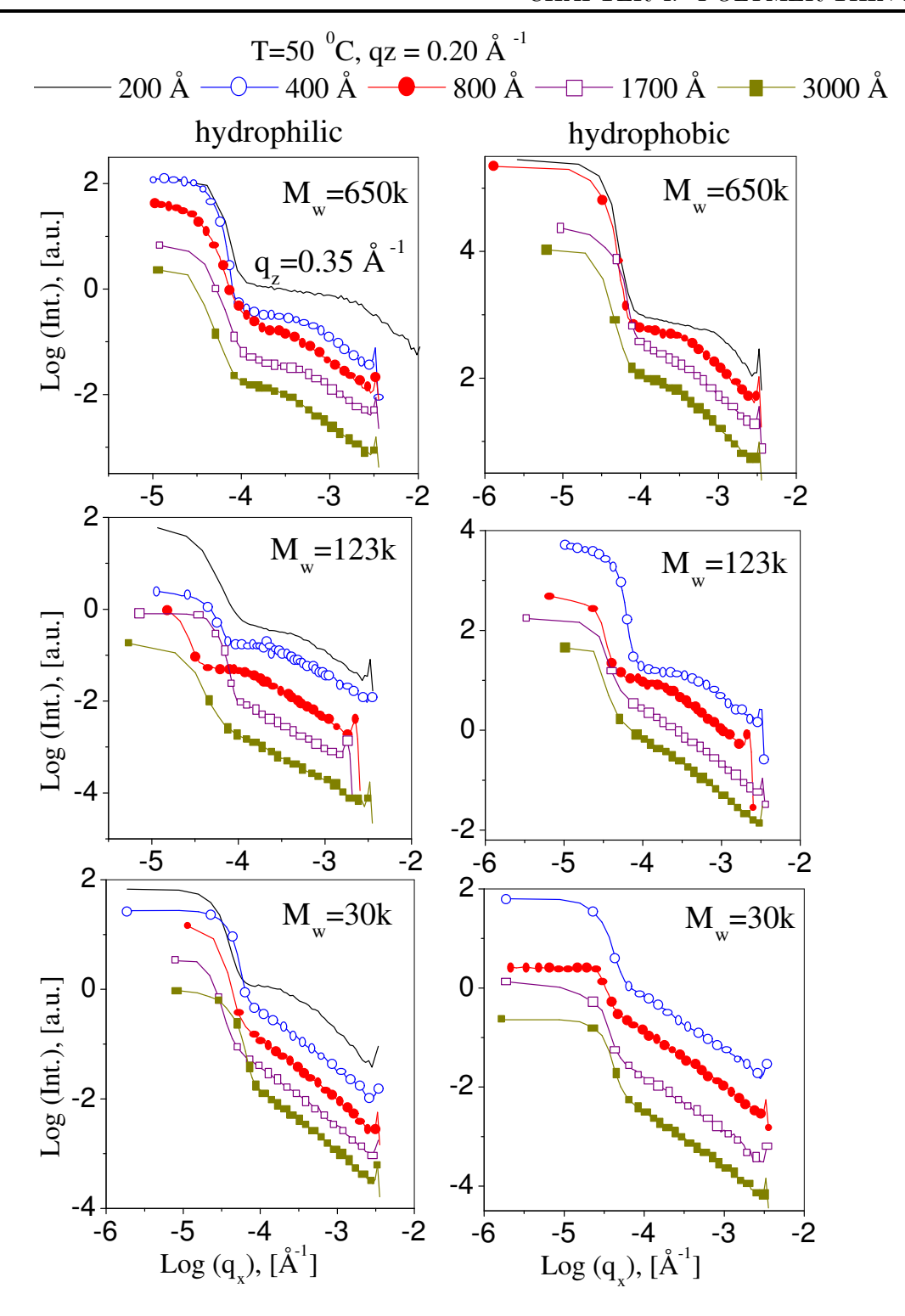


Figure 4.13: The transverse scans of the hydrophilic and hydrophobic samples in double logarithmic scale at 50°C (heating run).

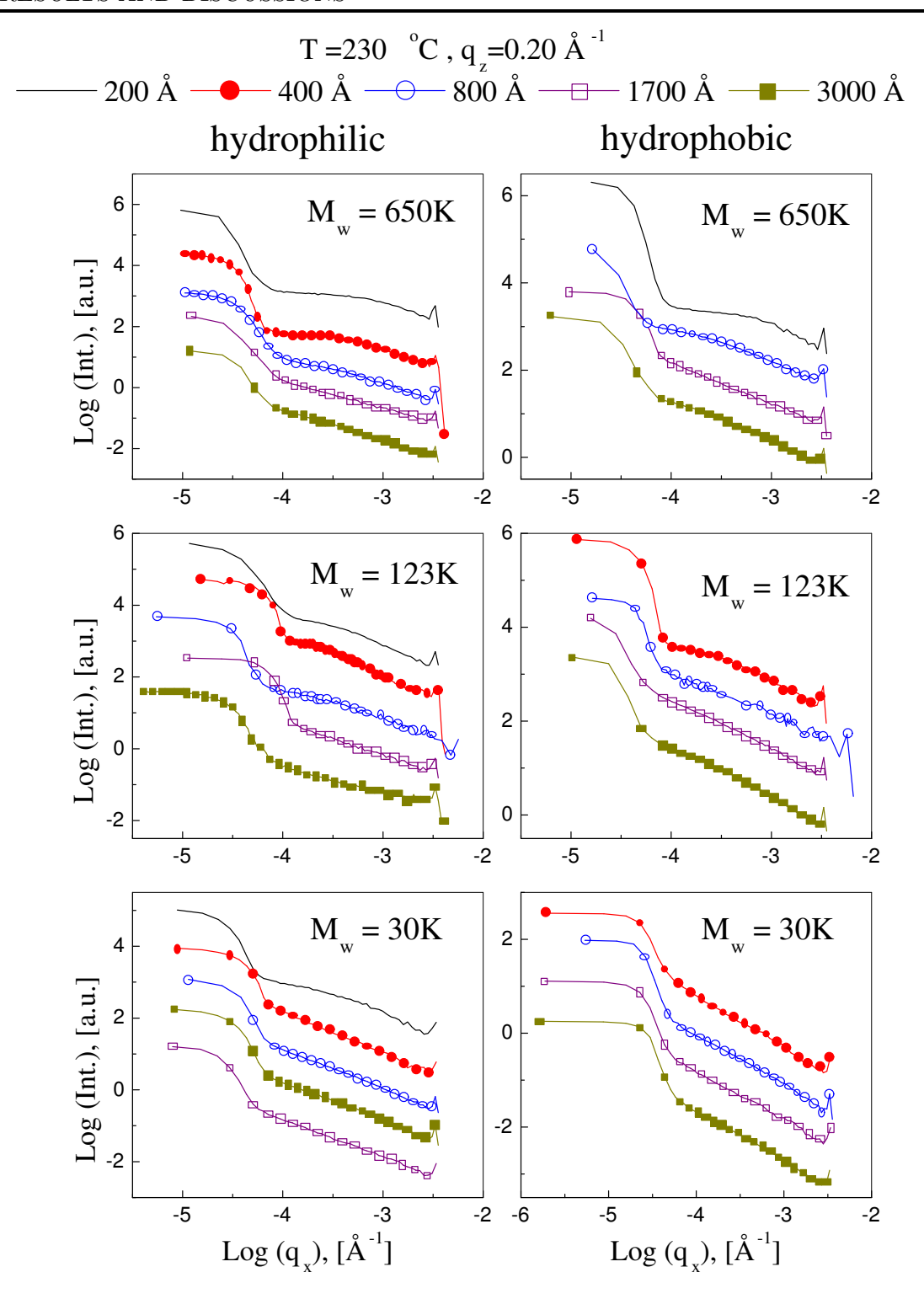


Figure 4.14: The transverse scans of the hydrophilic and hydrophobic samples in double logarithmic scale at 230°C.

($\approx 30 \text{ kg/mol}$) [64, 63]. Hence, from the studied samples the films with nominal thickness 200 Å and the films with molecular mass 30 kg/mol may be suspected to dewet during the annealing and temperature measurements. However, the reflectivity curves of those samples at 50°C do not show evidence for dewetting after annealing (with the exception of sample **h21**, **Fig. 4.6** and **Fig. 4.7**). Additionally, if it supposed that the kinks are a result of the droplet structure, they should be measured mainly on samples with molecular mass of 30 kg/mol but not on samples with a molecular weight of 650 kg/mol. The fact that a temperature increase does not lead to kinks from any of the samples, which do not possess them at 50°C, is also an argument against the explanation of the kinks on the diffuse scattering curves with a droplet structure of the polymer film (compare **Fig. 4.13** and **Fig. 4.14**). According to the discussion above, it is supposed that the kinks on the transverse scans depend on the molecular mass and the thickness of the polymer film rather than being a result of the droplet structure.

The diffuse scattering curves (the transverse and longitudinal scans) of each sample at a given temperature were refined simultaneously using Eq. 3.37. Two layer systems on the top of the substrate were considered, corresponding to the model used for the refinement of the reflectivity curves (polymer film and layer 1, see the inset of **Fig. 4.8**). The correlation function describing the polymer/air interface is either described by Eq. 2.10 or Eq. 2.12 according to the model used for the refinement. Independently of the choice of the correlation function at the polymer/air interface, the other interfaces (the polymer/SiO_x and the SiO_x/substrate) were described by a self-affine correlation function. In summary, the description of the correlation function and the refined paremeters used in the Liquid and Fractal models are given in **Tab. 4.3**.

	Liquid model	Fractal model
corr. function for polymer/air interface	Eq. 2.10	Eq. 2.12
corr. function for other interfaces	Eq. 2.12	Eq. 2.12
refined paremeters	γ or A_{eff} of polymer/air interface σ_{jj}, ξ_{jj} and h_{jj} of the other interfaces	σ , ξ and h of polymer/air interface σ_{jj} , ξ_{jj} and h_{jj} of the other interfaces

Table 4.3: Summary of the correlation functions and refined parameters used in the Liquid and Fractal models.

Capillary waves are expected to be observed at temperatures exceeding the glass transition

temperature. Since after annealing the investigated samples were slowly cooled down to room temperature (from 150°C) but not quenched, the structure at 150° was not preserved and the data at 50°C cannot resonably be described with the Liquid model. Therefore, only the curves with temperatures equal to or higher than 150°C were refined with the Liquid model. The quality of the fits was not satisfactory in the cases, where the kinks in the curves are well pronounced, which canbe seen in the refinement results presented in the appendix. Some of the data sets of the films with a nominal thickness of 200 Å had to be fitted using a Hamaker constant three orders of magnitude less than that taken for the vast majority of the data. This Hamaker constant was $50 \cdot 10^{-20} J$. According to the literature [17, 56] the thinner films should be characterized by a stronger interaction with the substrate. Consequently, the diminishing of the Hamaker constant for films with a thickness of 200 Å can not be resonably explained by any physical argument and it should be assigned to a disagreement of the Liquid model with the experimental data.

The surface tension, γ , of the polymer films was calculated using the Liquid model refinement parameters. γ does not show any significant dependence neither on the film thickness and the type of the substrate nor on the molecular mass of the polymer and the temperature. Its average value is 0.0150 ± 0.0005 N/m, and it is about two times less than indicated in the literature [13, 15, 12]. The logarithm of the cutoff positions of the studied films, predicted by the capillary wave theory, was calculated using Eq. 2.7 and is presented in **Tab. 4.4**.

Film thickness, d ,[Å]	$\log(q_{vdW}/[\mathring{A}^{-1}]),$
200	-3.2
400	-3.8
800	-4.4
1700	-5.1
3000	-5.6

Table 4.4: The logarithm of the cutoff positions of the studied films predicted by the capillary wave theory. The diffractometer resolution, δ_{q_x} is about 10^{-4} Å⁻¹. The surface tension for the calculations was taken to be 0.015 N/m

Comparing the cutoff positions in **Tab. 4.4** with the transverse curves at 150°C (heating run) in **Fig. 4.15**, it is obvious that the cutoffs for films with a thickness exceeding 800 Å are smaller than the diffractometer resolution. Consequently, they should not be visible in the transverse scans. The observation of the kinks in the curves of the samples with a molecular mass of 650 kg/mol indicates that the kinks in the transverse scans do not have the meaning of cutoffs predicted by the capillary wave theory.

Considering the results up to this point, it can be supposed that the polymer films with larger molecular weight at 150°C still exhibit viscoelastic behaviour, and a further increase of the temperature is needed for the observation of capillary waves on the polymer surface. Indeed, at 230°C, the kinks vanish for almost all smaples (**Fig. 4.14**), but this does

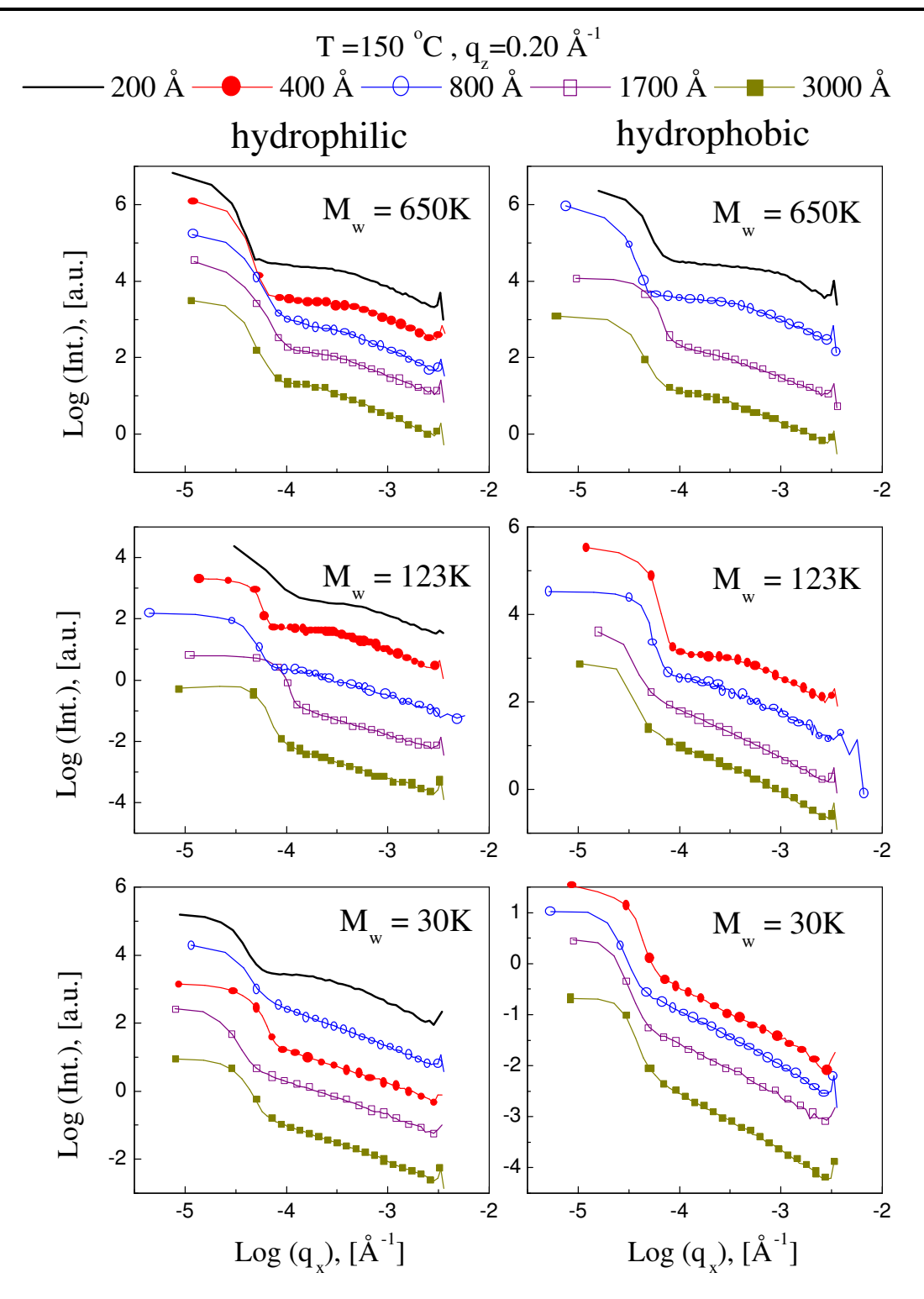


Figure 4.15: The transverse scans of the hydrophilic and hydrophobic samples in double logarithmic scale at 150°C (heating run).

not result into a better fit quality or a larger surface tension, even for samples, which do not show kinks at any of the investigated temperatures. Therefore, results from data refinements using the Liquid model suggest that the capillary wave theory can not describe the surfaces of the studied samples in the temperature interval from 50 to 230°C.

The data processing using the Fractal model shows satisfactory results at all investigated temperatures. The model indicates that the kinks are combinations of the correlation lenghts, ξ , and the Hurst parameters, h, of the polymer/air and polymer/layer 1 interfaces. The interface between the substrate and layer 1 does not contribute significantly to the scattered intensity.

The calculated correlation lengths and the Hurst parameters of the hydrophobic and hydrophilic coverings were similar. Therefore, they are decribed by the average values of ξ and h calculated from all studied samples and temperatures (**Tab. 4.5**). The average values of ξ and h of the substrate/layer 1 interface are also shown in **Tab. 4.5**.

	substrate/layer 1	layer 1/polymer
Hurst parameter, h	0.41 ± 0.02	0.23 ± 0.01
Correlation length, ξ , [Å]	$(1.5 \pm 0.2) \cdot 10^3$	$(0.65 \pm 0.07) \cdot 10^3$

Table 4.5: The Hurst parameter and the correlation length average values of the substrate/layer 1 and the layer 1/polymer interfaces calculated after refinement with the Fractal model.

The Hurst parameter of the polymer surface is about 0.2. It increases, if kinks are observed in the diffuse scattering curves (**Tabs. A.7, A.11, A.15 and A.19** in the appendix). The correlation length, ξ_{PS} , shows week dependence on the temperature and the effective thickness of the polymer film, d_{eff} . The effective film thickness was determined by dividing the measured thickness of the films by the radius of gyration, R_g , for the corresponding molecular mass (section 4.1.4). Thus, the thicknesses of the films were scaled in terms of the molecular dimensions and films with different molecular weights could be compared.

In **Fig. 4.16** the correlation lengths versus the effective thicknesses at 50°C of heating and cooling runs are compared. A slight increase of ξ_{PS} with the effective thickness was observed. Larger correlation lengths were found at the end of the cooling runs compared to the beginning of the heating. The temperature effect becomes visible after heating the samples above 200°C, i.e. the surface structure of the films began to relax. This observation seems to be resonable, since the melting temperature of PS is approximately 200°C.

Comparing the results for hydrophilic and hydrophobic samples in **Fig. 4.16**, it looks as if hydrophilic samples have smaller correlation lengths. The trend could be explained with a stronger interaction between the polymer and the hydrophilic substrate.

The error bars in **Fig. 4.16** exceed the corresponding values summarized in appendix **A**. The standard deviations presented there were obtained from the refinement parameters, and they seem to be unrealistically small. Therefore, the standard deviations in the figure are estimated taking the smallest change in the correlation length, which visibly affects the fit quality.

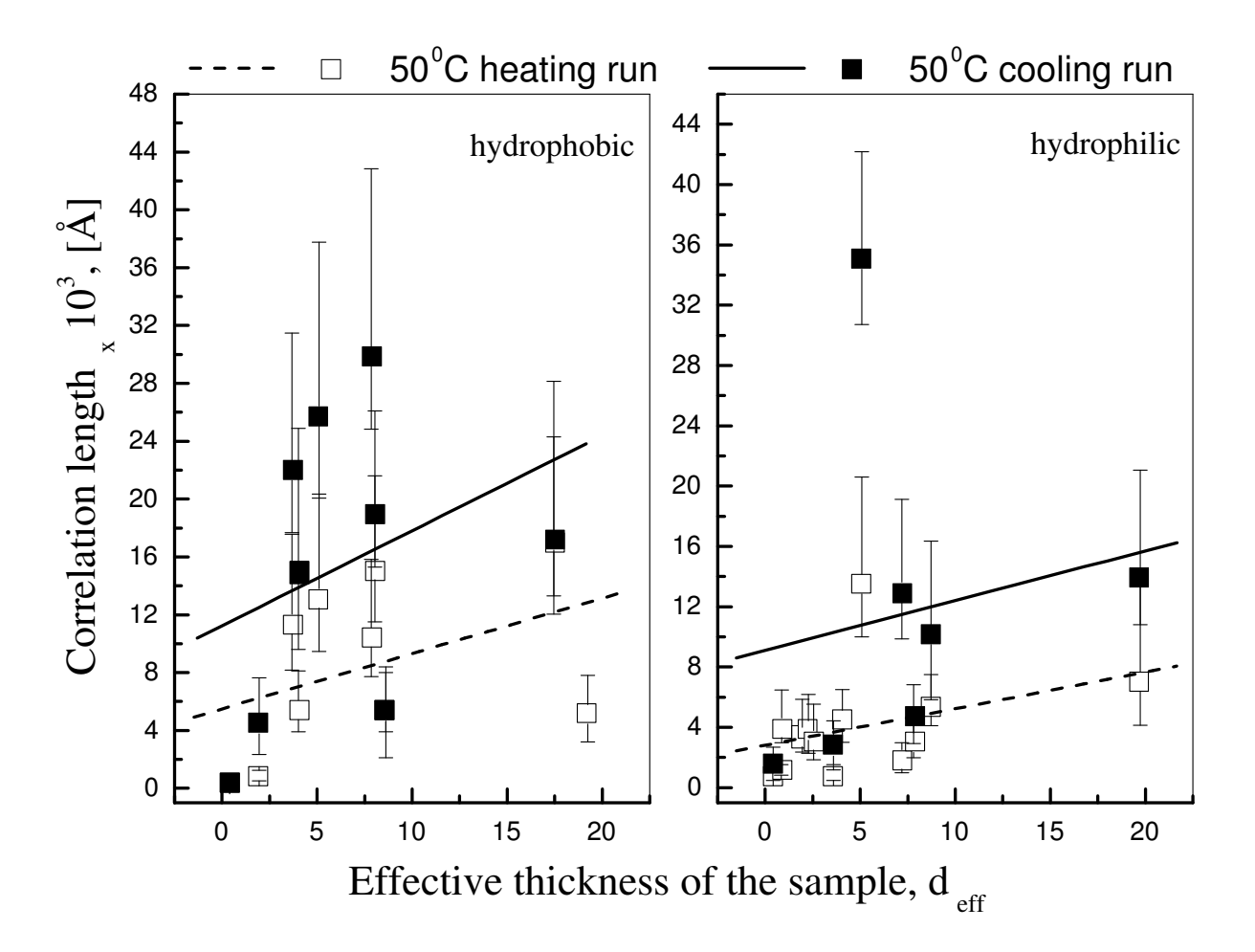


Figure 4.16: The correlation lengths of hydrophobic and hydrophilic samples versus the effective thickness at 50°C heating and cooling runs. The lines are linear regressions as a guide to the eye.

The roughness of the polymer/air interface obtained from the refinement of the reflectivity data does not coincide with the roughness obtained from refinements using the Fractal model. Both results were already compared in **Fig. 4.11**. Similar disagreement is also observed by other authors [14].

Comparing only the quality of the fits, it is difficult to prefer one of the two models. Concerning the agreement indices the quality of the Fractal model refinements are slightly better, i.e. the χ^2 is smaller in almost all cases, but since there are more refinement parameters in the Fractal model than in the Liquid model, the agreement indices cannot be considered as satisfactory. However, the Liquid model shows some disagreement with the experimental and the literature data. The Fractal model does not show any contradiction between theory and experiment, and the quality of the refinements are as good as using the Liquid model. Thus, the structure of polymer films in the studied temperature interval is marginally better descibed by the Fractal model.

4.2.3 Diffuse scattering data depending on the temperature and the film thickness

The dynamical properties of polymer thin films are determined by the polymer viscosity [19]. Polymers having large viscosities behave more like a solid than like a viscouse-liquid. The viscosity is related to the longest relaxation time in the system, and according to the reptation model of De Gennes [66] it scales with the chain length to the third power. The molecular mass is the practical expression of the chain length. Hence, the viscosity is strongly dependent on the molecular weight of the polymer. The presented results show significant relations between the kinks in the transverse scans and the molecular weight (Fig. 4.13). It is interesting to note that the transverse scans of unsupported PS films with molecular mass of 697 kg/mol does not show kinks [15]. Moreover, the kinks in the transverse scans of supported films "appear only after annealing" [14]. From this point of view it seems that the observation of the kinks is a manifest of the very slow dynamics of the polymer in combination with the interaction between the film and the substrate. In the beginning of the annealing due to the large amount of the solvent in the polymer, the films behave similar to a viscose liquid. After evaporation of the solvent the polymer freezes in a metastable state influenced by the interaction with the substrate. The assumption above is also in agreement with the fact that heating of the samples to 230°C moves the system closer to the viscose fluid, which results in the disappearence of the kinks in the curves (Fig. 4.14).

In the investigation of Hyunjung Kim et al. [12] the longest observed relaxtion time of the PS films with molecular mass 123 kg/mol at 160°C was 124 s at $q_x = 3.85 \cdot 10^{-4} \text{ Å}^{-1}$. The measured relaxation times were related to the dynamics of the polymer chains. The existence of such long relaxation times indicates that the system can not be regarded as quasy–static within the sampling time. The sampling time (the measuring time per step of the transverse scans) is even less than the obtained relaxation time. Thus, the integration over all ω in Eq. 2.3 is not allowed here. This is one more argument against the Liquid model.

During the measurements the studied samples may be in a metastable state but not in the equilibrium. Moreover, from the discussion above it is obvious that the viscosity of the polymer is large and the system should behave similar to a solid, even at temperatures of about 160° C. Indeed, according to the same authors the viscosity⁷ at 170° C (the maximum investigated temperature) is about $5 \cdot 10^4$ N·s/m. Increasing the temperature beyond the glass transition temperature permits only local molecular motions, but the relaxation of the system is dependent on the reptation time, which remains long up to the melting temperature of the polymer [67, 68]. An increase of the temperature up to the range of the melting temperature and a decrease of the molecular mass makes the system faster. On the other hand, the kinks in the diffuse scattering curves appear in scans, where the samples had a larger molecular mass and lower temperatures. Therefore, the observation

⁷In comparison, the viscosity of glycerol at 20°C is 1.53 N·s/m and the PS viscosity is about four orders of magnitude larger.

of the kinks could be understood as an indication for very slow dynamics. Thus, it could be supposed that the samples which show kinks have quasi-solid surfaces. Probably, this is the explanation for the better refinements using the Fractal model in the case of higher temperatures and lower molecular masses.

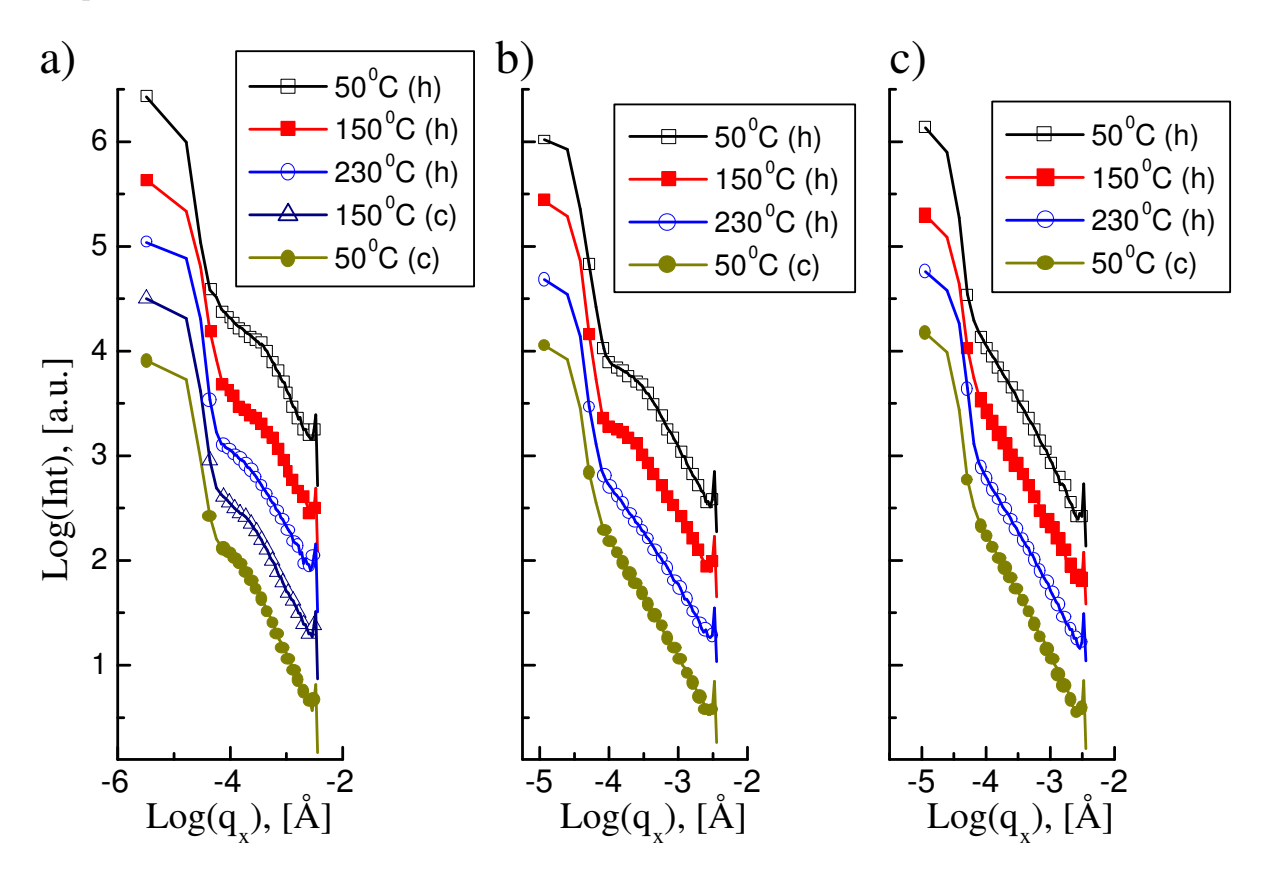


Figure 4.17: The temperature behaviour types of the investigated sample system; a) the films are in a solid metastable state and do not relax during the heating and cooling runs (sample h86 is presented.), b) the samples are in a solid metastable state but they relax at 230°C (sample n36 is presented.), c) the samples relax during the annealing (sample n83 is presented.). The letters h and c in the figure legendes denote heating and cooling run, respectively.

The temperature behaviour of the investigated sample system can be classified as presented in Fig. 4.17a, b and c. The interpretation of the data in the figure is done assuming that the kinks in the transverse scans are combinations of the viscoelastic properties of the film and the interaction with the substrate. Additionally, it is supposed that the samples are not in the equilibrium. The first type behaviour in Fig. 4.17a shows that the films at 50°C (heating run) are in a solid metastable state, which changes with temperature, but the heating up to 230°C does not really lead to a decrease of the viscosity, and a relaxation of the polymer film is not observed. At the end of the cooling run the samples are freezing in another metastable state. The samples of the type presented in Fig. 4.17b are in a

solid metastable state at the beginning of the heating. A temperature increase up to 230°C results in a relaxation of the polymer film. Again the films are freezing in a metastable state, but the strong influence of the substrate on the polymer film structure is lost. The samples of type **c** are probably in an intermediate solid/viscouse liquid state, which allows a relaxation of the films during the annealing.

Nominal thickness, [Å]	$M_w = 650 \text{ kg/mol}$	$M_w = 123 \text{ kg/mol}$	$M_w = 30 \text{ kg/mol}$
200	0.48 (a)	1.09 (a)	2.25 (a)
400	0.96 (a)	2.19 (a)	4.52 (c)
800	1.91 (a)	4.38 (b)	9.03 (c)
1700	4.07 (b)	9.30 (c)	19.20 (c)
3000	7.17 (b)	16.41 (c)	33.88 (c)

Table 4.6: The effective thicknesses, d/R_g , of the studied samples. The letters in brackets denote the type of the temperature behaviour of the corresponding sample (see text)

In **Tab. 4.6** the effective thicknesses⁸ of the investigated samples are presented. The temperature behaviour of each sample is also indicated here⁹. From the table it can be seen that the viscoelastic properties of films are significantly dependent on the film thickness and the molecular mass. The observed results support the idea of a development of inhomogeneities in the viscosity as a function of the depth of the film [69, 70]. According to the table, the layers with thicknesses of about two times of the radius of gyration are affected by the substrate.

4.2.4 Hydrophilic and hydrophobic substrates

In most of the published works concerning supported polymer thin films the question of how the interface between the substrate and the polymer behaves with time and temperature is not discussed. Usually it is supposed that the applied temperatures do not influence the substrate surface. The unexpected temperature dependence of the layer on HF–etched surfaces, shown at the end of section 4.2.1 provokes a more careful investigation of the hydrophobic substrates at different temperatures.

Hydrophobic substrates were obtained after treatment with HF solution. According to *Ubara et al.* [71] the fluorine terminated silicon complexes are not stable in HF solution. The strong polarization of Si⁻Si⁺F₃ facilitates attack by HF molecules, and a reaction of the following type occurs:

$$Si - SiF_3 + HF = SiH + SiF_4$$

⁸For the calculation of the effective thicknesses here, the nominal thicknesses of the films given in **Tab. 4.1** are taken.

⁹A difference between hydrophobic and hydrophylic samples was not observed. Thus a distinction between them was not made.

The silicon fluoride is released in the solution and the silicon atom on the surface is hydrogen terminated, which should be responsible for the hydrophobic nature of the sustrate. The SiH-bond is stable in the HF solution, because the reaction of the type

$$SiH + HF = SiF + H$$

has a larger activation barrier as the reaction above.

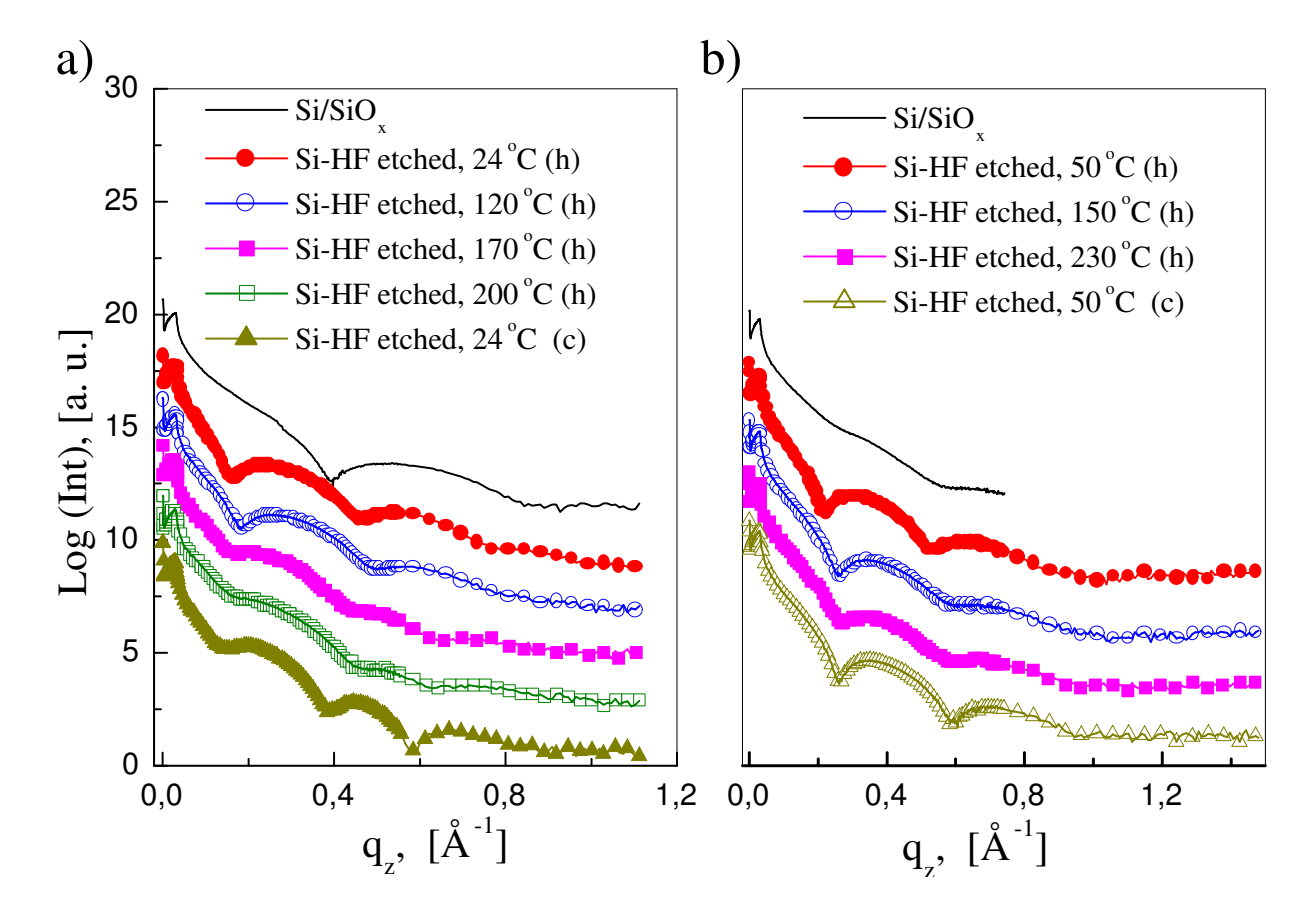


Figure 4.18: The reflectivity curves of HF–echted Si wafers measured at different temperatures. The letters in brackets **h** and **c** denote heating and cooling run, respectively. **a**) The sample was etched in 4% water solution of HF. **b**) The sample was etched in 0.8% water solution of HF.

Additional reflectivity measurements of bare Si wafers treated with 4% and 0.8% water HF solution at different temperatures have been carried out. Similar to the measurements of polymer films, the wafers were heated and then cooled down to the initial temperature. Before the measurements the wafers were etched with HF solution for 2 min and rinsed with DI water. The samples were left to dry in the sample chamber used for the measurements at 30° C for 30 min in vacuum (10^{-5} mbar). The recorded reflectivity curves for both concentrations are shown in **Fig. 4.18a** and **b**. The results from the data refinements are

presented in Fig. 4.19a and b and Tab. 4.7. For comparison purposes the reflectivity curves of the initial wafer covered with native SiO_x are also included in the figures.

4% water solution of HF				
	Layer 1			Substrate
	$\delta \cdot 10^{-6}$	σ , [Å]	d, [Å]	σ , [Å]
Si/SiO _x	4.2822 ± 0.0007	1.459 ± 0.004	11.669 ± 0.004	$1.00^{(f)}$
24°C	2.462 ± 0.005	2.778 ± 0.006	20.29 ± 0.01	3.89 ± 0.01
120°C	2.65 ± 0.01	2.763 ± 0.008	18.71 ± 0.01	3.73 ± 0.01
170°C	1.005 ± 0.006	1.47 ± 0.01	11.581 ± 0.007	3.969 ± 0.006
200°C	0.666 ± 0.002	1.8171 ± 0.0007	12.330 ± 0.002	3.603 ± 0.001
24 °C	0.969 ± 0.008	1.50 ± 0.01	12.74 ± 0.01	3.629 ± 0.006
	C	0.8% water solution	n of HF	
Si/SiO _x	3.740 ± 0.003	2.306 ± 0.002	8.234 ± 0.008	3.878 ± 0.007
50°C	2.79 ± 0.01	3.30 ± 0.02	8.93 ± 0.02	3.15 ± 0.02
150°C	2.67 ± 0.02	3.62 ± 0.02	5.94 ± 0.02	3.48 ± 0.02
230°C	2.775 ± 0.006	3.705 ± 0.005	6.229 ± 0.006	3.494 ± 0.006
50°C	3.052 ± 0.001	3.9422 ± 0.007	6.357 ± 0.001	2.602 ± 0.001
	4% water solution of HF			
	Layer 2 Total			Total
	δ	σ , [Å]	d, [Å]	thickness, [Å]
Si/SiO _x	3.290 ± 0.004	3.878 ± 0.002	8.735 ± 0.004	20.404 ± 0.008
24°C	_	_	_	20.29 ± 0.01
120°C	_	_	_	18.71 ± 0.01
170°C	1.266 ± 0.006	4.302 ± 0.007	10.89 ± 0.01	22.45 ± 0.02
200°C	1.316 ± 0.001	3.4147 ± 0.0008	10.381 ± 0.008	22.71 ± 0.01
24 °C	1.403 ± 0.007	2.86 ± 0.01	12.74 ± 0.01	25.48 ± 0.02
0.8% water solution of HF				
Si/SiO _x	2.301 ± 0.003	2.237 ± 0.004	5.852 ± 0.003	14.09 ± 0.01
50°C	1.80 ± 0.01	2.54 ± 0.01	8.08 ± 0.01	17.01 ± 0.03
150°C	1.40 ± 0.02	2.44 ± 0.02	8.92 ± 0.03	14.86 ± 0.05
230°C	1.262 ± 0.002	2.612 ± 0.002	8.975 ± 0.007	15.20 ± 0.01
50°C	1.4752 ± 0.0006	2.593 ± 0.001	8.856 ± 0.002	15.213 ± 0.003

Table 4.7: Results obtained after refinement of the reflectivity data. The 'effective-density model' has been used (Eq. 3.24). The parameter indexed with $^{(f)}$ is kept fixed during the refinement.

The wafers treated with higher HF concentrations show drastical changes of their structures

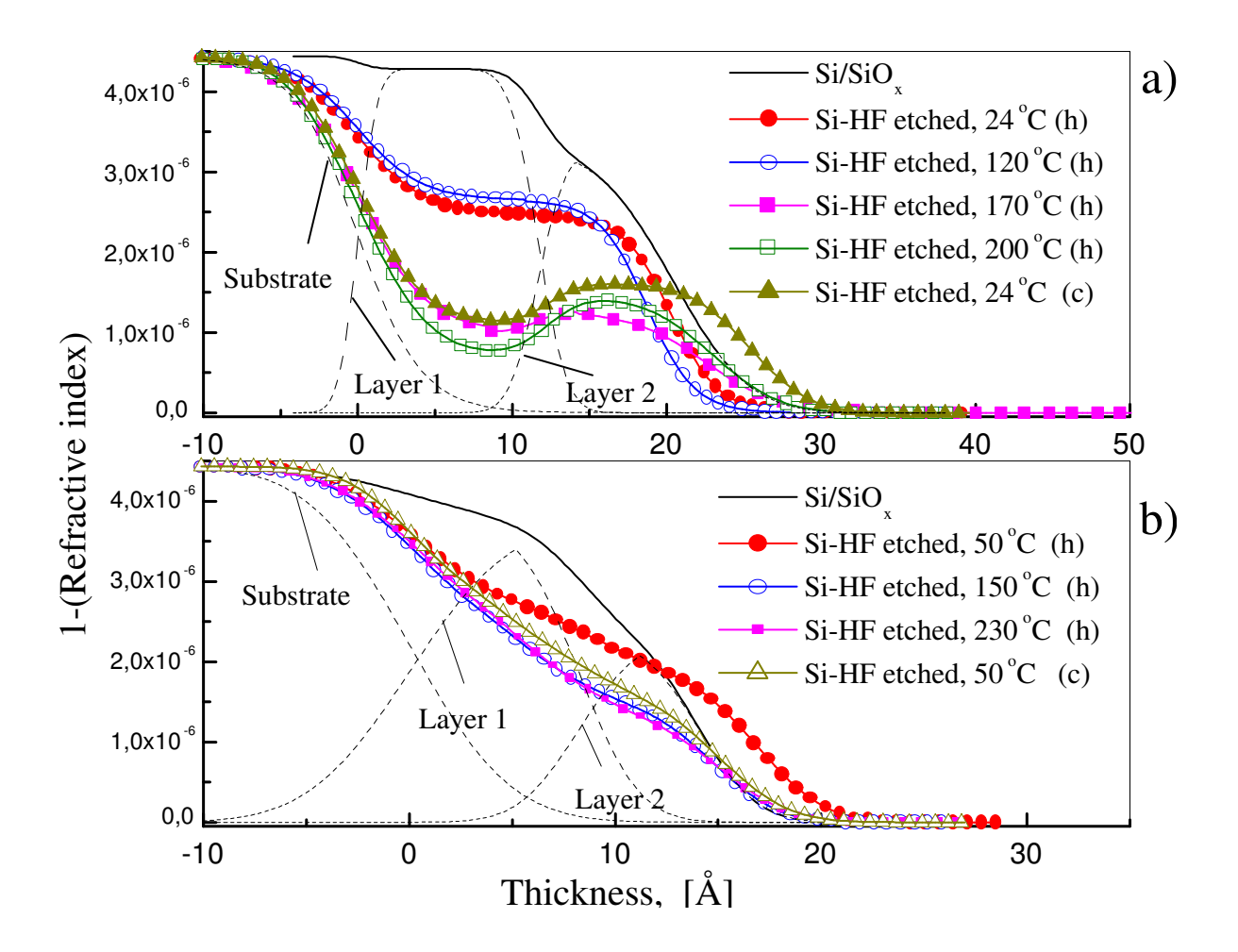


Figure 4.19: The δ -profiles of the HF–echted Si wafers obtained after data refinement. The letters in brackets **h** and **c** denote heating and cooling run, respectively. **a**) The sample was etched in 4% water solution of HF. **b**) The sample was etched using 0.8% water solution of HF.

with temperature. At the beginning of the heating runs the film thickness slightly decreases (compare the results for 24°C and 120°C heating runs). This is probably due to a partial desorption of water molecules from the surface. The coverings at 24°C and 120°C (heating run) can be described with one uniform layer model, and the obtained δ -profiles are very similar to the δ -profile published by *Shin et al.* [72] for HF-etched samples at 22°C. Increasing the temperature up to 170°C leads to an increase of the thickness and drastical changes in the δ - profile (**Fig.4.19a**). The curves measured at 170, 200 and 24°C (cooling run) are described with two layer models. At the final stage the total thickness (the thickness of layer 1 + layer 2) of the film is larger than at the beginning of the run (**Tab. 4.7**). The abrupt change in the δ -profile beyond 170°C can be ascribed to a replacement of the Si-H bond by Si-OH or Si-O bonds. The OH- groups and oxygen atoms could be supplied from the absorbed water on the surface.

The wafer treated with a lower concentration HF shows a completely different behaviour. The heating up to 150°C leads to a decrease of the total thickness of the film (**Tab.** 4.7), but a further heating and cooling run does not change the δ -profiles or increase the thicknesses. It seems that in this case only desorption of water molecules from the surface occurs during the temperature treatment.

Differences between surfaces treated with different concentrations of HF solution were also observed by Higashi et al. [73]. The authors stated that the quality of the surfaces obtained after treatment with HF-solution is dependent on the pH of the solution. The best results were obtained, if the pH exceeds 4. Since even in very diluted solutions of HF in water (from 10% to 1%) the pH varies from 1 to 2, larger pH values can be achieved using buffer solutions (for instance a buffer solution of NH₃: H₂, v:v=1:1.25 and HF (49%) in ratio 6:1 [72]). Treating the wafers with a water solution of HF even in very low concentrations leads to a creation of all type hydride species (mono-, di-, and tri-hydride) on the surface. Ideal termination of a Si surface with silicon mono-hydride surfaces can be achieved by the control of the pH in buffer solution [73]. It was established that di-, and tri-hydride are more unstable with respect to the oxidation compared to an ideal H-terminated Si surface. The presence of OH⁻ groups facilitated the oxidation process. As a consequence during the rinsing in DI water the amount of Si-H bonds decreases, and they are mainly replaced by Si-O-Si groups [74]. According to Shin et al. [72] the HF-etched surfaces are very unstable in air and within a few minutes most of the Si-H bonds have oxidized. As the processing of the polymer film on the surface needs longer time the authors suppose that the H- terminated bonds were already lost, before the polymer film could be spun cast. They suggest that the difference in the hydrophobicities in the two type of surfaces is due to a water absorption at the SiO_x surface.

Concerning all statements above and taking into account that the substrates used in the present investigation were prepared with 10% HF solution in water, it should be expected that on the substrate all types of hydride species have been created. Hence, the Si-H bond on the surfaces were not stable and the behavior of the hydrophobic substrates should be similar to the sample treated with 4% HF solution. Therefore, the hydrophobic substrates show very unstable character with temperature variation and storage time. The instability of Si-H bonds additionally decreases the hydrophobic properties of the surfaces, and according to [72] increases the ability of water absorption. The diffuse scattering data of the hydrophobic and hydrophilic films do not show a significant difference (e.g. Fig. **4.13** and **Fig. 4.14**). This fact could support the interpretation that the HF-etched surfaces prepared for the experiment have very week hydrophobic character because of the instability of the Si-H bonds. However, the results of the presented experiments are not convincing in order to interpret the difference between HF-etched substrates and substrates with native SiO_x. For a better understanding of the hydrophilic and hydrophobic surface behaviour it is necessary to examine which kind of chemical reactions happens on the surface with increasing temperature and storage time. In contrast to the assumptions in most works, this investigation shows that even in the studied temperature region not only the polymer films but also the properties of the HF-etched substrates changes.

Chapter 5

Confined liquids and polymer films

5.1 Experimental setup for X-ray scattering from confined liquid and polymer films.

5.1.1 The experimental cell

The main part of the work, related to the experiments with fluids in confined geometry, was dedicated to the development and testing of the experimental cell. Therefore, in the following a detailed description of the cell and the experimental conditions are given.

The initial version of the cell was designed by Herrn Ing. Küssel, FZ Jülich. The first experiments had shown that the vacuum system of the cell has to be improved and a new mechanism moving the upper wafer has to be constructed. Thus, the decision to completely rebuild the cell was made.

The actual version of the sample–cell is shown in **Fig. 5.1**. It consists of a base plate, the sample–chamber and a cage. The base plate is hollow and finishes with tubes on both sides, where a circulator type F25–HP (Julabo Labortechnik GmbH) is connected. The circulator is used for an adjustment of the cell temperature. The device works in the temperature range 10°C to 200°C¹.

The sample–chamber has two Kapton X–ray windows and can be evacuated down to 10^{-4} mbar. In the chamber two identical wafers (Si or sapphire) are mounted. The bottom wafer is fixed to the base plate. The upper wafer is connected to a piezo crystal (**Fig. 5.1**, #2) (Physik Instrumente GmbH&Co., Modell: E–471.00) by means of an articulated bearing. It can be tilted independently in two dimensions. This construction provides a parallel self–alignment of the upper wafer with respect to the lower one. The tilting of the upper wafer can also be controlled via side screws (**Fig. 5.1**, #3).

The wafers have diameters of 26 mm (**Fig. 5.2**). The special shape of the substrates is required in order to reduce the radiation absorption at closed gap during the reflectivity and out–of–plane scans. The size of the confinement area, which has the shape of a bridge, is about 3 mm along the beam direction and 5 mm perpendicular to the propagation of

 $^{^{1}}$ In the circulator $Thermal\ H2OS$ (Bayer) liquid is used.

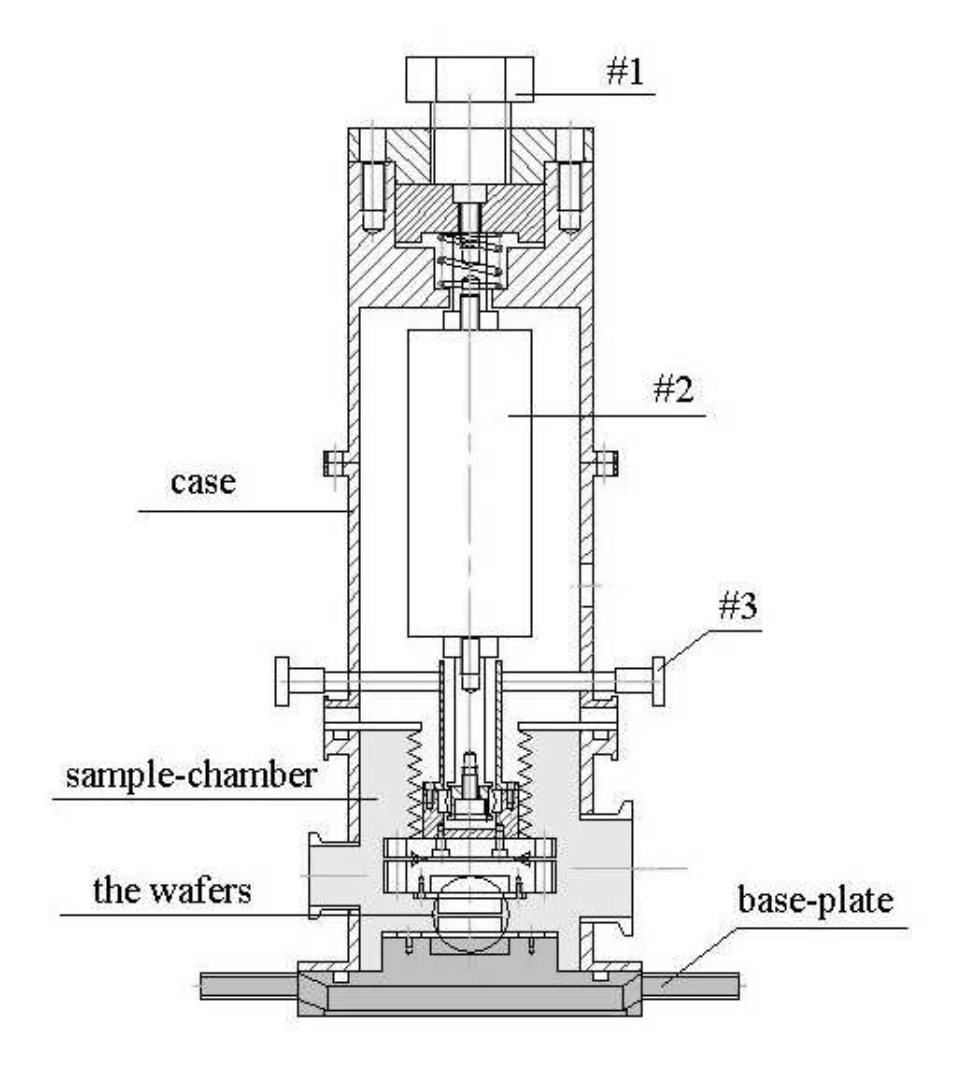


Figure 5.1: The sample–cell. The cell has a height of 410 mm. The diameter of the base plate is 140 mm. The weight of the complete device is about 15 kg. This vertical section shows the plane perpendicular to the beam.

the beam. Both wafers are adjusted in a close contact using the screw #1 in (**Fig. 5.1**). The final movement (pressing) is done by the piezo crystal, which presses the top wafer onto the bottom. The piezo crystal is supplied with a sensor that allows to control the relative movement with respect to the initial upper wafer position. The maximum travel range of the piezo crystal is $100 \ \mu \text{m}$ and the maximum force is about $30 \ \text{kN}$. The opening of the gap can also be controlled via the output voltages of the piezo driver, where $0 \ \text{V}$ corresponds to no pressure and $1000 \ \text{V}$ to maximum pressure, respectively. There is no device for a measurement of the absolute value of the gap size. Instead, the gap is calculated via the oscillations observed in the reflectivity curves. The contact area of the

wafer is about $2.7 \cdot 10^{-4} m^2$. Assuming a homogeneously distributed force on the wafer surface, the maximum applied pressure is about 1.1 kbar.

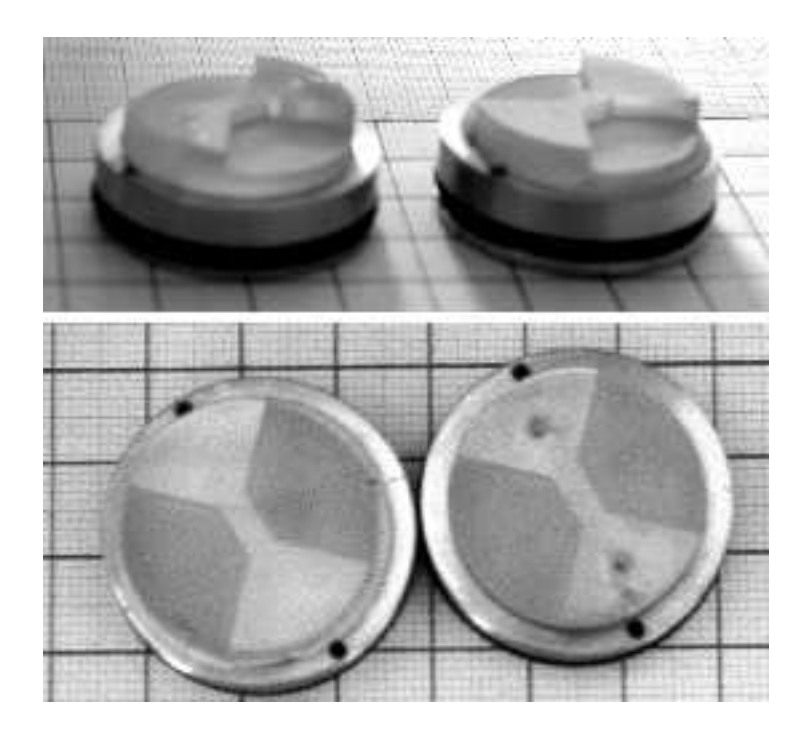


Figure 5.2: The shape of the wafers.

Heater and Pt100 temperature sensors are mounted below the bottom wafer and above the upper wafer (**Fig. 5.6**). Both substrates are heated simultaneously, thus allowing a proper temperature stabilization during the experiment (see section: Confined polymer measurements). The heater is controlled via a Lakeshore temperature controller model type 340 or 330, respectively.

5.1.2 The beamline

Most of the experiments have been performed at beamline D4.1 at HASYLAB/DESY (Fig. 5.3 and 5.4). The applied energy regime was between 22 and 25 keV, which is well within the appropriate range of 20 to 30 keV. The energy should be high enough to penetrate the bridge, but it should also be low enough to investigate films with thicknesses of 1000 Å. The beamline D4.1 is located at a bending magnet. The beam is collimated via the first slits. Higher harmonic radiation is suppressed by means of a mirror. The beam is monochromatized by a Si (111) single crystal monochromator. The monochromatic beam enters the first flight tube (labelled #1 in Fig. 5.3) and passes trough the pre–sample slit #2 and the monitor #3. Behind the monitor the beam hits the sample. The radiation scattered by the sample passes a guard slit #4, the second flight tube #5 and the detector slit. In Fig. 5.4 a scheme of the diffractometer is shown. The first and second flight tubes

can be tilted and vertically aligned by tilting stages **R1**, **R2** and translation stages **Z1**, **Z2**, respectively.

The beamline goniometer is presented in **Fig. 5.5**. It consists of an upper tilting stage **GUS**, a lower tilting stage **GLS** and horizontal translations parallel and perpendicular to the beam **XS** and **YS**, respectively. The sample can be rotated with respect to the Z-axes by the rotation stage **OMS**. The detector is rotated about the Z-axes by the rotation stage for the detector arm **2TS**. On top of the tilting stage **GUS** an additional translation table was mounted (#6 in **Fig. 5.3**). It was used to align the sample (the confined area) with respect to the rotation center of the goniometer.

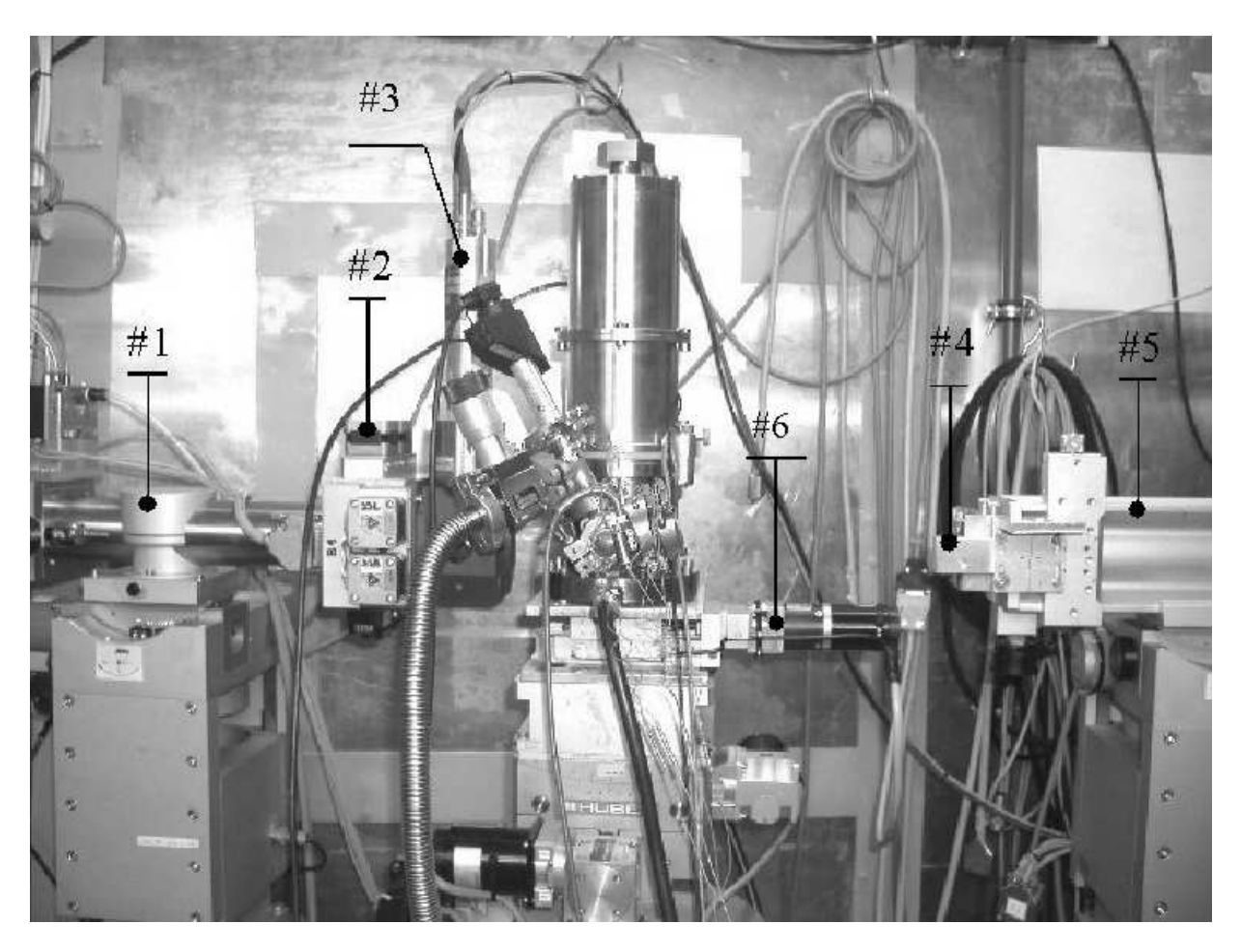


Figure 5.3: A photo of the confined liquid setup at the beamline D4.

The reflectivity curves were recorded by simultaneously moving the tilting stage **R2**, the vertical translation **Z2** and the tilting stage **GUS**. The movement of **R2** and **Z2** defines the outgoing angle α_f and the tilting of **GUS** the incoming angle α_i . The rocking curves²

²The rocking curves are similar to the transverse scans defined in 4.1, but here the scans are performed only in the range of the specular peak for alignment purposes.

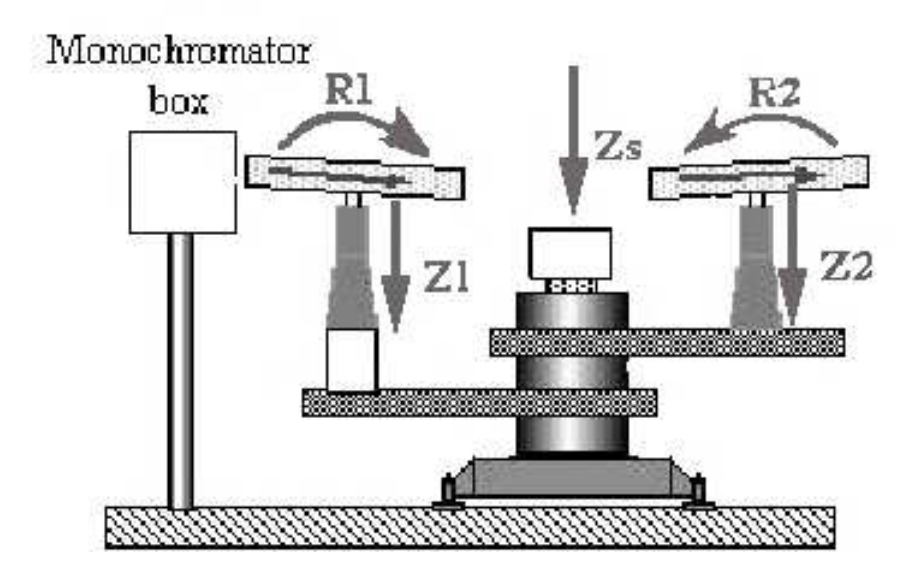


Figure 5.4: The scheme of the diffractometer (taken from the D4 homepage, DESY, Hasylab)

were measured by scanning the tilting stage **GUS** at fixed positions of the tilting stage **R2** and vertical translation **Z2**. The scans out of the incidence plane were done by rotation of **2TS** at fixed positions of **OMS** and **GUS**.

A Cyberstar X1000 detector was used for the experiments. The beam size was defined by adjusting the pre–sample slit to 0.2 mm in the vertical and 1 mm in the horizontal direction. During the reflectivity measurements, the apertures of the guard slit, the detector slit and the pre–sample slit were kept at equal sizes. Additional information of the beamline is presented in [75].

5.1.3 Preparation of the confined films

Liquid films (CCl₄ or Octamethylcyclotetrasiloxane) on the upper and lower wafers were created during the experiments at temperatures below (cooling runs) or above (heating runs) room temperature. The following procedure was used to build up the films:

- Evacuation of the cell down to the minimum possible pressure (10^{-4} mbar) .
- Closing of the valve to the vacuum pump (Fig. 5.6).
- Injection of the liquid through the rubber seal on the flange (**Fig. 5.6**, #3) at open gap (two times 2.5 ml).

During cooling runs the working temperature T_w of the set point at the heat/cool circulator had always to be adjusted 2°C less than the desired temperature at the bottom temperature

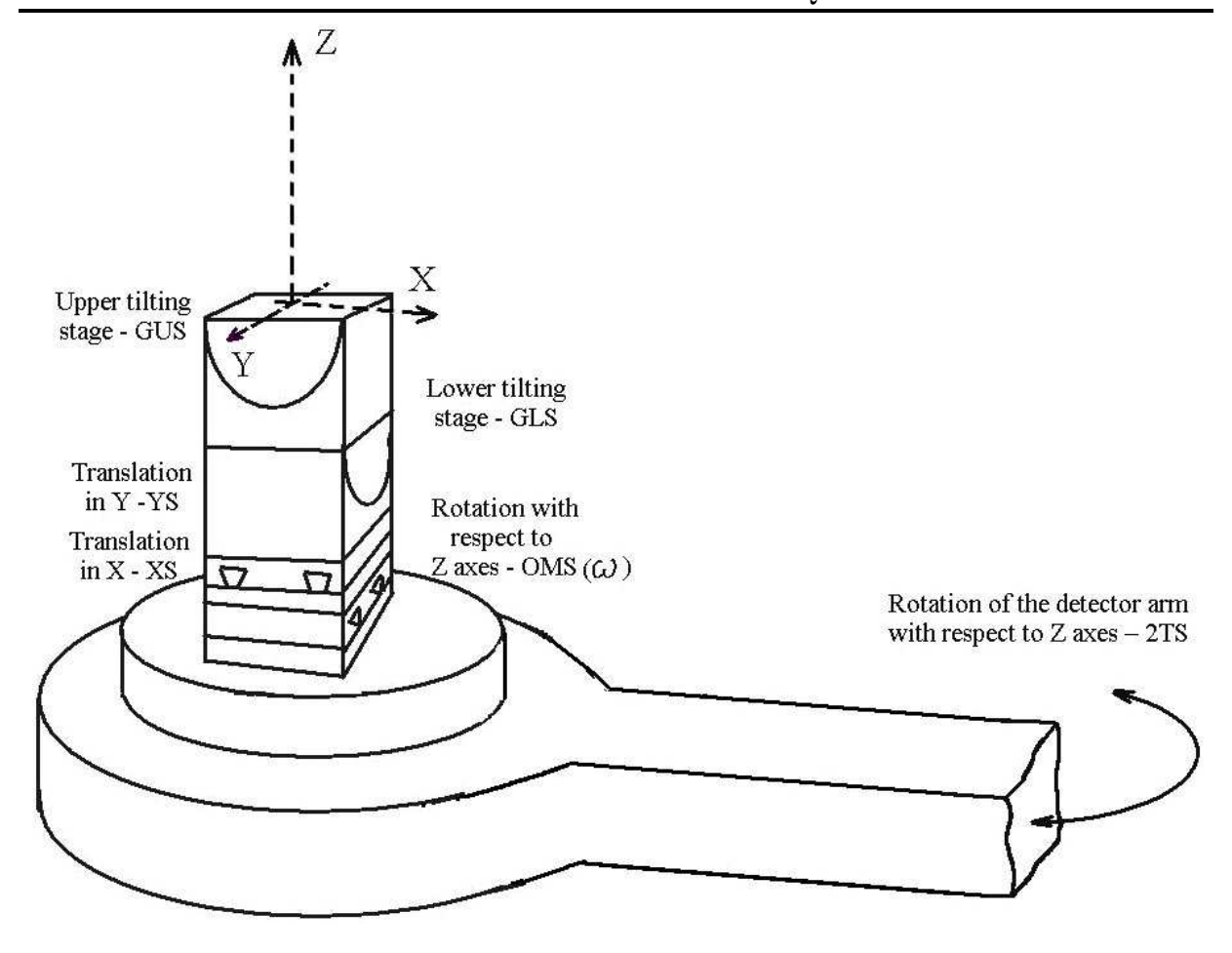


Figure 5.5: A sketch of the goniometer.

sensor - T_{low} (**Fig. 5.6**), because of losses in the viton pipes. An additional temperature offset of 2°C existed between the upper and lower wafers due to the initial open gap between them. After injection the liquid condenses at the bottom of the sample cell (the reservoir). During heating runs the temperature T_3 was lower than T_{low} and T_{up} (**Fig. 5.6**). It was found that in order to prevent condensation of the liquid on the walls of the vacuum pipes the temperature T_3 must exceed these limits. This implied heating of the vacuum pipes by means of the heater #3.

There are two parameters that determine the thickness of the liquid films at a surface above the reservoir ([76] and the works referred whithin [77, 78, 79, 80]). First, the thickness l_0 depends on the temperature difference, ΔT , between the reservoir and the surface:

$$l_0 = \left(\frac{A_{eff} N_A}{6\pi Q_A \Delta \rho^*} \frac{T}{\Delta T}\right)^{1/3},\tag{5.1}$$

where Q_A is the latent heat at evaporation of one Mol liquid, N_A Avogadro's constant, T the temperature of the reservoir, A_{eff} the effective Hamaker constant and $\Delta \rho^* = \Delta \rho/m = \rho_l^* - \rho_q^*$ the specific density difference between the liquid and the gas phase.

The second parameter is the height, h, of the surface with respect to the liquid surface of the reservoir:

$$l_0 = \left(\frac{-A_{eff}}{6\pi\Delta\rho gh}\right)^{1/3},\tag{5.2}$$

Here g denotes the gravitation constant.

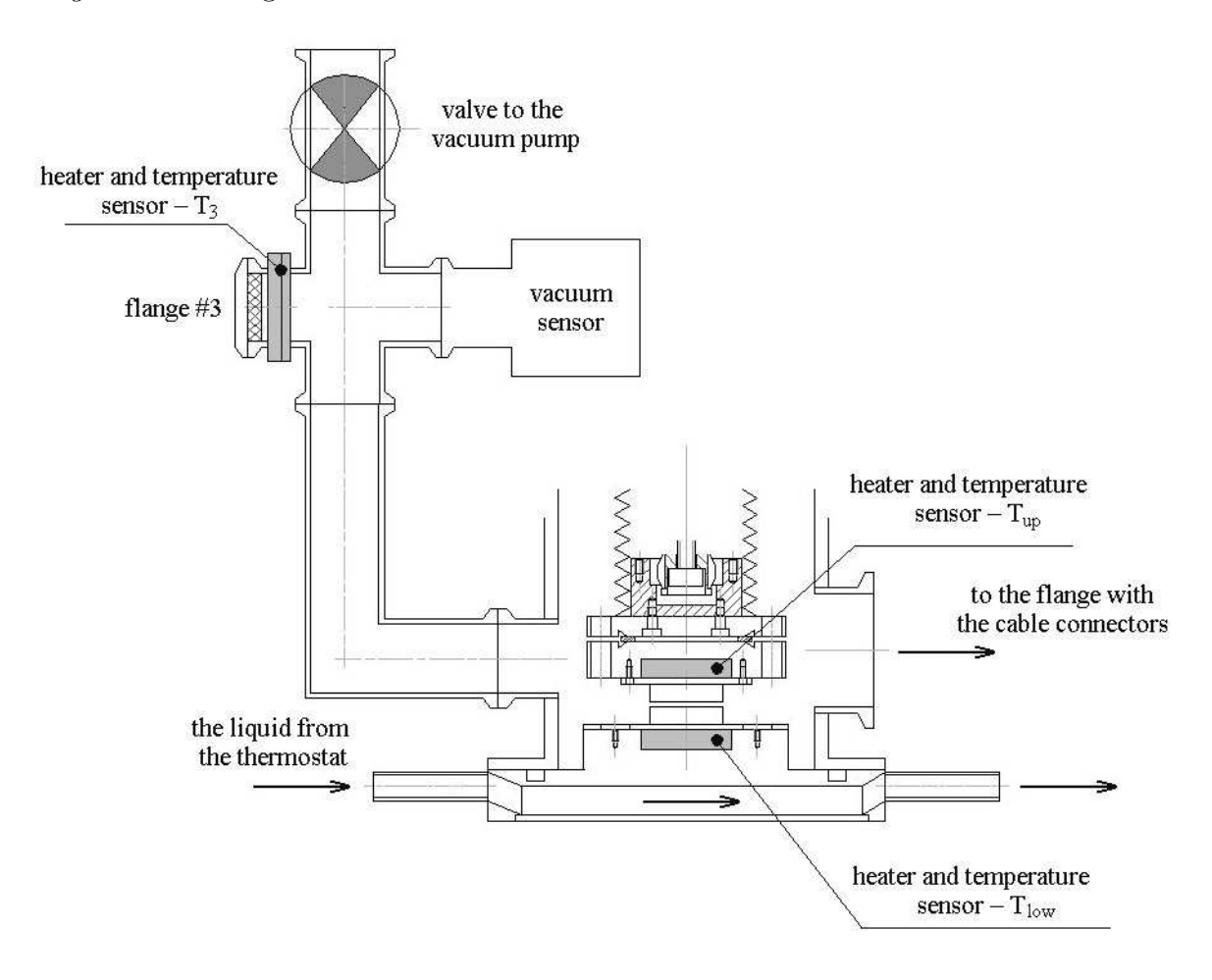


Figure 5.6: Additional vacuum setup for the cell.

From Eqs. 5.1 and 5.2 it turns out that the film thickness on the wafer becomes thinner with increasing ΔT and height h. Since the position and the temperature difference of the upper wafer with respect to the reservoir are higher than those of the lower wafer, the film on the upper wafer is much thinner.

An example for a typical experiment is as follows:

• Cooling run; for $T_w = 13$ °C, T_{low} and T_{up} are equal to 15.9°C and 17.6°C, respectively. On the lower wafer, a CCl₄ film with thickness of 244 Å was observed (**Fig. 5.7**, curve 1).

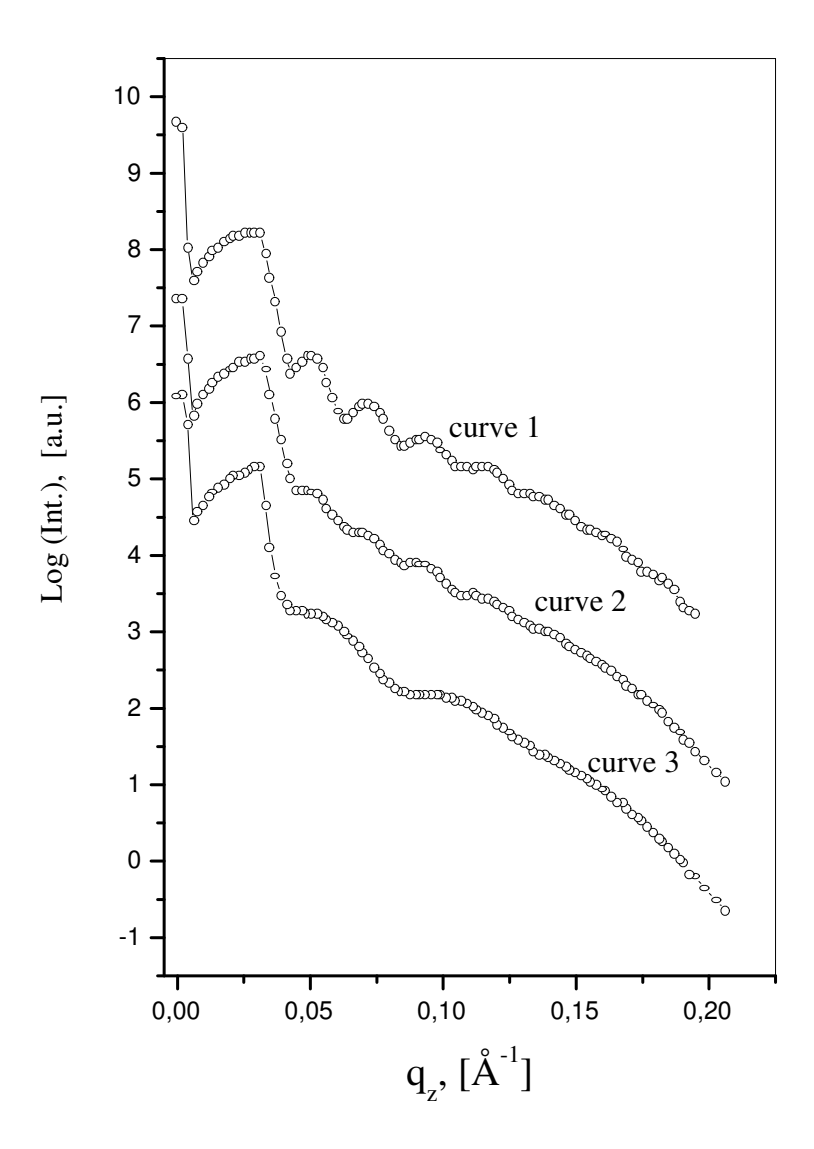


Figure 5.7: Reflectivity curves of a CCl_4 film at open gap. Curve 1 is the reflectivity curve of a film on the lower wafer obtained at a cooling run. Curve 2 and 3 are the reflectivity curves of films observed at a heating run on the lower and upper wafer, respectively.

• Heating run; for $T_w = 27^{\circ}\text{C}$ and $T_3 = 35^{\circ}\text{C}$, T_{low} and T_{up} are 26.7°C and 25.6°C, respectively. At these conditions the CCl₄ films obtained on the lower and upper wafer have thicknesses of 249 Å, and 83 Å, respectively (**Fig. 5.7**, curve 2 and 3).

The experiments showed that films obtained at cooling runs were more stable than those from heating runs. Reasonable confined layers were not observed during heating runs. It is supposed that this behaviour is mainly due to insufficient confinement and not due to the elevated temperatures.

During the process of closing the gap additional liquid evaporates from the surface of the lower wafer because of the temperature difference between the wafers. Thus, the real initial

thickness of the confined film could not be estimated from the thicknesses of the films on the upper and lower wafers. Shortly after closing the gap the temperatures of both wafers became identical. The side walls of the upper wafer also wetted, and after the experiment during the reopening procedure of the gap the liquid flowed down. This behaviour inhibited measurements of film thicknesses immediately after opening of the gap.

Confined polymer films

The samples were prepared by *Denitza Lambreva* Ph.D. student in the group of *Prof. Wim de Jeu*, FOM Institute AMOLF, Amsterdam. The polymer film was created only on the bottom wafer by spin—coating a solution of poly(ethyleneoxide—b—ethylene/butylene) diblock copolymer in dichloromethane [81].

The polymer measurements were performed in the temperature range from 30°C to 125°C. For temperatures above 40°C heat losses in the pipes of the circulator were noticeable. T_w has to exceed the desired T_{low} by about 5°C. For the fine regulation of the temperature the heater system at the lower and upper wafer (**Fig. 5.6**) was used together with the Lakeshore temperature controller. The temperature of the lower wafer was regulated. In the case of $T_{low} = 90$ °C for instance, at open gap the values of T_w and T_{up} were 95°C and 76°C, respectively. After closing the gap the temperatures T_{low} and T_{up} became identical.

5.1.4 Preparation of the wafer surface

Confined liquid experiments at small gap sizes (less than 100\AA) require almost molecular smooth and clean surfaces. Additionally, the special shape of the crystals complicate the situation. Thus, the first sets of wafers (one silicon and one sapphire) were manufactured at the crystal laboratory of the Institut für Festkörperforschung at the Forschungszentrum Jülich. The next sets (silicon only) were produced from a wafer with a diameter of 100 mm, a thickness of 10 mm and a curvatures $1/4 \cdot \lambda$ (polished by Zeiss). The surface of the wafer was cut parallel to (111). The crystal was separated into small cylindrical pieces with diameters of 26 mm at the crystal laboratory in Hasylab. The butterfly shape (Fig. 5.2) was created at the crystal laboratory of the Institut für Feskörperforschung. Before cutting, the surface was covered with wax. It was removed at the final stage using Acetone. The surface roughness of the top and bottom wafers was measured during the X-ray measurements, and it was about 5 Å in the beginning of the confinement.

Right before the experiment with the liquids the crystals were cleaned using a mixture of 60 ml $\rm H_2O_2$ and 100 ml $\rm H_2SO_4^3$. In order to prevent dust particles to settle between the substrates the wafers were mounted into the cell in a clean room. The system was evacuated during the experiment.

5.1.5 The accuracy in the parallel alignment of the substrates

The alignment of the substrates was performed by taking rocking curves. The two peaks in these scans represent the upper and the lower wafer, respectively. Thus, the angular

³This solution removes organic impurities.

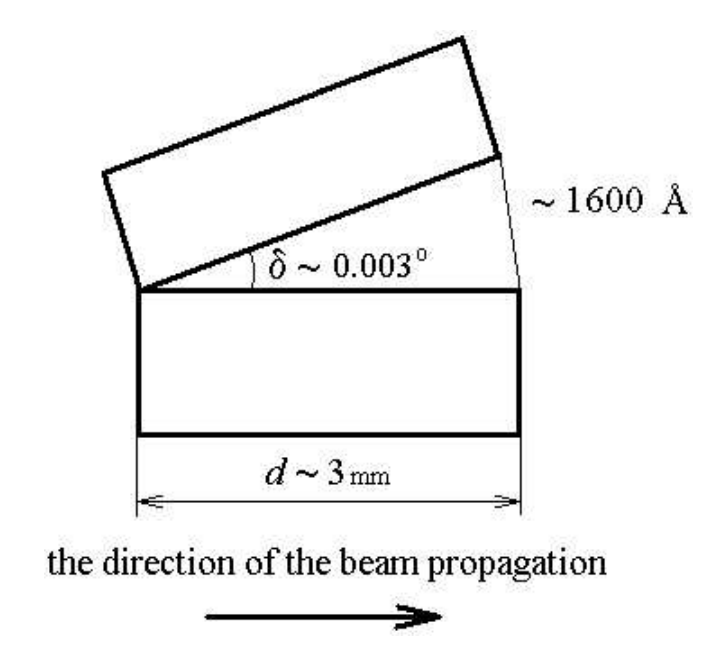


Figure 5.8: The upper wafer is tilted at an angle δ with respect to the lower one.

difference of the reflection positions directly indicates the tilting angle δ (**Fig.5.8**). Adjusting the peak positions to a single value is therefore equivalent to a parallelization with a precision better than the FWHM of the rocking curve ($\approx 0.003^{\circ}$).

In order to check, if the precision is sufficient for the experiment, a simple estimation was applied. Assuming that the surfaces of the wafers are molecularly smooth and misaligned by $\delta = 0.003^{\circ}$, the film thickness difference between the two edges of the bridge in the direction of the beam propagation is 1600 Å (**Fig. 5.8**). Here, the advantage of the self–align system becomes obvious. If an interferometer is used for the alignment, the precision would be restricted to the properties of the beam. If, in contrast, a self–align system is used, the precision is only restricted to the smoothness of the wafer surfaces.

5.1.6 The procedure of the sample confining

Before starting the confinement the lower wafer was aligned parallel to the primary beam, and the position, where the lower wafer was in the half cut of the primary beam, was defined as vertical zero. After closing the gap the sample was scanned vertically through the beam in order to check, if the gap was completely closed. Then, the rocking scans at angles in the beginning and in the middle of the reflectivity curve were performed in order to control, if the upper wafer was tilted with respect to the lower one. A last evidence for the confinement was the vanishing of the critical angle effect from the reflectivity curve.

5.2 Description of the fluids used as samples

5.2.1 Structure and properties of carbon tetrachloride (CCl₄) and Octamethylcyclotetrasiloxane (OMCTS)

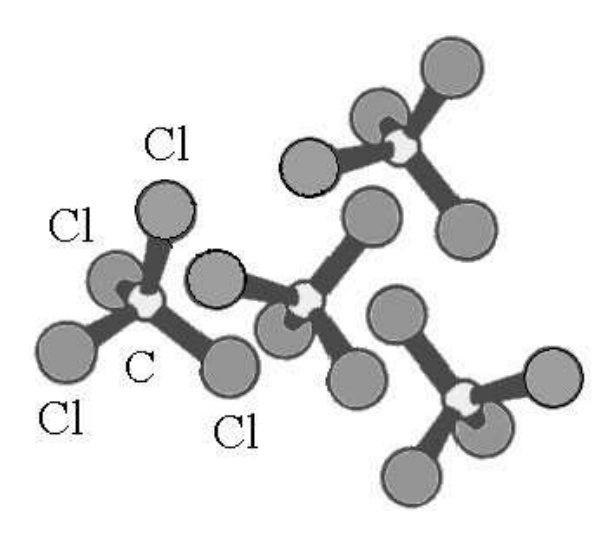


Figure 5.9: The structure of the CCl₄ molecule.

Carbon tetrachloride

The liquid structure of CCl₄ has been a subject of numerous diffraction studies [82, 83, 84, 85]. The molecule of carbon tetrachloride is highly symmetrical and it has a tetrahedral shape (Fig. 5.9). The intramolecular distances C-Cl and Cl-Cl reported from various authors are about 1.77 Å and 2.89 Å, respectively [83, 84, 85]. Because of the small C-Cl distance in comparison with other tetrachlorides [85] the CCl₄ molecule can be approximated by a sphere with an average radius of about 5 Å [83, 84]. The slight difference of the molecule from the spherical shape imposes very week orientational correlation in the structure of the liquid. The orientational correlation was explained by most of the authors, e.g. [82, 86, 83], in terms of the so-called Apollo-type model, where the Cl of a neighbouring molecule is nested into a hollow formed by three Cl atoms of the central molecule (see Fig. 5.9). This configuration is also known as a corner-to-face arrangement. The Apollo model was rejected by Pusztai and McGreevy [84] and recently by Jovari et al. [85]. The latter authors suggested that the presence of a corner-to-face arrangement of the nearest neighbor is only 4\%, whereas the corner-to-corner and corner-to-edge arrangement is 63\% and 27%, respectively. Some additional properties of the liquid CCl₄ are given in **Tab. 5.1**.

According to the work of *Bridgman* [87], CCl₄ also exists in solid phases. At room temperature CCl₄ crystallizes in phase I at approximately 1.3 kbar [88]. The maximum pressure between the wafers in the experimental cell was about 1.1 kbar, but the experiments were

melting point	$T_{\rm sm}$	-23.0°C
boiling point	T_{kp}	76.6°C
saturation pressure	p_{g}	$1.333 \cdot 10^{6.894 - \frac{1220}{227.2 + T}} \text{ mbar}$
density of fluid	$ ho_{ m f}$	$(1.6337 - 0.002 \cdot T) \text{ g/cm}^3$
surface tension	γ	$(2.921 - 0.0126 \cdot T) \cdot 10^{-2} \text{ Jm}^{-2}$
Hamaker constant	A	$\approx 45 \cdot 10^{-20} \text{ J}$
molecular mass	M_M	153.8 · amu
van der Waals diameter	d_{CCl_4}	5–7Å
dispersion at 22 keV	δ	$0.6548 \cdot 10^{-6}$
absorption at 22 keV	β	$0.0038 \cdot 10^{-6}$
critical angle at 22 keV	Θ_c	0.065°

Table 5.1: Physical properties of CCl₄ [77, 83, 84].

performed at 15 – 19°C. Therefore, during the confinement it may happen that the liquid-crystal phase line is crossed. Thus, the information about phase I may be important here. Rudman and Post [89] have shown that phase I in the Bridgman diagram consists of two different crystal modifications, and the authors called them phase Ia and phase Ib. The phases Ia and Ib exist as plastic crystals⁴. Phase Ia is metastable [90] and it could be considered as an intermediate phase between the liquid and the solid crystal structure [86]. Additional information of the other high pressure phases II and III can be found in [91, 88]

Octamethylcyclotetrasiloxane

Experimental results dedicated to the investigation of OMCTS properties and structure data are not available despite of the fact that it is used by almost all groups performing SFA confined experiments. A few data are taken mainly from SFA experimental works (e.g. [36]). It is a quasispherical molecule with an effective diameter of about 7.8 Å to 9 Å⁵. The melting and the middle fraction boiling temperatures at normal pressure are 17°C and 175°C, respectively. The structure peak of OMCTS is shown in **Fig. 5.10**. It was obtained by an out–of–plane scan (scanning of angle θ (**Fig. 3.1**)). OMCTS and CCl₄ were bought from Merck/Merck KGaA.

5.2.2 Self–assemble diblock copolymer systems

A diblock copolymer molecule consists of two connected chemically different fragments, which are called blocks. The blocks themselves have the same properties as the low molecular weight single polymers. In most cases chemically different macromolecules do not mix. In spite of the chemical bond between the blocks the diblock systems also undergo two phase separations. In most systems the phase separation is accompanied by order-

⁴Only the carbon atoms have fixed places in the unit cell. The orientation of the chlor atoms is free.

⁵These values differ from author to author.

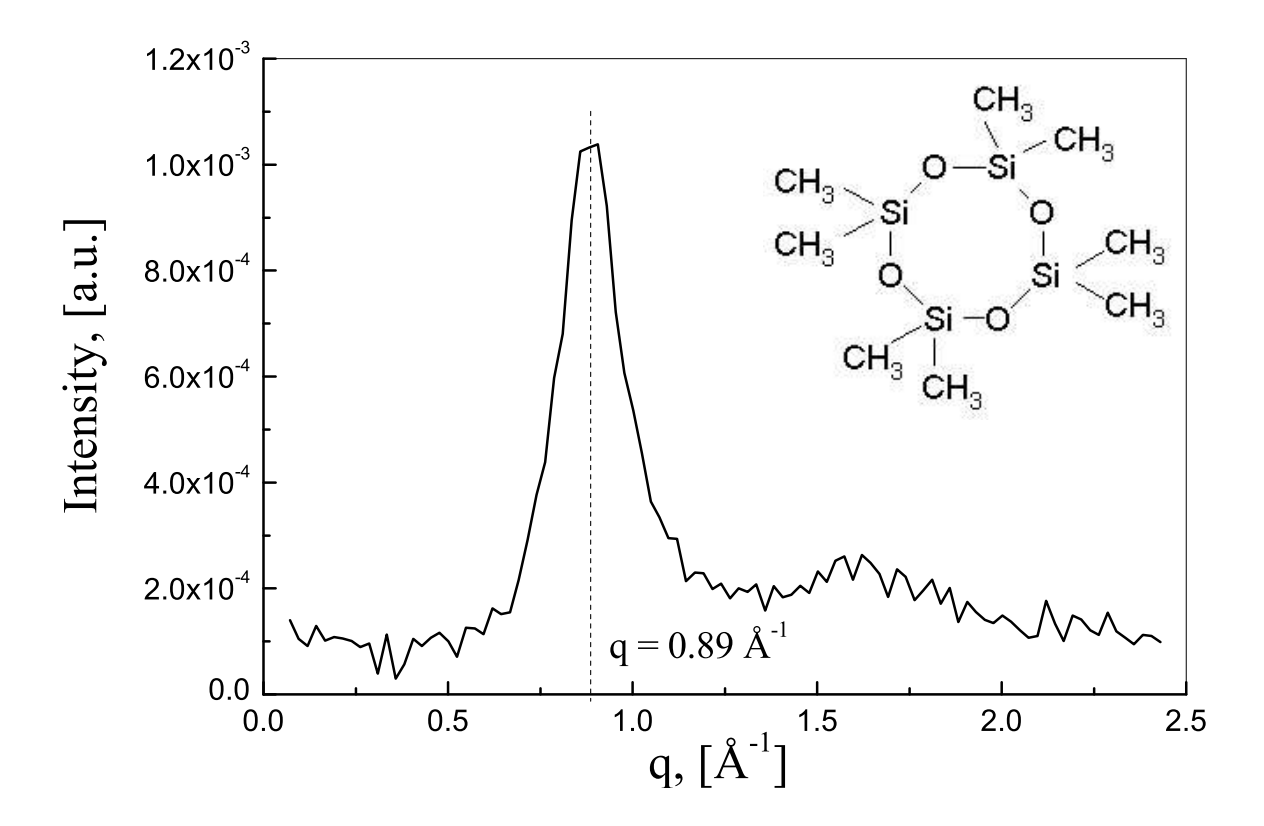


Figure 5.10: The liquid structure factor of OMCTS. The intensity was normalized to the monitor counts and the background was subtracted. The chemical composition of OMCTS is shown in the inset.

	PEO	PB_h
M_n [g/mol]	4300	3700
number of monomers	98	66
volume fraction	0.46	0.54
radius of gyration [nm]	1.1	1.3
lenght of nonfolded block [nm]	27.4	25.4
polydispersity	1.02	1.02

Table 5.2: Characteristics of the investigated diblock copolymers.

ing (e.g. [92]). The temperature, where the ordering is observed, is called order–disorder transition temperature. The phenomenon is also known as spontaneous self–assembling. The type of the ordered structure depends on the molecular architecture of the copolymer molecule.

Poly(ethyleneoxide-b-ethylene/butylene) (PEO-b-PBh) is a representative of the self-assemble diblock copolymers. The first block of the copolymer molecule is Poly(ethylene oxide) (PEO) (**Fig. 5.11a**). PEO is a well investigated polymer (e.g. [93, 94, 95, 96, 11]).

a)
$$\left\{ \begin{array}{l} -\operatorname{CH}_2 - \operatorname{CH}_2 - \operatorname{C} \right\}_n \\ \\ \operatorname{b} \cdot \left\{ -\operatorname{CH}_2 - \operatorname{CH}_2 - \operatorname{CH}_2 - \operatorname{CH}_2 \right\}_n \\ -\operatorname{CH}_2 - \operatorname{CH}_1 \\ -\operatorname{CH}_2 - \operatorname{CH}_2 \\ \\ \operatorname{CH}_2 \\ -\operatorname{CH}_2 \\ \\ \operatorname{CH}_3 \end{array} \right.$$
 N-type

Figure 5.11: The monomers that form the poly(ethyleneoxide-b-ethylene/butylene) block copolymer. **a)** Monomer of the poly(ethylene oxide). **b)** N and M type monomers of the hydrogenated poly(butadiene).

It has a flexible molecule and, following from the regular chemical structure, the PEO-block is able to crystallize [97]. The second block hydrogenated poly(butadiene) (PBh) consists of two type monomers N and M (**Fig. 5.11b**), where the amount of the N-type is equal to the amount of the M-type, and they are statistical distributed along the chain. The molecule chain of the second block has a non-regular structure, and it cannot crystallize. The PBh-blocks form an amorphous matrix, in which the PEO-blocks crystallize. In other terms, the crystallization of PEO happens in confinement of the amorphous matrix. The additional characteristics of the PEO-b-PBh are given in **Tab. 5.2** [81, 96].

After spin-coating an alternating layer structure consisting of PEO and PBh layers is created parallel to the surface of the silicon wafer (see the inset in Fig. 5.12). Since the substrate was not etched prior to the spin-coating, a layer of native SiO₂ existed between the silicon and the polymers. Thus, due to the strong hydrophilic properties of PEO, the diblock attaches via the PEO-block at the surface. As a result from the PEO and PBh alternating structure, the third and the fifth order Bragg peaks appear in the reflectivity curve (Fig. 5.12). In the presented curve the Kissing fringes from the whole film thickness are missing, because the investigated film is thicker than 3000 Å. The thickness of the multilayer period decreases with the temperature increasing from 220 Å at 40°C to 187 Å at 90°C [81, 96].

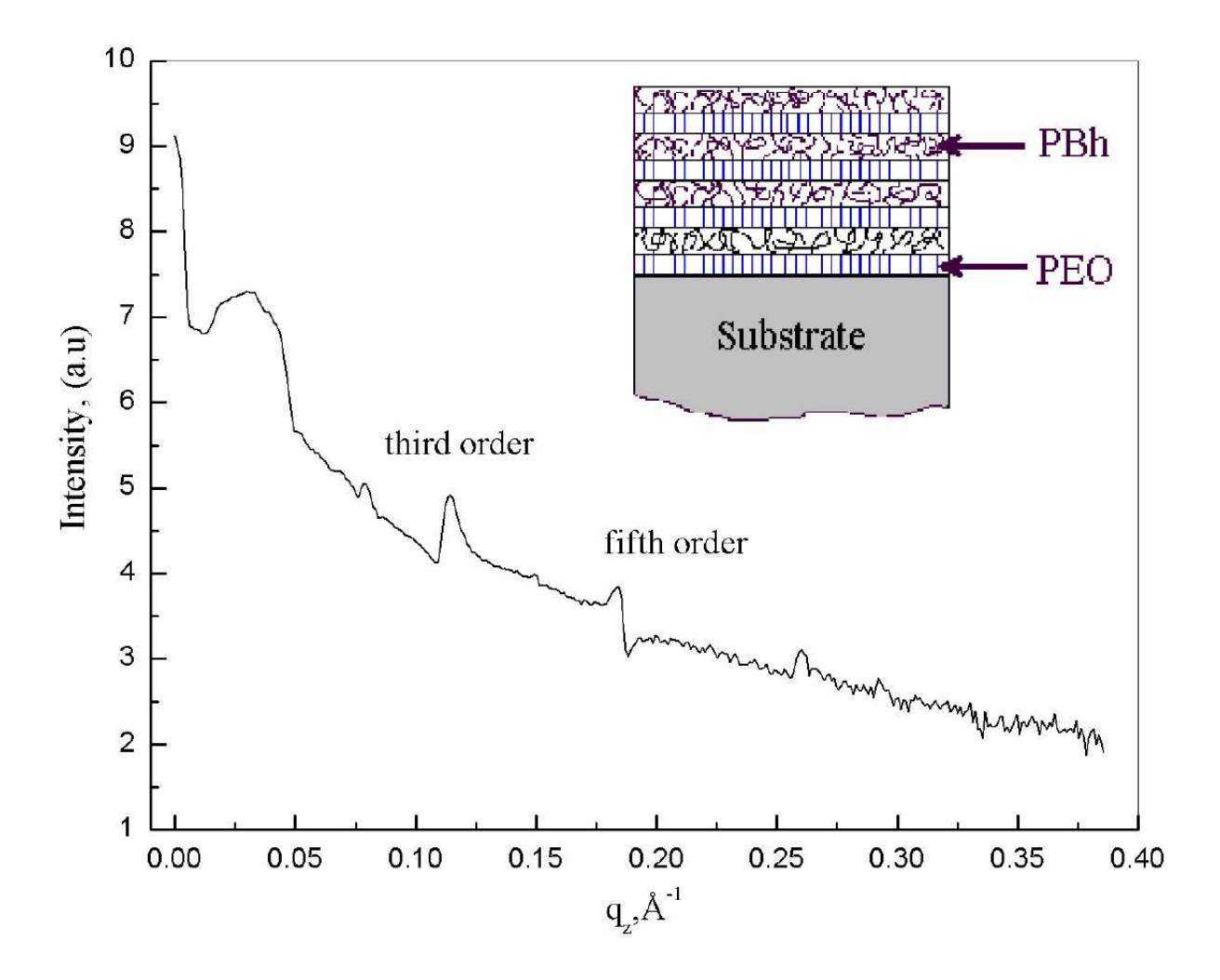


Figure 5.12: The reflectivity curve of the PEO-b-PBh film on the silicon substrate. The thickness of the film exceeds 3000Å. The layer structure is shown in the inset (see text). The first order Bragg peak appears in the region of the total reflection.

5.3 Results and discussions

5.3.1 Confined liquids

Fig. 5.13a shows the results obtained from a confinement of a CCl₄ film created at temperatures of the wafers and the circulator as indicated in the figure. The first and the second curves (from the top) were recorded at non-confined conditions. The first curve is the reflectivity curve of the lower bare wafer and the second is the reflectivity curve recorded after creation of the CCl₄ film on the lower wafer. The other curves were recorded after confinement at different readings of the sensor giving the relative travel of the upper wafer. The increase of the relative movement corresponds to an increase of the pressure applied to the sample. The last curve is taken at the maximum relative movement of the upper

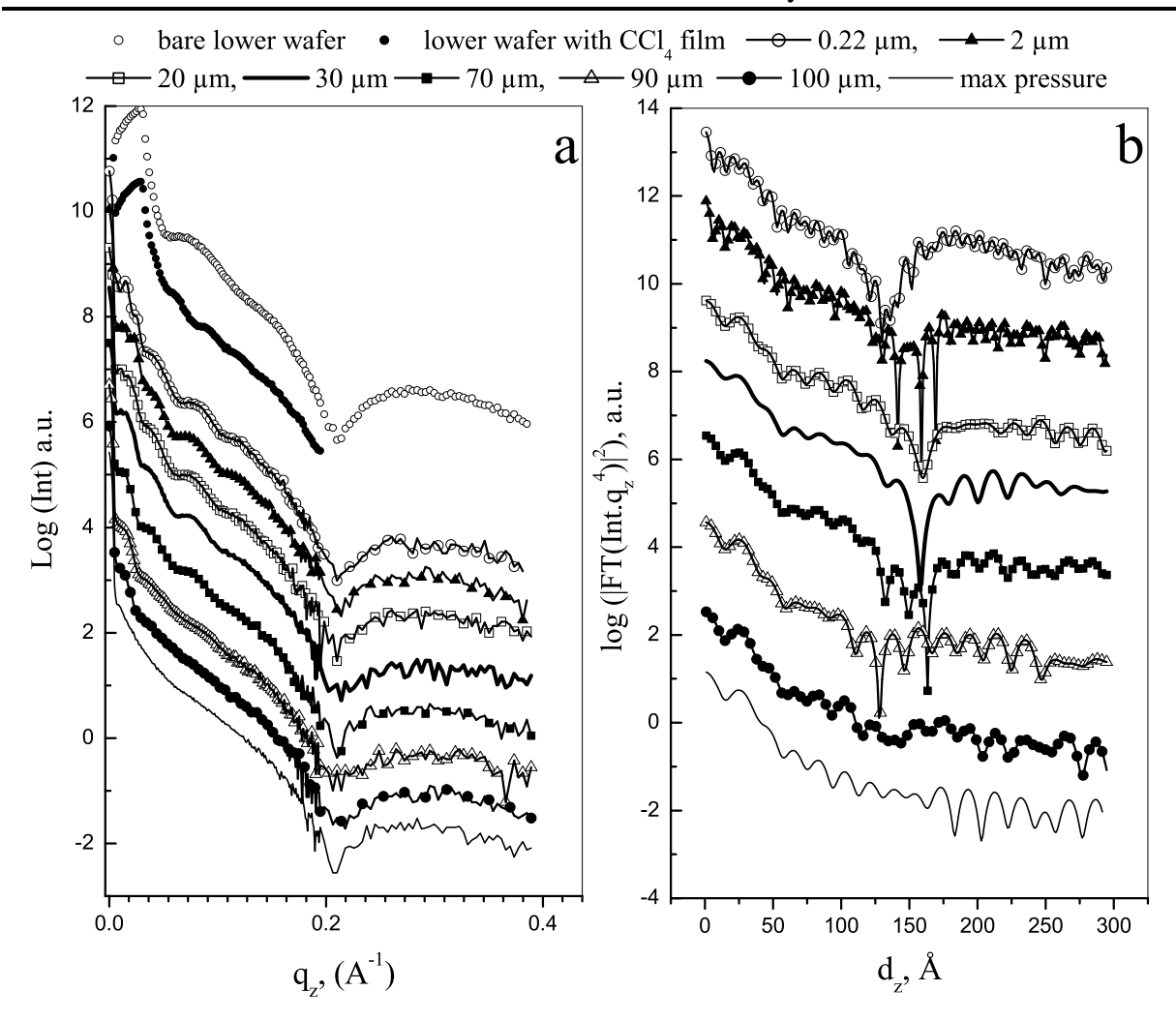


Figure 5.13: a) Reflectivity curves obtained at confinement of CCl_4 film. The first and the second curves (from the top) were recorded at non-confined conditions. b) The Fourier transforms of the confined reflectivity curves. The fast oscillations are due to a cut-off effect. Only the minimum at 150 Å is significant.

wafer and additional forcing of screw #3 (Fig. 5.1). The non-regular oscillations seen in the confined curves reveal that the CCl_4 film has a non-uniform thickness. The Fourier transforms of the confined reflectivity curves (Fig. 5.13b) show that the average film thickness is about 150 Å and with increase of the pressure it does not diminish. On the other hand, higher pressure leads to the disappearence of the oscillations in the reflectivity curves (compare the last two curves with the rest confined curves in Fig. 5.13a). This behaviour suggests that with an increase of the pressure the interference between the intensities reflected from the upper and the lower wafer surfaces becomes worse. The lost of interference can be due to dust particles settled between the wafers that damage and bend the wafer surfaces, if the pressure is applied. Usually, after the experiment the quality of the wafer surfaces was degraded.

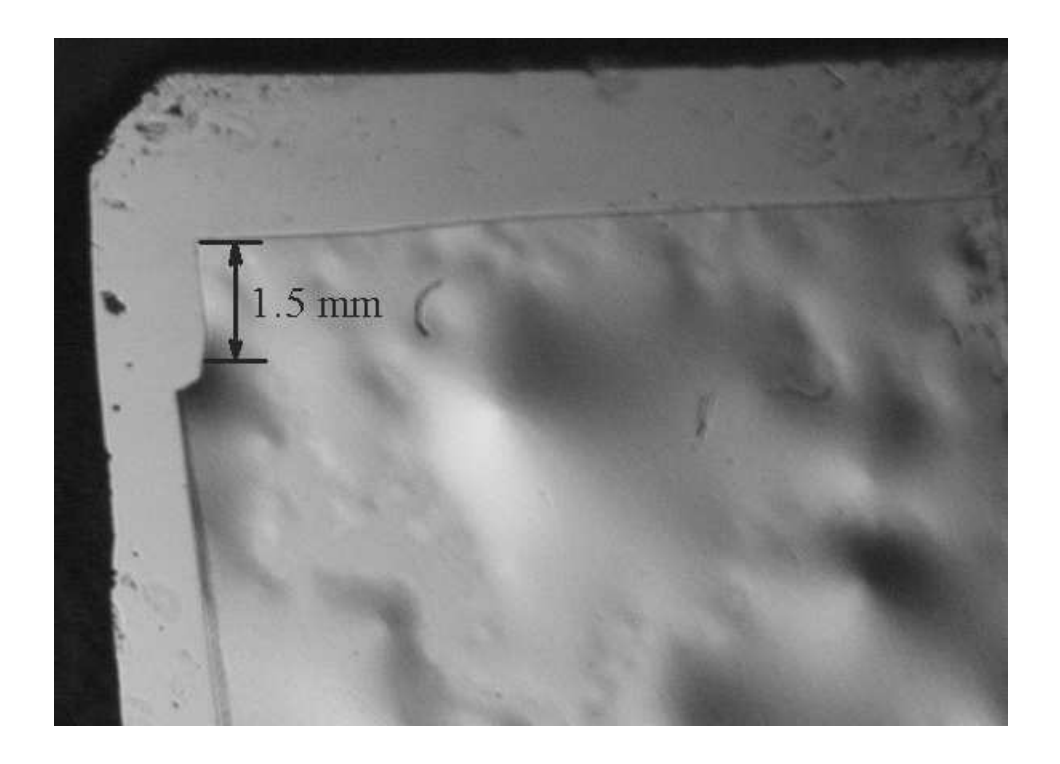


Figure 5.14: Microscope photo of two Si wafers fixed together by a thin liquid layer of OMCTS.

Further experiments confirmed the assumption about the impurities between the wafers. In **Fig. 5.14** a microscope photo of two Si wafers fixed together by thin liquid layer of OMCTS is shown. The lower substrate is a conventional wafer with a thickness of 0.5 mm, but the upper is very thin with a thickness of only 20 μ m. Both wafers were cleaned using the usual cleaning procedure right before the experiment. The wafers were put in contact to each other in the OMSTS liquid. Nevertherless, the surface shows hills due to the capture of dust particles between the wafers.

The scans out—of—the incident plane were performed in order to study the structure of the film in the plane of the wafer surfaces. The geometry of the experiment (**Fig. 3.5**) does not allow to use the enhancement of the scattered intensity as usually done by grazing incidence diffraction. Therefore, the scans were carried out at angles $\alpha_i = \alpha_f = 0$.

In some of the experiments with confined CCl_4 films, structure peaks were observed in the out-of-plane scans. One of the observed curve is compared in Fig. 5.15 with the structure factors of the liquid CCl_4 and of the CCl_4 crystal phase Ia. The first peak from the scan is very sharp and shifted at higher q values in comparison with the first peak of curves taken from literature. The second and the third peaks from the scan correspond to the valley peaks of the phase Ia and liquid CCl_4 structure factors. The measured curve does not completely match the structure factors of the liquid CCl_4 or of the crystal phase Ia. However, the suspicion that the CCl_4 is crystallized can not be completely rejected. The temperature and the applied pressure on the sample have to result in a crossing of

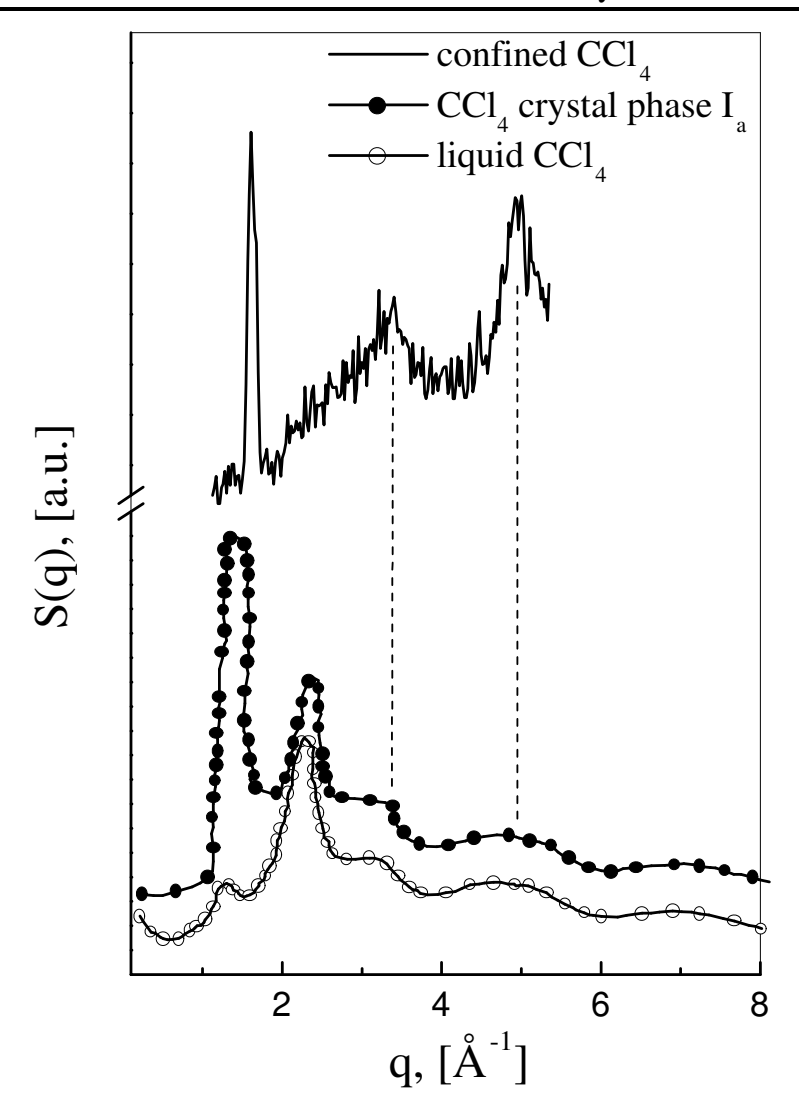


Figure 5.15: Out–of–incidence plane scan on a confined CCl₄ film and the structure factors of liqud CCl₄ [83] and of CCl₄ crystal phase Ia [86].

the liquid–crystal co–existants line in the Brigman diagram [87]. Since the first peak is very narrow, it also supports the assumption that a crystal phase appears in the confined CCl_4 liquid film. Moreover, according to literature the change in the density provoked by an increase of the pressure implies a shift of the first peak position to higher q values [83, 98]. The observed peaks may also match the structure factor of the more stable CCl_4 crystal phase Ib or correspond to a hybrid structure obtained under the influence of the substrates.

Unfortunately, the phenomenon could not be appropriately investigated. The fact that the grazing incidence diffraction effect is not applicable here as well as the small amount of scattering material and the low intensity of the primary beam inhibited the obtainment of reliable measurements.

5.3.2 Confined polymers

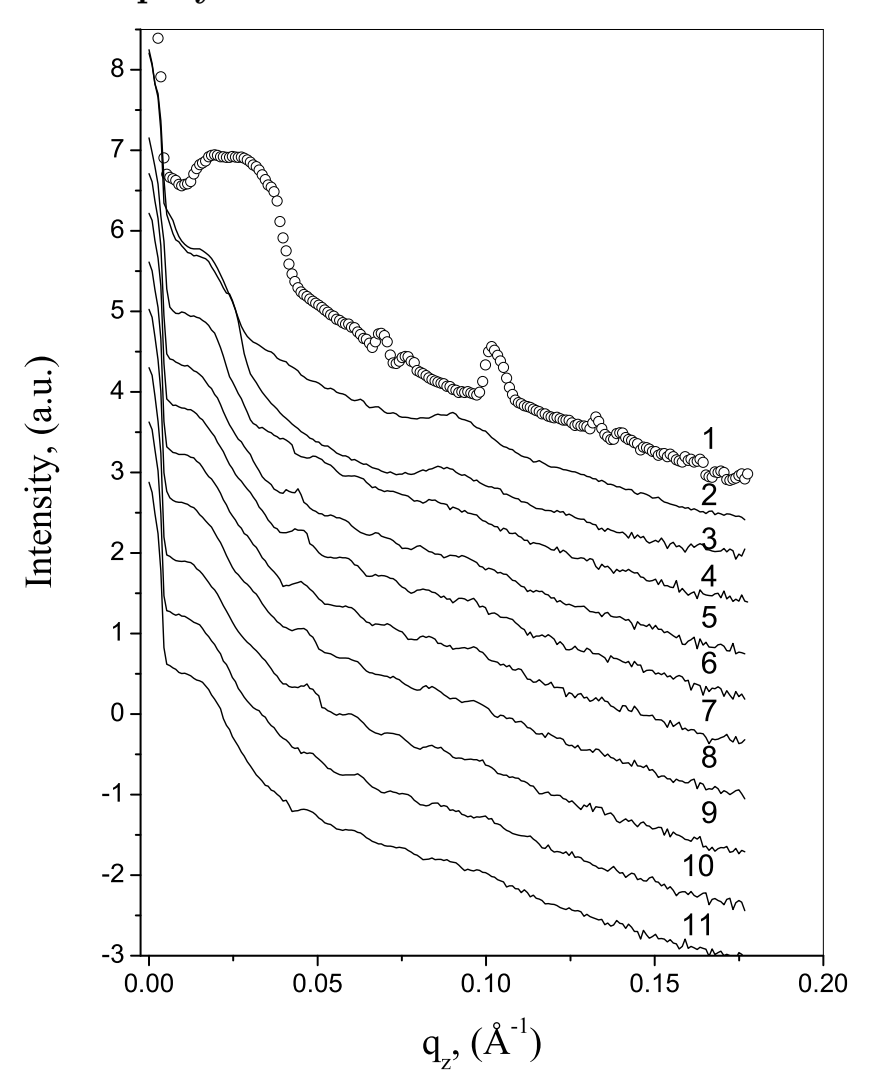


Figure 5.16: Confined PEO-b-PB film: The behaviour of the sample during a cooling run from 125°C down to 38°C and a fixed gap size. The curves are presented in a chronological sequence from the top to the bottom. The first curve is recorded on a non-confined sample. Curves 1,2,3,4 were measured at 125°C, curve 5 at 104°C, curve 6 at 93°C, curve 7 at 83°C, curve 8 at 72°C, curve 9 at 63°C curve 10 at 38°C and curve 11 at 124°C.

From previous investigations it was known that the thickness of crystal lamela and the whole polymer film increases, if the temperature decreases [81, 96]. If the gap size has a fixed value at certain temperatures it happens that only a non-integer number of the layer period fits into the gap. A reorientation of the lamelae is expected. The rearrangement is visible by the disappearence or recovering of the 3rd order Bragg peak, the strongest peak in the reflectivity curve (**Fig. 5.12**). Following this conception, the reflectivity curves of the confined PEO-b-PB film presented in **Fig. 5.16** were taken during a cooling run from

125°C down to 38°C. Starting from lamelae arranged parallel to the wafer surface, it was expected that during the run the initial structure will disappear and it may reappear at lower temperatures or when the sample is heated back to 124°C. Therefore, for the last curve in Fig. 5.16, the temperature was set back to 124°C. For comparison purposes, the reflectivity measured at 125°C, before the sample confinement, is additionally shown in the figure (curve number one). The second curve was taken immediately after the confinement at 1000 V (maximum presure)⁶ and 125°C. After waiting for 12 h at these conditions, curve 3 was recorded. Then, the piezo-crystal was completely released to zero and turned back to the maximum value. A measurement (curve 4) was taken at 125°C. The rest of the curves in the figure were recorded at temperatures indicated in the figure caption.

The rearrangement starts during the confinement (compare the second with the first curve). The shape of the second curve suggests that the layer structure was distorted, but it did not disappear completely (the third order Bragg peak became smaller and broader). The distorted structure did not change significantly during the 12 h relaxation period. Similar structure freezing after confinement was observed also for other investigated samples. The explanation of the effect can be found in the experimental observations of confined systems, which indicate that the confinement leads to a retarding of the molecular motions (diminishing of the diffusion coefficients and increase of the viscosity was observed at confined systems (section 2.2)). The polymer crystallization studies show that the transport of the molecules may play an important role in the reorganization (recrystallization) process. Consequently, it can be assumed that the conservation of the structure obtained after the confinement is due to a suppression of the molecular movement in the system. The assumption is also supported by the observation of a further reorganization after release of the pressure on the sample (the third order peak vanishes, compare the third and the fourth curve in Fig. 5.16).

If it is accepted that the confined structure could not reorganize, then an explanation for the fact that the subsequent temperature change did not provoke the expected recovering of the primary structure is found. The gap size was fixed at 125°C and the following temperature decrease causes the expansion of the film, i.e. an increase of the pressure. Hence, the suppression of the reorganization rises continuously with a temperature decrease. Returning back to 124°C should lead to a slight relaxation of the system, but it still will not be free for reorganization, because it was already frozen at 125°C.

The release of the pressure (opening of the gap by decreasing the piezo crystal voltage) should allow the molecular rearrangement. Therefore, investigations at different pressures (gap—sizes) and temperatures were performed. The results are presented in **Fig. 5.16**. The oscillations observed in some of the curves in **Fig. 5.17** recorded at 0 V are a fingerprint of the dewetting here⁷. In this case a thin polymer layer of about 100 Å remains on the substrate⁸, and it gives rise to the oscillations observed in the curves.

⁶The increase of the relative movement is equivalent to an increase of the voltage applied to the piezo crystal. It corresponds to an increase of the pressure on the sample. 1000 V means that the maximum possible pressure is applied.

⁷The dewetting phenomenon was shortly discussed in the beginning of section 4.2.2.

⁸The dewetting process, where part of the polymer remains on the wafer surface, is in literature known

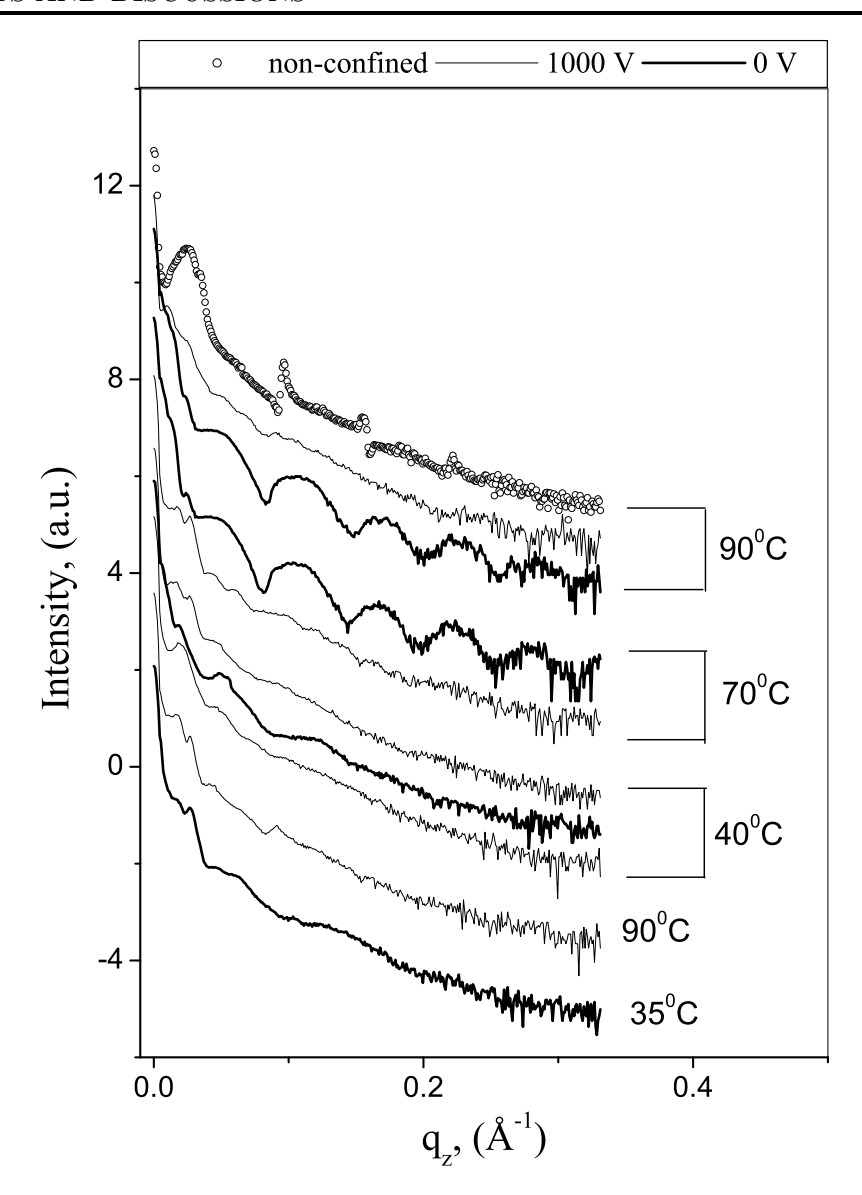


Figure 5.17: Confinemet of PEO-b-PB: The sample behavior at combined variations of the temperature and the gap-size. The curves are given in a chronological sequence from the top to the bottom. The first curve was recorded at non-confined conditions and 90°.

The last experiment shows that opening of the gap caused damages of the film integrity and dewetting of the polymer film occured. In spite of the dewetting the third order Bragg peak partially recovers after heating back to 90°C (**Fig. 5.17**). Since the maximum pressure was applied at 40°C, one may expect that at 90°C the film is not so strongly compressed and molecular movements are allowed. The partial recovering of the third order Bragg peak could be an evidence that the confined structure can in fact reorganize in dependence on the temperature, if the molecules are not frozen.

as pseudo-dewetting [99, 16].

Out-of-plane scans were also performed during the experiments with confined polymer films, but the primary beam in Y-direction (**Fig. 3.1**) was too broad and it was not possible to observe objects larger than 100 Å. The lamelae structure of the investigated polymer has a period around 200 Å. Therefore, only higher order Bragg peaks could be registered. Structure peaks have not been recorded during the scans. It may happen that the structure obtained after confinement has a behavior of two dimensional crystal powder. Hence, the scattered intensity will be uniformly distributed in all direction and the intensity of the higher order Bragg peaks will be insufficient to be distinguished from the background. Additionally, it is known that, if the lamelae structure is not perfect, the higher order Bragg peaks do not appear.

Chapter 6

Conclusions and Outlook

Supported polymer thin films

Polystyrene thin films have been studied depending on the molecular mass, film thickness, temperature and the hydrophobisites of the substrate. The diffuse scattering X–ray data have been refined using the Liquid model based on the capillary wave theory and the Fractal model describing the solid surfaces.

The Liquid model is derived for fluids in equilibrium, but the investigated system shows very slow dynamics resulting in a nonergodic behaviour. Therefore, the Liquid model is not appropriate for a description of the studied samples. The application of the Fractal model yields a reasonable description of the surface structure, because the high viscosity of the samples allows to regard the polymer surface as quasi-solid. However, using this model may not be completely correct at temperatures around the melting point of the polymer, especially in the case of low molecular polymer films. The most suitable model for the system would be a model, which takes into account the viscosity and the mechanical modulus of the polymer.

The temperature behaviour of the samples depends on the film thickness and the molecular mass of the polymer. Thin films and films with high molecular masses do not relax with increasing temperatures. On the other hand, thick films and films with low molecular masses seem to have comparatively mobile surfaces. In this case, at high temperatures the propagation of capillary waves on the sample surface could be possible.

The results and discussions show that the interpretation of the static diffuse scattering may become very complicated in the temperature range, where the films are in an intermediate solid/viscose liquid state. In this case the relaxation time of the films is comparable to the sampling time and the investigated system is no longer ergodic.

From the presented results and the literature data it follows that the kinks in the transverse scans have not the meaning of cut-offs like defined in the capillary wave theory. They appear after evaporation of the solvent (4.2.3). Therefore, the effect may be a result from a combination of slow motion waves on the surface, artefacts from evaporation and interaction of the polymer film with the substrate.

The presented results do not reveal significant differences between samples with hydrophilic

and hydrophobic substrates. The additional experiments show that this is due to the instability of the samples with temperature and storage time of the used hydrophobic substrates, which may be already hydrophilic at the beginning of the X-ray experiments. Further dynamic and static diffuse scattering experiments during annealing of the polymer films should explain the kinks appearing in the transverse scans. It should be interesting to compare the transverse scans of various samples, where the evaporation of the solvent differ. A slow evaporation of the solvent will result into a slow increase of the viscosity and keep the polymer molecules relatively mobile for a longer time. Thus, the ability of the molecules to resist against the attracting potential of the substrate will be enhanced. Hence, the final stucture of a film, which solvent is slowly evaporated, would be closer to the equilibrium state and the kinks probably will not appear in the diffuse scattering curves.

Confined liquid and polymer films

In the frame of the experiments with liquids and polymers in confined geometry it was possible to build and test a special cell, which allows scattering measurements of confined fluids over areas in the mm² range and with gap sizes of some hundreds of angstroms. The experiments with this setup give useful hints for further experimental developments.

The structure of confined liquids and polymers can only be solved with high quality reflectivity data showing pronounced oscillations. Large roughness of the wafer surfaces and/or a misalignment of the upper and the lower wafer inhibit the observation of Kissing fringes in the curves. During the last experiments the misalignment problems were solved and the need for a proper cleaning procedure becomes obvious. The experiment with the thin Si wafer is a step forward, because it provides a method to visualize the impurities on the wafers.

The problem with the dust particles on the wafer surfaces can also be solved by the use of a liquid as the lower substrate (mercury, for instance). This solution implies a complete reconstruction of the experimental cell and may require the use of a diffractometer designed for investigations of liquid surfaces (surface diffractometer).

In order to develop a proper confined polymer experiment it is important to determine the orientation of the PEO lamelae after confinement and cooling of the sample. Since the copolymer is phase—separated also at higher temperatures, it is clear that the sample will possess PEO crystals at low temperatures, even if it is confined. The determination of the structure after vanishing of the 3rd order Bragg peak in the reflectivity curve will shed more light on the processes happening during the confinement. Additionally, a measurement of the relaxation times of the confined polymer system may support or reject the idea of the retarding of molecular motions after the confinement.

From the polymer experiments it turned out that due to the small confinement area it is not possible to spin-coat a uniform film less then a few thousands of Å on the wafers. Since the diffractometer resolution at the used energy allows the measurement of films with a maximum thickness of about 1000 Å the total thickness of the polymer film remains one more unknown parameter in the experiment. Probably, neutron diffraction would help in

this case. Here, the substrates shoud not have a special form, because the radiation losses will be not so critical. Increasing the sample area will increase the scattering centers, and the scattering contrast can be enhanced by deuteration of the PEO or PBh blocks. Larger surface areas lead to more dust particles and problems for the alignment as well, but for the investigation of the lamelae structure in—plane it is not that crucial. From this point of view, it seems that a neutron scattering experiment would be suitable for the investigation of confined polymers. In contrast, the experiments with confined liquids require a beamline which can supply high intense, very well collimated X—rays with an energy in the range of 20 to 30 keV. The beamline also should allow reflectivity measurements and small angle diffraction in the plane of the sample.

Bibliography

- [1] J. Kraus, P. Müller-Buschbaum, T. Kuhlmann, D. W. Schubert and M. Stamm. Confinement effects on the chain conformation in thin polymer films. *Europhys. Lett.* **49**, 210–216 (2000).
- [2] R. L. Jones, S.K. Kumar, D. L. Ho, R. M. Briber and T. P. Russell. Chain conformation in ultrathin polymer films. *Nature* **400**, 146–149 (1999).
- [3] B. M. Discher, You-Yeon Won, D.S. Ege, J.C-M. Lee, F. S. Bates, D. E. Discher and D. A. Hammer. Polymersomes: tough vesicles made from diblock copolymers. *Science* **284**, 1143–1146 (1999).
- [4] M. Lüt, M. R. Fitzsimmons and De Quan Li. X—ray reflectivity study of self–asscembled thin films of macrocycles and macromolecules. *J. Phys. Chem. B* **102**, 400–405 (1998).
- [5] H.-G. Braun, E. Meyer and M. Wang. Dendritic growth of polyethylene oxide on patterned surface. In J.-U. Sommer and G. Reiter, editors, *Polymer Crystallization* pages 238–251. Springer–Verlag, Berlin 2003.
- [6] S. Walheim, E. Schäffer, J. Mlynek and U. Steiner. Nanophase—separated polymer films as high–performance antireflection coatings. *Science* **283**, 520–522 (1999).
- [7] J. J. M. Hall, C. A. Walsh, N.C. Greenham, E.A. Marseglia, R.H. Friend, S.C.Moratii and A.B.Holmes. Efficient photodiodes from interpenetrating polymer networks. *Nature* 376, 498–500 (2002).
- [8] H. Reichert, O. Klein, H. Dosch, M. Denk, V. Honkimäki and T. Lippmann. Observation of five-fold local symmetry in liquid lead. *Nature* 408, 839–841 (2000).
- [9] C.J. Yu, A.G. Richter, A. Datta, M.K. Durbin and P. Dutta. Observation of Molecular Layering in Thin Liquid Films Using X-Ray Reflectivity. *Phys. Rev. Lett.* 82, 2326– 2329 (1999).
- [10] M. AL-Hussein and G. Strobl. A comparative study of the mechanisms of initial crystallization and recrystallization after melting in syndiotactic polypropylene and isotactic polystyrene. In J.-U. Sommer and G. Reiter, editors, *Polymer Crystallization* pages 48–63. Springer-Verlag, Berlin 2003.

[11] G. Reiter, G. Castelein and J.-U. Sommer. Crystallization of polymers in thin films: Model experiments. In J.-U. Sommer and G. Reiter, editors, *Polymer Crystallization* pages 131–152. Springer–Verlag, Berlin 2003.

- [12] Hyunjung Kim, A. Rühm, L. B. Lurio, J. K. Basu, J. Lal, D.Lumma, S. G. J. Mochrie and S. K. Sinha. Surface dynamics of polymer films. *Phy. Rev. Lett.* 90, 068302–1–068302–4 (2003).
- [13] L. Lurio, Hyunjung Kim, A. Rühm, J. Basu, J. Lal, S. Sincha and S. G. J. Mochrie. Surface tension and surface roughness of supported polystyrene films. *Macromolecules* 36, 5704–5709 (2003).
- [14] J. Wang, M. Tolan, O. H. Seeck, S. K. Sinha, O. Bahr, M. H. Rafailovich and J. Sokolov. Surfaces of strongly confined polymer thin films studied by X-ray scattering. *Phys. Rev. Lett.* 83, 564–567 (1999).
- [15] K Shin, Y.Pu, M. H. Rafailovich, J. Sokolov, O. H. Seeck, S. K. Sinha, M. Tolan and R. Kolb. Correleted surfaces of free—standing polystyrene thin films. *Macromolecules* 34, 5620–5626 (2001).
- [16] M. Tolan, O.H. Seeck, J.-P. Schlomka, W. Press, J. Wang, S. K. Sinha, Z. Li, M. H. Rafailovich and J. Sokolov. Evidence for capillary waves on dewetted polymer film surfaces: A combined X-ray and atomic force microscopy study. *Phys. Rev. Lett.* 81, 2731–2734 (1998).
- [17] A. K. Doerr, M. Tolan, T. Seydel and W. Press. The interface structure on thin liquid hexane films. *Physica B* **248**, 263–268 (1998).
- [18] L. D. Landau and E. M. Lifshitz. Fluid mechanics. Pergamon Press, London 1959.
- [19] J. Jäckle. The spectrum of surface waves on viscoelastic liquids of arbitrary depth. *J. Phys.: Condens. Matter* **10**, 7121–7131 (1998).
- [20] J. L. Harden, H. Pleiner and P.A. Pincus. Hydrodynamic surface modes on concentrated polymer solutions and gels. *J. Chem. Phys.* **94**, 5208–5220 (1991).
- [21] H. Pleiner, J. L. Harden and P. Pincus. Surface modes on a viscoelastic medium. *Europhys. Lett.* 7, 383–387 (1988).
- [22] I.N. Bronstein and K.A. Semendjajew. *Taschenbuch der Mathematik*. Nauka, Moskau and BSB B.G. Teubner Verlagsgesellschaft, Leipzig 1983.
- [23] S. K. Sinha, E. B. Sirota, S. Garoff and H.B. Stanley. X-ray and neutron scattering from rough surfaces. *Phys. Rev. B* **38**, 2297–2311 (1988).
- [24] G. Palasantzas. Roughness spectrum and surface width of self-affine fractal surfaces via the K-correlation model. *Phys. Rev. B* **48**, 14472–10547 (1993).

[25] B. Bushan, J.N. Israelachvili and U. Landman. Nanotribology: friction, wear and lubrication at the atomic scale. *Nature* **374**, 607–616 (1995).

- [26] S. Granick. Soft matter in a tight spot. Physics Today 52, 26–31 (1999).
- [27] R.G. Horn and J.N. Israelachvili. Direct measurement of structural forces between two surfaces in a nonpolar liquid. *J. Chem. Phys.* **75**, 1400–1411 (1981).
- [28] H.K. Christenson. Experimental measurements of solvation forces in nonpolar liquids. J. Chem. Phys. 78, 6906–6913 (1983).
- [29] S. Karaborni. Order-Disorder Transition during Approach and Separation of Two Parallel Surfaces. *Phys. Rev. Lett.* **73**, 1668–1671 (1994).
- [30] J. Baschnagel and K. Binder. On the influence of hard walls on structural properties in polymer glass simulations. *Macromolecules* **28**, 6808–6818 (1995).
- [31] J. Gao, W.D. Luedtke and U. Landman. Structure and solvation forces in confined films: Linear and branched alkanes. *J. Chem. Phys.* **106**, 4309–4318 (1997).
- [32] F. Porcheron, M. Schoen and A.H. Fuchs. Monte Carlo simulation of a complex fluid confined to a pore with nanoscopically rough walls. *J. Chem. Phys.* **116**, 5816–5824 (2002).
- [33] B. Smit and T.L.M. Measen. Commensurateé freezing' of alkanes in channels of zeolite. Nature 374, 42–44 (1995).
- [34] J. Klein and E. Kumacheva. Confinement–induced phase transition in simple liquids. *Science* **269**, 816–818 (1995).
- [35] J.N. Israelachvili. *Intramolecular Surface Forces*. 2nd Ed., Academic Press, London 1991.
- [36] J. Klein and E. Kumacheva. Simple liquids confined to molecularly thin layers. I. Confinement-induced liquid-to-solid phase transitions. J. Chem. Phys. 108, 6996–7008 (1998).
- [37] M. Heuberger and M. Zaech. Nanofluides: Structural forces, density anomalies, and the pivotal role of nanoparticles. *Langmuir* 19, 1943–1947 (2003).
- [38] I. Koltover, S.H.J. Idziak, P. Davidson, Y. Li, C.R. Safinya, M. Ruths, S. Steinberg and J.N. Israelachvili. Alignment of complex fluids under confinement and flow. J. Phys. II France 6, 893–907 (1996).
- [39] T. Cosgrove, P.F. Luckham, R.M. Richardson, J.R.P. Webster and A. Zarbakhsh. The measurement of volume fraction profiles for adsorbed polymers under compression using neutron reflectometry. *Colloids and Surfaces A: Physicochemical and Engineering* Aspects 86, 103–110 (1994).

[40] M. Plischke and D. Henderson. Pair correlation functions and density profiles in the primitive model of the electric double layer. *J. Chem. Phys.* 88, 2712–2718 (1988).

- [41] M. Schoen, D.J. Diestler and J.H. Cushman. Fluids in micropores. I. Structure of a simple classical fluid in a slit–pore. *J. Chem. Phys.* 87, 5464–5476 (1987).
- [42] R.G. Horn, S.J. Hirz, G. Hadziioannou, C.W. Frank and J.M. Catala. A reevaluation of forces measured across thin polymer films: Nonequilibrium and pinning effects. *J. Chem. Phys.* 90, 6767–6774 (1989).
- [43] M. Ruths and S. Granick. Tribology of Confined Fomblin–Z Perfluoropolyalkyl Ethers: Role of Chain–End Chemical Functionality. J. Phys. Chem. B 103, 8711–8721 (1999).
- [44] I. Bitsanis and G. Hadziioannou. Molecular dynamics simulations of the structure and dynamics of confined polymer melts. *J. Chem. Phys.* **92**, 3827–3847 (1990).
- [45] M. Heuberger, M. Zaech and N. B. Spencer. Density Fluctuations under confinement: when is a fluid not a fluid. *Science* **192**, 905–908 (2001).
- [46] M. Schoen, D.J. Diestler and J.H. Cushman. Stratification-induced order-disorder phase transitions in molecularly thin confined films. J. Chem. Phys. 101, 6865–6873 (1994).
- [47] J. van Alsten and S. Granick. Shear rheology in a confined geometry: Polyxiloxane melts. *Macromolecules* **23**, 4856–4862 (1990).
- [48] A. Muhopadhyay, J. Zhao, S. Chul Bae and S. Granick. Contrasting Friction and Diffusion in Molecularly Thin Confined Films. *Phys. Rev. Lett.* **89**, 136103–1–136103–4 (2002).
- [49] O.M. Braun and M. Peyrard. Dynamics and melting of a thin confined films. *Phys. Rev. E* **68**, 011506 (2003).
- [50] H. Bock. Fluids confined by nanopatterned substrates. PhD thesis, Technischen Univ. Berlin 2001.
- [51] O.H. Seeck, K. Hyunjung, D.R. Lee, D. Shu, I.D. Kändler, J.K. Basu and S.K. Sinha. Observation of thickness quantization in liquid films confined to molecular dimension. *Europhys. Lett.* 60, 376–382 (2002).
- [52] D.J. Diestler, M. Schoen and J.H. Cushman. On the termodynamic stability of confined thin films under shear. *Science* **262**, 545–547 (1993).
- [53] M. Born and E. Wolf. *Principles of optics (7th edition)*. Cambridge University Press, Cambridge 1999.
- [54] H. Dosch. Critical phenomena at surfaces and interface. In G. Hoehler, editor, *Springer tracts in modern physics*, vol. 126. Springer Verlag, Berlin 1992.

[55] L.G. Parratt. Surface studies of solids by total reflection of X-rays. *Phys. Rev.* **95**, 359–369 (1954).

- [56] M. Tolan. X-ray scattering from soft-matter thin film. Springer Verlag, Berlin 2002.
- [57] F. Stanglmeier, B. Lengeler, W. Weber, G. Görbel and M. Schuster. Determination of the dispersive correction f'(E) to the atomic form factor from X–ray reflection. *Acta Cryst. A* **48**, 626–639 (1992).
- [58] G. H. Vineyard. Grazing-incidence diffraction and distorted-wave approximation for the study of surfaces. Phys. Rev. B 26, 4146–4159 (1982).
- [59] V. Holy and T. Baumbach. Nonspecular X-ray reflection from rough multilayers. *Phys. Rev. B* **49**, 10668–10675 (1994).
- [60] J. Brandrup, E. H. Immergut and E. A. Grulke Eds. Polymer Handbook. John Wiley & Sons, New York, 4th Edition 1999.
- [61] T. Nakaoki and M. Kobayashi. Conformational order in crystalline states and gels of isotactic, syndiotactic and atactic polystyrenes studied by vibrational spectroscopy. J. Mol. Struct. 241, 315–331 (1991).
- [62] P. J. Flory. Statistical mechanics of chain molecules. Interscience Publishers, New York 1969.
- [63] P. Müller-Buschbaum, J.S. Gutmann and M. Stamm. Dewetting of confined polymer films: an X-ray and neutron scattering study. *Phys. Chem. Chem. Phys.* 1, 3857–3863 (1999).
- [64] G. Reiter. Dewetting of thin polymer films. Phys. Rev. Lett. 68, 75–78 (1992).
- [65] W. Zhao, M. H. Rafailovich, J. Sokolov, L.J. Fetters, R. Plano, M. K. Sanyal and S. K. Sinha. Wetting properties of thin liquid polyethylene propylene films. *Phys. Rev. Lett.* 70, 1453–1456 (1993).
- [66] P. G. De Gennes. Reptation of polymer chain in the presence of fixed obstacles. *J. Chem. Phys.* **55**, 572–579 (1971).
- [67] P. Schleger, B. Farago, C. Lartigue, A. Kollmar and D. Richter. Clear evidence of reptation in polyethylene from neutron spin-echo spectroscopy. *Phys. Rev. Letters* 81, 124–127 (1998).
- [68] D. Richter and M. Monkelbuch. Neutron scattering and glass transition in polymers – present status and future opportunities. J. Non-Crystalline Solids 287, 286–296 (2001).
- [69] A. N. Semeonov. Dynamics of Entangled polamer layers: The effect of fluctuations. *Phys. Rev. Lett.* **80**, 1908–1911 (1998).

[70] A. Datta M. K. Sanyal, J. K. Basu and S. Banerjee. Determination of small fluctuations in electron density profiles of thin films: Layer formation in a polystyrene film. Europhys. Lett. 36, 265–270 (1996).

- [71] H.Ubara, T. Imura and A. Hiraki. Formation of Si–H bonds on the surface of microcrystalline silicon covered with SiO_x by HF treatment. Solid State Commun. 50, 673–675 (1984).
- [72] K. Shin, X. Hu, X. Zeng, M.H. Rafailovich, J. Sokolov, V. Zaitsev and S.A. Shwarz. Silicon oxide surface as a substrate of polymer thin films. *Macromolecules* 34, 4993–4998 (2001).
- [73] G.S. Higashi, Y.J. Chabal, G.W. Trucks and K. Raghavachari. Ideal hydrogen termination of the Si(111) surface. *Appl. Phys. Lett* **56**, 665–658 (1990).
- [74] E. P. Boonekamp, J. J. Kelly, J. van de Ven, and A. H. M. Sondag. The chemical oxidation of hydrogen-terminated silicon (111) surfaces in water studied in situ with Fourier transform infrared spectroscopy. J. Appl. Phys. 75, 8121–8127 (1994).
- [75] J. Als-Nielsen. Solid and liquid surfaces studied by Synchrotron X-ray diffraction. In W. Schommers and P. von Blanckenhagen, editors, *Topics in current physics Vol 43*. Structure and Dynamics of Surfaces II. Springer-Verlag, Heidelberg 1987.
- [76] A. Doerr. Untersuchung der strukturellen Eigenschaften dünner Benetzungsfilme. PhD thesis, Univ. Kiel 1999.
- [77] O.H. Seeck. Untersuchung des Wetting-Systems auf Si-SiO₂ mittels diffuser Röntgenstreuung. Master's thesis, Univ. Kiel 1993.
- [78] S. Dietrich. Wetting Phenomena. In C. Domb and J.L. Lebowitz, editors, *Phase transitions and Critical Phenomena*. Academic Press, New York 1988.
- [79] R. Becker. Theorie der Wärme. Springer-Verlag, Heidelberg 1985.
- [80] J. Frenkel. Kinetic theory of liquids. Dover Publications INC., New York 1955.
- [81] R. Opitz, D.M. Lambreva and W.H. Jeu. Confined crystallization of ethyleneoxide—butadiene di-block copolymers in lamellar films. *Macromolecules* 35, 6930–6936 (2002).
- [82] A.H. Narten. Liquid carbon tetrachloride: Atom pair correlation functions from neutron and X-ray diffraction. *J. Chem. Phys.* **65**, 573–579 (1976).
- [83] M. Misawa. Temperature dependence of the structure of liquid carbon tetrachloride measured by pulsed neutron total scattering. J. Chem. Phys. 91, 5648–5654 (1989).
- [84] L. Pusztai and L. McGreevy. The structure of liquid CCl₄. Molec. Phys. **90**, 533–539 (1997).

[85] P. Jovari, G. Meszaros, L. Pusztai and E. Svab. The structure of liquid tetrachlorides CCl₄, SiCl₄, GeCl₄, TiCl₄, VCl₄ and SnCl₄. J. Chem. Phys. **91**, 5648–5654 (2001).

- [86] K. Nishikawa and T. Kazuyuki. The intermolecular arrangement in the plastic crystal (phase Ia) of carbon tetrachloride studied by X-ray diffraction. J. Chem. Phys. 74, 5817–5823 (1981).
- [87] P.W. Bridgman. Change under pressure. *Phys. Rev.* **3**, 153–203 (1914).
- [88] G.J. Piermarini and A.B. Braun. Crystal and molecular structure of CCl₄ III: A high pressure polymorph at 10 kbar. *J. Chem. Phys.* **58**, 1974–1982 (1973).
- [89] R. Rudman and B. Post. Carbon tetrachloride: A new crystalline modification. *Science* **154**, 1009–1010 (1966).
- [90] M. Djabourov, C. Levy-Mannheim, J. Lblond and P. Paron. Liquid scattering carbon tetrachloride: Liquid and plastic crystal phases. *J. Chem. Phys.* **66**, 5748–5756 (1977).
- [91] C.E. Weir, G.J. Piermarini and S. Block. Crystallography of some high–pressure forms of C₆H₆, CS, Br, CCl₄, KNO₃. *J. Chem. Phys.* **50**, 2089–2093 (1969).
- [92] K. R. Shull. Mean-field theory of block copolymers: Bulk melts, surfaces and thin films. *Macromolecules* **25**, 2122–2133 (1992).
- [93] S.Z.D. Cheng and B. Wunderlich. Molecular segregation and nucleation of Poly(ethylene acide) crystallized from the melt. I. Calorymetric study. J. Polym. Sci. B 24, 577 (1986).
- [94] S.Z.D. Cheng and B. Wunderlich. Molecular segregation and nucleation of Poly(ethylene oxide) crystallized from the melt. II. Kinetic study. J. Polym. Sci. B 24, 595 (1986).
- [95] S.Z.D. Cheng, H.S. Bu and B. Wunderlich. Molecular segregation and nucleation of Poly(ethylene oxide) crystallized from the melt. III. Morphological study. *J. Polym.* Sci. B 26, 1947 (1998).
- [96] W. H. de Jeu. Lamellar ethylene oxide—butadiene block copolymer films as model systems for confined crystallisation. In J.-U. Sommer and G. Reiter, editors, *Polymer Crystallization* pages 196–207. Springer–Verlag, Berlin 2003.
- [97] H. Tadokoro. Crystalline Polymers. John Wiley & Sons, New York 1979.
- [98] P. Bhattarai, M. D. Zeidler and P. Chieux. Determination of pair-correlation function of liquid carbon tetrachloride under pressure. *J. Mol. Liquids* **76**, 127–138 (1998).
- [99] N. Torikai, I. Noda, A. Karim, S. Satija, Ch. Han, Y. Matsushita and T. Kawakatsu. Neutron reflection studies on segment distribution of block chains in lamellar microphase–separated structure. *Macromolecules* **30**, 2907–2914 (1997).

Appendix A

Results after refinement of the scattering data.

In this part of the appendix the results from refinements of the reflectivity and diffuse scattering curves are presented. In the following tables the numbers denoted with ^(f) have been kept fixed during the refinement. Some of the data are not recorded at the temperature given in the table caption. For these the correct temperature is given behind the table. Data of samples **h21**, **h23** and **h46** are not presented for the following reasons: Sample **h21** was not correctly prepared (section 4.2.1). The diffuse scattering data of sample **h23** are not available, since during the measurement, due to heating, the samples has misaligned itself. A mistake has also happened in the preparation procedure of sample **h46**. Instead of 400 Å, it has a thickness of 800 Å (**Tab. A.3**). Therefore, its diffuse scattering curves are not conceded.

The transverse scans are presented in **double-logarithmic scale**. Each transverse curve has a notation at the top, e.g. **r15015m.n31**. The first letter **r** indicates that the **r**ight side of the transverse scan was taken. The number **150** shows the temperature at which the curve was recorded. The next number **15** gives the value of q_x in reciprocal space, where the curve was recorded. In the example, it has a value of 0.15 Å⁻¹. The longitudinal diffuse scattering curves have notations of the type **ld15005m.n31**. Here, the number **150** again shows the measurement temperature. **05** indicates a longitudinal diffuse scan at offset 0.05°(section 4.1). The longitudinal scattering curves are presented in 2θ , **linear scale**, and the intensity is in **logarithmic scale**.

A.1 Results from refinements of reflectivity curves.

Sample number	Dispersion	Roughness	Thickness
	δ_{SiO_x}	$\sigma_{SiO_x}, [ext{Å}]$	$[\mathring{\mathrm{A}}]$
n26	4.137 ± 0.004	2.412 ± 0.04	10.143 ± 0.004
n46	4.136 ± 0.004	2.255 ± 0.005	9.958 ± 0.006
n86	4.12 ± 0.01	2.30 ± 0.02	10.07 ± 0.02
n16	4.097 ± 0.003	2.086 ± 0.005	10.015 ± 0.006
n36	4.021 ± 0.03	2.077 ± 0.005	10.283 ± 0.006
n21	4.127 ± 0.005	2.88 ± 0.03	9.95 ± 0.03
n41	4.15 ± 0.01	2.561 ± 0.004	10.033 ± 0.007
n81	4.092 ± 0.004	2.28 ± 0.01	9.87 ± 0.01
n11	4.094 ± 0.004	2.14 ± 0.02	10.25 ± 0.01
n31	$4.11^{(f)}$	3.12 ± 0.03	9.80 ± 0.02
n23	4.14 ± 0.01	$2.19^{(f)}$	10.57 ± 0.02
n43	3.98 ± 0.02	2.50 ± 0.02	9.80 ± 0.03
n83	4.234 ± 0.007	2.29 ± 0.01	9.94 ± 0.03
n13	4.099 ± 0.009	2.344 ± 0.008	10.09 ± 0.02
n33	$4.16^{(f)}$	2.1 ± 0.02	10.02 ± 0.03
h26	3.66 ± 0.02	1.61 ± 0.02	8.35 ± 0.03
h46	3.83 ± 0.02	1.92 ± 0.03	7.74 ± 0.04
h86	4.056 ± 0.004	3.266 ± 0.006	8.728 ± 0.006
h16	4.169 ± 0.03	4.43 ± 0.01	7.75 ± 0.01
h36	$4.18^{(f)}$	3.44 ± 0.03	9.26 ± 0.03
h21	_	_	_
h41	3.073 ± 0.005	1.67 ± 0.02	4.62 ± 0.02
h81	2.77 ± 0.01	1.778 ± 0.007	7.52 ± 0.03
h11	3.786 ± 0.005	2.39 ± 0.02	8.40 ± 0.03
h31	3.575 ± 0.005	2.03 ± 0.03	8.56 ± 0.02
h23	3.741 ± 0.008	2.25 ± 0.01	8.37 ± 0.01
h43	3.78 ± 0.01	1.76 ± 0.01	8.76 ± 0.02
h83	3.85 ± 0.01	1.57 ± 0.02	8.43 ± 0.02
h13	3.84 ± 0.01	1.56 ± 0.02	8.88 ± 0.03
h33	3.880 ± 0.004	1.57 ± 0.03	8.54 ± 0.03

Table A.1: Dispersion, roughness and thickness of the first layer obtained after the refinement of reflectivity curves measured at 50° C .

Sample number	Dispersion,	Roughness,	Thickness,
	δ_{ps}	$\sigma_{ps},$ [Å]	[Å]
n26	1.991 ± 0.005	5.037 ± 0.009	172.87 ± 0.01
n46	2.145 ± 0.006	5.98 ± 0.01	353.07 ± 0.01
n86	1.86 ± 0.03	5.46 ± 0.04	818.23 ± 0.02
n16	2.271 ± 0.005	4.50 ± 0.01	1497.21 ± 0.02
n36	2.145 ± 0.005	3.21 ± 0.03	3007.37 ± 0.02
n21	1.653 ± 0.006	6.58 ± 0.02	166.25 ± 0.01
n41	1.291 ± 0.007	$4.13^{(f)}$	415.36 ± 0.01
n81	1.756 ± 0.005	5.04 ± 0.04	741.05 ± 0.03
n11	1.921 ± 0.005	4.65 ± 0.02	1428.32 ± 0.07
n31	1.20 ± 0.03	9.57 ± 0.04	_
n23	1.982 ± 0.006	5.691 ± 0.008	219.75 ± 0.02
n43	$1.65^{(f)}$	4.92 ± 0.03	437.52 ± 0.02
n83	1.82 ± 0.02	4.83 ± 0.01	749.95 ± 0.04
n13	1.914 ± 0.005	4.89 ± 0.03	1697.35 ± 0.06
n33	1.67 ± 0.03	_	_
h26	2.05 ± 0.02	5.34 ± 0.03	165.59 ± 0.03
h46	$1.93^{(f)}$	5.18 ± 0.07	856.17 ± 0.08
h86	2.018 ± 0.008	6.33 ± 0.01	810.25 ± 0.01
h16	1.60 ± 0.01	11.04 ± 0.04	1534.19 ± 0.06
h36	$2.75^{(f)}$	6.22 ± 0.04	3280.12 ± 0.06
h21	_	_	_
h41	2.197 ± 0.004	6.26 ± 0.03	420.42 ± 0.03
h81	2.023 ± 0.005	$6.07^{(f)}$	736.35 ± 0.02
h11	$2.10^{(f)}$	6.33 ± 0.01	1472.75 ± 0.04
h31	1.53 ± 0.01	6.87 ± 0.04	3195.97 ± 0.03
h23	$1.98^{(f)}$	$5.82^{(f)}$	216.01 ± 0.03
h43	1.65 ± 0.01	5.44 ± 0.04	439.59 ± 0.04
h83	$1.99^{(f)}$	5.53 ± 0.03	740.37 ± 0.04
h13	1.99 ± 0.01	$4.68^{(f)}$	1654.43 ± 0.06
h33	$1.99^{(f)}$		_

Table A.2: Dispersion, roughness and thickness of the polymer film obtained after the refinement of reflectivity curves measured at 50°C.

Samples n46, n41, n86 and n81 were measured at $40^{\circ}\mathrm{C}$

Sample number	Thickness at	$d_{150(h)}/d_{50(h)}$	$d_{230}/d_{50(h)}$	$d_{50(c)}/d_{50(h)}$
	$50^{\circ}\text{C}, d_{50(h)}, \text{Å}$, , , , ,	, ,	, , , , , ,
n26	172.87	1.00	1.11	1.13
n21	160.25	_	1.72	1.35
n23	219.75	1.11	1.16	_
h26	165.59	1.04	1.17	1.21
h21	_	_	_	_
h23	216.01	1.08	_	1.04
n46	$353.07^{(40)}$	1.03	$1.06^{(200)}$	_
n41	$415.36^{(40)}$	1.02	$1.04^{(200)}$	_
n43	437.52	1.07	1.15	1.04
h46	856.17	1.04	_	0.99
h41	420.42	1.03	$1.05^{(200)}$	_
h43	439.59	1.07	1.11	1.02
n86	818.23 ⁽⁴⁰⁾	1.02	$1.03^{(200)}$	_
n81	741.05 ⁽⁴⁰⁾	1.03	$1.04^{(200)}$	_
n83	749.95	1.03	1.07	1.00
h86	810.25	1.02	1.13	_
h81	736.35	1.05	1.10	1.00
h83	740.37	_	1.07	0.98
n16	1497.21	1.04	1.14	1.03
n11	1428	1.04	1.14	1.03
n13	1697.35	1.04	1.07	1.00
h16	1534.19	_	1.07	1.00
h11	1472.75	1.01	1.08	0.99
h13	1654.43	1.08	_	_
n36	3007.37	1.13	1.16	1.00
n31	_	_	_	_
n33	_	_	_	_
h36	3280.12		1.00	1.00
h31	3195.97	1.00	1.00	1.00
h33	_	_		_

Table A.3: Thickness of the polymer films at different temperatures. The measured film thickness at 50°C heating run is given in the first column. The thicknesses in the next columns are divided by the thickness in the first column. (h) and (c) denote heating and cooling runs, respectively. Values denoted with ⁽⁴⁰⁾ and ⁽²⁰⁰⁾ were obtained from reflectivity curves measured at 40°C and 200°C, respectively.

- A.2 The Liquid and the Fractal models refinements.
- A.2.1 Samples studied at 150° C
- A.2.1.1 Hydrophilic samples

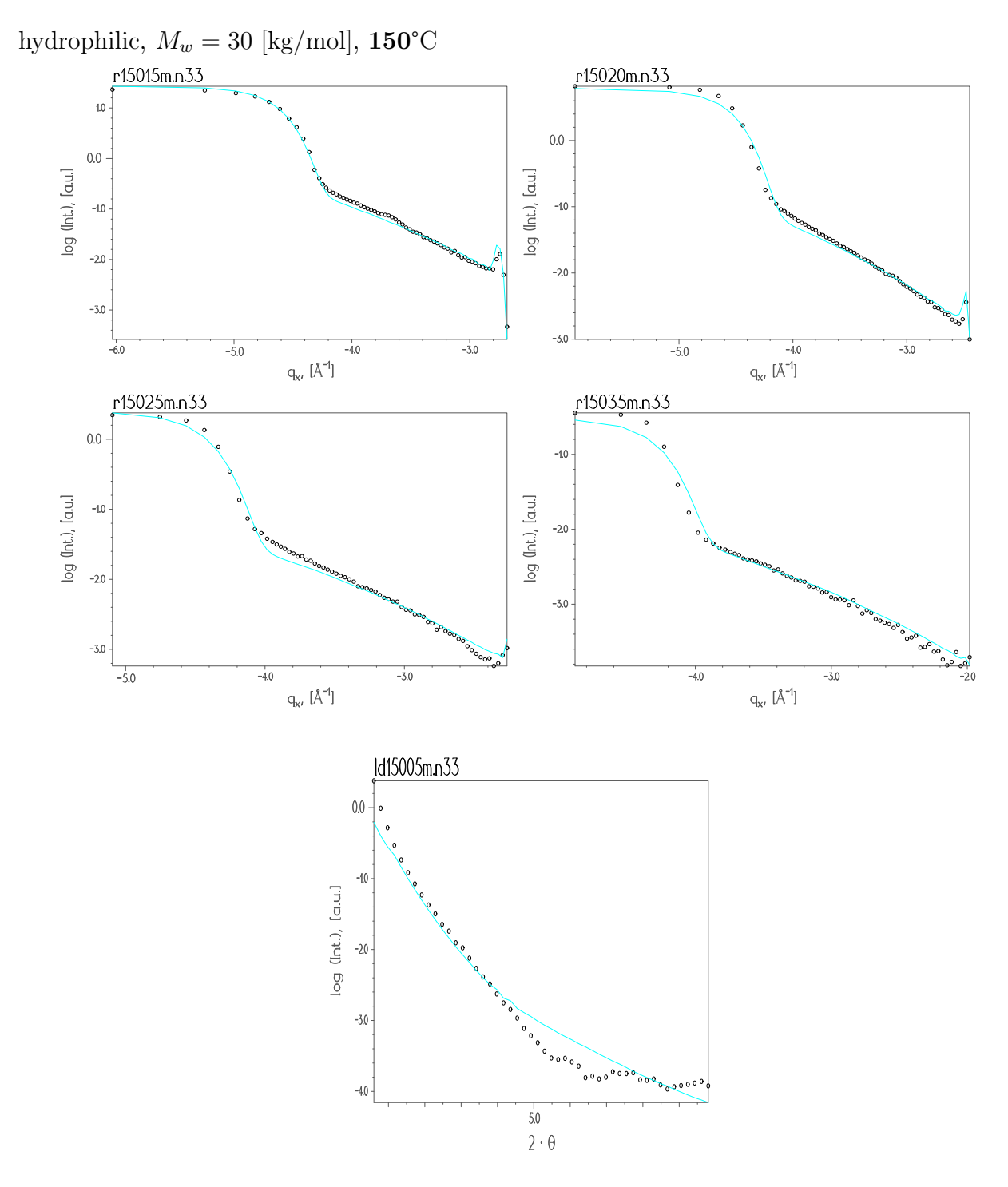


Figure A.1: Longitudinal and transverse scans of sample **n33** at **150**°C refined with the *Liquid model*. The curves with the symbols are the experimental data and the lines are the fits.

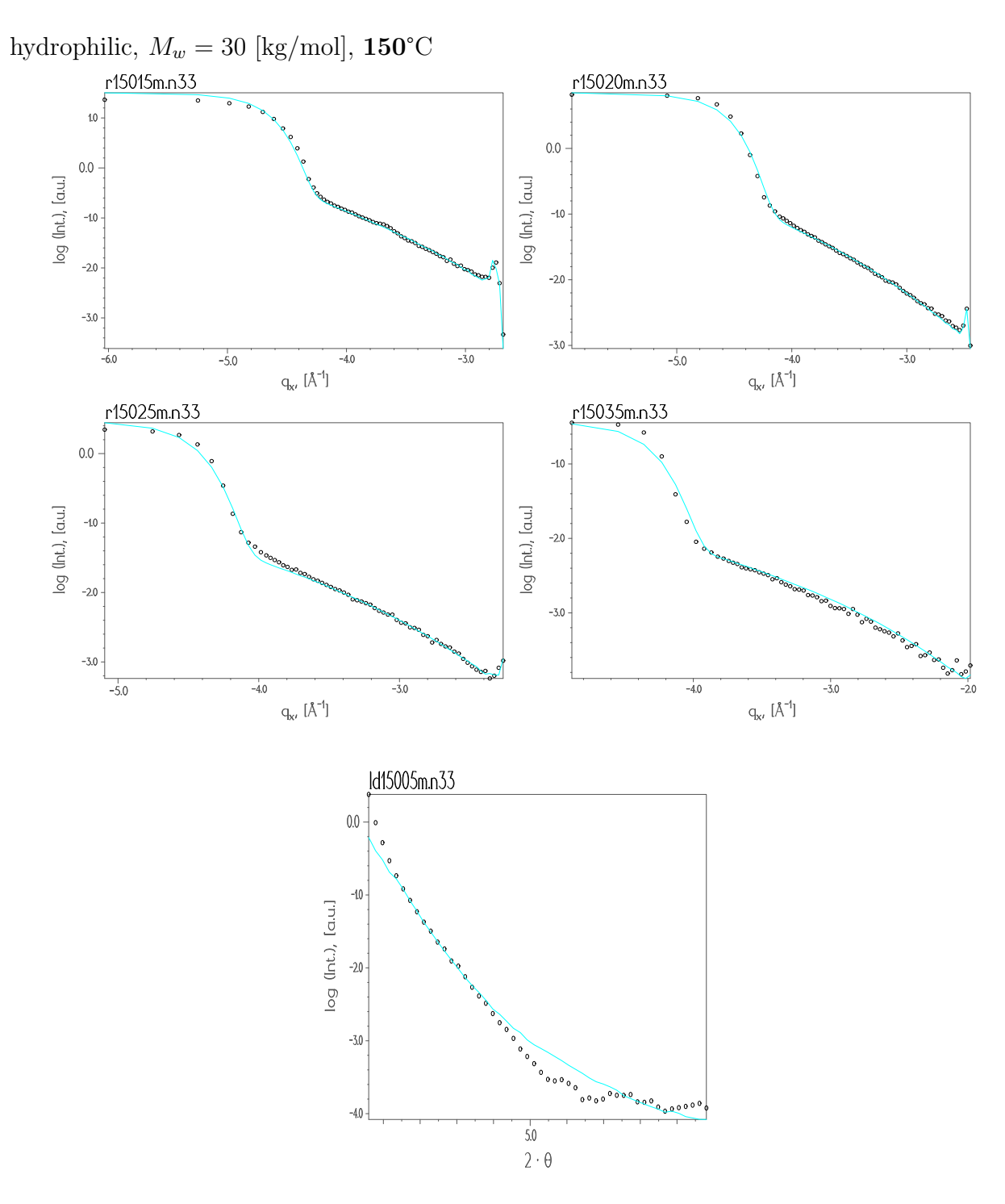


Figure A.2: Longitudinal and transverse scans of sample **n33** at **150**°C refined with the *Fractal model*. The curves with the symbols are the experimental data and the lines are the fits.

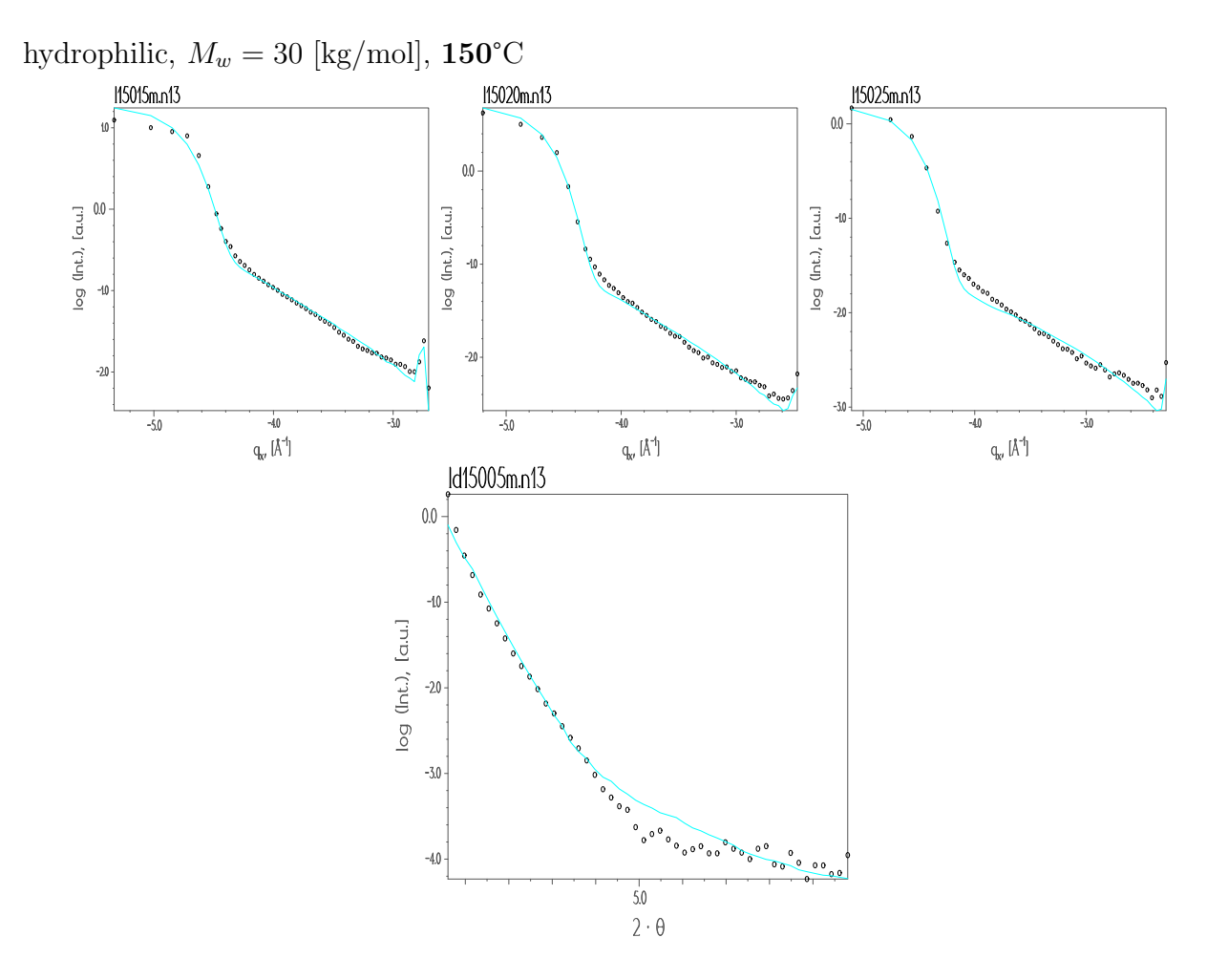


Figure A.3: Longitudinal and transverse scans of sample **n13** at **150**°C refined with the *Liquid model*. The curves with the symbols are the experimental data and the lines are the fits.

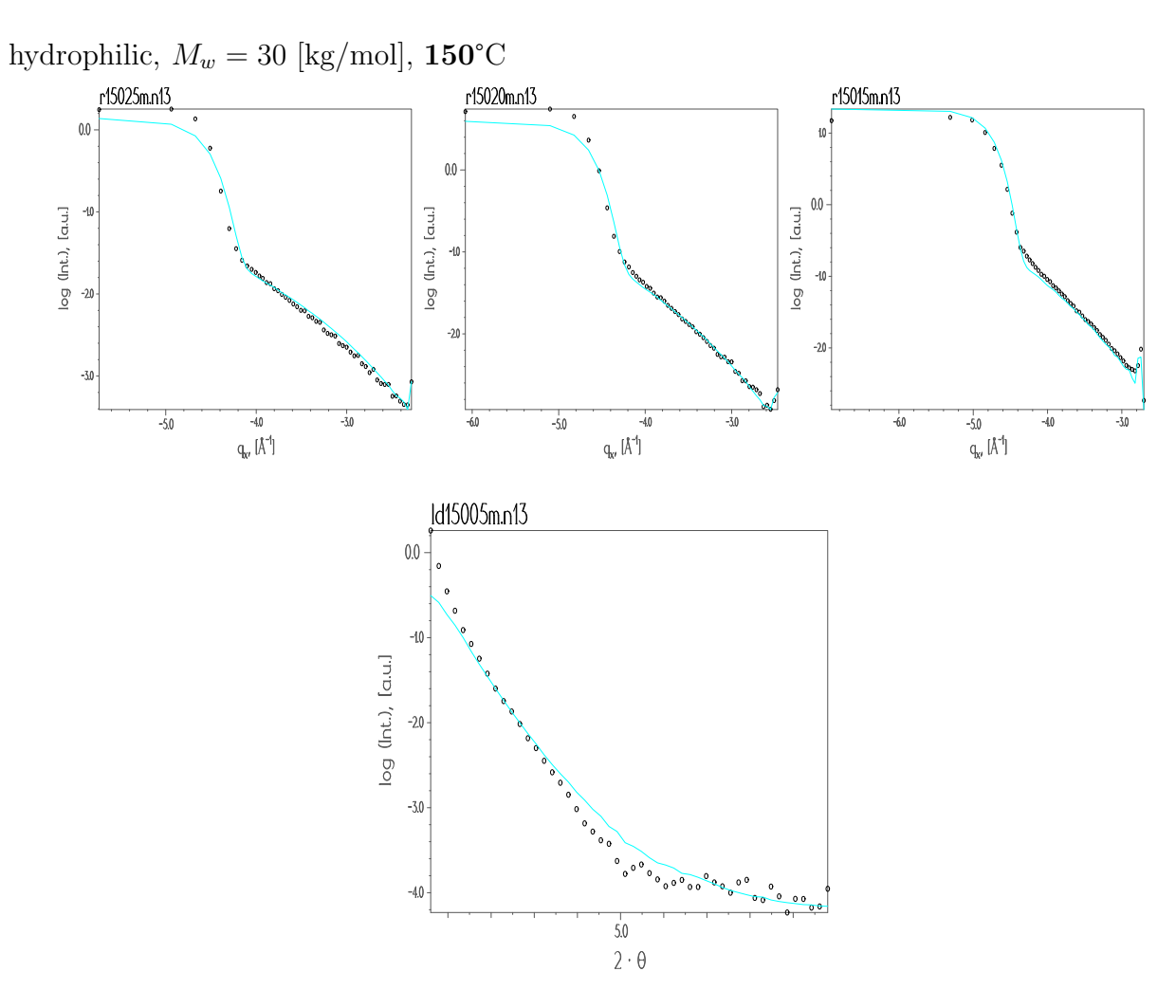


Figure A.4: Longitudinal and transverse scans of sample **n13** at **150**°C refined with the *Fractal model*. The curves with the symbols are the experimental data and the lines are the fits.

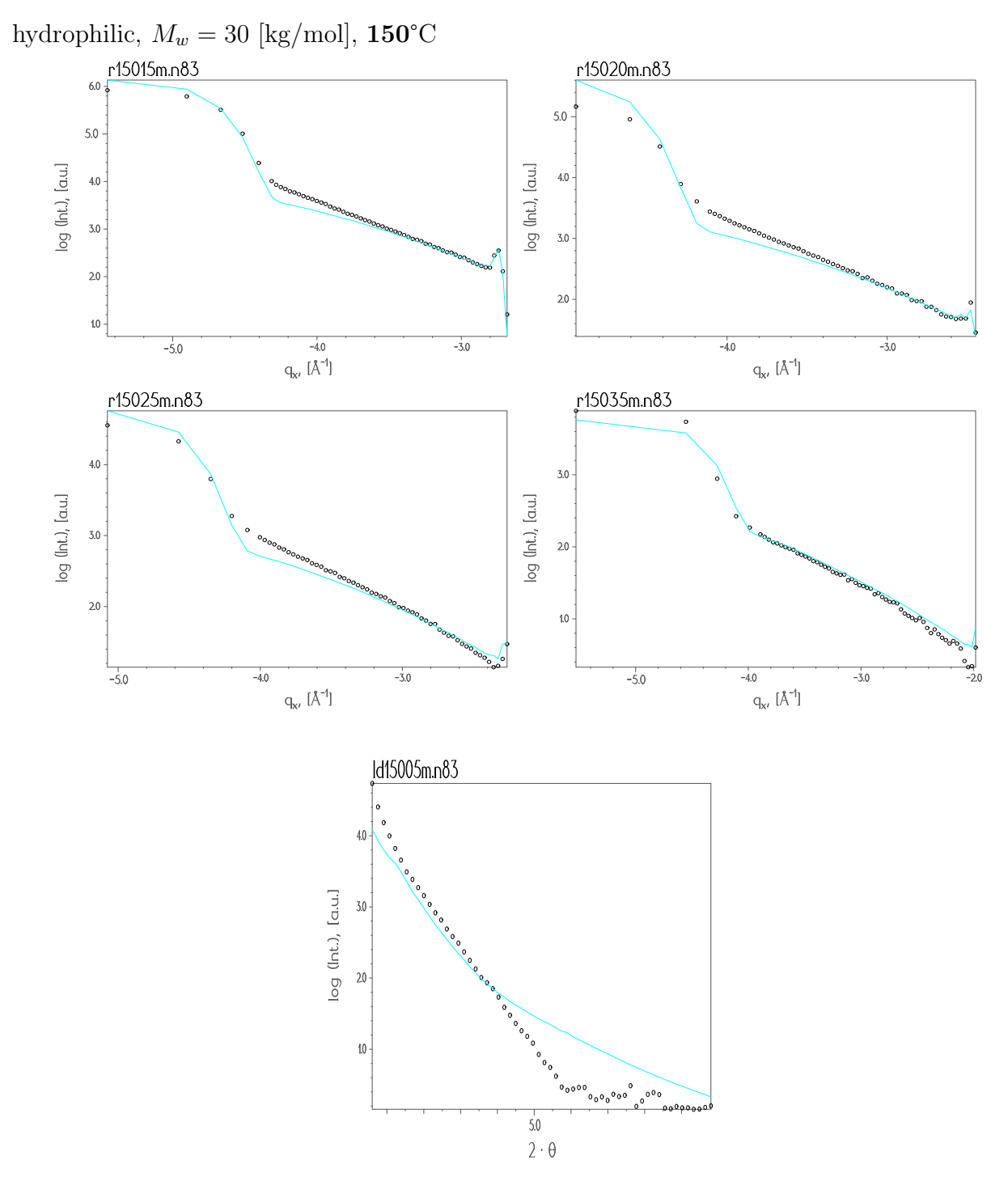


Figure A.5: Longitudinal and transverse scans of sample **n83** at **150**°C refined with the *Liquid model*. The curves with the symbols are the experimental data and the lines are the fits.

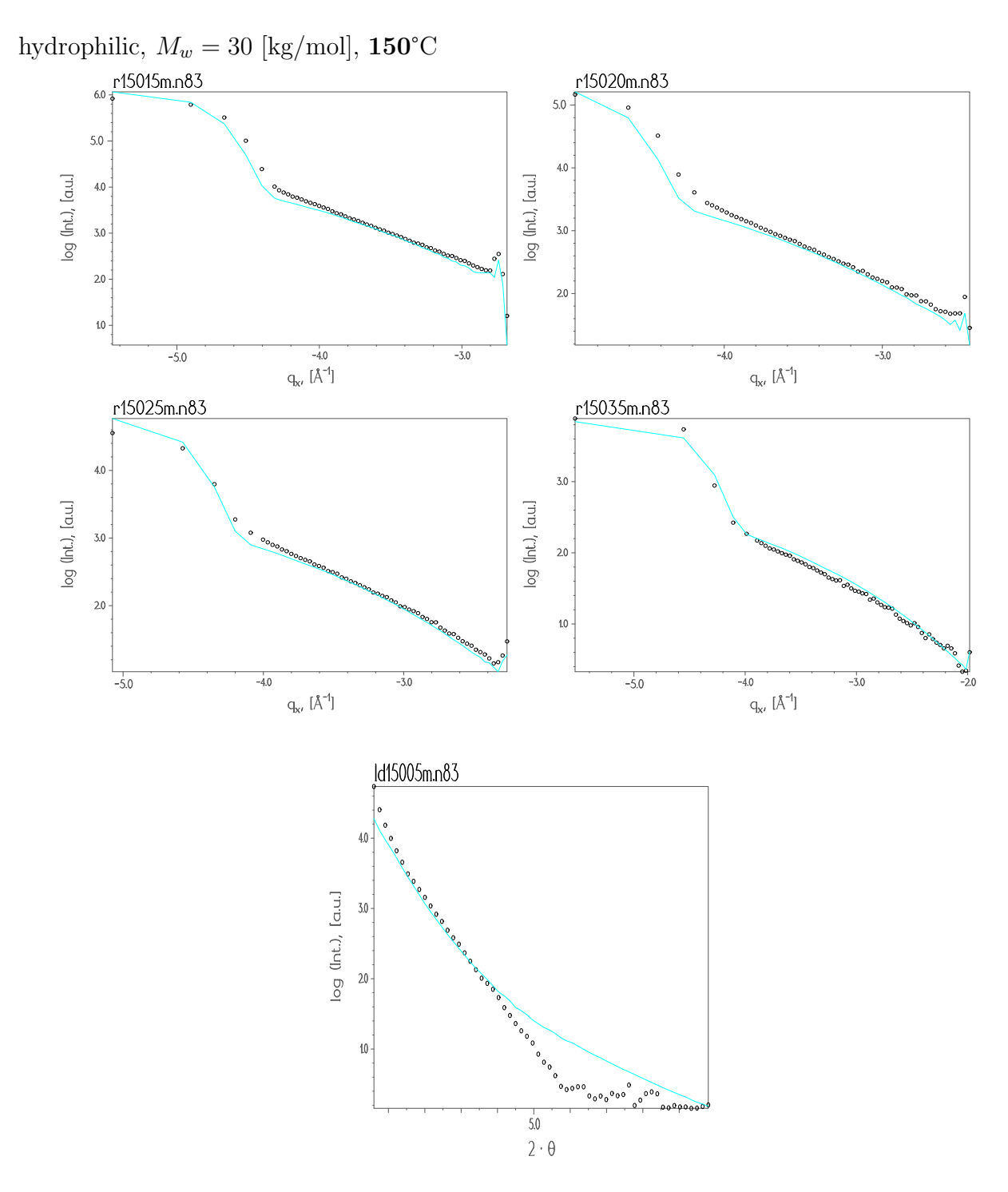


Figure A.6: Longitudinal and transverse scans of sample **n83** at **150°**C refined with the *Fractal model*. The curves with the symbols are the experimental data and the lines are the fits.

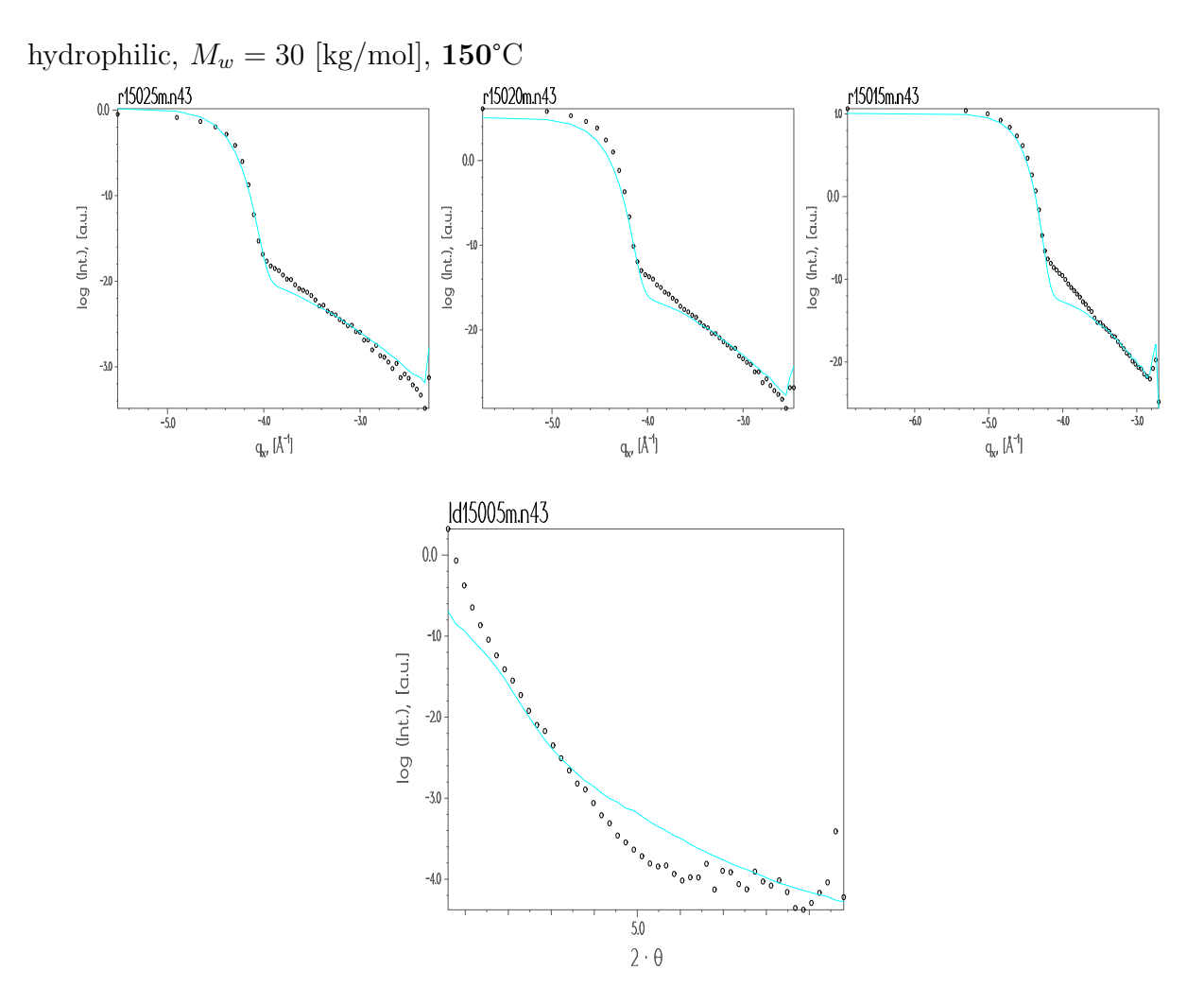


Figure A.7: Longitudinal and transverse scans of sample n43 at 150° C refined with the Liquid model. The curves with the symbols are the experimental data and the lines are the fits.

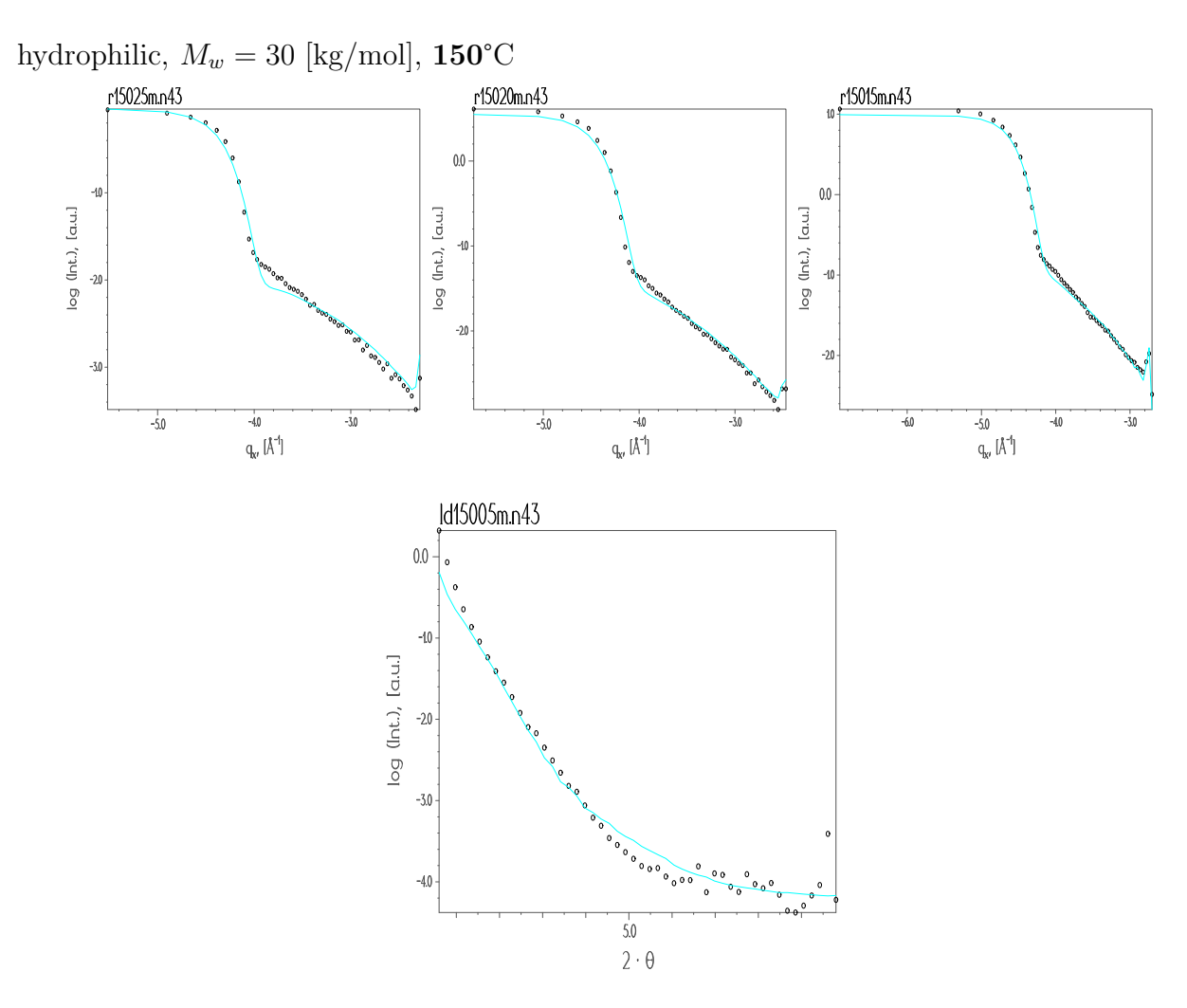


Figure A.8: Longitudinal and transverse scans of sample **n43** at **150**°C refined with the *Fractal model*. The curves with the symbols are the experimental data and the lines are the fits.

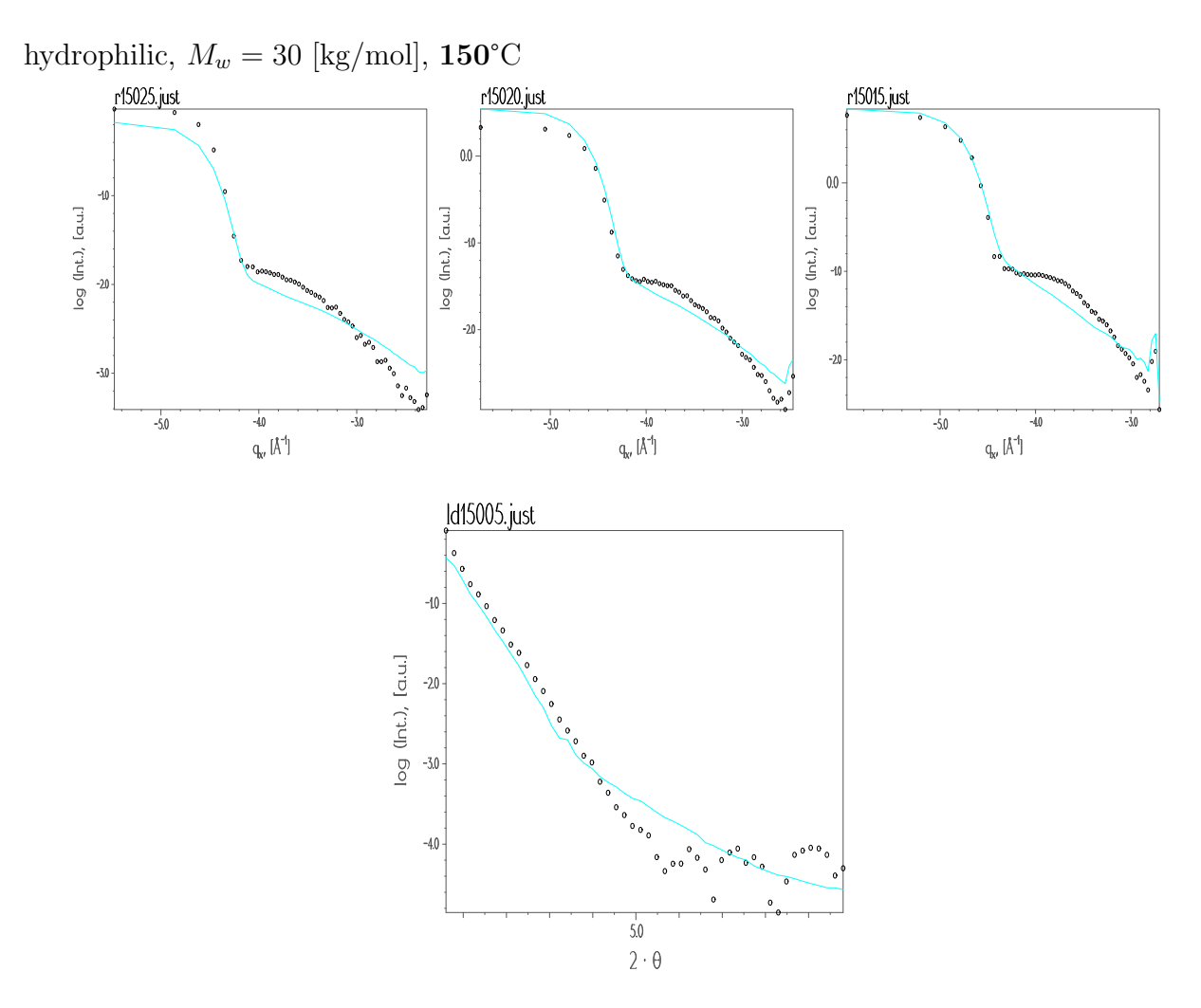


Figure A.9: Longitudinal and transverse scans of sample n23 at 150°C refined with the Liquid model. The curves with the symbols are the experimental data and the lines are the fits.

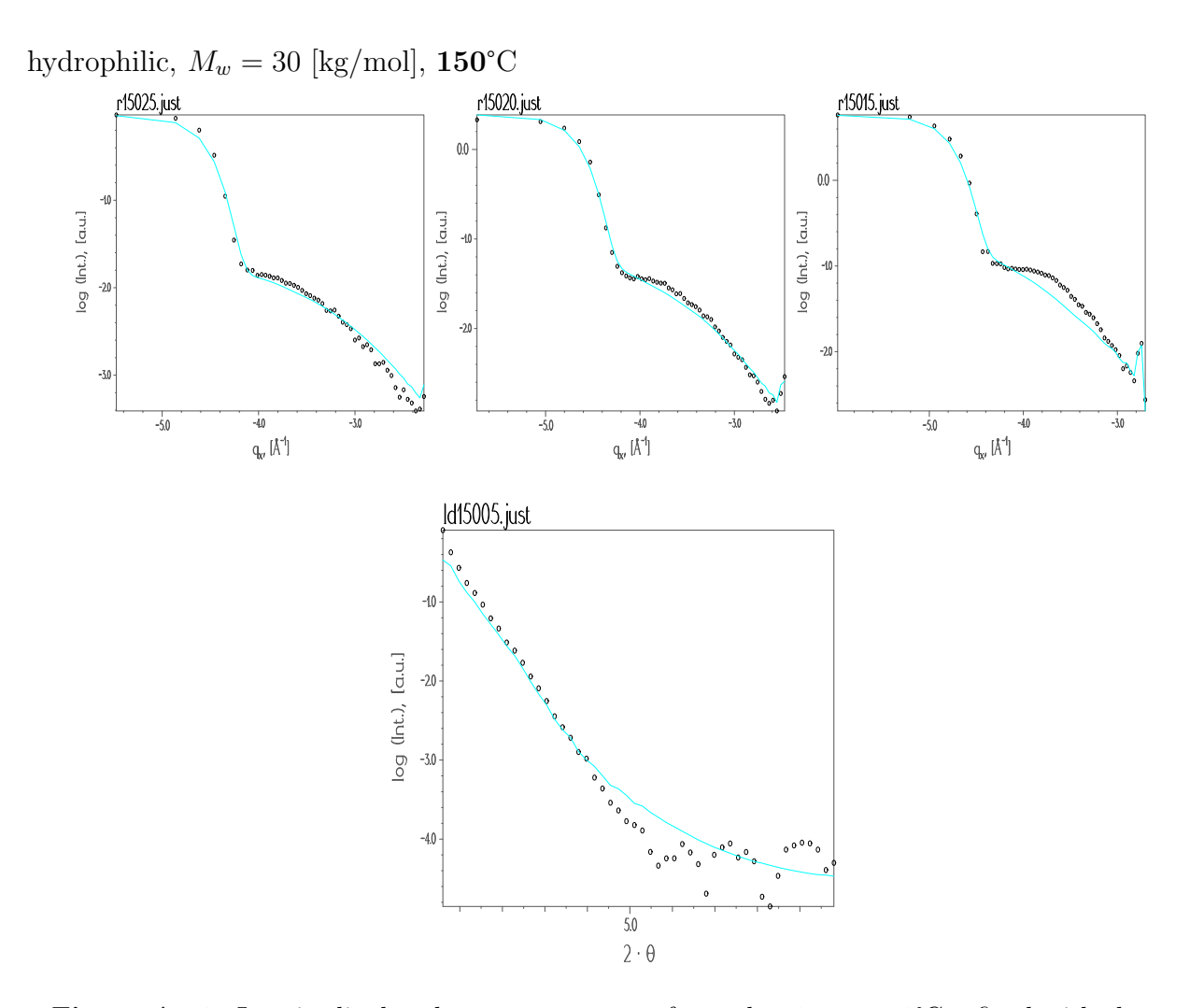


Figure A.10: Longitudinal and transverse scans of sample n23 at 150° C refined with the Fractal model. The curves with the symbols are the experimental data and the lines are the fits.

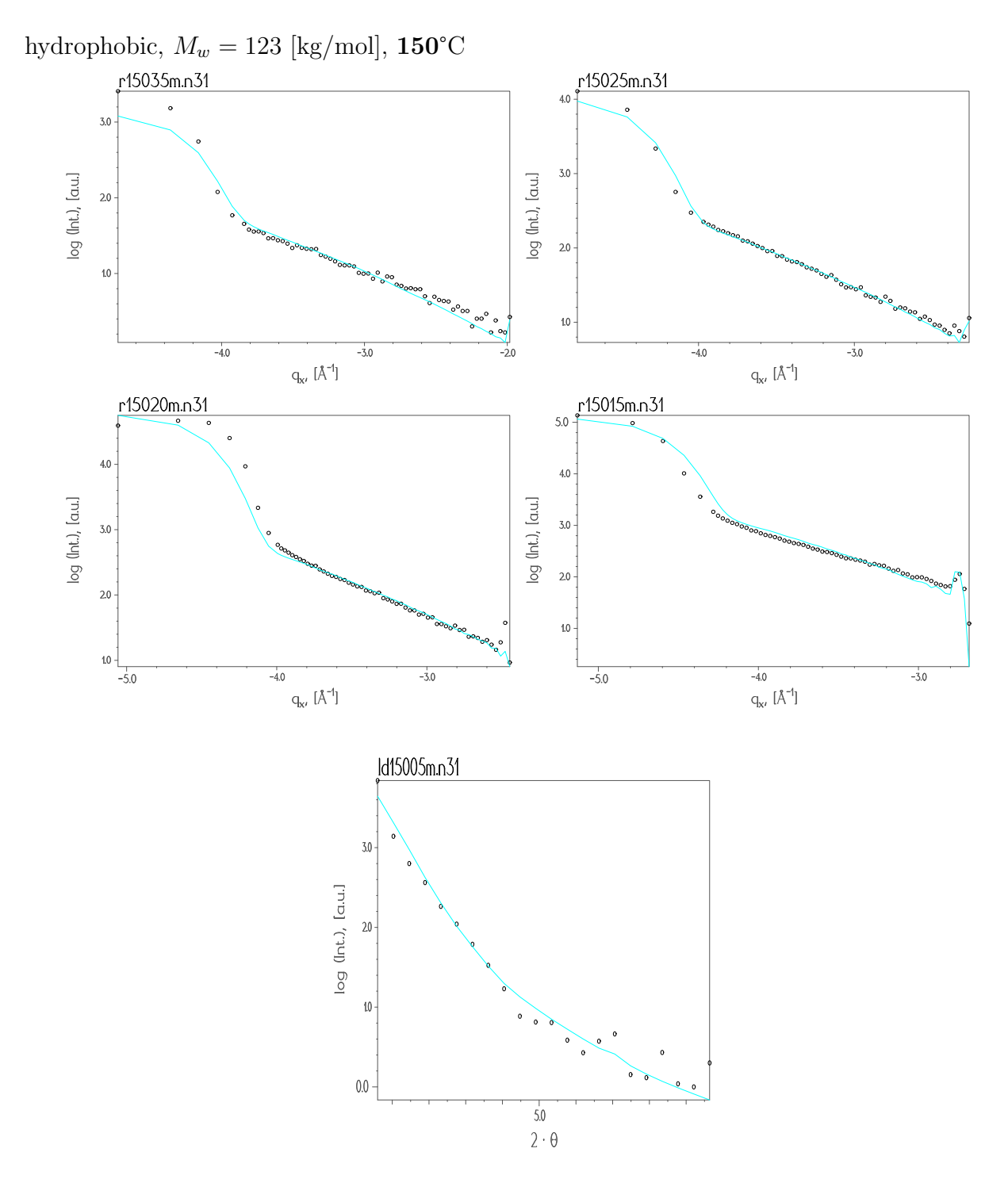


Figure A.11: Longitudinal and transverse scans of sample n31 at 150° C refined with the Liquid model. The curves with the symbols are the experimental data and the lines are the fits.

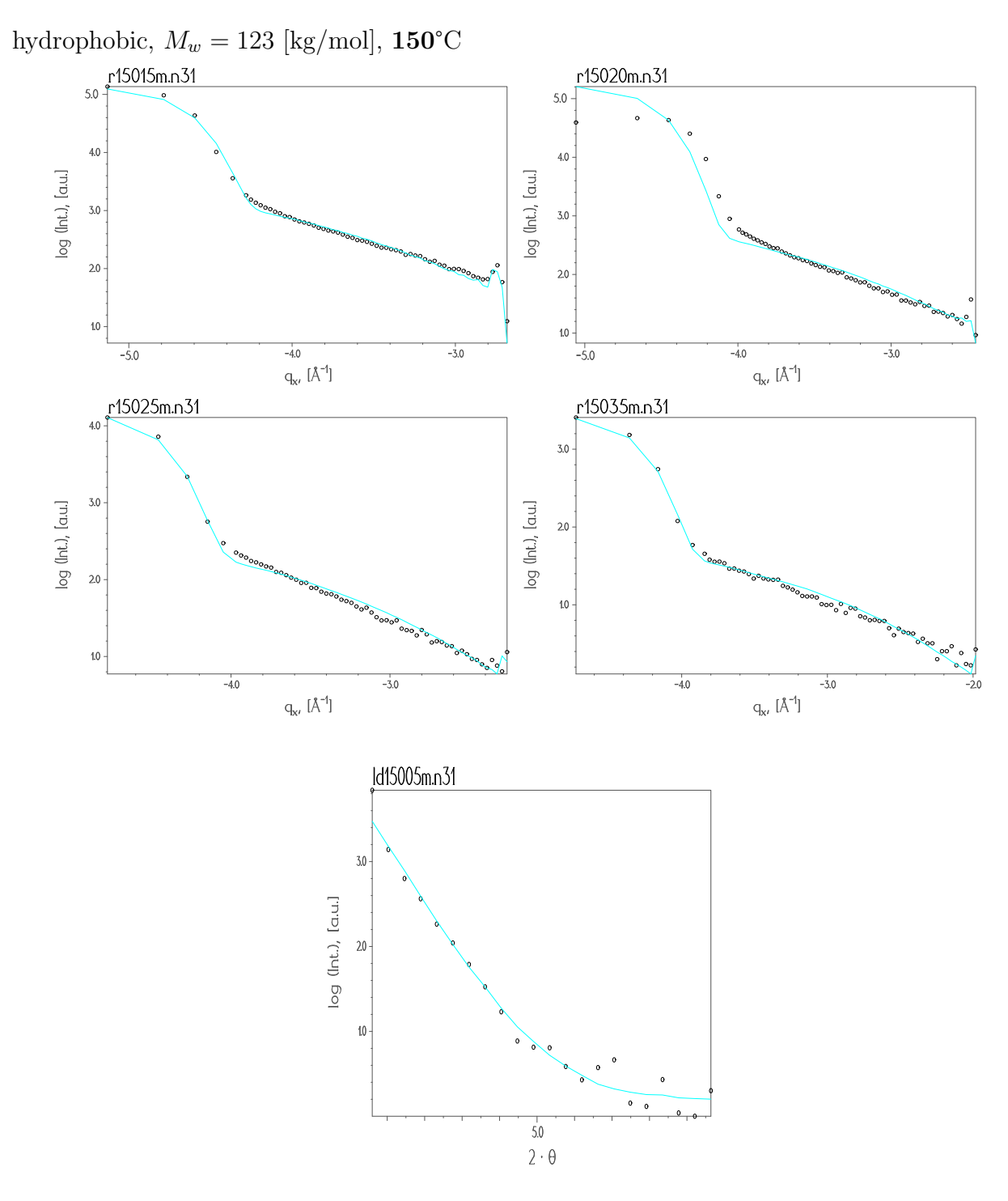


Figure A.12: Longitudinal and transverse scans of sample **n31** at **150**°C refined with the *Fractal model*. The curves with the symbols are the experimental data and the lines are the fits.

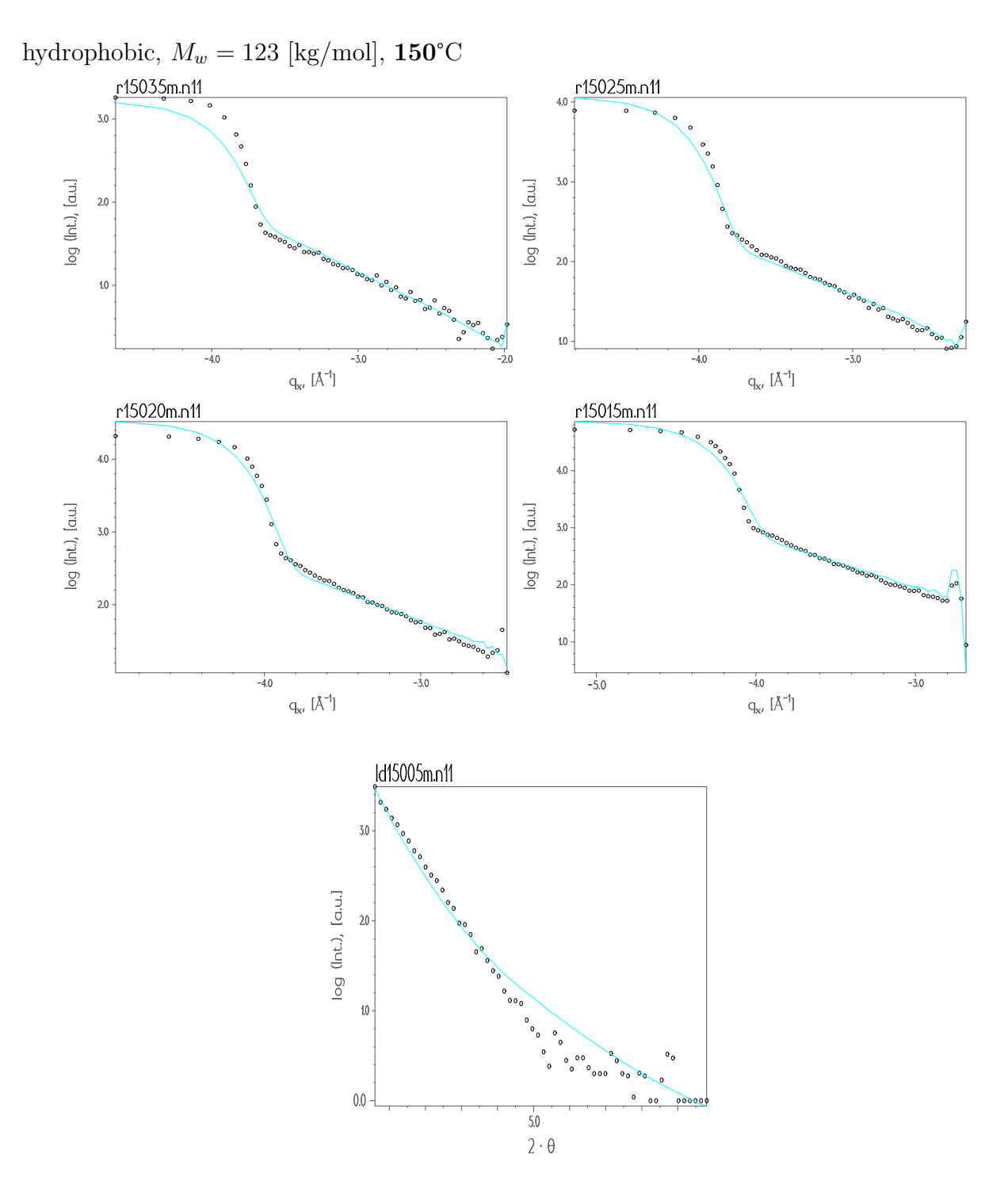


Figure A.13: Longitudinal and transverse scans of sample n11 at 150° C refined with the Liquid model. The curves with the symbols are the experimental data and the lines are the fits.

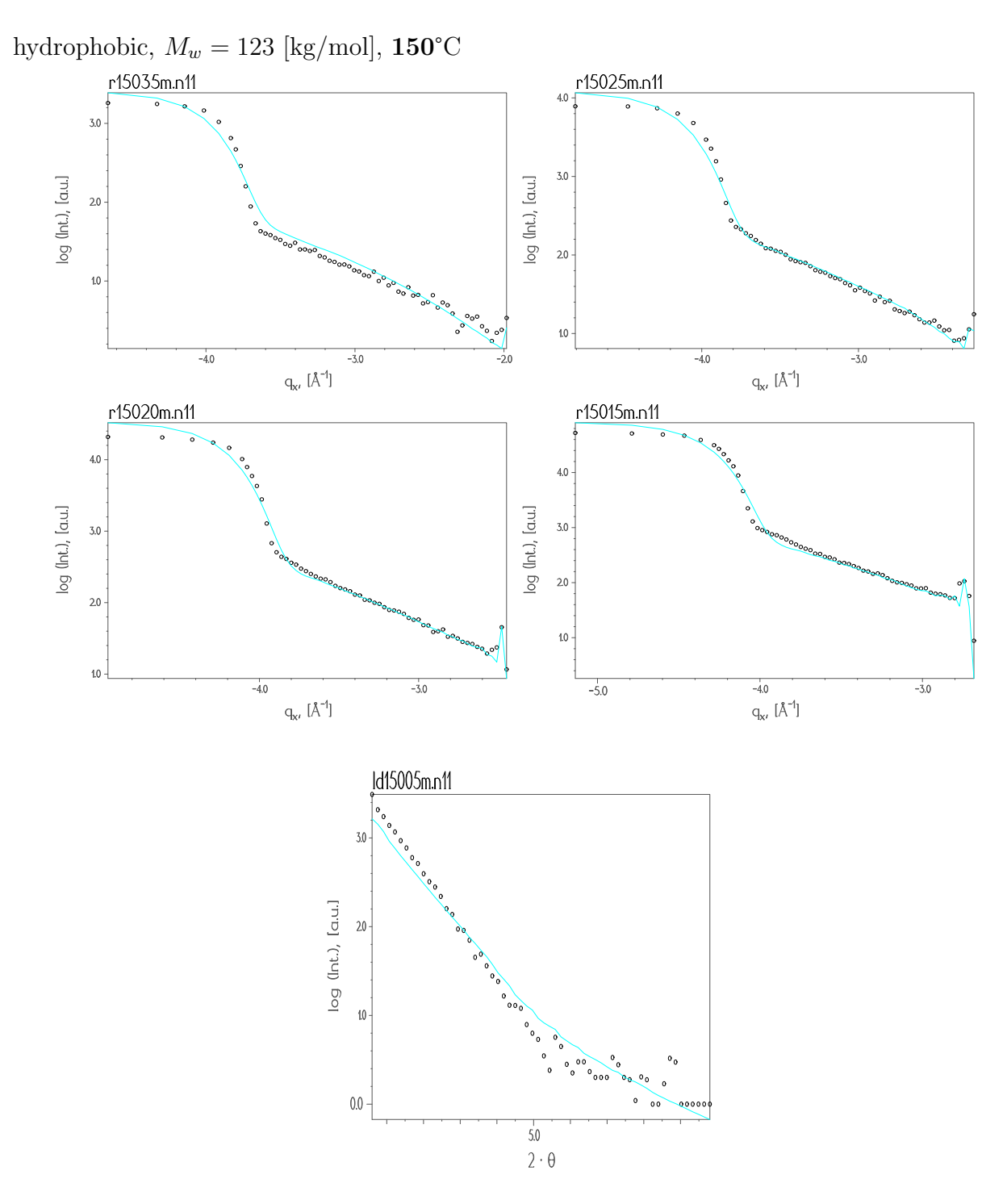


Figure A.14: Longitudinal and transverse scans of sample **n11** at **150**°C refined with the *Fractal model*. The curves with the symbols are the experimental data and the lines are the fits.

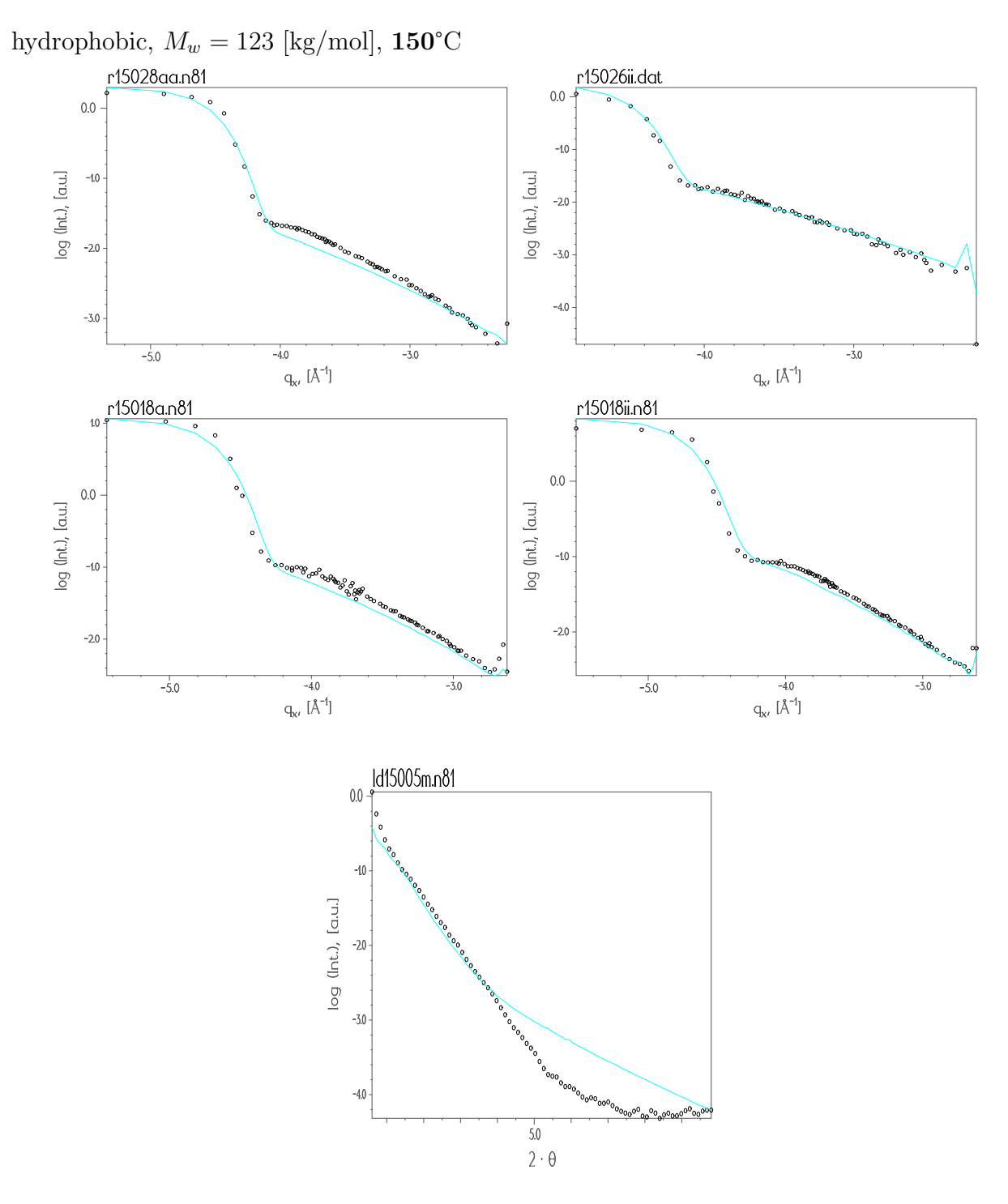


Figure A.15: Longitudinal and transverse scans of sample n81 at 150° C refined with the Liquid model. The curves with the symbols are the experimental data and the lines are the fits.

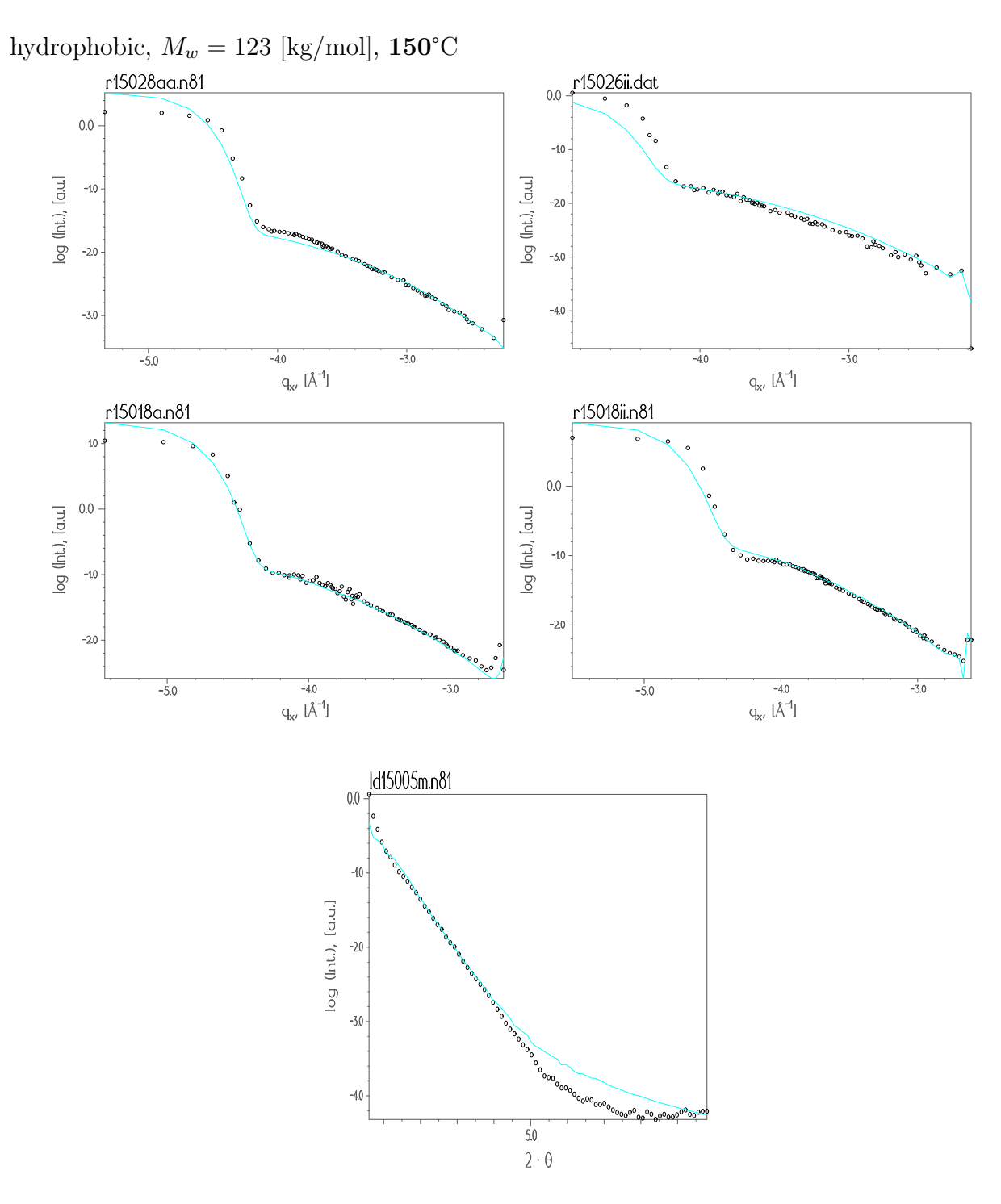


Figure A.16: Longitudinal and transverse scans of sample **n81** at **150**°C refined with the *Fractal model*. The curves with the symbols are the experimental data and the lines are the fits.

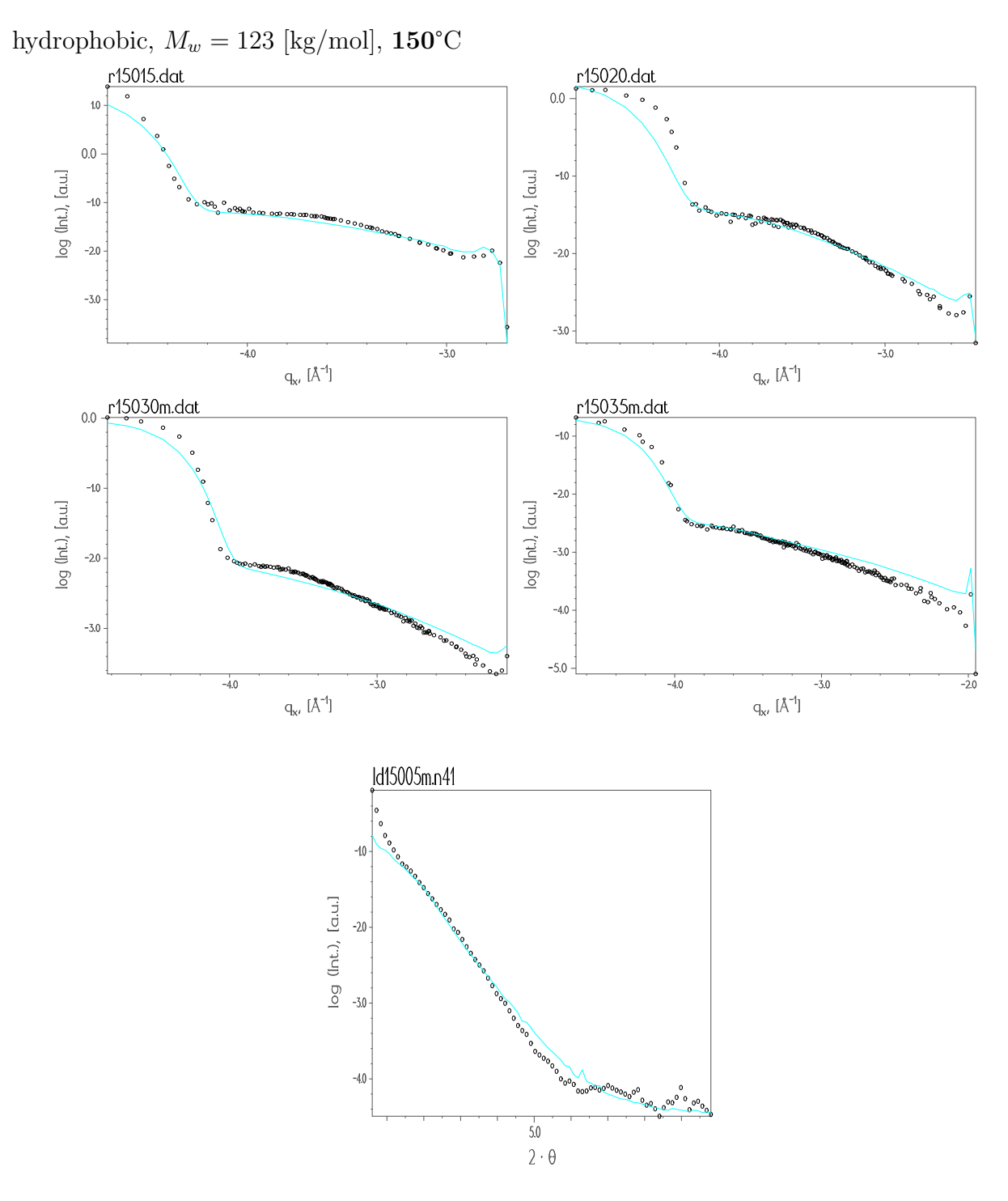


Figure A.17: Longitudinal and transverse scans of sample n41 at 150° C refined with the Liquid model. The curves with the symbols are the experimental data and the lines are the fits.

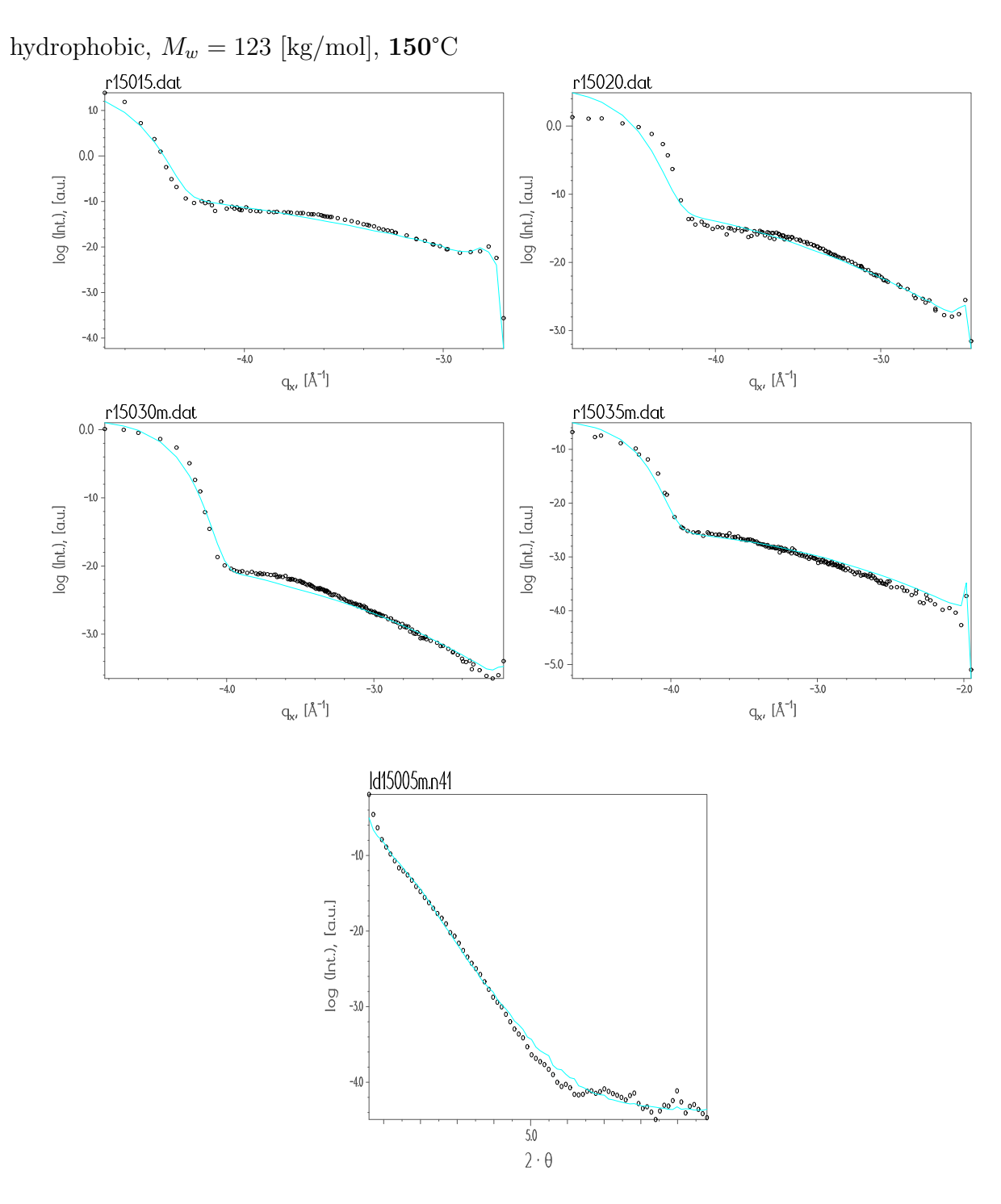


Figure A.18: Longitudinal and transverse scans of sample **n41** at **150**°C refined with the *Fractal model*. The curves with the symbols are the experimental data and the lines are the fits.

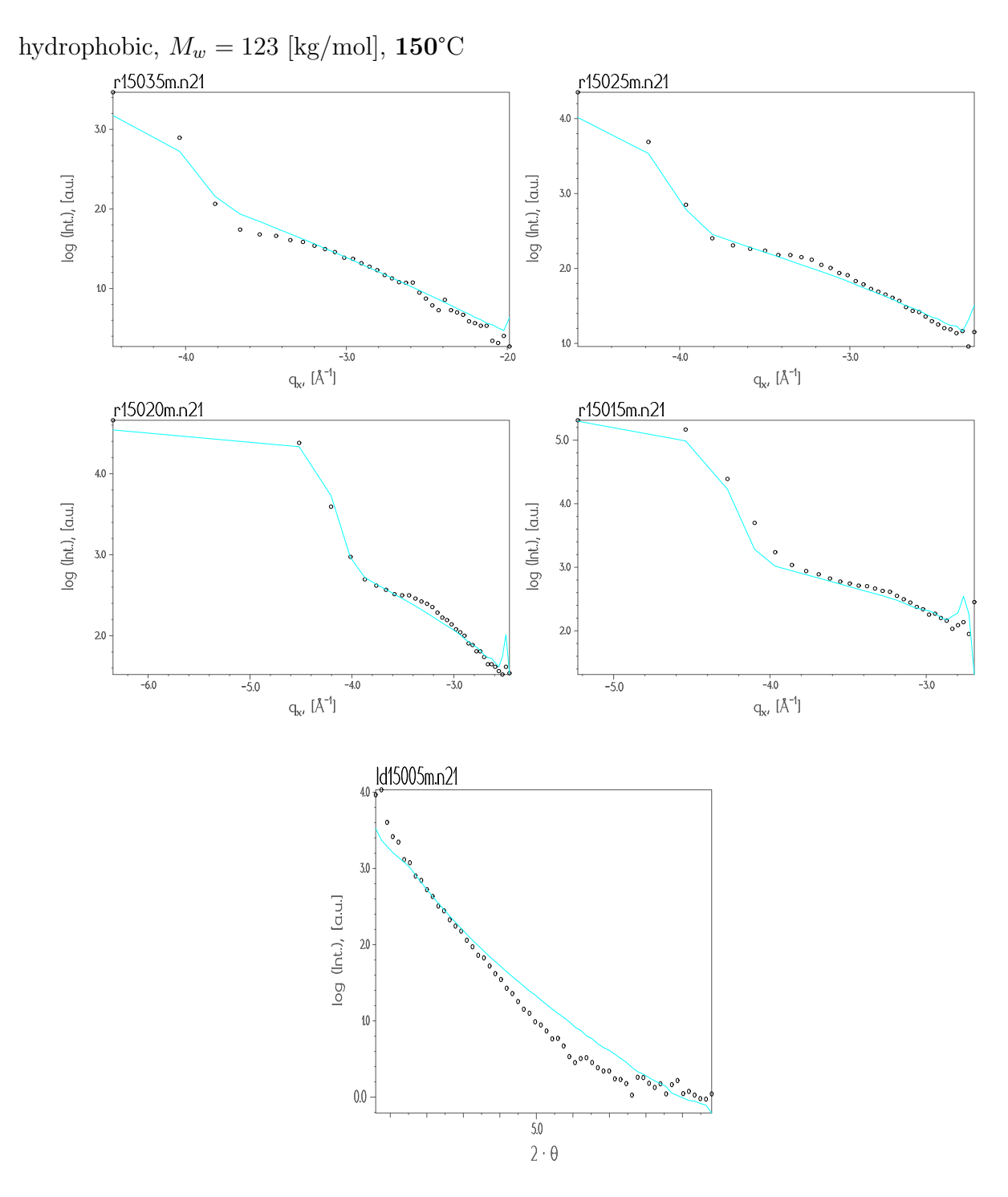


Figure A.19: Longitudinal and transverse scans of sample n21 at 150° C refined with the Liquid model. The curves with the symbols are the experimental data and the lines are the fits.

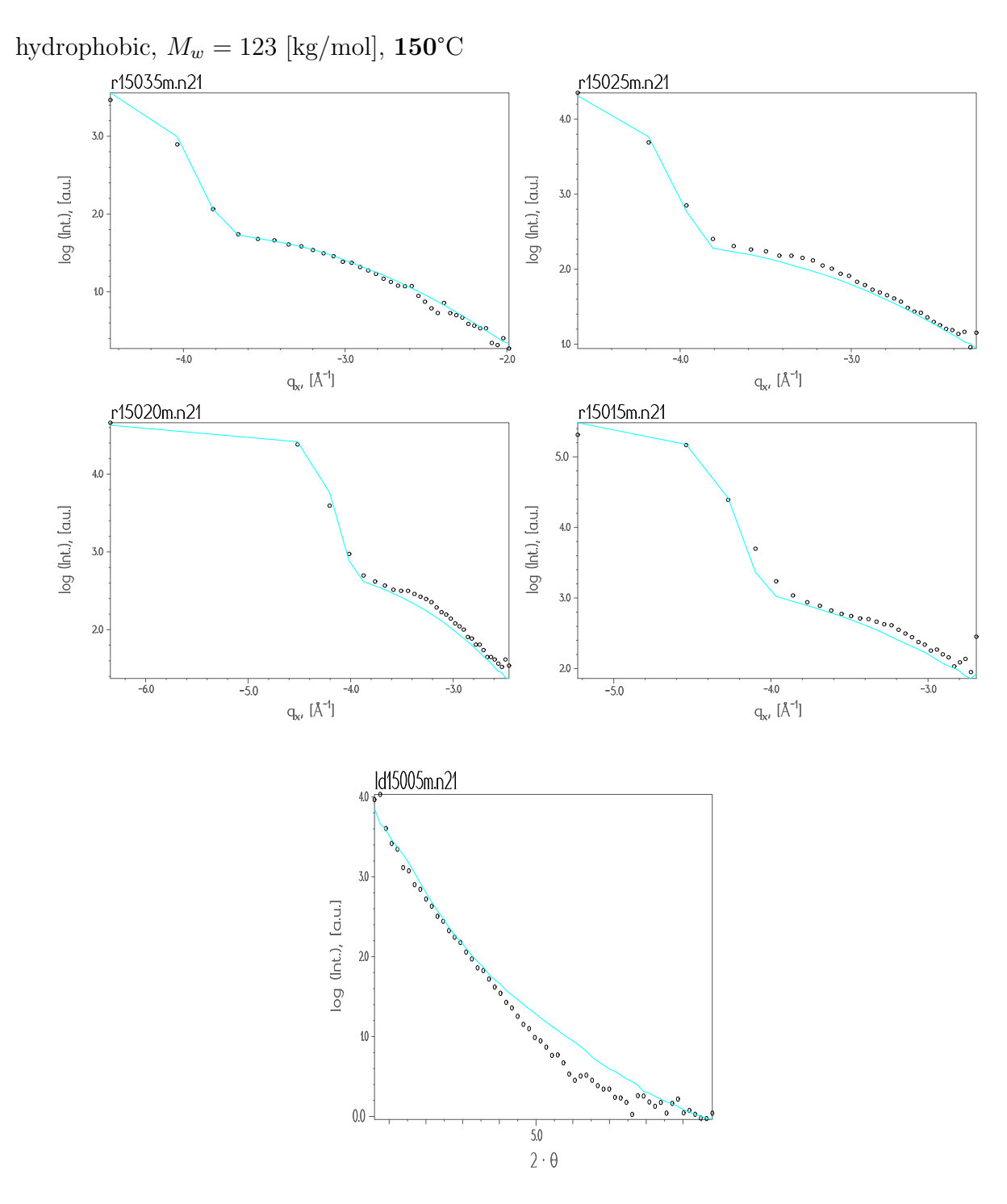


Figure A.20: Longitudinal and transverse scans of sample **n21** at **150**°C refined with the *Fractal model*. The curves with the symbols are the experimental data and the lines are the fits.

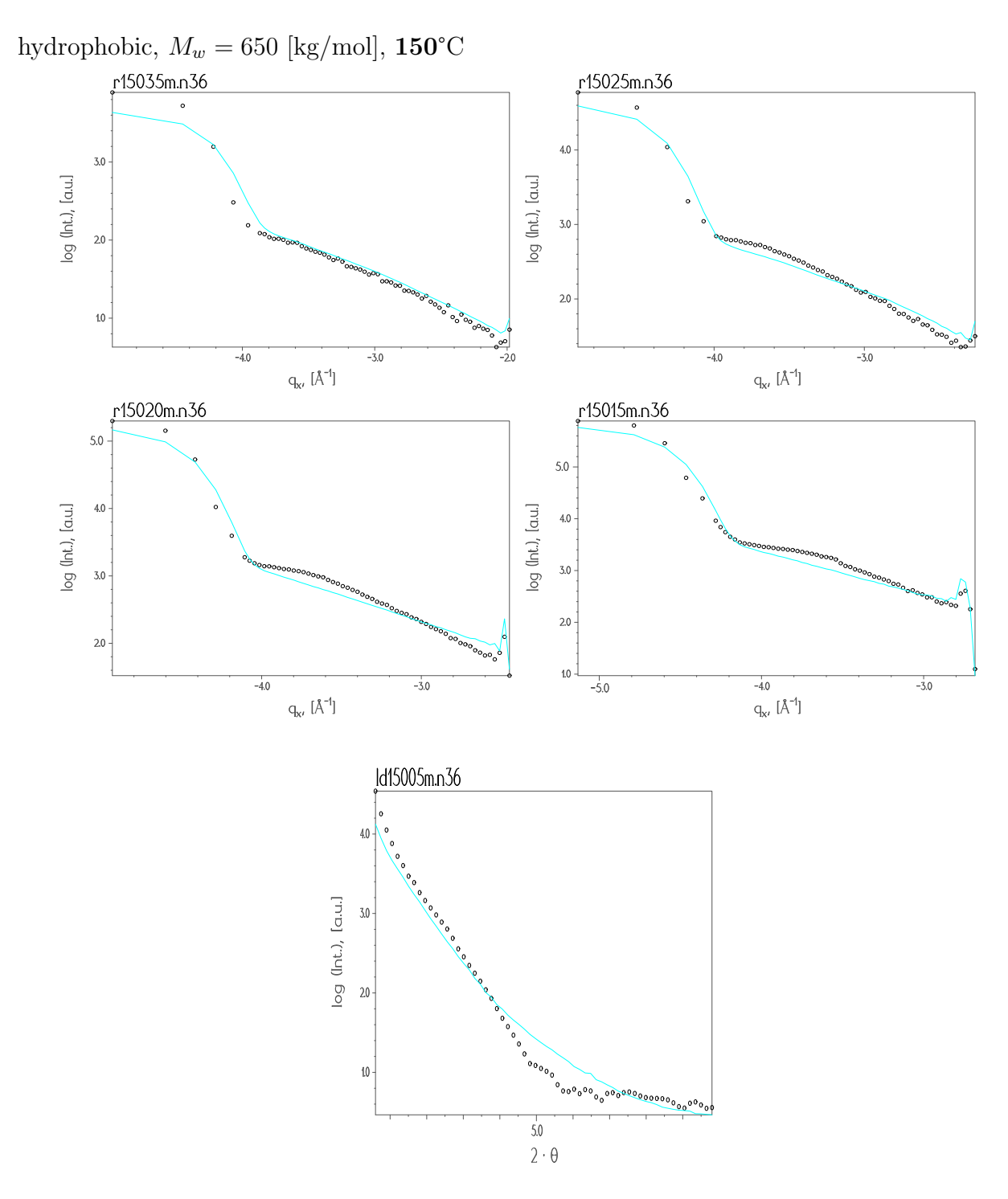


Figure A.21: Longitudinal and transverse scans of sample n36 at 150° C refined with the Liquid model. The curves with the symbols are the experimental data and the lines are the fits.

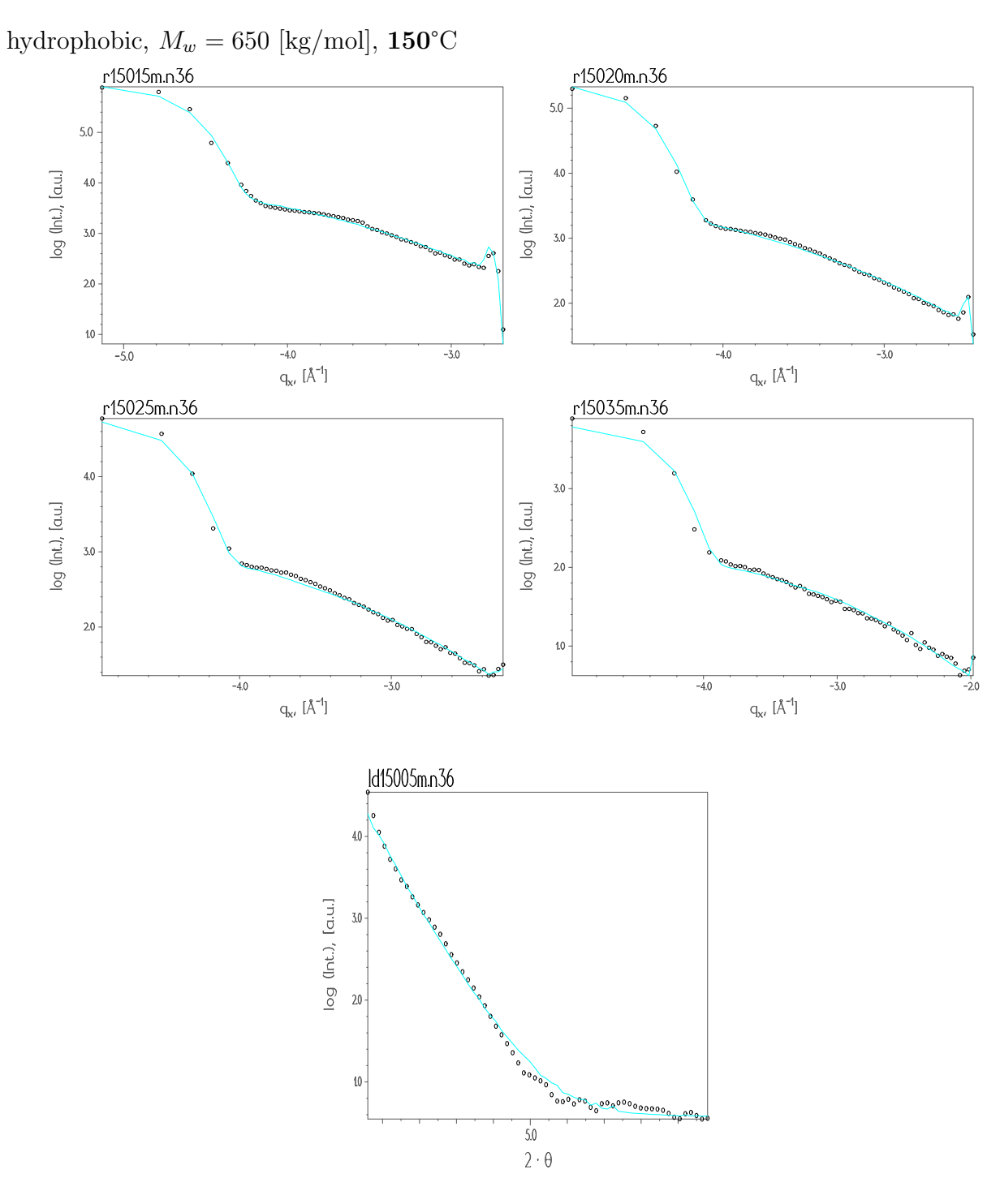


Figure A.22: Longitudinal and transverse scans of sample **n36** at **150**°C refined with the *Fractal model*. The curves with the symbols are the experimental data and the lines are the fits.

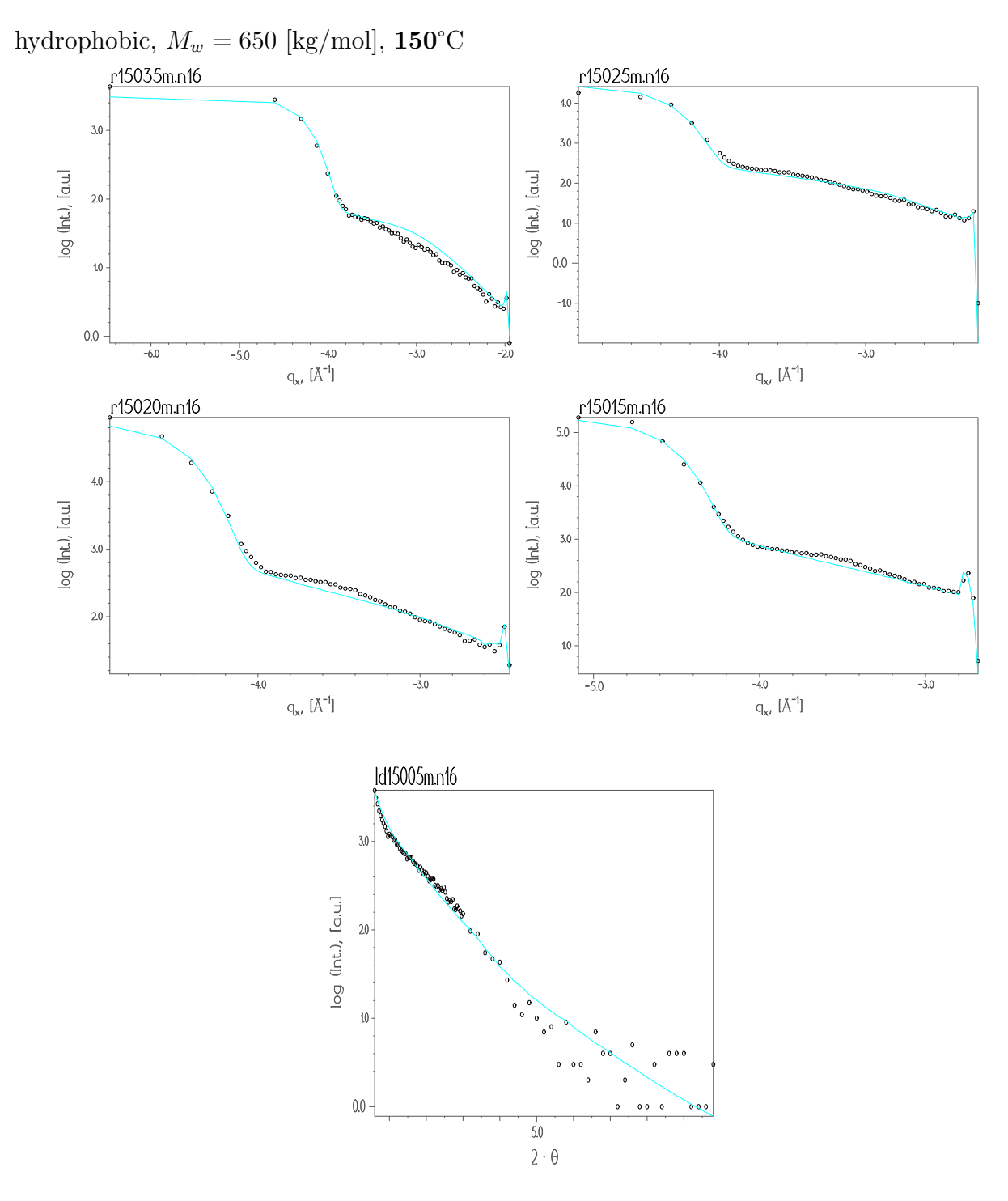


Figure A.23: Longitudinal and transverse scans of sample n16 at 150° C refined with the Liquid model. The curves with the symbols are the experimental data and the lines are the fits.

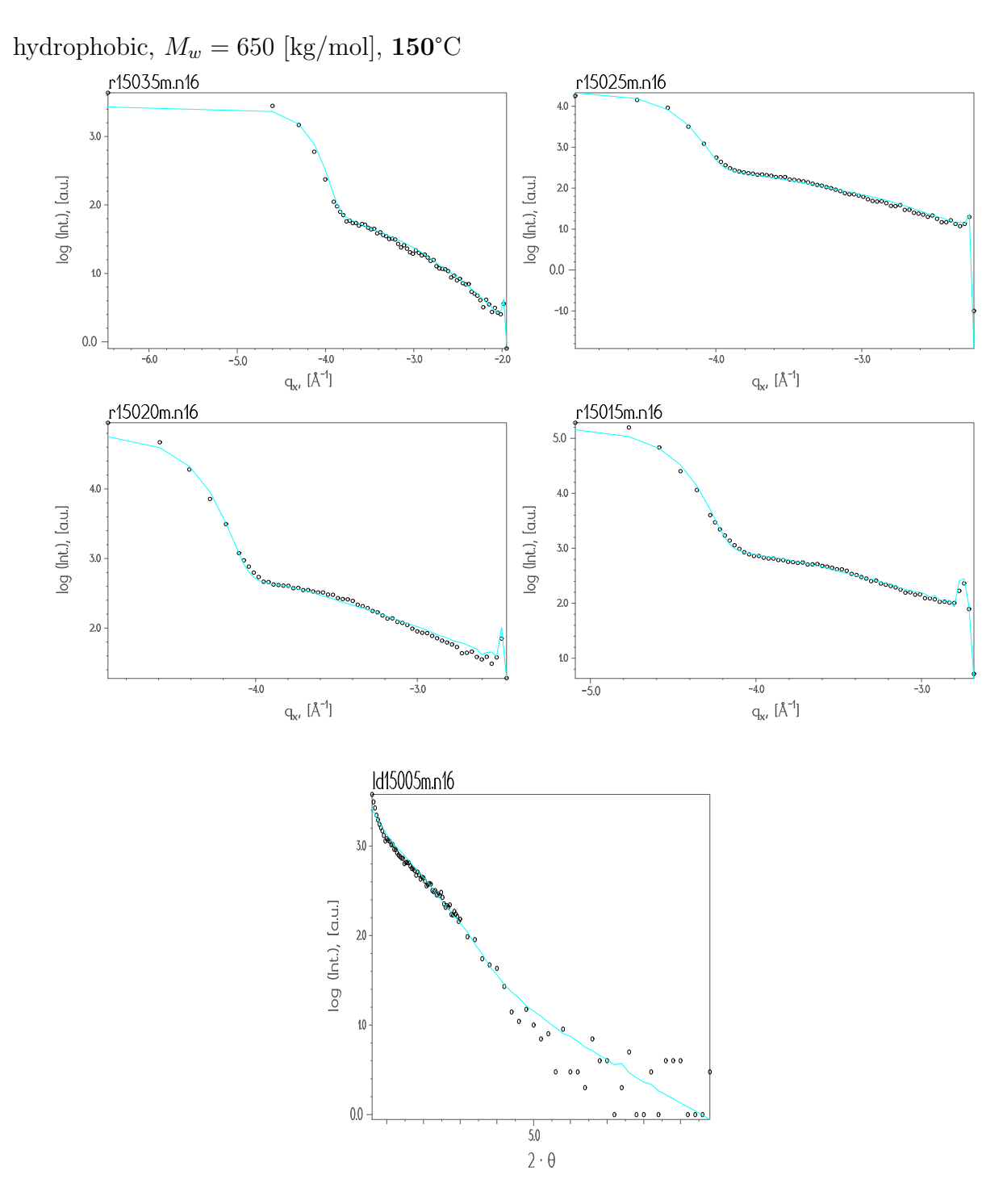


Figure A.24: Longitudinal and transverse scans of sample **n16** at **150**°C refined with the *Fractal model*. The curves with the symbols are the experimental data and the lines are the fits.

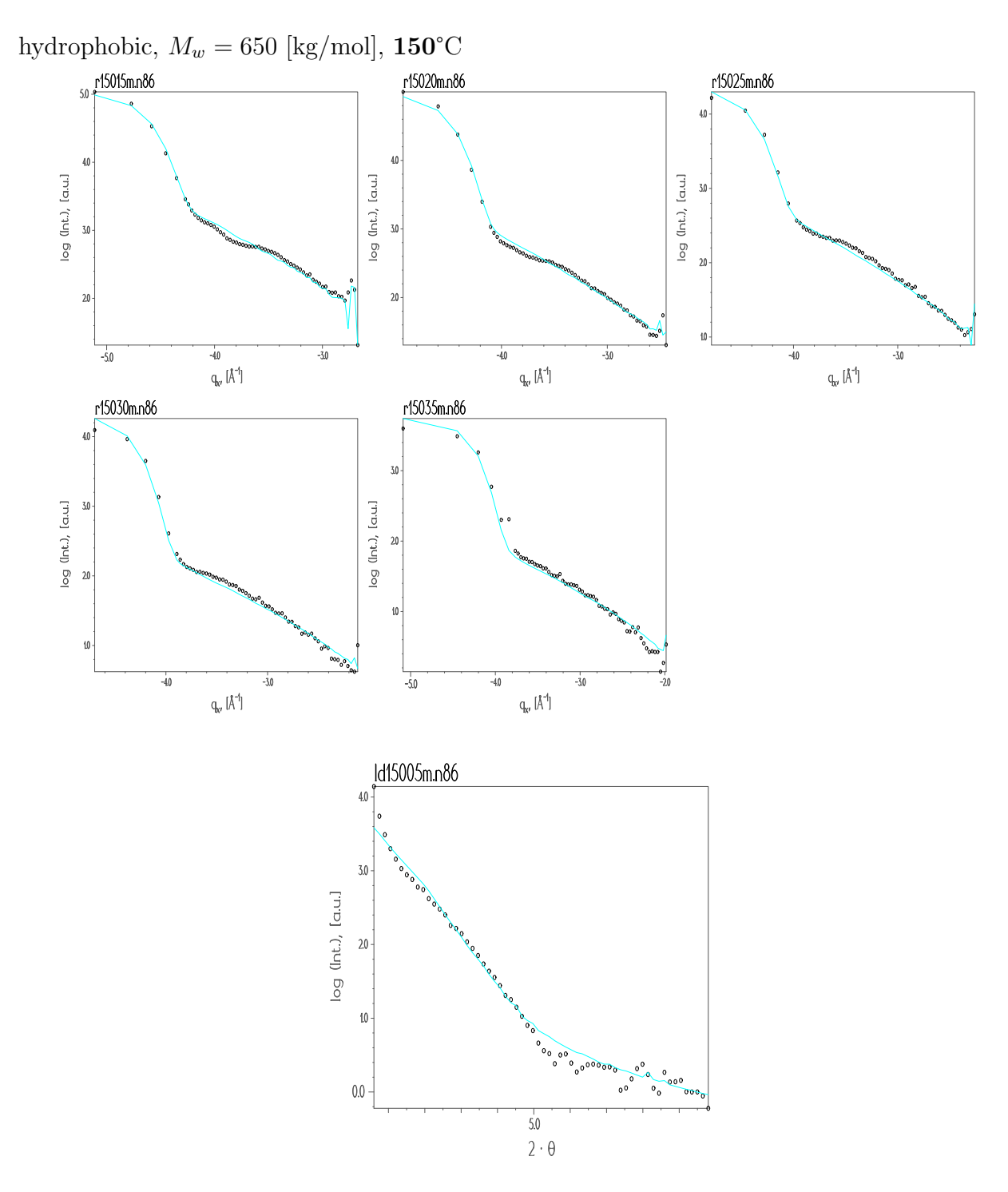


Figure A.25: Longitudinal and transverse scans of sample n86 at 150° C refined with the Liquid model. The curves with the symbols are the experimental data and the lines are the fits.

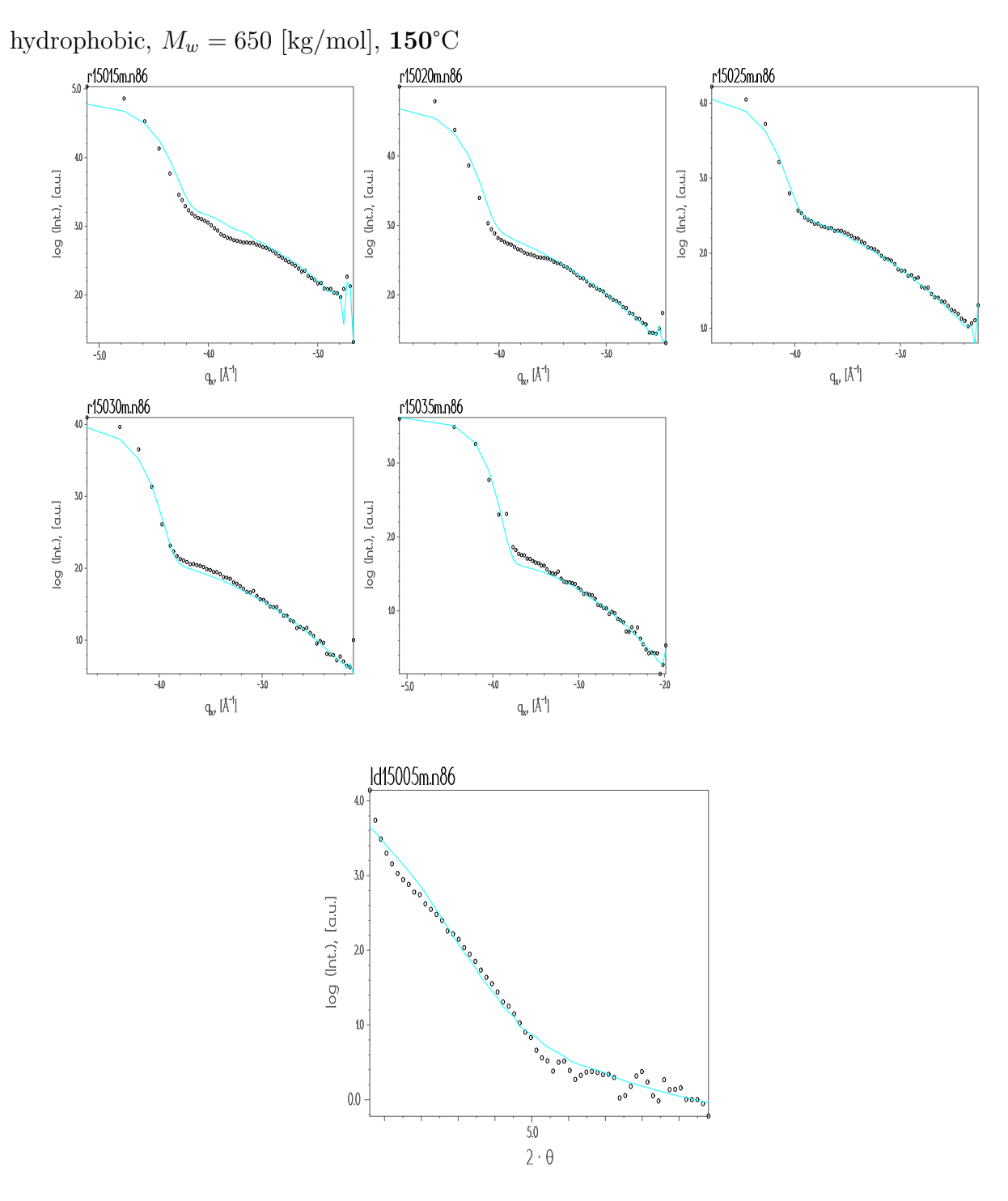


Figure A.26: Longitudinal and transverse scans of sample n86 at 150° C refined with the Fractal model. The curves with the symbols are the experimental data and the lines are the fits.

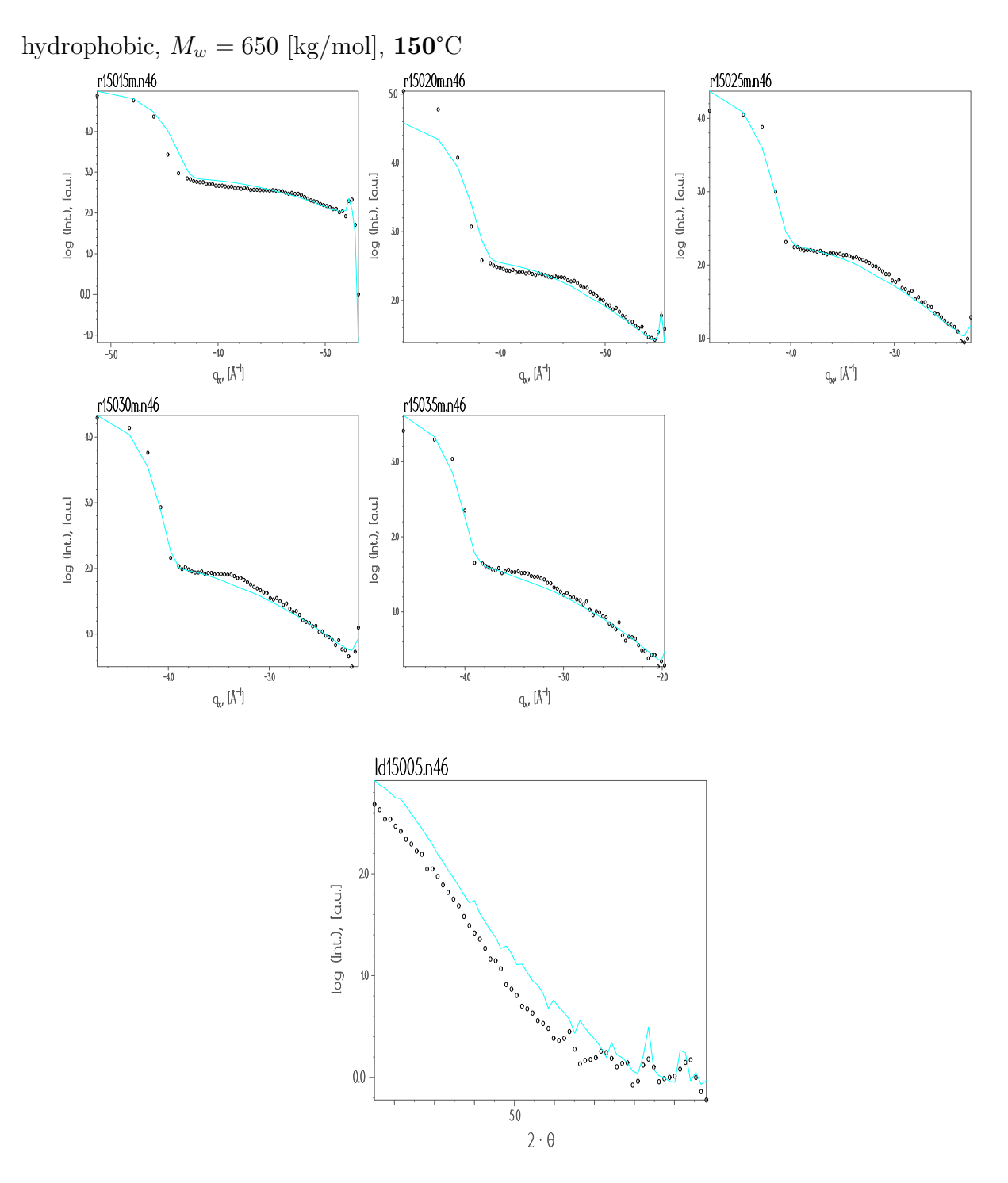


Figure A.27: Longitudinal and transverse scans of sample n46 at 150° C refined with the Liquid model. The curves with the symbols are the experimental data and the lines are the fits.

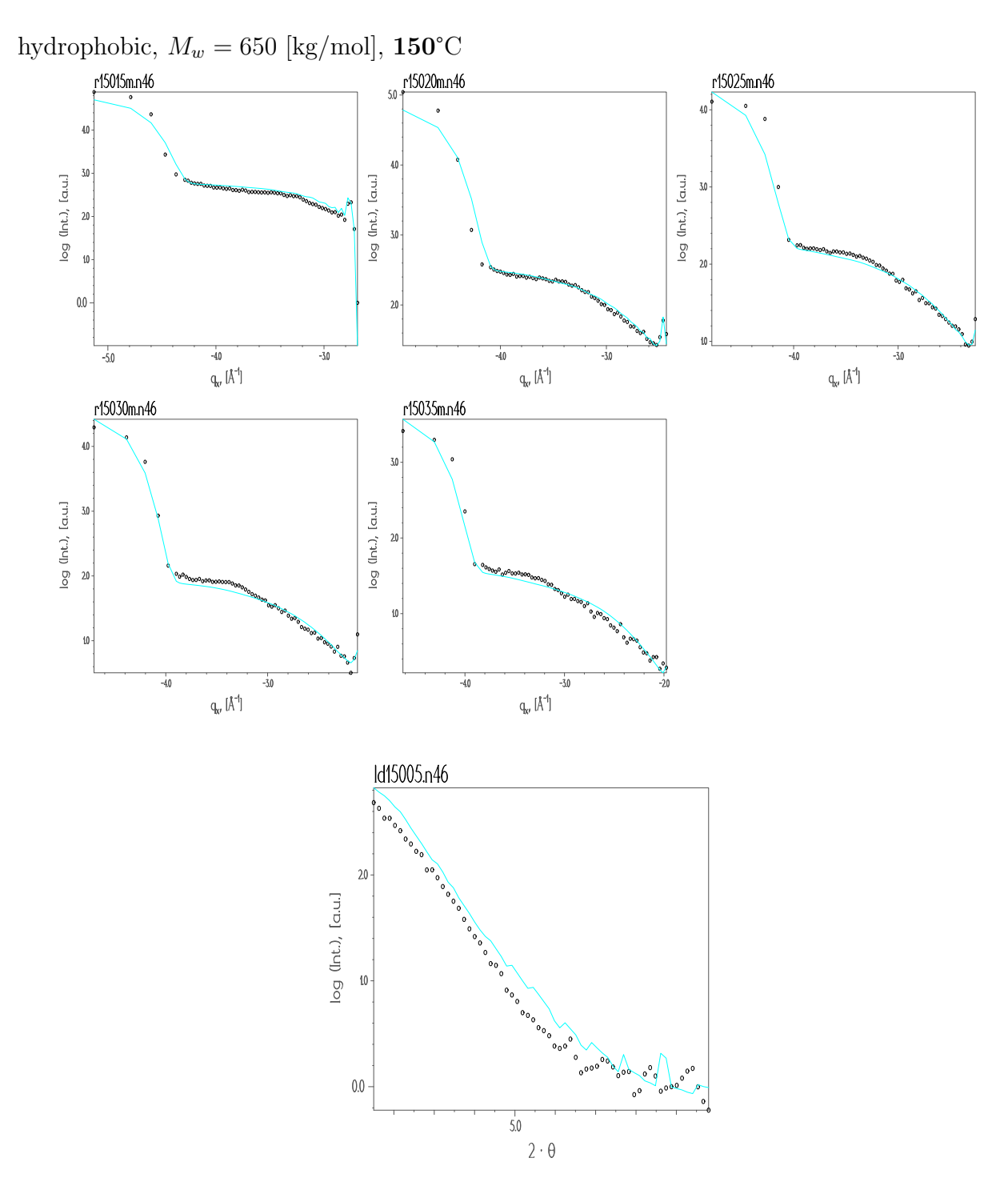


Figure A.28: Longitudinal and transverse scans of sample n46 at 150° C refined with the Fractal model. The curves with the symbols are the experimental data and the lines are the fits.

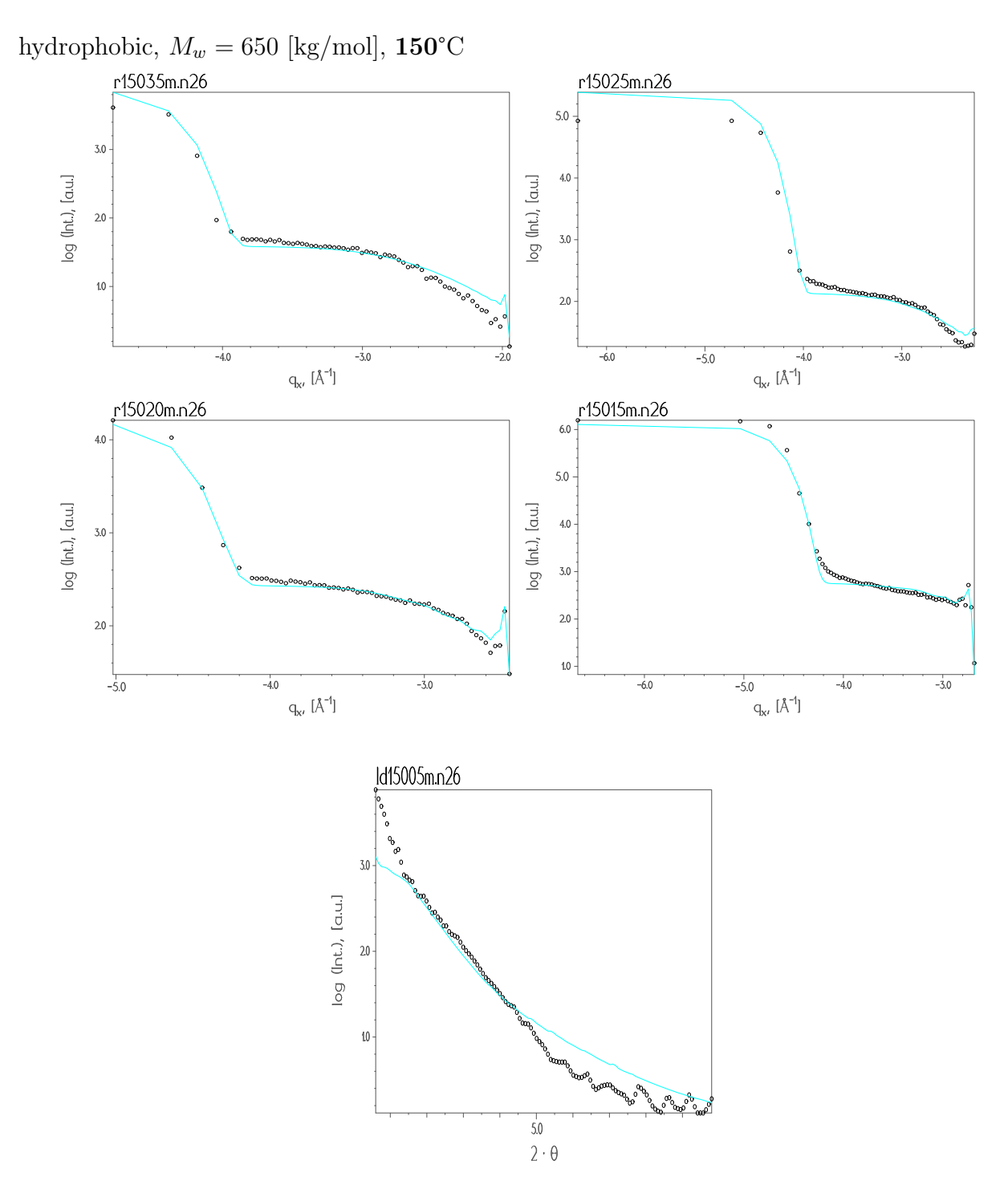


Figure A.29: Longitudinal and transverse scans of sample n26 at 150° C refined with the Liquid model. The curves with the symbols are the experimental data and the lines are the fits.

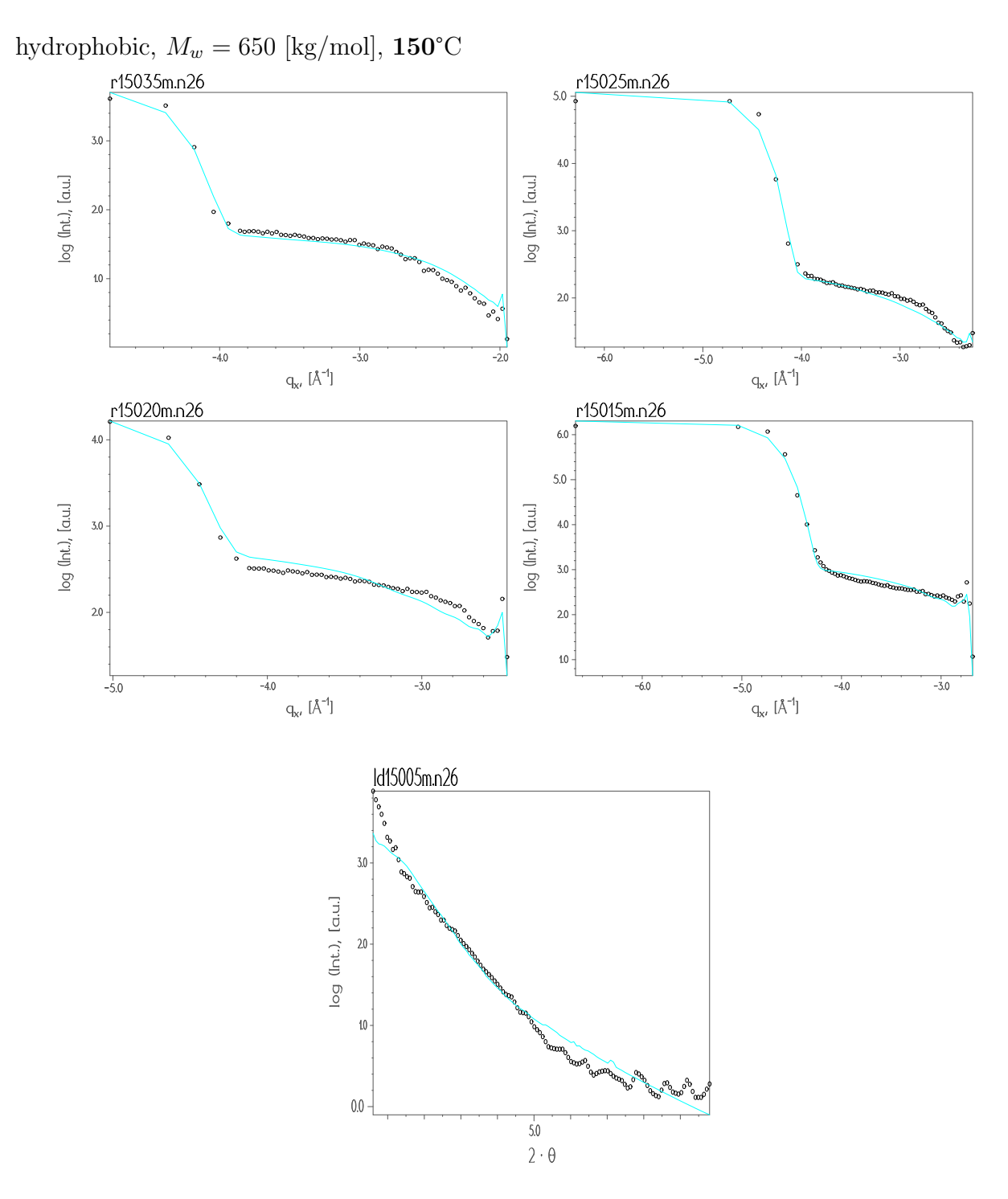


Figure A.30: Longitudinal and transverse scans of sample n26 at 150° C refined with the Fractal model. The curves with the symbols are the experimental data and the lines are the fits.

G 1	C 1 1: 1 11	I TT	G 1 1: 1 1	TT ,
Sample	Correlation length	Hurst parameter	Correlation length	Hurst parameter
number	of the substrate,	of the substrate,	of the first layer,	of the first layer
	$\xi_{sub} \cdot 10^3$,[Å]	h_{sub}	$\xi_{SiO_x} \cdot 10^3$, [Å]	h_{SiO_x}
n26	1.177 ± 0.002	0.950 ± 0.001	0.293 ± 0.001	0.456 ± 0.002
n46	1.0928 ± 0.0001	$0.38^{(f)}$	0.379 ± 0.006	$0.20^{(f)}$
n86	0.100 ± 0.004	0.39 ± 0.002	11.560 ± 0.001	$0.20^{(f)}$
n16	0.779 ± 0.002	$0.60^{(f)}$	0.858 ± 0.002	$0.20^{(f)}$
n36	0.546 ± 0.002	$0.58^{(f)}$	1.653 ± 0.003	$0.20^{(f)}$
n21	0.9415 ± 0.0003	0.3365 ± 0.0003	3.0195 ± 0.0004	$0.20^{(f)}$
n41	1.0150 ± 0.0001	$0.42^{(f)}$	0.557 ± 0.001	$0.20^{(f)}$
n81	1.237 ± 0.002	$0.38^{(f)}$	2.732 ± 0.002	$0.20^{(f)}$
n11	0.9307 ± 0.0003	0.3399 ± 0.0005	3.0124 ± 0.0004	$0.20^{(f)}$
n31	0.882 ± 0.001	$0.34^{(f)}$	3.052 ± 0.001	$0.20^{(f)}$
n23	0.10899 ± 0.0004	$0.45^{(f)}$	$0.10^{(f)}$	$0.20^{(f)}$
n43	0.773 ± 0.001	$0.30^{(f)}$	$0.58^{(f)}$	$0.20^{(f)}$
n83	0.6908 ± 0.0001	$0.21^{(f)}$	1.188 ± 0.0002	$0.23^{(f)}$
n13	1.052 ± 0.003	$0.58^{(f)}$	$0.10^{(f)}$	$0.20^{(f)}$
n33	1.195 ± 0.002	$0.58^{(f)}$	0.8977 ± 0.0003	$0.20^{(f)}$

Table A.4: Correlation length and Hurst parameter of the substrate and the first layer obtained after the refinement of diffuse scattering curves measured at 150°C (*Liquid model*).

Sample	Surface tension,	χ^2
number	$\eta, [N/m]$	
n26	0.0131 ± 0.0001	10.91
n46	0.0176 ± 0.0007	4.96
n86	0.0223 ± 0.0001	3.21
n16	0.0191 ± 0.0002	6.06
n36	0.0127 ± 0.0003	5.96
n21	0.0118 ± 0.0002	6.92
n41	0.01315 ± 0.00001	9.53
n81	0.01605 ± 0.00002	16.16
n11	0.0133 ± 0.0001	5.45
n31	0.01665 ± 0.00003	4.04
n23	0.01323 ± 0.00006	21.13
n43	0.0109 ± 0.0001	8.44
n83	0.01583 ± 0.00003	14.35
n13	0.01361 ± 0.0002	2.27
n33	0.0178 ± 0.0001	4.19

Table A.5: Surface tension at the polymer/air interface and χ^2 obtained from refinements of diffuse scattering curves measured at 150°C (*Liquid model*).

Sample	Correlation length	Hurst parameter	Correlation length	Hurst parameter
number	of the substrate,	of the substrate,	of the first layer,	of the first layer
	$\xi_{sub}\cdot 10^3, [{\rm \AA}]$	h_{sub}	$\xi_{SiO_x} \cdot 10^3$, [Å]	h_{SiO_x}
n26	0.957 ± 0.002	0.590 ± 0.003	0.286 ± 0.002	0.631 ± 0.002
n46	0.51 ± 0.03	0.710 ± 0.008	0.482 ± 0.003	$0.20^{(f)}$
n86	0.536 ± 0.001	0.781 ± 0.002	0.903 ± 0.001	$0.20^{(f)}$
n16	0.873 ± 0.007	0.55 ± 0.03	0.839 ± 0.006	$0.20^{(f)}$
n36	0.279 ± 0.003	0.225 ± 0.002	0.748 ± 0.001	$0.20^{(f)}$
n21	$0.90^{(f)}$	0.642 ± 0.003	0.5401 ± 0.0001	0.2671 ± 0.0004
n41	0.214 ± 0.002	0.601 ± 0.003	0.725 ± 0.001	$0.20^{(f)}$
n81	2.0811 ± 0.0003	0.608 ± 0.001	0.361 ± 0.002	$0.20^{(f)}$
n11	0.451 ± 0.001	$0.20^{(f)}$	1.047 ± 0.001	$0.20^{(f)}$
n31	0.337 ± 0.001	$0.75^{(f)}$	0.226 ± 0.001	$0.20^{(f)}$
n23	3.829 ± 0.007	$0.20^{(f)}$	$0.10^{(f)}$	$0.30^{(f)}$
n43	$1.00^{(f)}$	$0.30^{(f)}$	$0.10^{(f)}$	$0.20^{(f)}$
n83	0.379 ± 0.001	$0.20^{(f)}$	2.946 ± 0.001	$0.20^{(f)}$
n13	1.088 ± 0.003	$0.20^{(f)}$	0.1050 ± 0.0002	$0.20^{(f)}$
n33	$0.20^{(f)}$	$0.20^{(f)}$	$0.10^{(f)}$	$0.20^{(f)}$

Table A.6: Correlation length and Hurst parameter of the substrate and the first layer obtained after the refinement of diffuse scattering curves measured at 150°C (*Fractal model*).

Sample	Correlation length	Hurst parameter of	Roughness of	
number	of the polym. film,	the polym. film,	the polym. film,	χ^2
	$\xi_{PS} \cdot 10^3, [\text{Å}]$	h_{PS}	$\sigma_{PS},~ [{ m \AA}]$	
n26	0.782 ± 0.002	0.2621 ± 0.0004	$5.91^{(f)}$	5.47
n46	1.351 ± 0.009	0.541 ± 0.005	6.828 ± 0.009	3.91
n86	3.364 ± 0.001	0.2385 ± 0.0001	6.845 ± 0.001	3.95
n16	0.825 ± 0.006	0.202 ± 0.001	5.967 ± 0.006	4.46
n36	2.143 ± 0.001	$0.20^{(f)}$	7.003 ± 0.001	3.91
n21	3.998 ± 0.003	0.214 ± 0.001	7.899 ± 0.004	4.19
n41	3.596 ± 0.001	$0.20^{(f)}$	7.780 ± 0.002	5.20
n81	4.184 ± 0.001	0.2547 ± 0.0001	6.5737 ± 0.0004	7.55
n11	3.111 ± 0.001	$0.19^{(f)}$	6.0010 ± 0.0001	4.72
n31	2.0175 ± 0.0004	$0.20^{(f)}$	$6.04^{(f)}$	3.17
n23	6.953 ± 0.004	0.2778 ± 0.0003	8.739 ± 0.002	4.85
n43	13.461 ± 0.002	0.2214 ± 0.0003	10.380 ± 0.002	2.91
n83	9.875 ± 0.001	0.2341 ± 0.0002	7.5956 ± 0.0006	9.52
n13	7.024 ± 0.002	$0.20^{(f)}$	6.802 ± 0.002	2.88
n33	17.979 ± 0.005	$0.20^{(f)}$	8.198 ± 0.007	2.30

Table A.7: Correlation length, Hurst parameter and roughness of the polymer film as well as χ^2 obtained from refinements of diffuse scattering curves measured at 150°C (*Fractal model*).

A.2.1.2 Hydrophobic samples

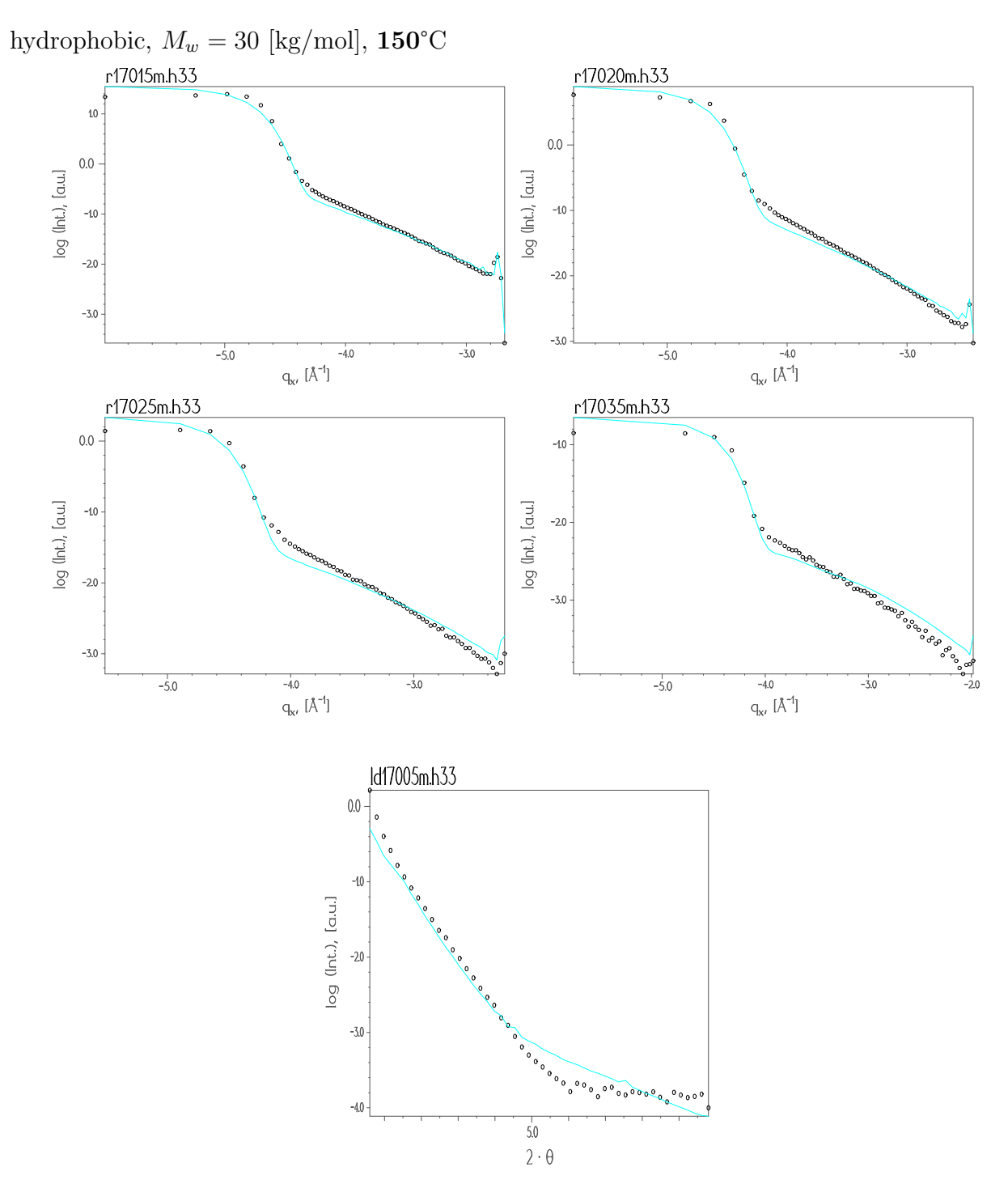


Figure A.31: Longitudinal and transverse scans of sample h33 at 170° C refined with the *Liquid model*. The curves with the symbols are the experimental data and the lines are the fits.

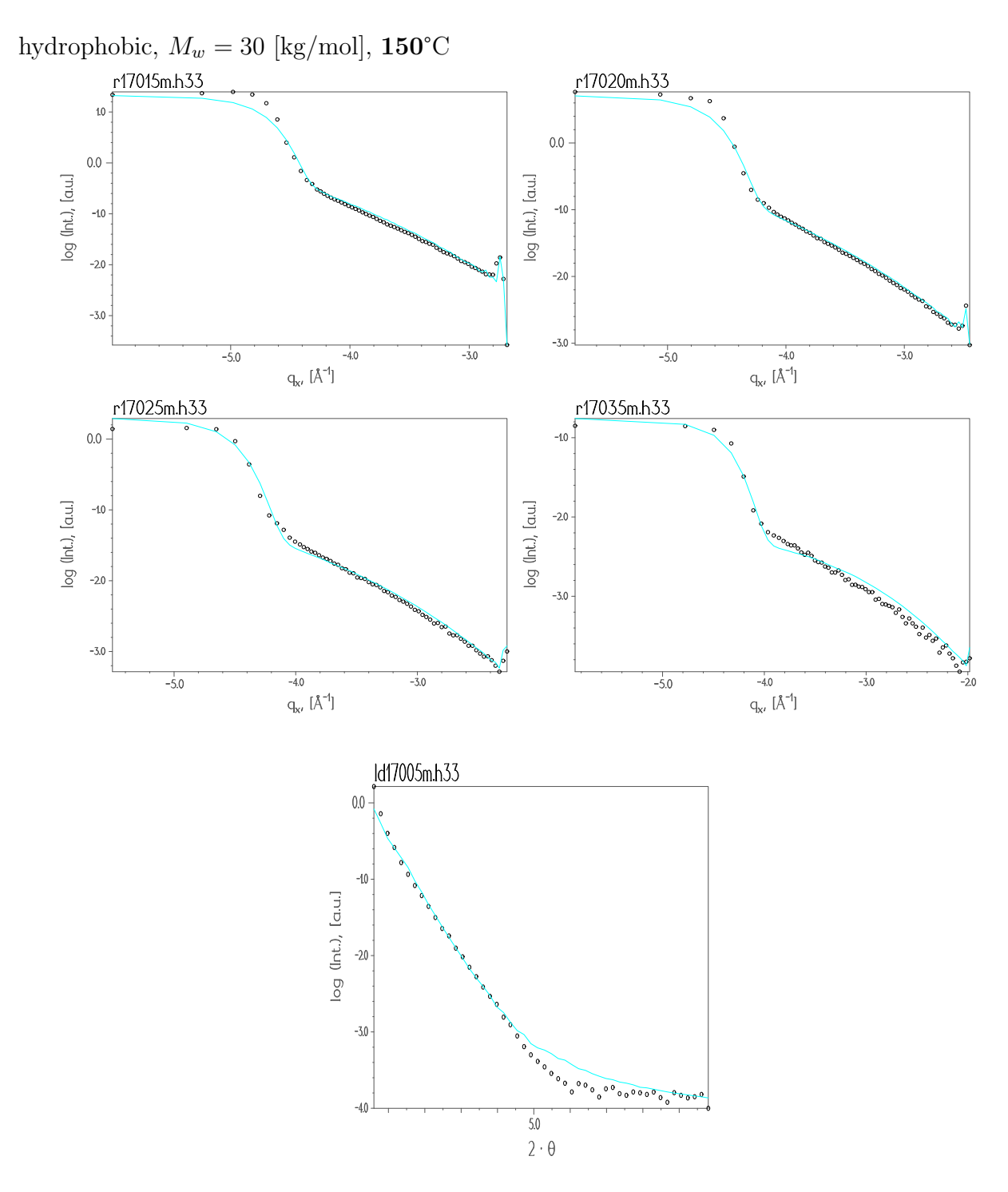


Figure A.32: Longitudinal and transverse scans of sample **h33** at **170**°C refined with the *Fractal model*. The curves with the symbols are the experimental data and the lines are the fits.

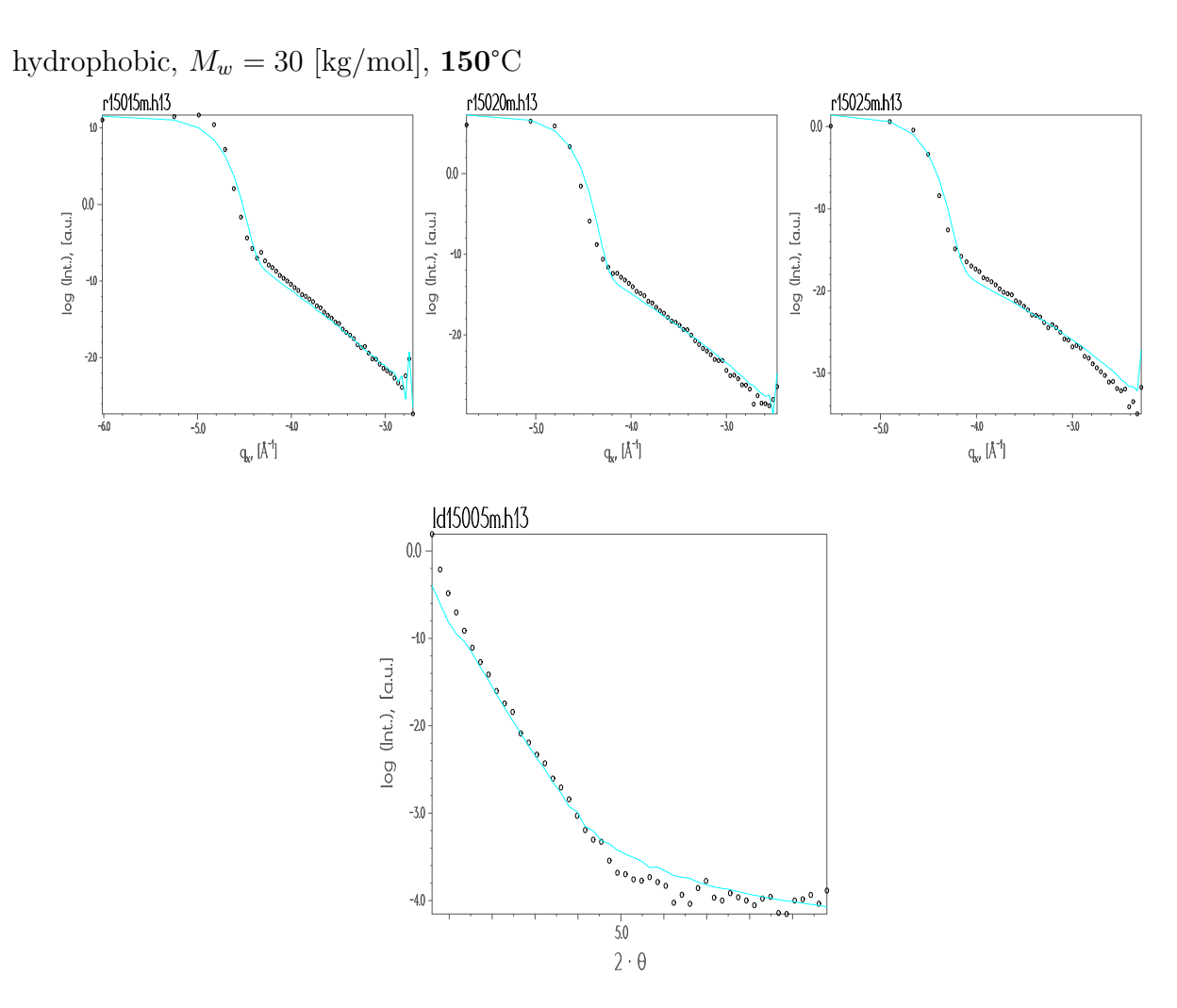


Figure A.33: Longitudinal and transverse scans of sample h13 at 150° C refined with the Liquid model. The curves with the symbols are the experimental data and the lines are the fits.

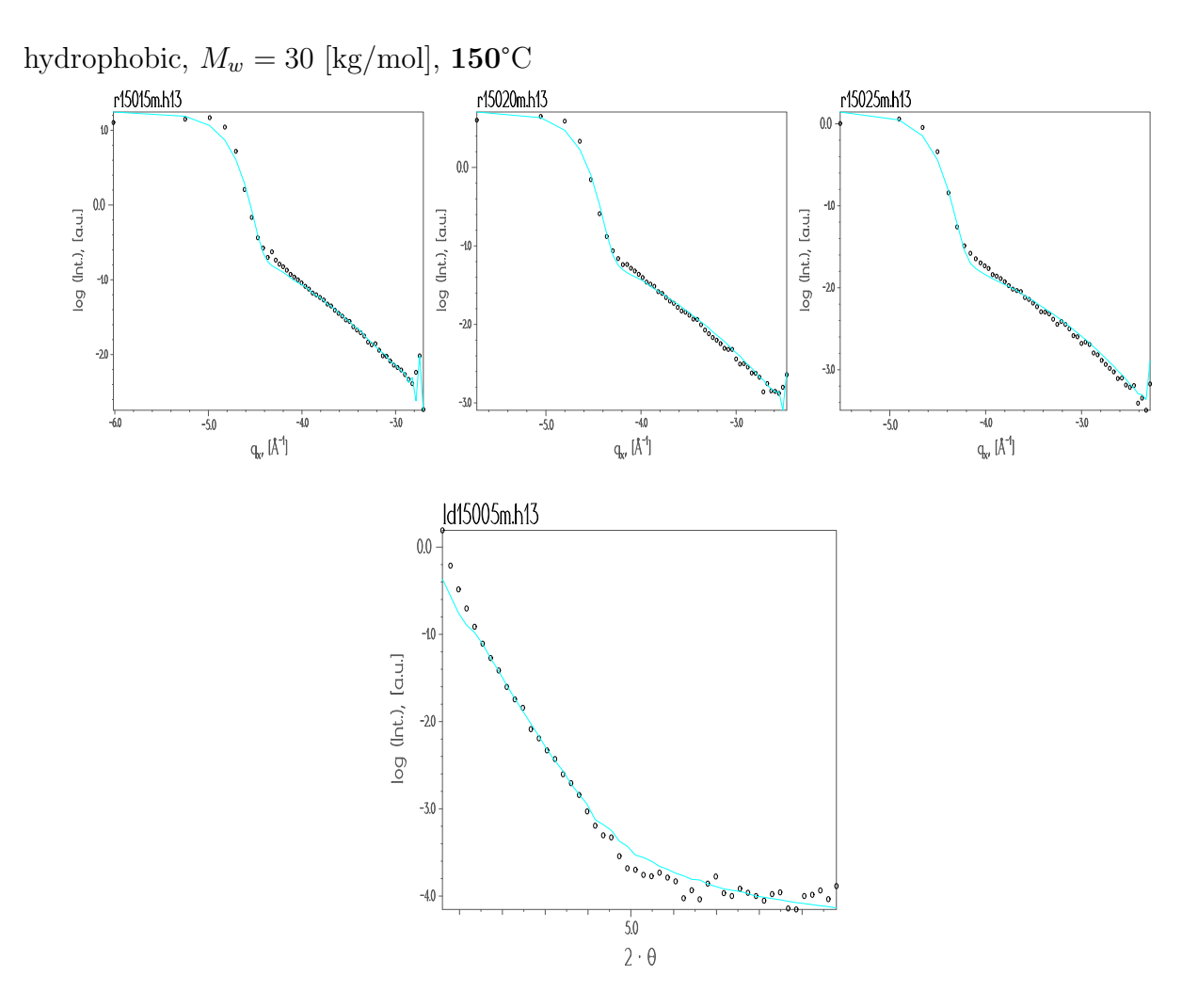


Figure A.34: Longitudinal and transverse scans of sample h13 at 150° C refined with the Fractal model. The curves with the symbols are the experimental data and the lines are the fits.

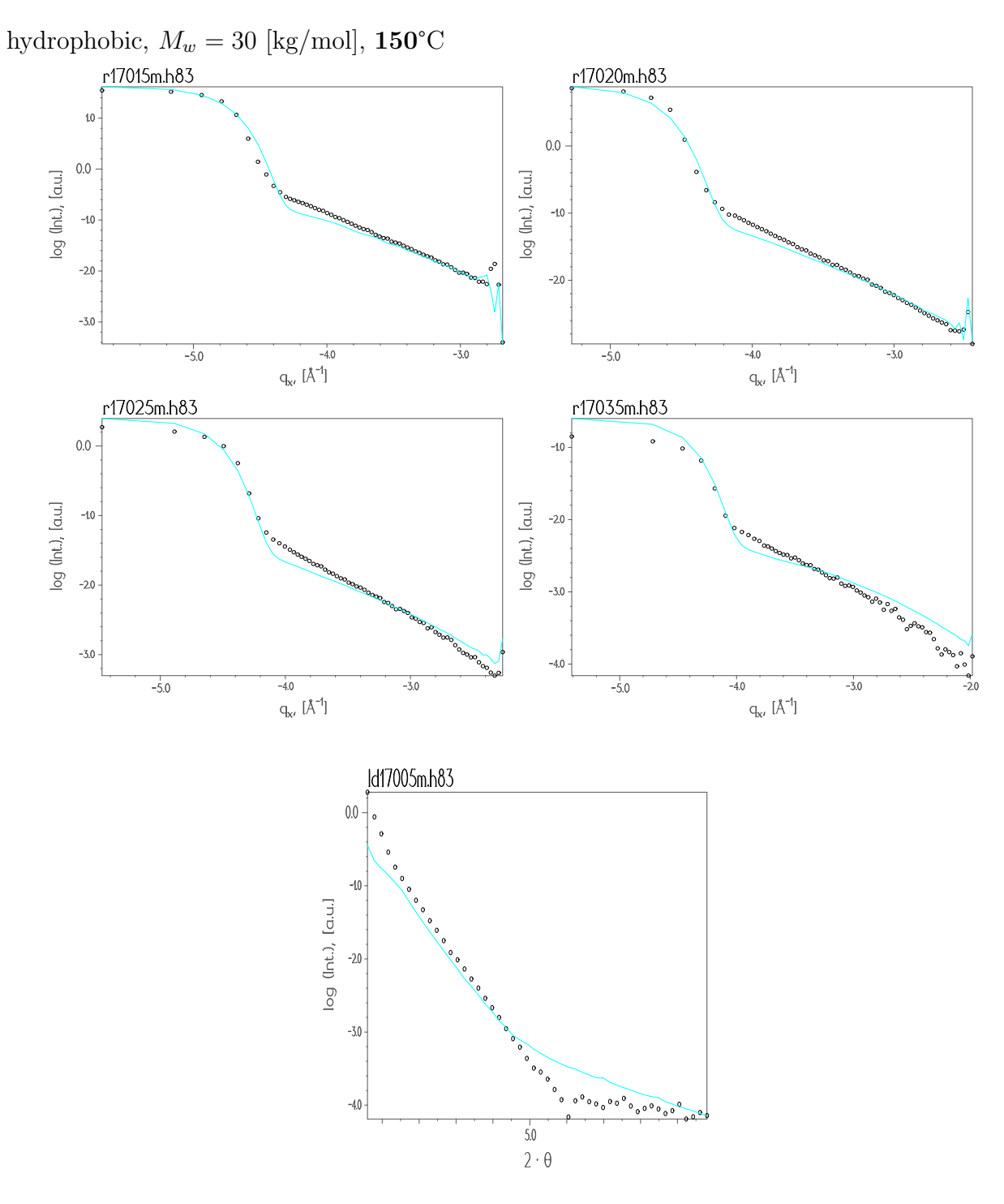


Figure A.35: Longitudinal and transverse scans of sample h83 at 170° C refined with the Liquid model. The curves with the symbols are the experimental data and the lines are the fits.

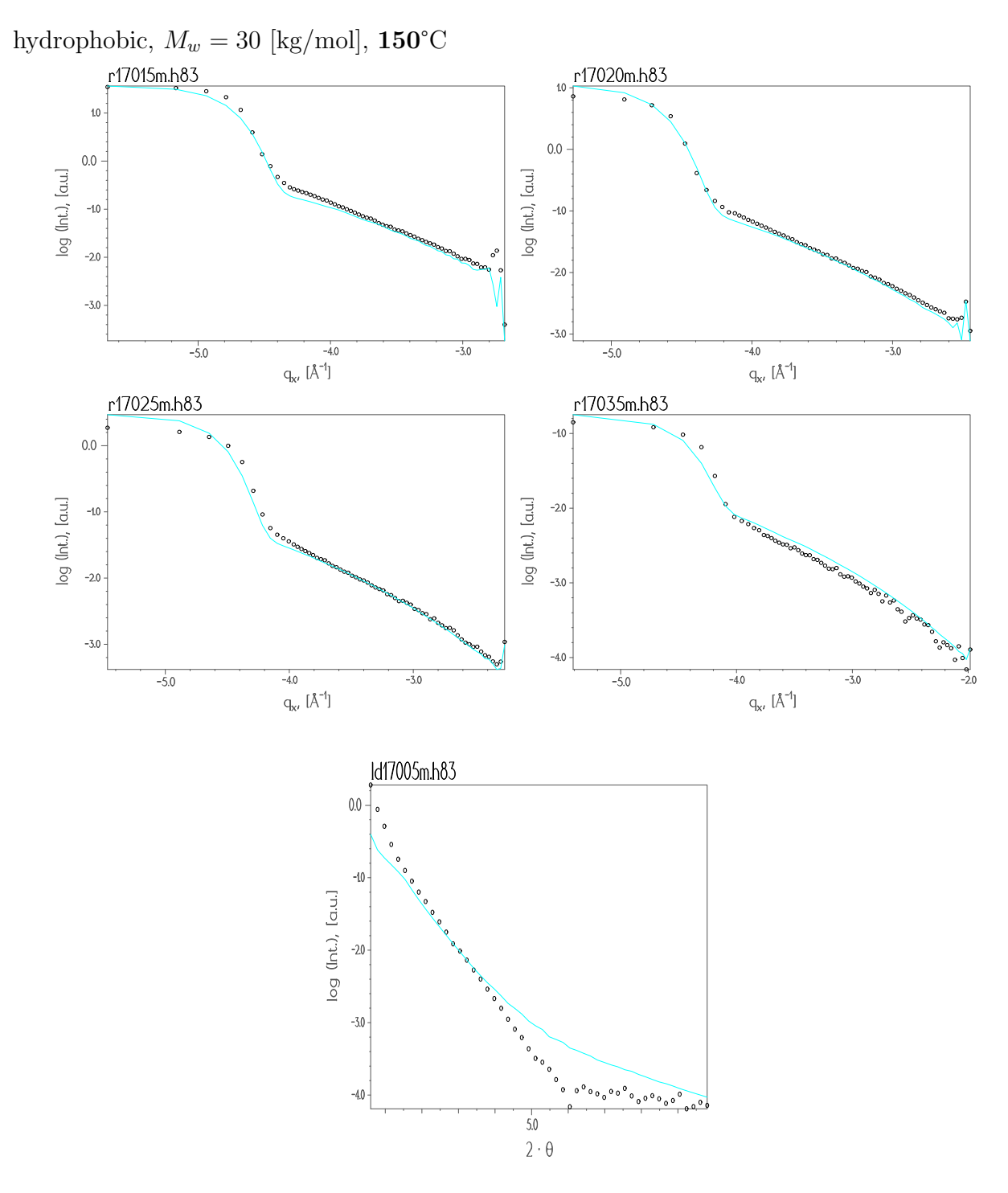


Figure A.36: Longitudinal and transverse scans of sample **h83** at **170**°C refined with the *Fractal model*. The curves with the symbols are the experimental data and the lines are the fits.

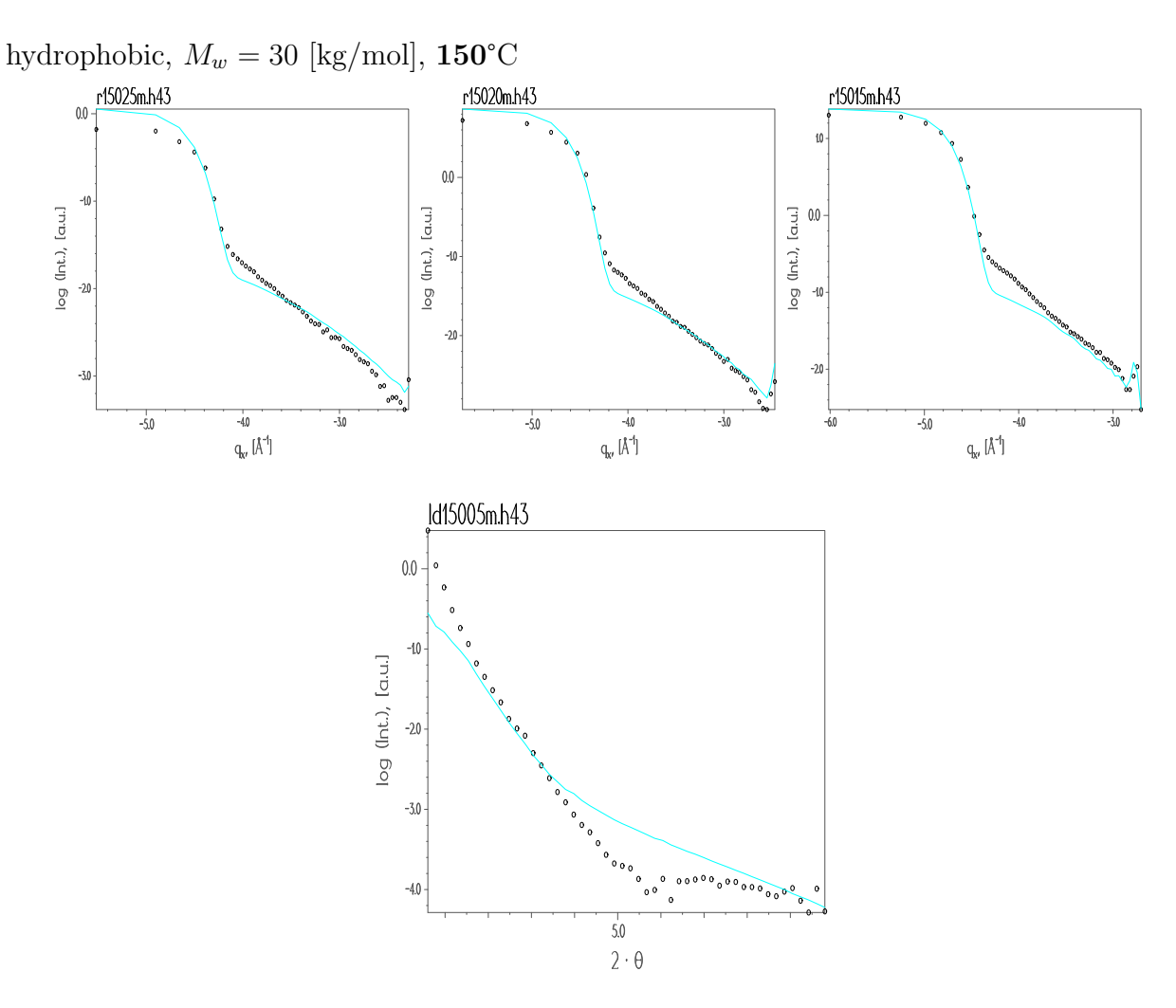


Figure A.37: Longitudinal and transverse scans of sample $\mathbf{h43}$ at $\mathbf{150}^{\circ}\mathrm{C}$ refined with the Liquid model. The curves with the symbols are the experimental data and the lines are the fits.

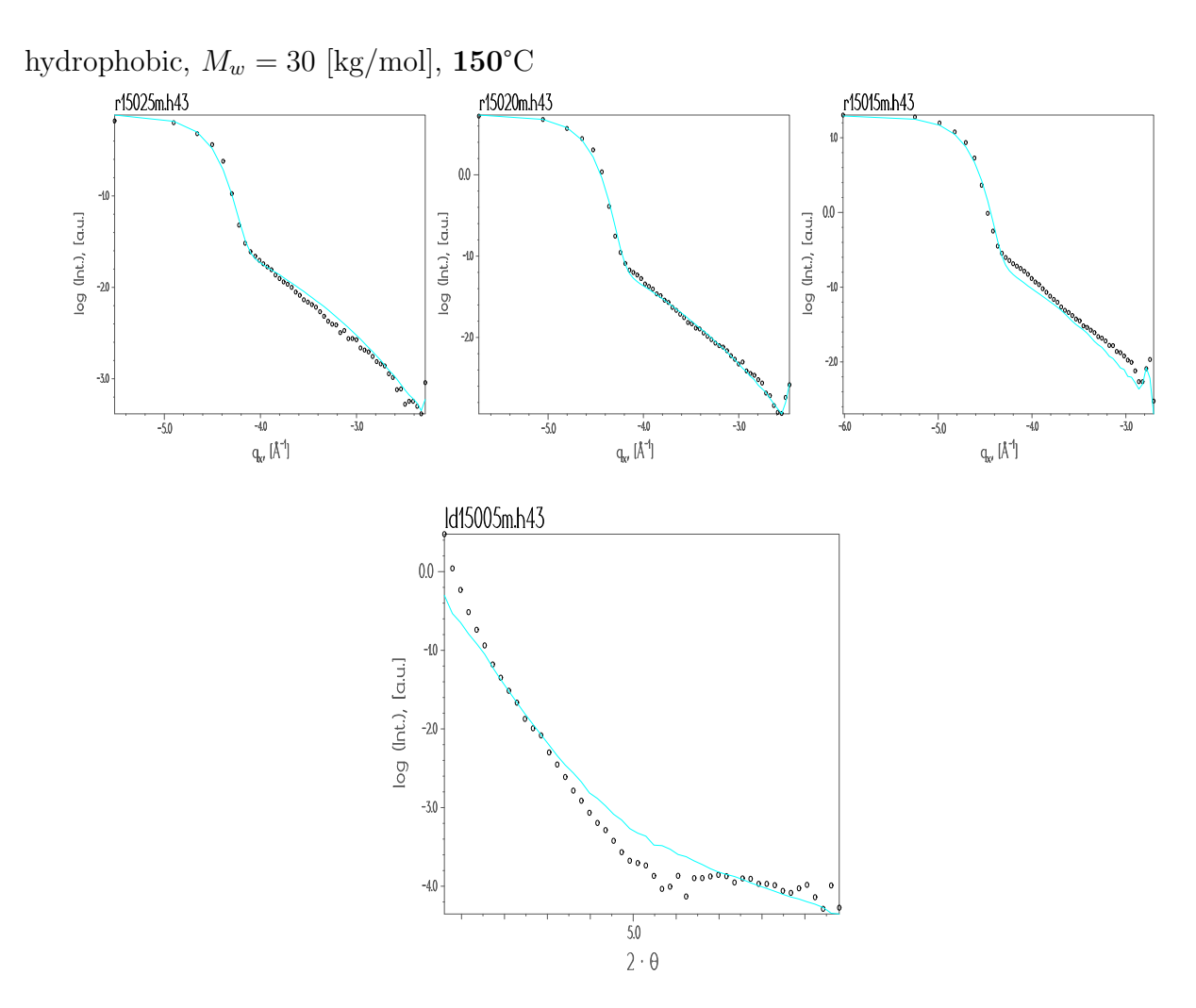


Figure A.38: Longitudinal and transverse scans of sample $\mathbf{h43}$ at $\mathbf{150}^{\circ}\mathrm{C}$ refined with the Fractal model. The curves with the symbols are the experimental data and the lines are the fits.

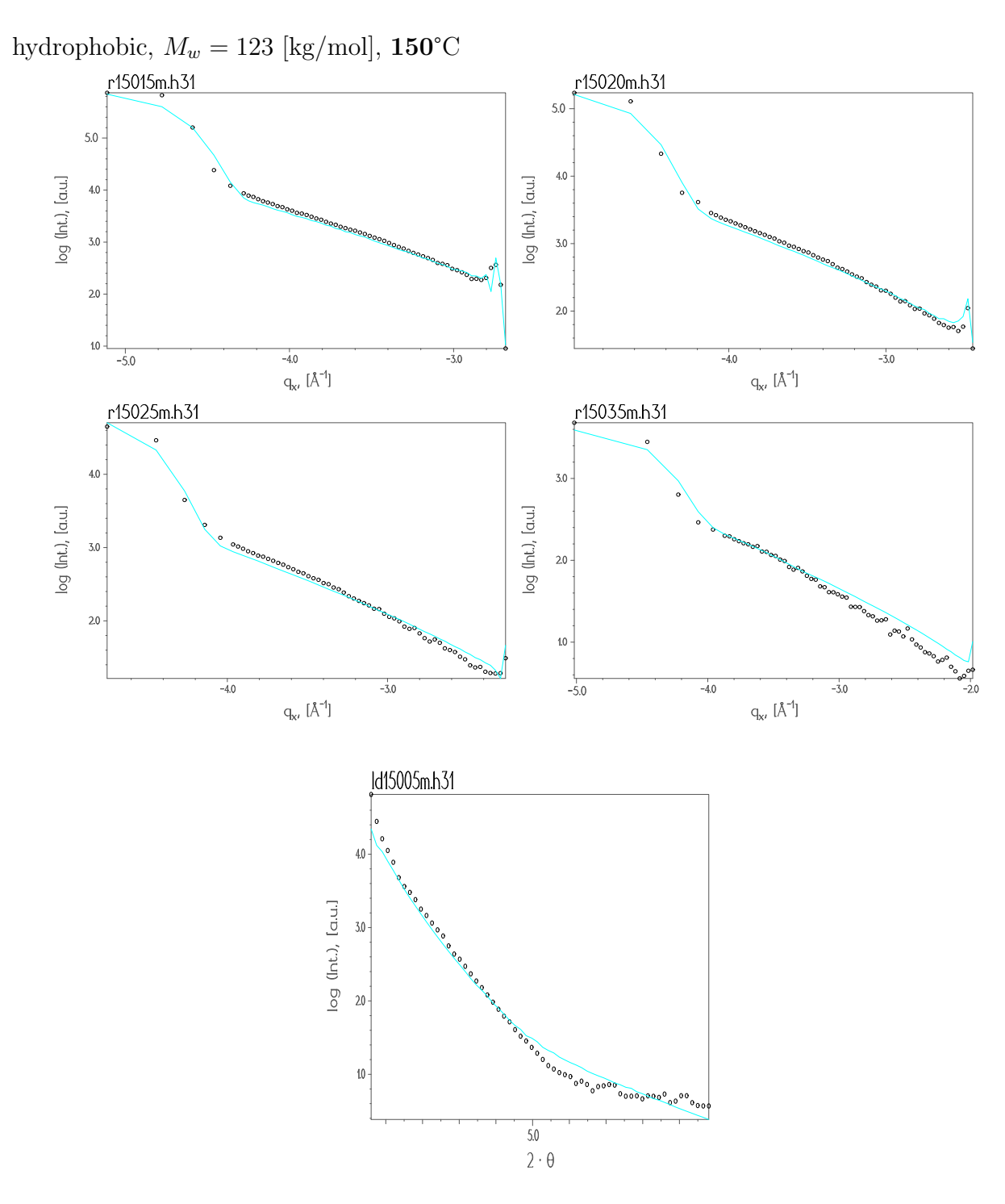


Figure A.39: Longitudinal and transverse scans of sample h31 at 150° C refined with the Liquid model. The curves with the symbols are the experimental data and the lines are the fits.

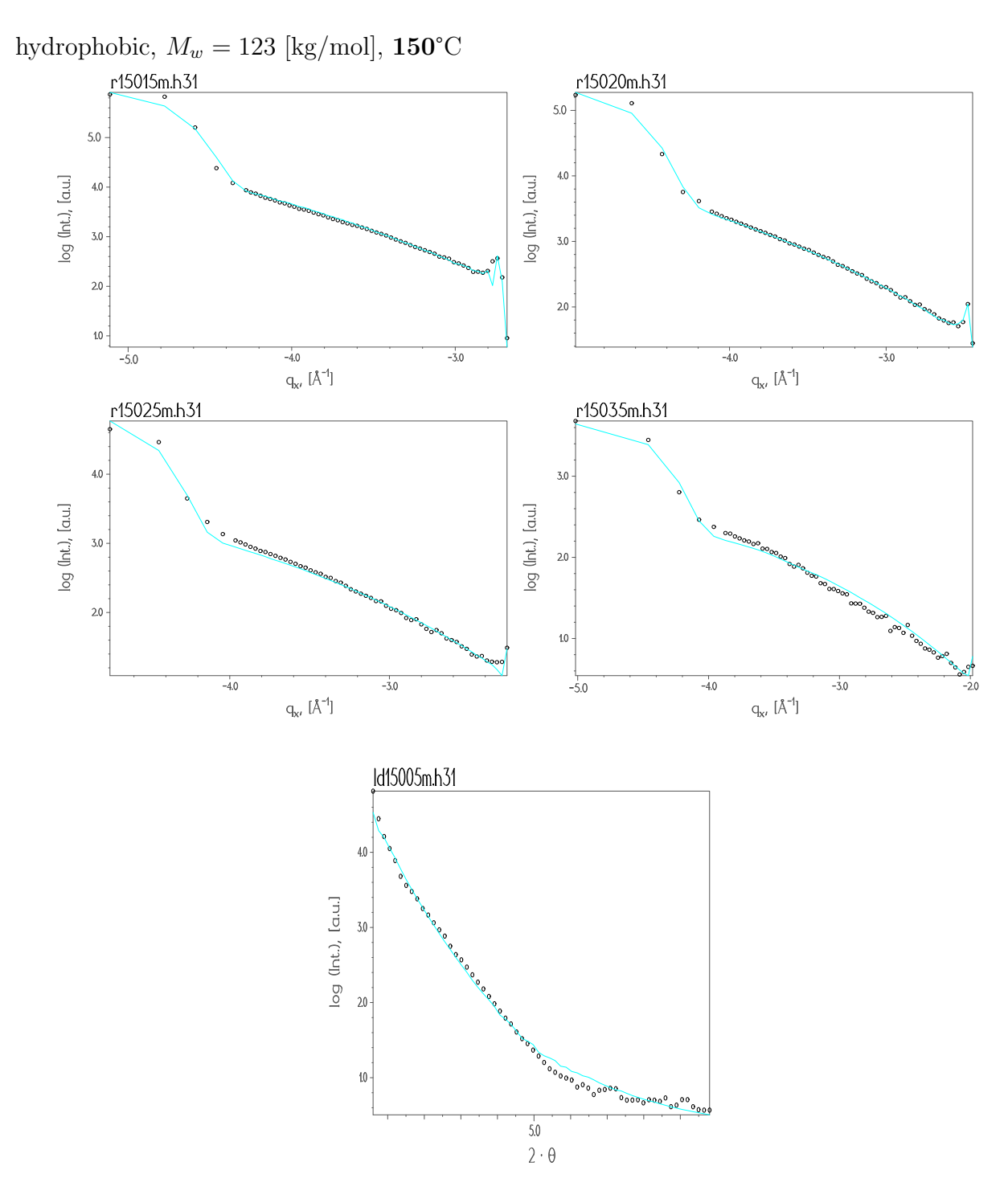


Figure A.40: Longitudinal and transverse scans of sample **h31** at **150°**C refined with the *Fractal model*. The curves with the symbols are the experimental data and the lines are the fits.

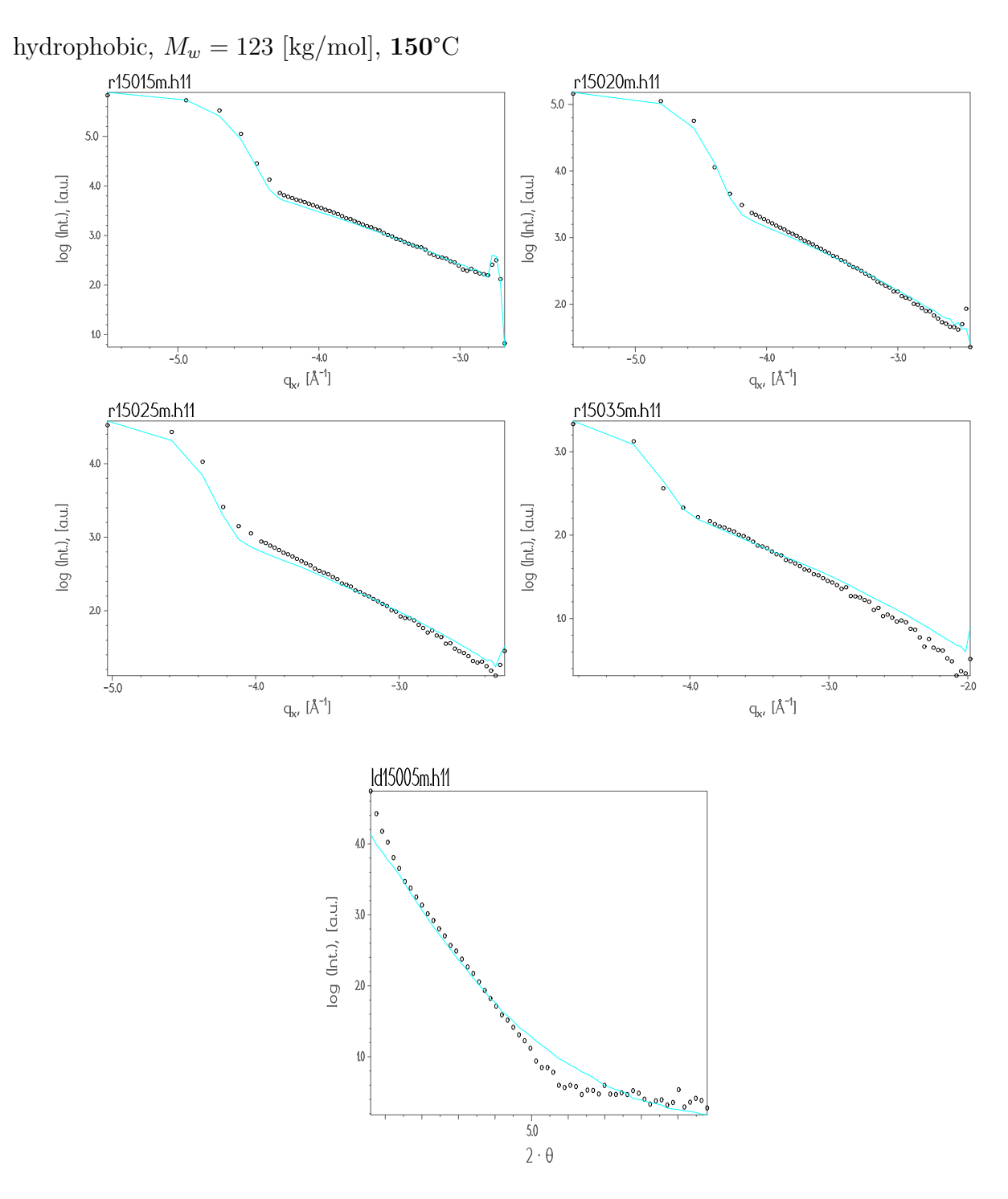


Figure A.41: Longitudinal and transverse scans of sample h11 at 150° C refined with the Liquid model. The curves with the symbols are the experimental data and the lines are the fits.

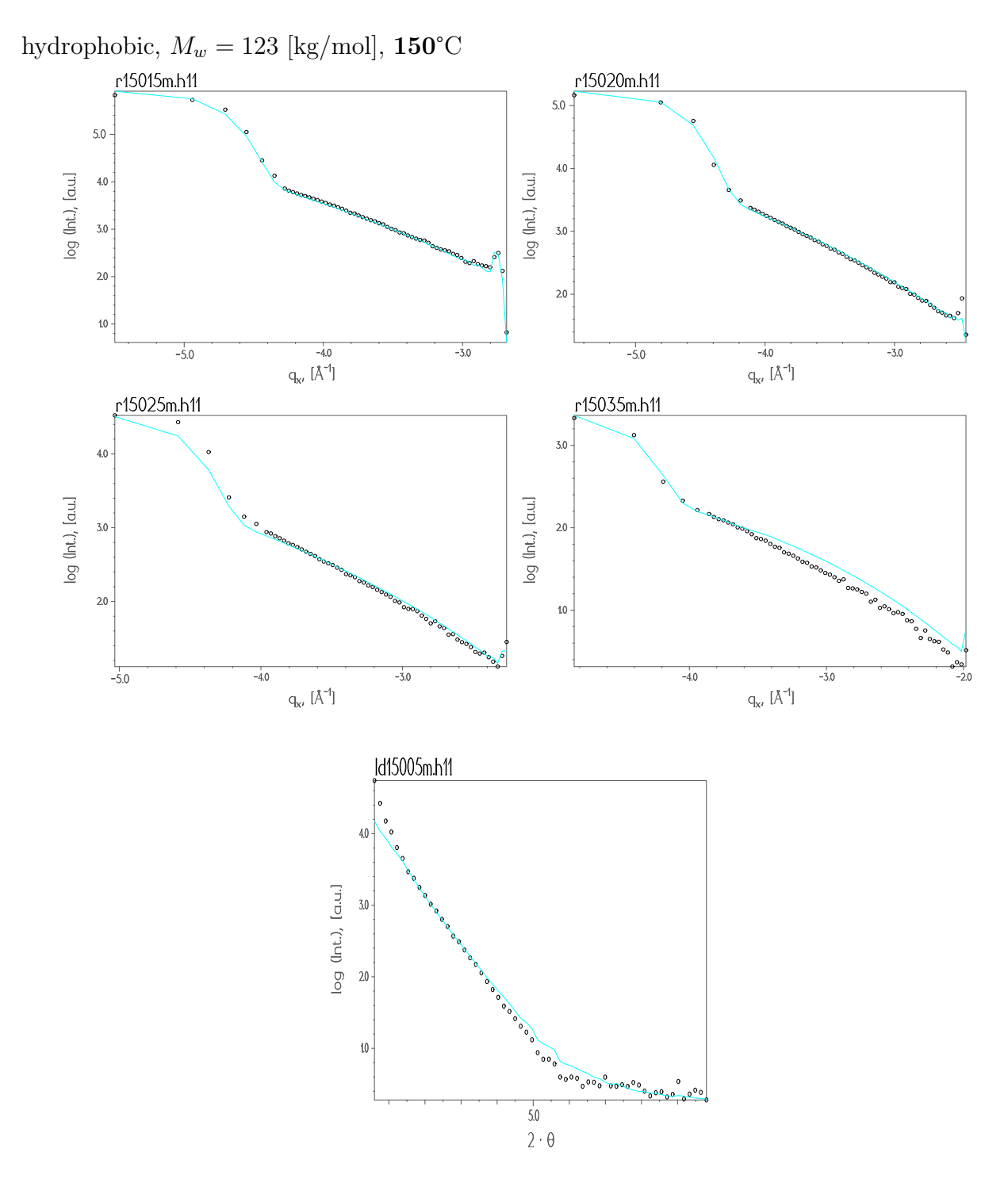


Figure A.42: Longitudinal and transverse scans of sample **h11** at **150**°C refined with the *Fractal model*. The curves with the symbols are the experimental data and the lines are the fits.

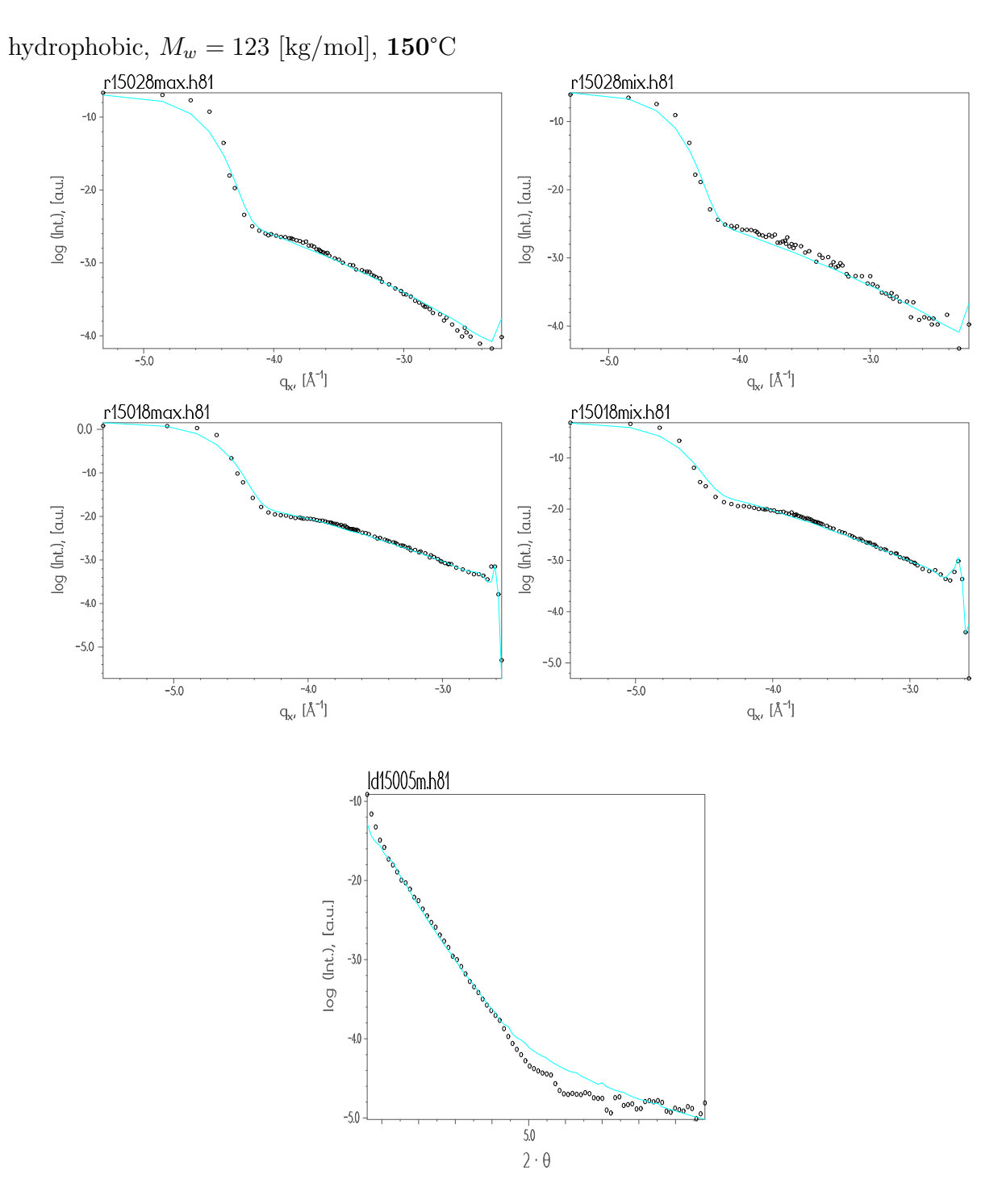


Figure A.43: Longitudinal and transverse scans of sample h81 at 150° C refined with the Liquid model. The curves with the symbols are the experimental data and the lines are the fits.

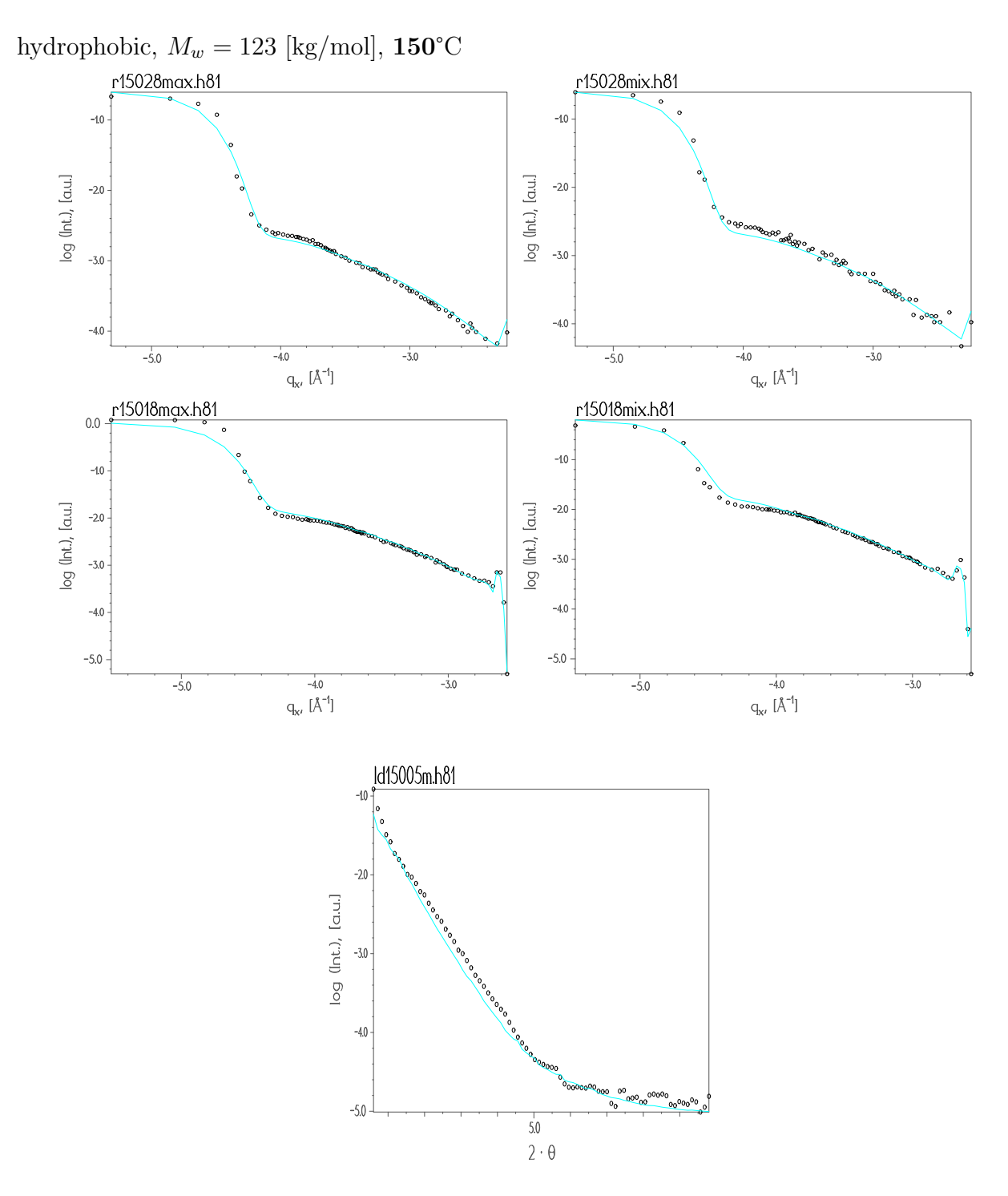


Figure A.44: Longitudinal and transverse scans of sample **h81** at **150**°C refined with the *Fractal model*. The curves with the symbols are the experimental data and the lines are the fits.

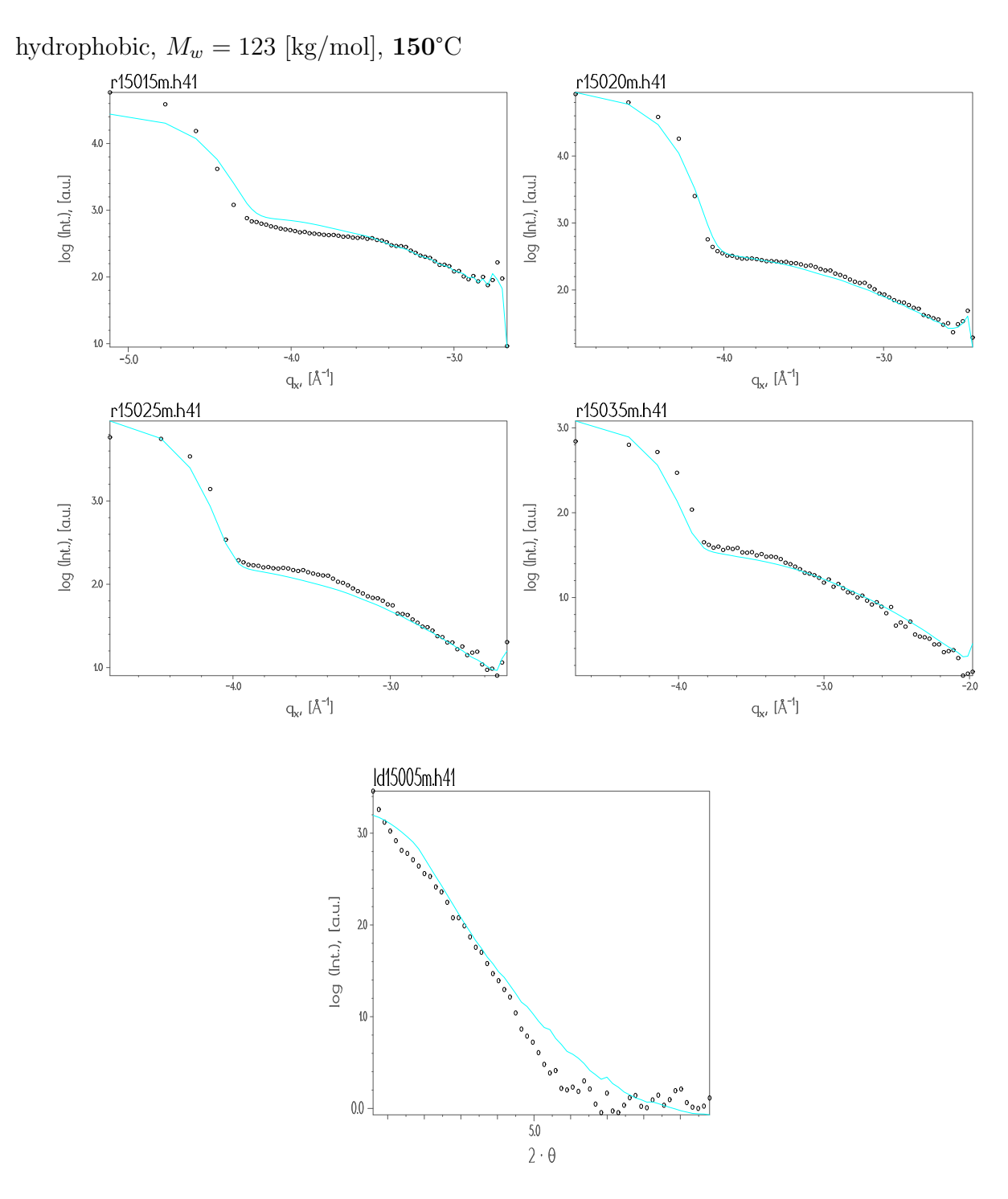


Figure A.45: Longitudinal and transverse scans of sample h41 at 150° C refined with the Liquid model. The curves with the symbols are the experimental data and the lines are the fits.

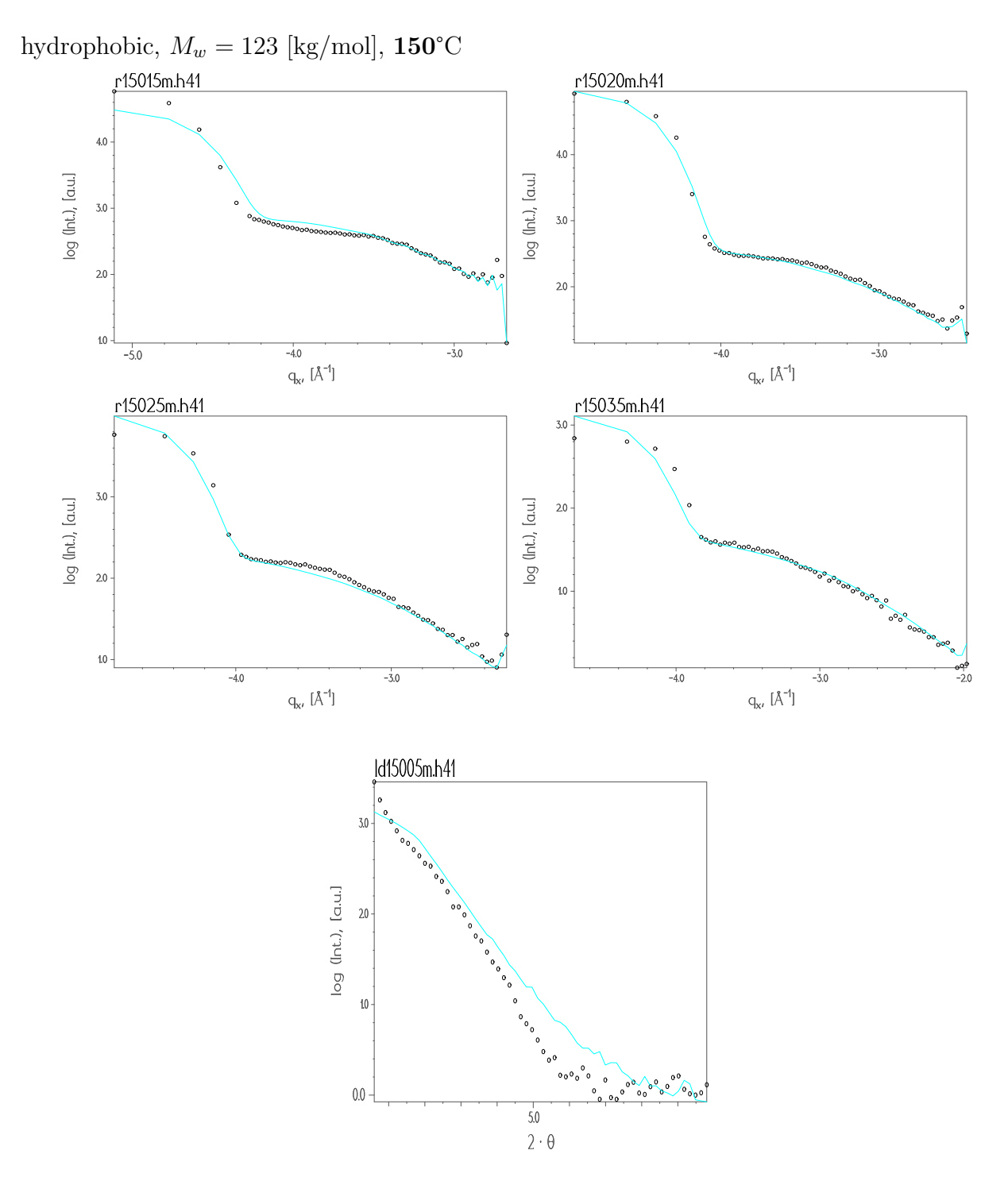


Figure A.46: Longitudinal and transverse scans of sample **h41** at **150**°C refined with the *Fractal model*. The curves with the symbols are the experimental data and the lines are the fits.

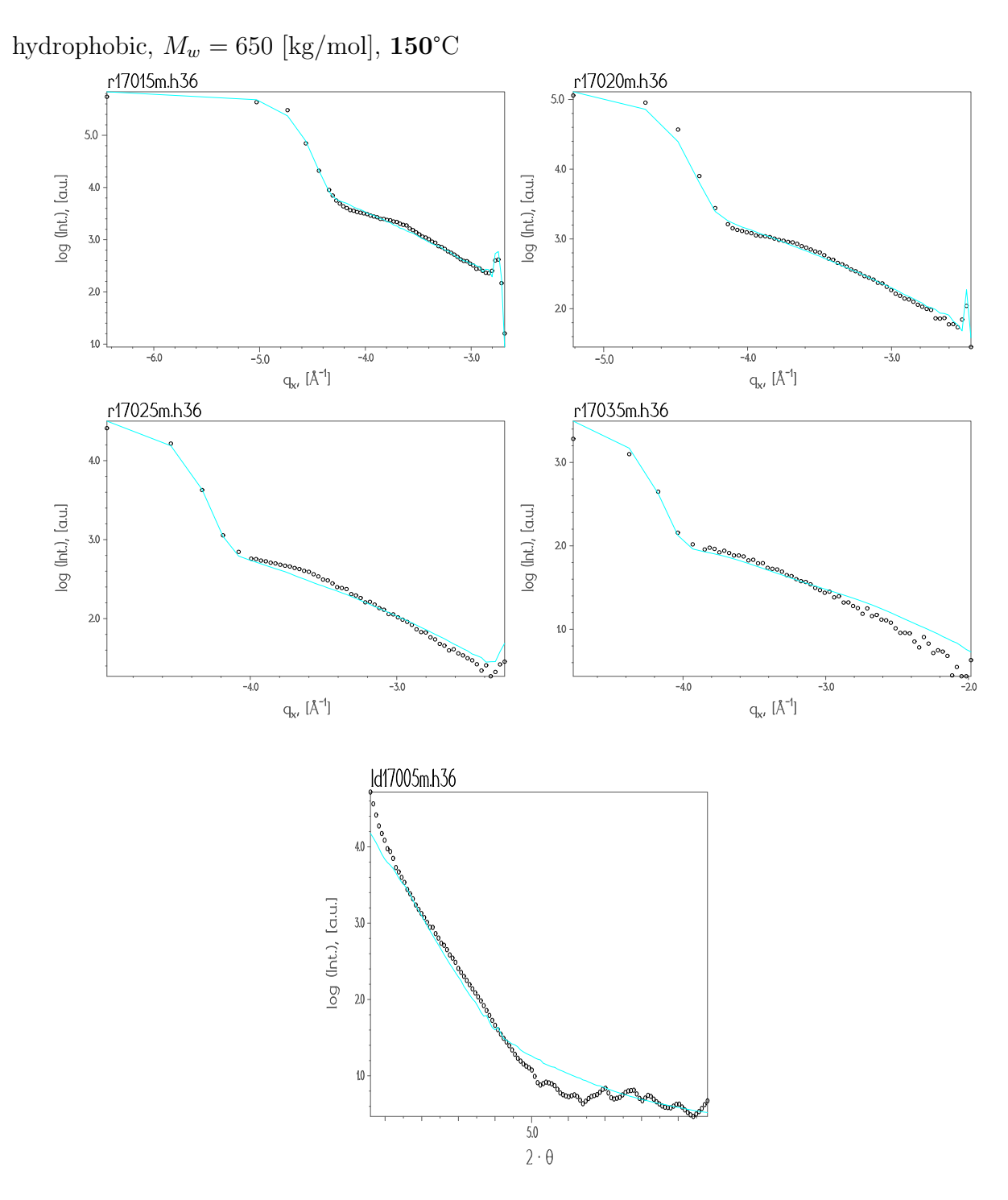


Figure A.47: Longitudinal and transverse scans of sample **h36** at **170**°C refined with the *Liquid model*. The curves with the symbols are the experimental data and the lines are the fits.

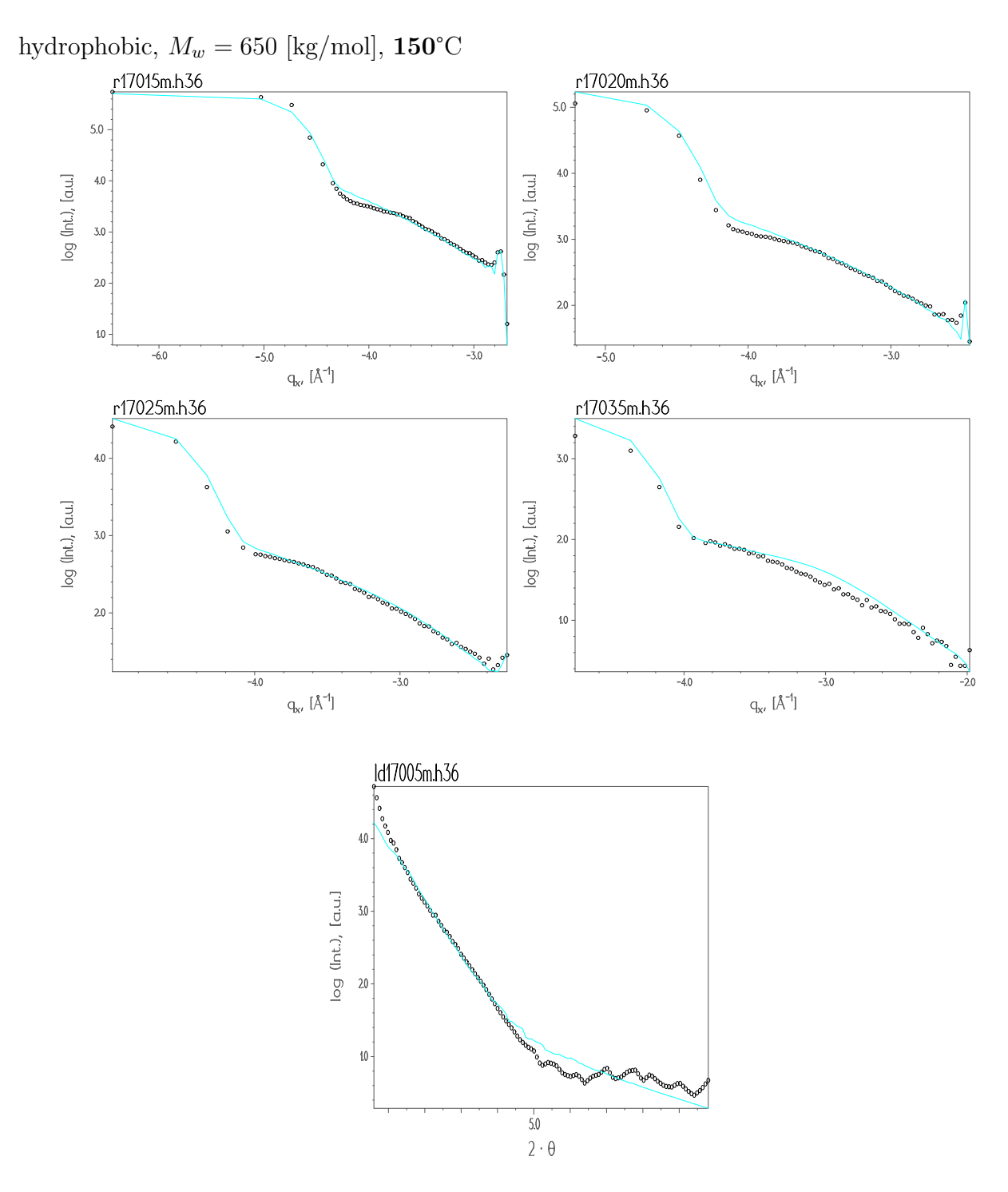


Figure A.48: Longitudinal and transverse scans of sample **h36** at **170**°C refined with the *Fractal model*. The curves with the symbols are the experimental data and the lines are the fits.

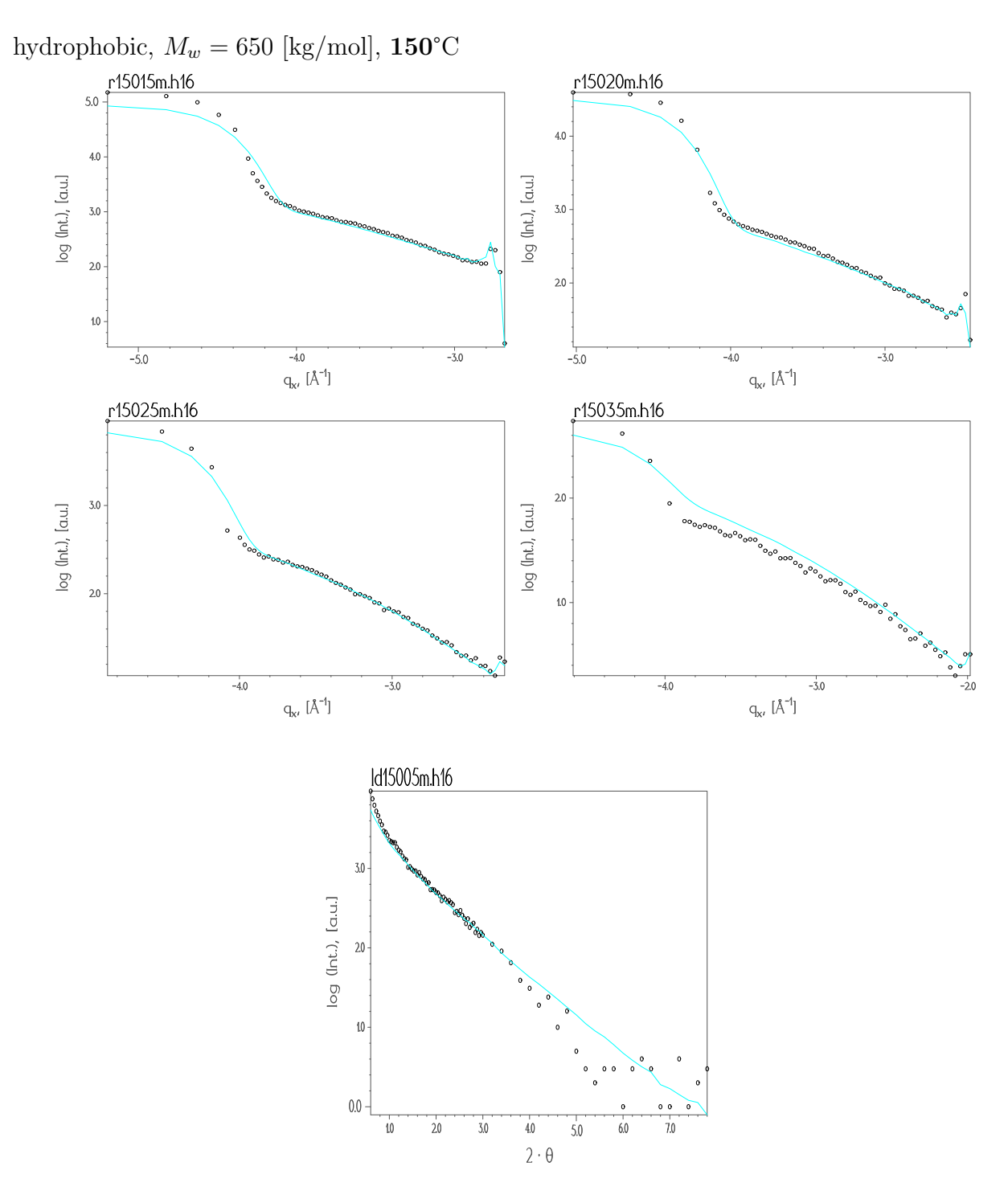


Figure A.49: Longitudinal and transverse scans of sample h16 at 150° C refined with the Liquid model. The curves with the symbols are the experimental data and the lines are the fits.

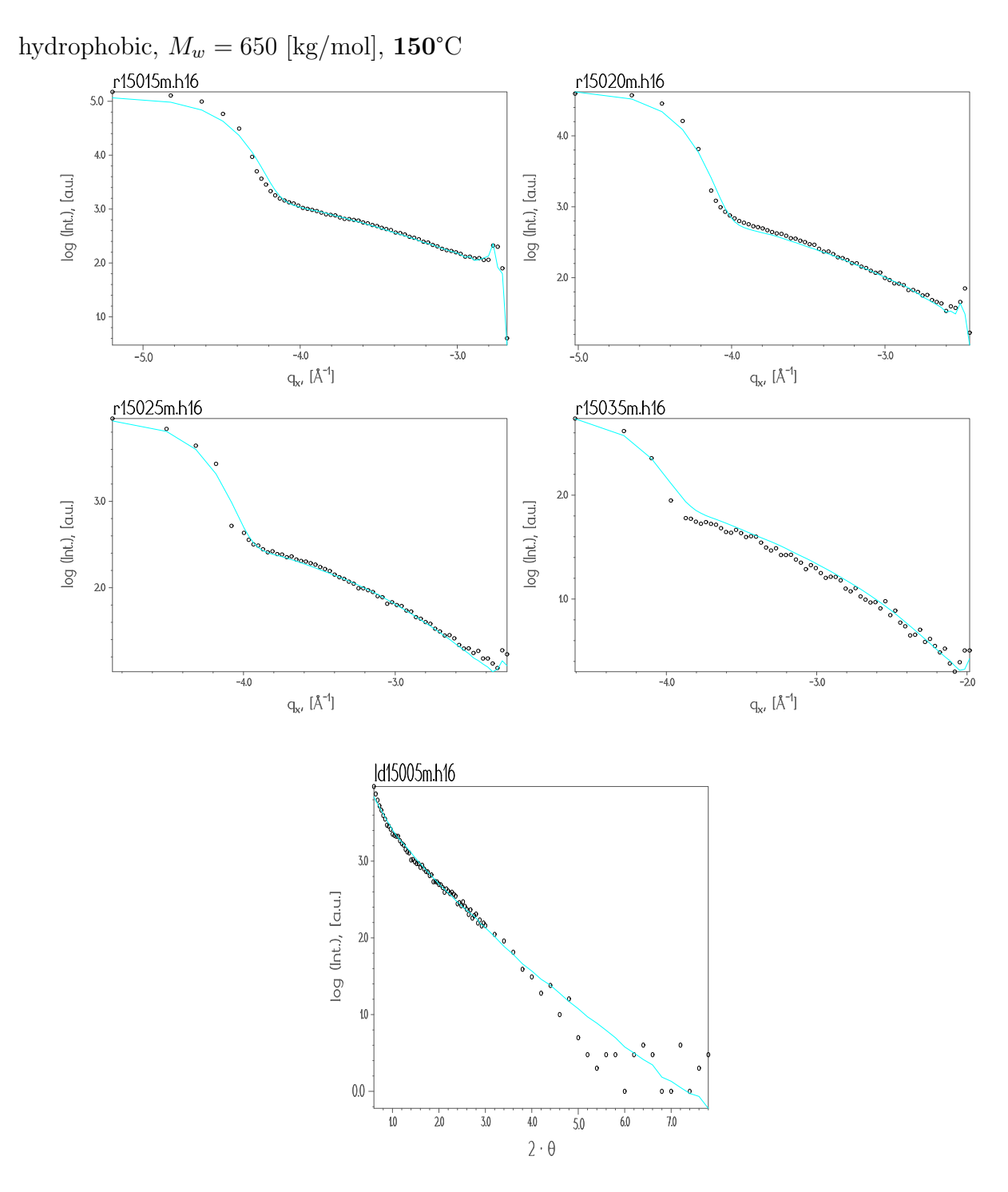


Figure A.50: Longitudinal and transverse scans of sample h16 at 150° C refined with the Fractal model. The curves with the symbols are the experimental data and the lines are the fits.

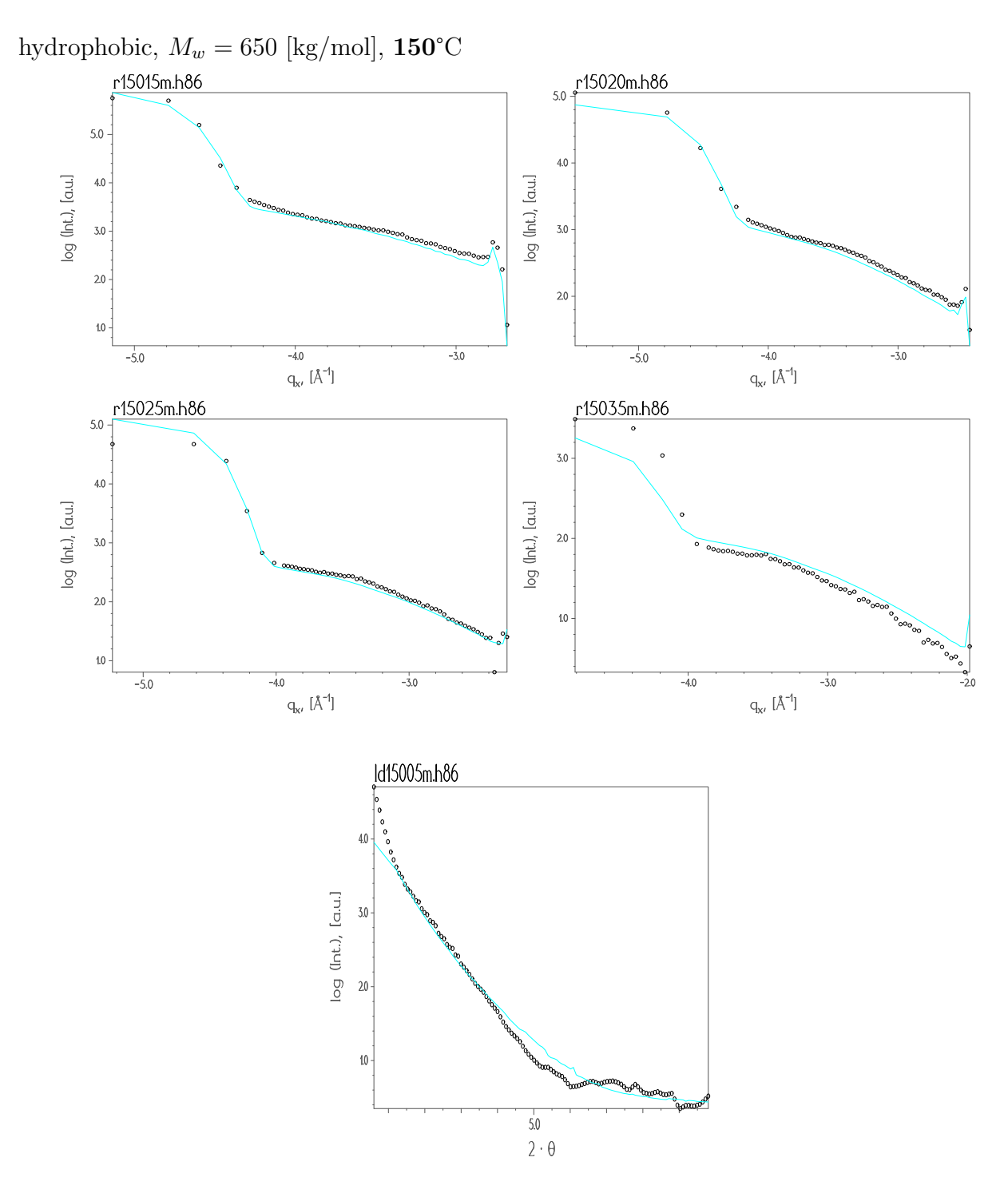


Figure A.51: Longitudinal and transverse scans of sample h86 at 150° C refined with the Liquid model. The curves with the symbols are the experimental data and the lines are the fits.

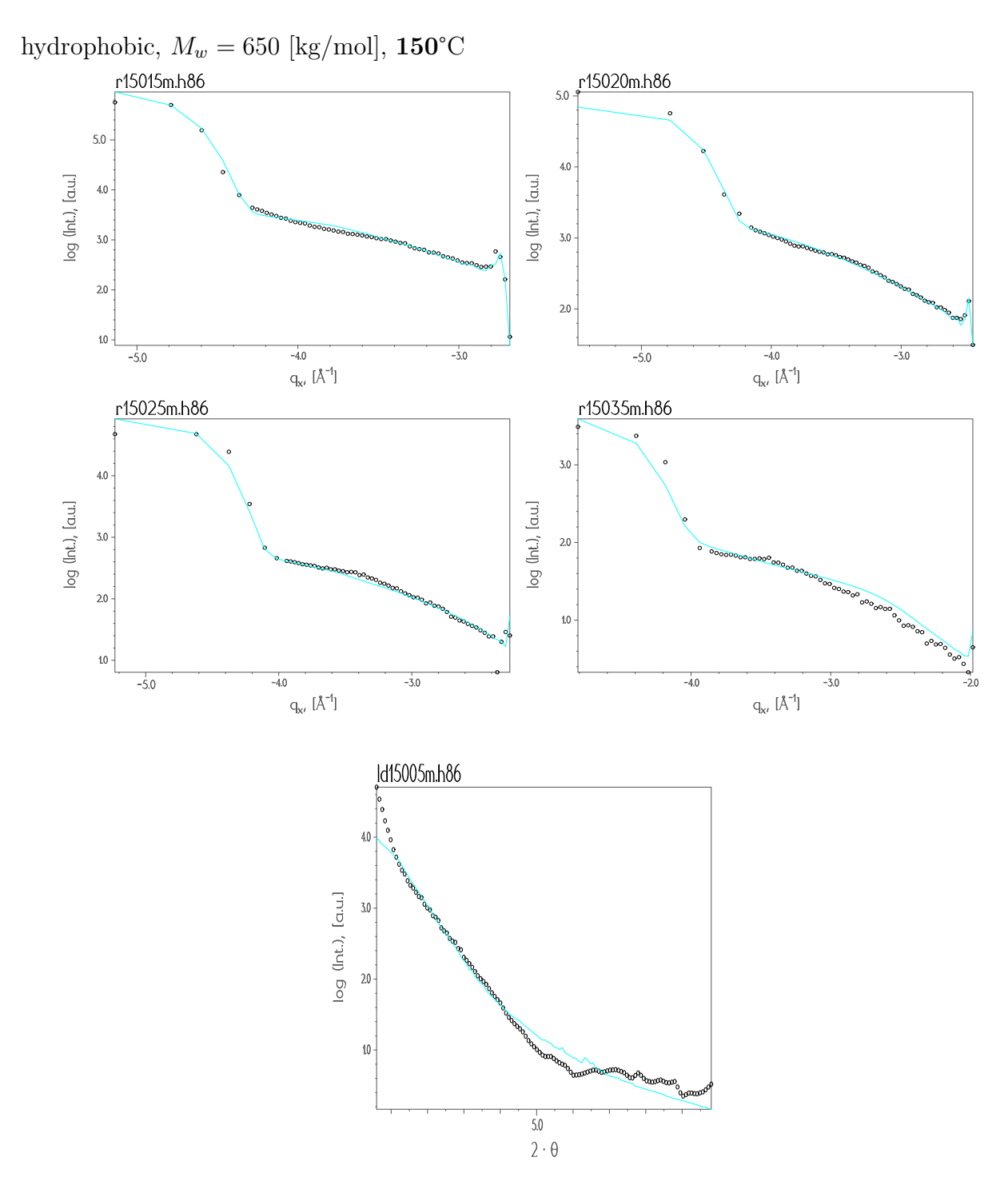


Figure A.52: Longitudinal and transverse scans of sample **h86** at **150**°C refined with the *Fractal model*. The curves with the symbols are the experimental data and the lines are the fits.

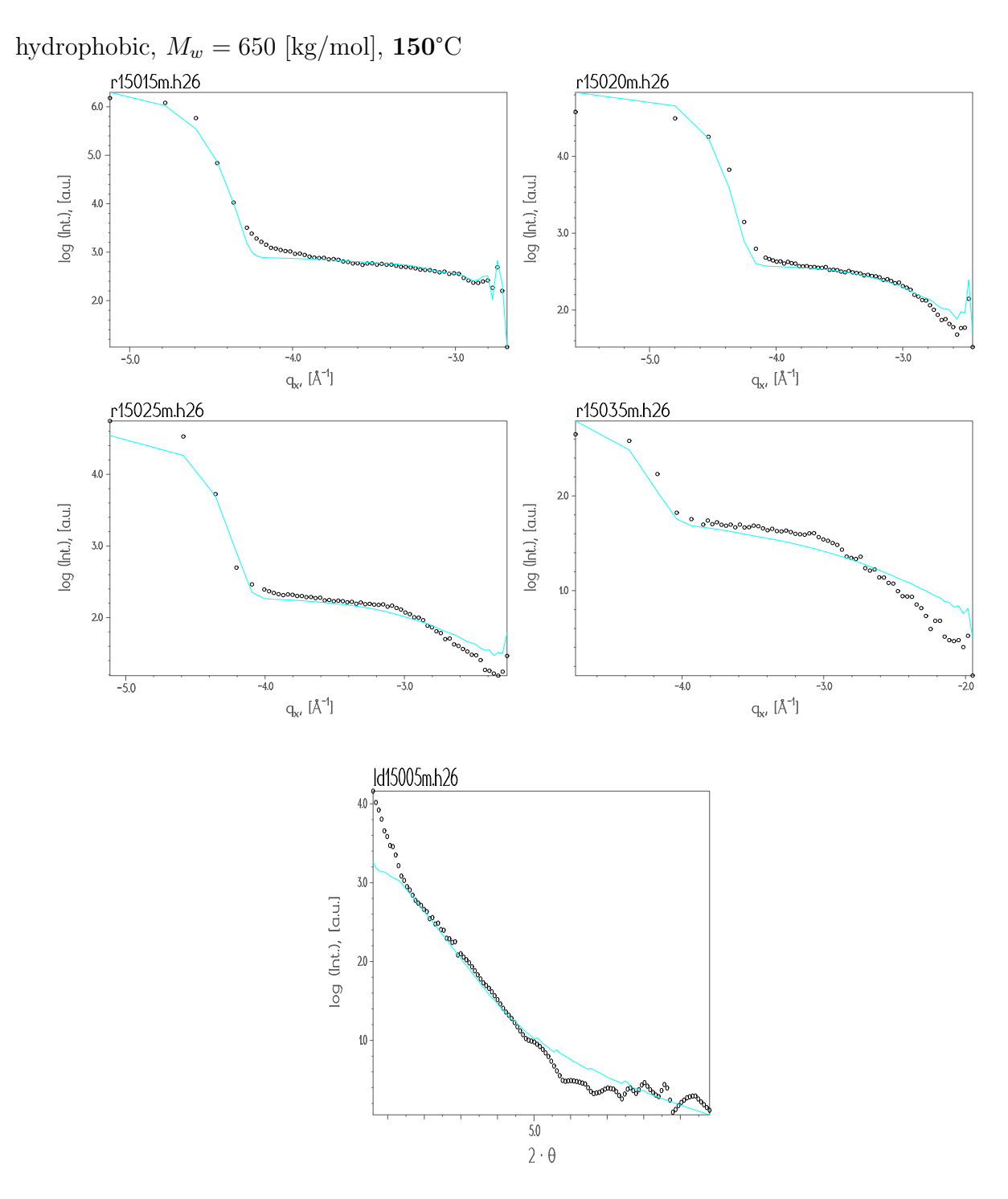


Figure A.53: Longitudinal and transverse scans of sample h26 at 150° C refined with the Liquid model. The curves with the symbols are the experimental data and the lines are the fits.

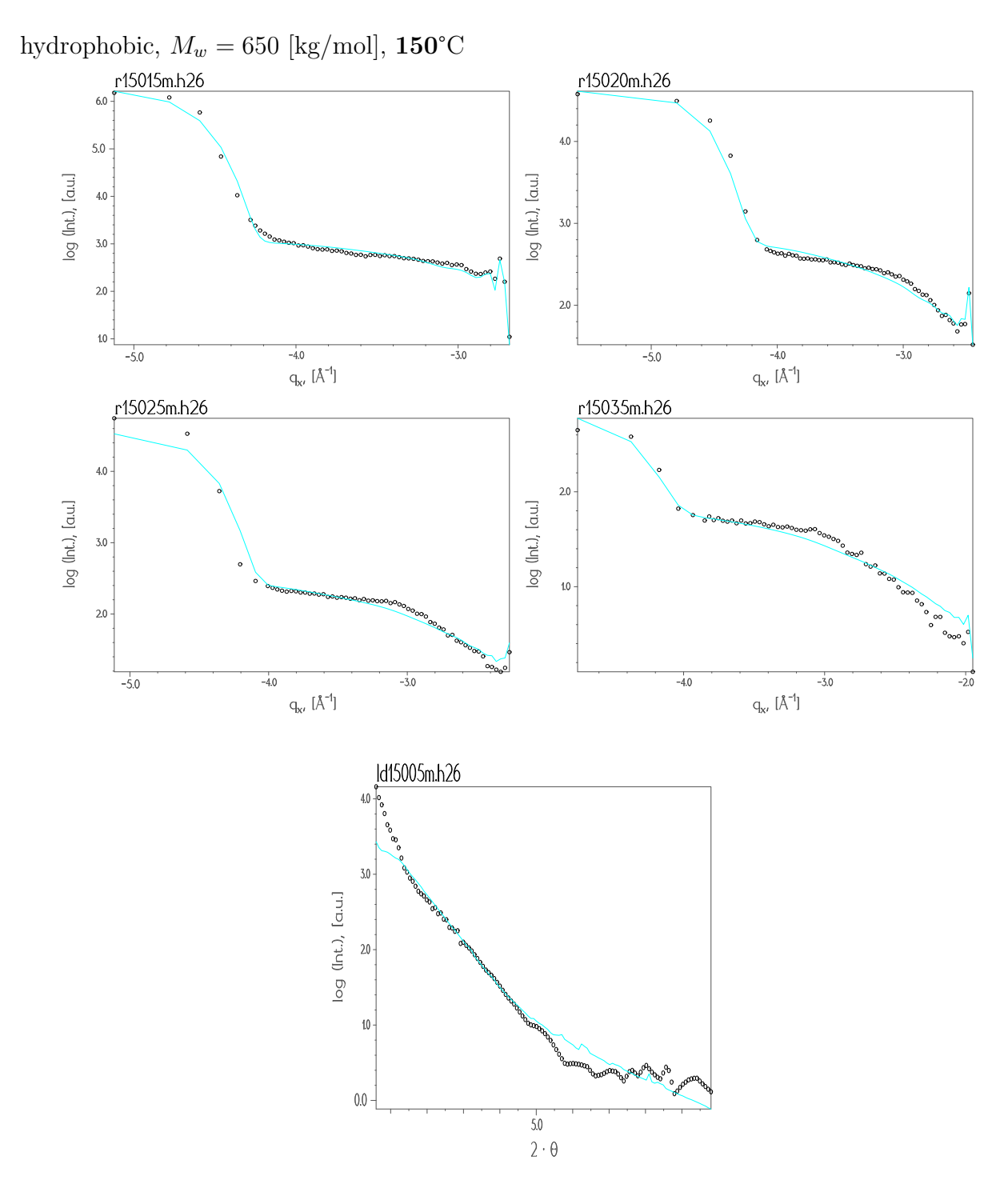


Figure A.54: Longitudinal and transverse scans of sample **h26** at **150**°C refined with the *Fractal model*. The curves with the symbols are the experimental data and the lines are the fits.

Sample	Correlation length	Hurst parameter	Correlation length	Hurst parameter
number	of the substrate,	of the substrate,	of the first layer,	of the first layer
	$\xi_{sub}\cdot 10^3, [{ m \AA}]$	h_{sub}	$\xi_{SiO_x} \cdot 10^3$, [Å]	h_{SiO_x}
h26	0.011 ± 0.003	$0.20^{(f)}$	0.011 ± 0.001	0.442 ± 0.002
h46	_	_	_	_
h86	0.352 ± 0.005	$0.79^{(f)}$	0.770 ± 0.006	$0.25^{(f)}$
h16	0.708 ± 0.009	$0.50^{(f)}$	1.630 ± 0.001	$0.25^{(f)}$
h36	$0.10^{(f)}$	$0.79^{(f)}$	0.844 ± 0.004	$0.25^{(f)}$
h21	_	_	_	_
h41	0.8989 ± 0.0001	$0.30^{(f)}$	0.7945 ± 0.0001	0.3424 ± 0.0001
h81	1.283 ± 0.004	$0.20^{(f)}$	1.107 ± 0.002	$0.20^{(f)}$
h11	0.930 ± 0.003	$0.20^{(f)}$	4.995 ± 0.002	$0.20^{(f)}$
h31	26.83 ± 0.02	$0.2^{(f)}$	4.969 ± 0.008	$0.20^{(f)}$
h23	_	_	_	_
h43	0.013 ± 0.001	$0.58^{(f)}$	0.1938 ± 0.0002	$0.20^{(f)}$
h83	0.128 ± 0.006	$0.30^{(f)}$	0.134 ± 0.001	$0.20^{(f)}$
h13	$0.10^{(f)}$	$0.58^{(f)}$	$0.10^{(f)}$	$0.20^{(f)}$
h33	0.1578 ± 0.0009	$0.30^{(f)}$	0.1762 ± 0.0009	$0.20^{(f)}$

Table A.8: Correlation length and Hurst parameter of the substrate and the first layer obtained after the refinement of diffuse scattering curves measured at 150°C (*Liquid model*).

Sample	Surface tension,	χ^2
number	$\eta, [N/m]$	
h26	0.0144 ± 0.0003	9.82
h46	_	_
h86	0.013 ± 0.001	6.95
h16	0.0095 ± 0.0001	4.30
h36	0.0164 ± 0.0003	5.24
h21	_	_
h41	0.01628 ± 0.00007	3.86
h81	0.02186 ± 0.00007	5.01
h11	0.01798 ± 0.0001	4.30
h31	0.0235 ± 0.0001	3.52
h23	_	_
h43	0.0149 ± 0.0001	9.84
h83	0.0228 ± 0.0001	9.39
h13	0.0173 ± 0.0001	3.44
h33	0.0201 ± 0.0001	5.36

Table A.9: Surface tension at the polymer/air interface and χ^2 obtained from refinements of diffuse scattering curves measured at 150°C (*Liquid model*).

Sample	Correlation length	Hurst parameter	Correlation length	Hurst parameter
number	of the substrate,	of the substrate,	of the first layer,	of the first layer
	$\xi_{sub} \cdot 10^3$,[Å]	h_{sub}	$\xi_{SiO_x} \cdot 10^3$, [Å]	h_{SiO_x}
h26	0.206 ± 0.001	$0.20^{(f)}$	0.047 ± 0.001	$0.23^{(f)}$
h46	_	_	_	_
h86	0.588 ± 0.007	0.947 ± 0.009	1.741 ± 0.006	$0.20^{(f)}$
h16	$1.0^{(f)}$	$0.50^{(f)}$	$1.6^{(f)}$	$0.25^{(f)}$
h36	1.06 ± 0.03	0.40 ± 0.03	0.34 ± 0.02	0.25 ± 0.03
h21	_	_	_	_
h41	1.470 ± 0.002	0.760 ± 0.003	0.8335 ± 0.0003	0.2240 ± 0.0005
h81	$0.10^{(f)}$	0.206 ± 0.001	0.7581 ± 0.0004	$0.19^{(f)}$
h11	0.1514 ± 0.0003	$0.40^{(f)}$	$0.10^{(f)}$	$0.20^{(f)}$
h31	8.727 ± 0.005	$0.20^{(f)}$	1.084 ± 0.004	$0.20^{(f)}$
h23	_	_	_	_
h43	0.1087 ± 0.0006	$0.20^{(f)}$	$0.10^{(f)}$	$0.20^{(f)}$
h83	0.100 ± 0.001	$0.20^{(f)}$	2.616 ± 0.004	$0.20^{(f)}$
h13	$0.10^{(f)}$	$0.20^{(f)}$	$0.10^{(f)}$	$0.20^{(f)}$
h33	$0.10^{(f)}$	$0.20^{(f)}$	$0.10^{(f)}$	$0.20^{(f)}$

Table A.10: Correlation length and Hurst parameter of the substrate and the first layer obtained after the refinement of diffuse scattering curves measured at 150°C (*Fractal model*).

Sample	Correlation length	Hurst parameter of	Roughness of	
number	of the polym. film,	the polym. film,	the polym. film,	χ^2
	$\xi_{PS} \cdot 10^3, [\text{Å}]$	h_{PS}	$\sigma_{PS},~ [{ m \AA}]$	
h26	0.2865 ± 0.0006	$0.23^{(f)}$	$5.30^{(f)}$	6.48
h46	_	_	_	-
h86	0.826 ± 0.006	$0.20^{(f)}$	$6.83^{(f)}$	5.24
h16	10.60 ± 0.05	0.23 ± 0.01	$10.59^{(f)}$	3.78
h36	10.28 ± 0.02	$0.20^{(f)}$	$7.79^{(f)}$	6.13
h21	_	_	_	_
h41	0.985 ± 0.001	0.2962 ± 0.0003	5.778 ± 0.001	3.52
h81	5.433 ± 0.003	0.2821 ± 0.0007	$7.20^{(f)}$	3.42
h11	21.00 ± 0.01	$0.20^{(f)}$	7.230 ± 0.009	2.77
h31	16.881 ± 0.004	$0.20^{(f)}$	7.890 ± 0.002	1.50
h23	_	_	_	_
h43	12.959 ± 0.004	$0.20^{(f)}$	7.784 ± 0.001	4.84
h83	5.271 ± 0.001	$0.20^{(f)}$	6.102 ± 0.001	9.71
h13	5.818 ± 0.001	$0.20^{(f)}$	7.315 ± 0.001	2.02
h33	17.5151 ± 0.0005	$0.20^{(f)}$	8.3139 ± 0.0001	2.60

Table A.11: Correlation length, Hurst parameter and roughness of the polymer film as well as χ^2 obtained from refinements of diffuse scattering curves measured at 150°C (*Fractal model*).

Samples h36, h83, h33 were measured at 170° C.

A.2.2 Samples studied at $230^{\circ}C$

A.2.2.1 Hydrophilic samples

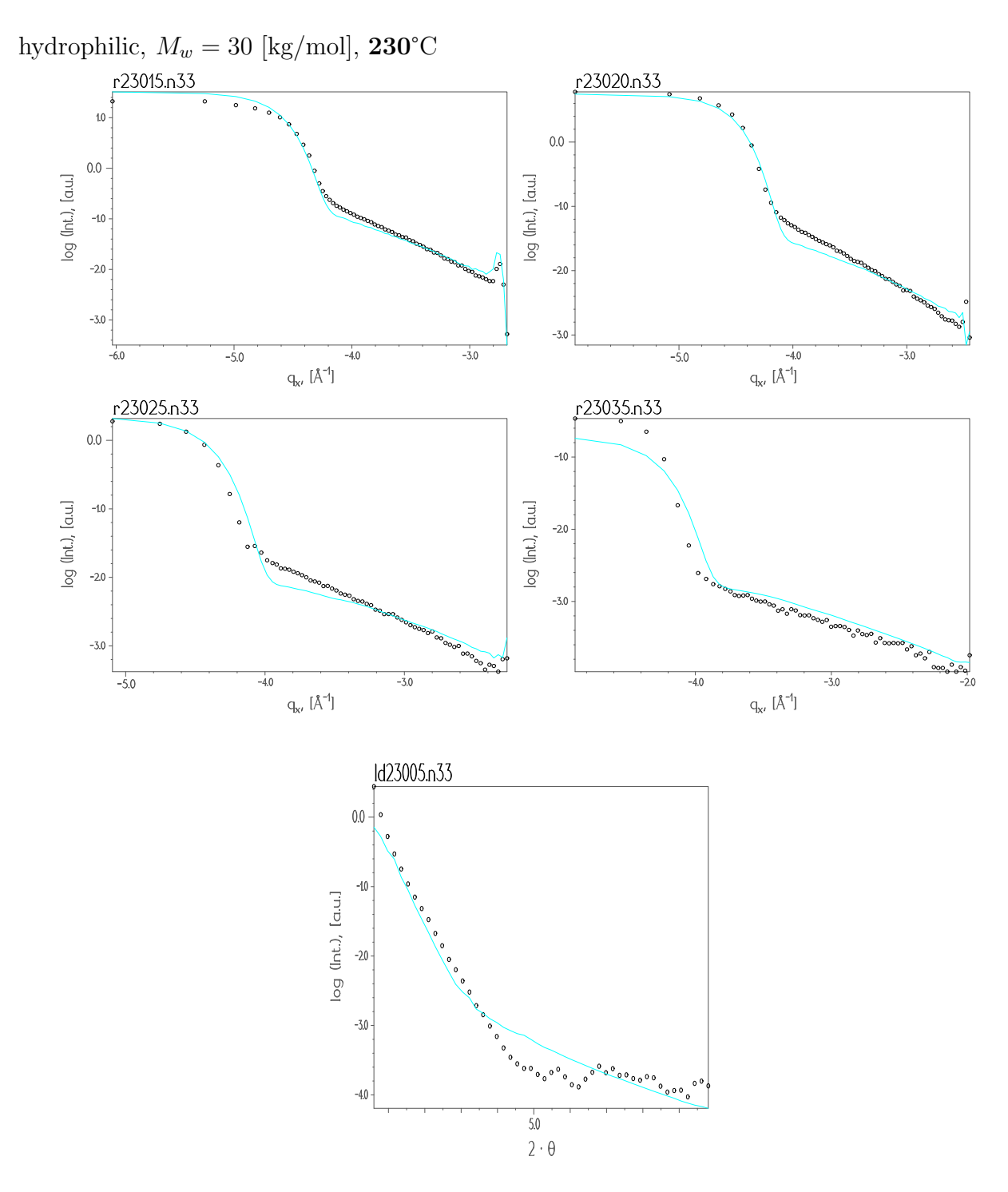


Figure A.55: Longitudinal and transverse scans of sample n33 at 230° C refined with the Liquid model. The curves with the symbols are the experimental data and the lines are the fits.

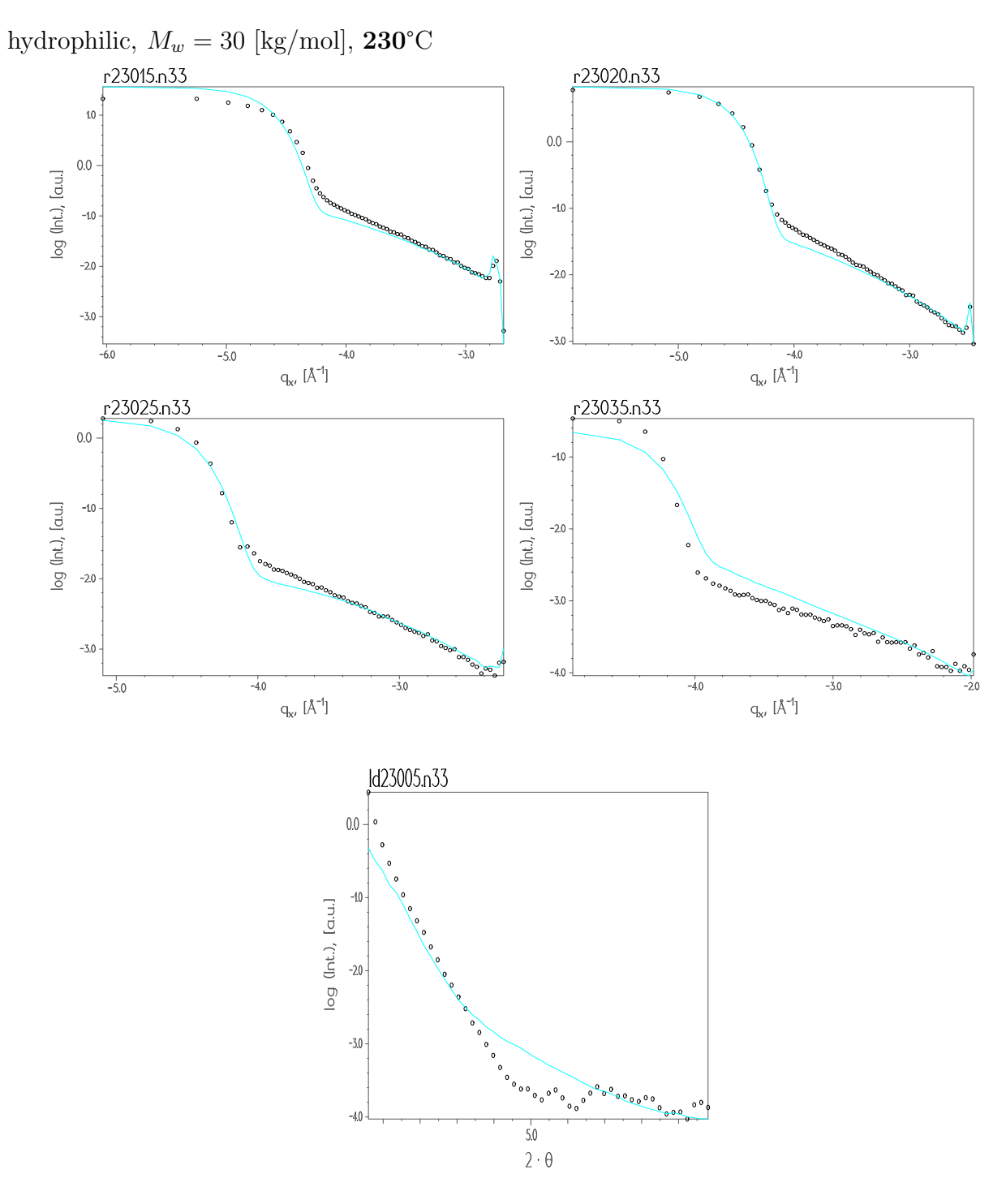


Figure A.56: Longitudinal and transverse scans of sample **n33** at **230**°C refined with the *Fractal model*. The curves with the symbols are the experimental data and the lines are the fits.

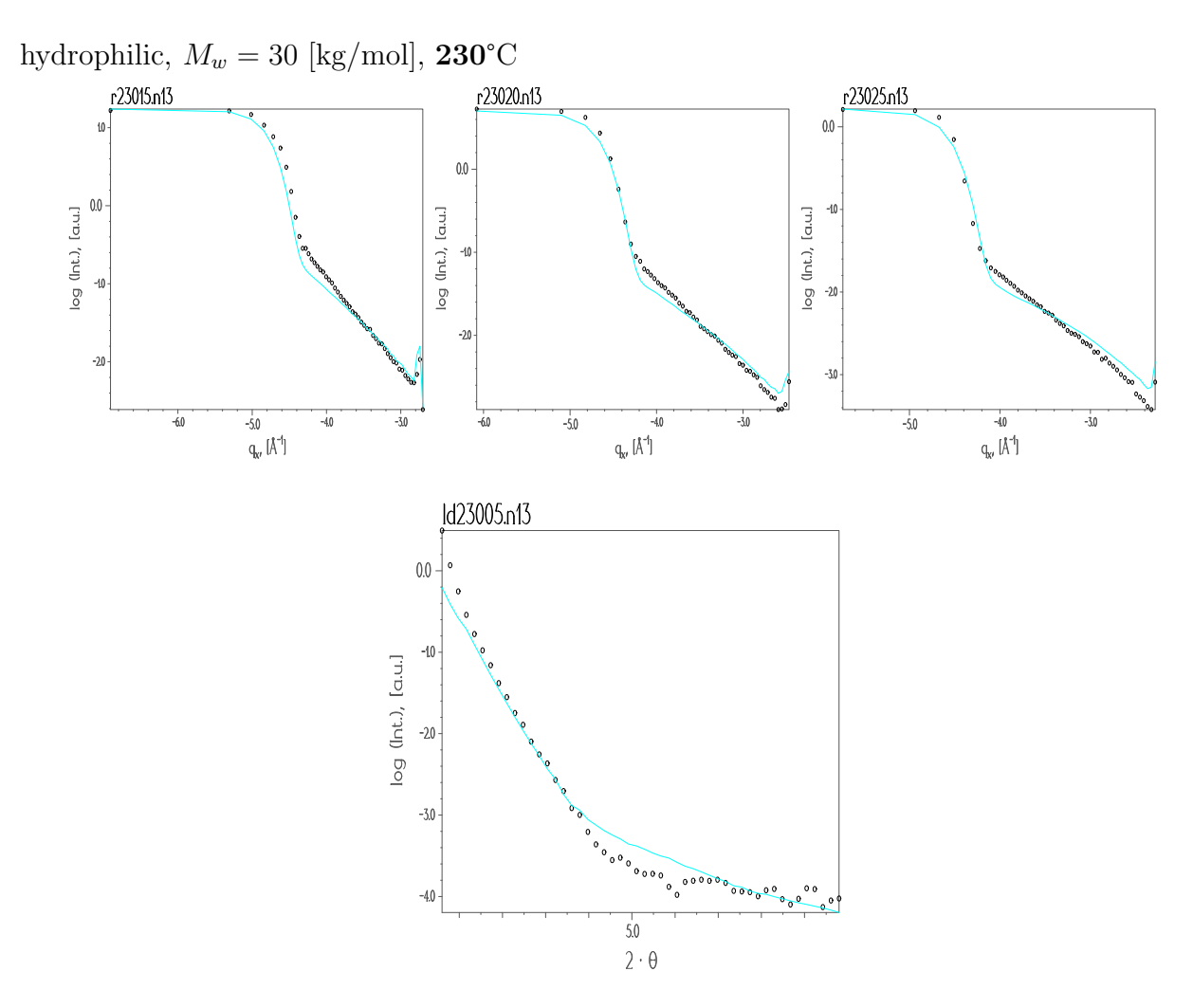


Figure A.57: Longitudinal and transverse scans of sample n13 at 230° C refined with the Liquid model. The curves with the symbols are the experimental data and the lines are the fits.

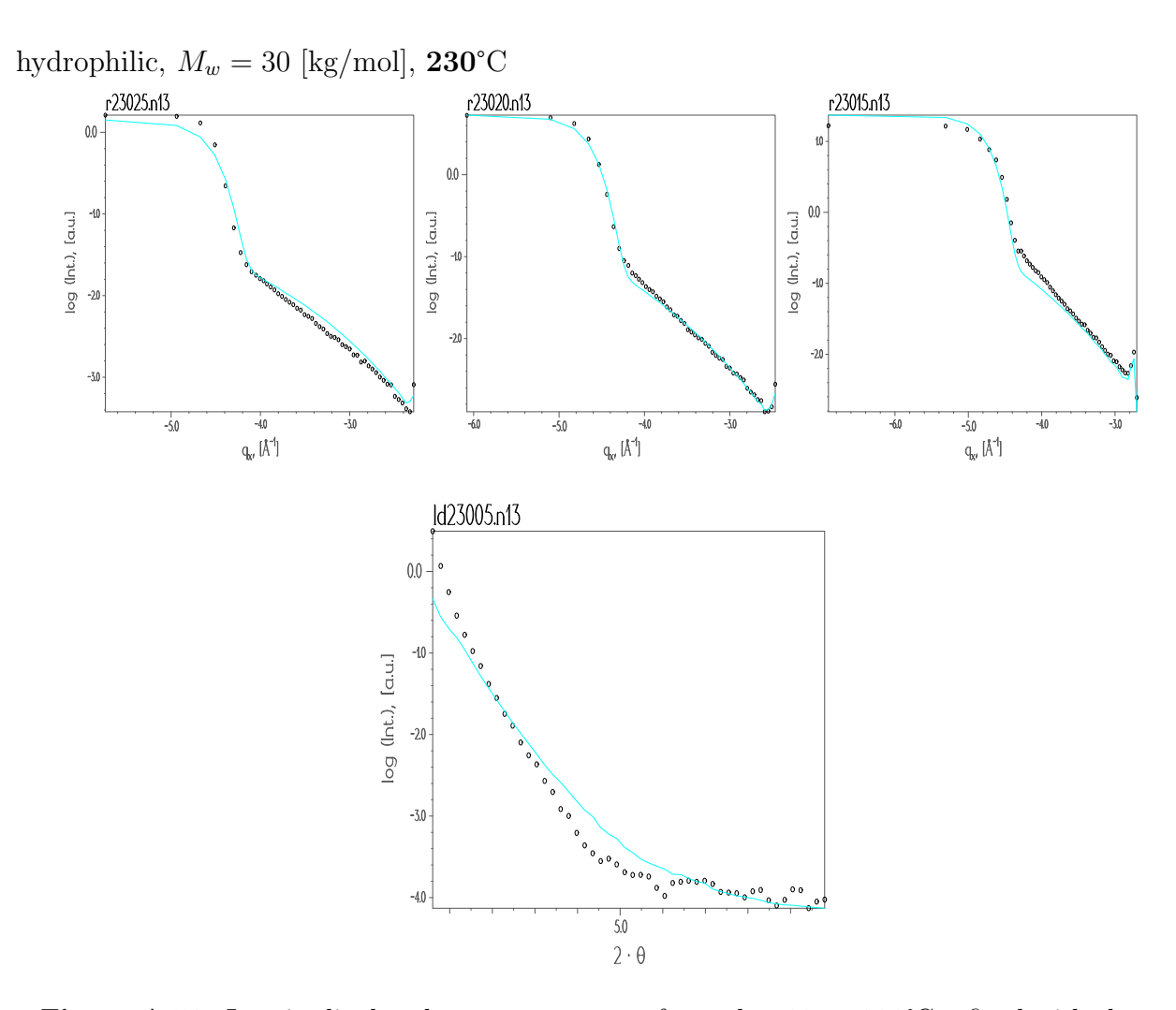


Figure A.58: Longitudinal and transverse scans of sample **n13** at **230**°C refined with the *Fractal model*. The curves with the symbols are the experimental data and the lines are the fits.

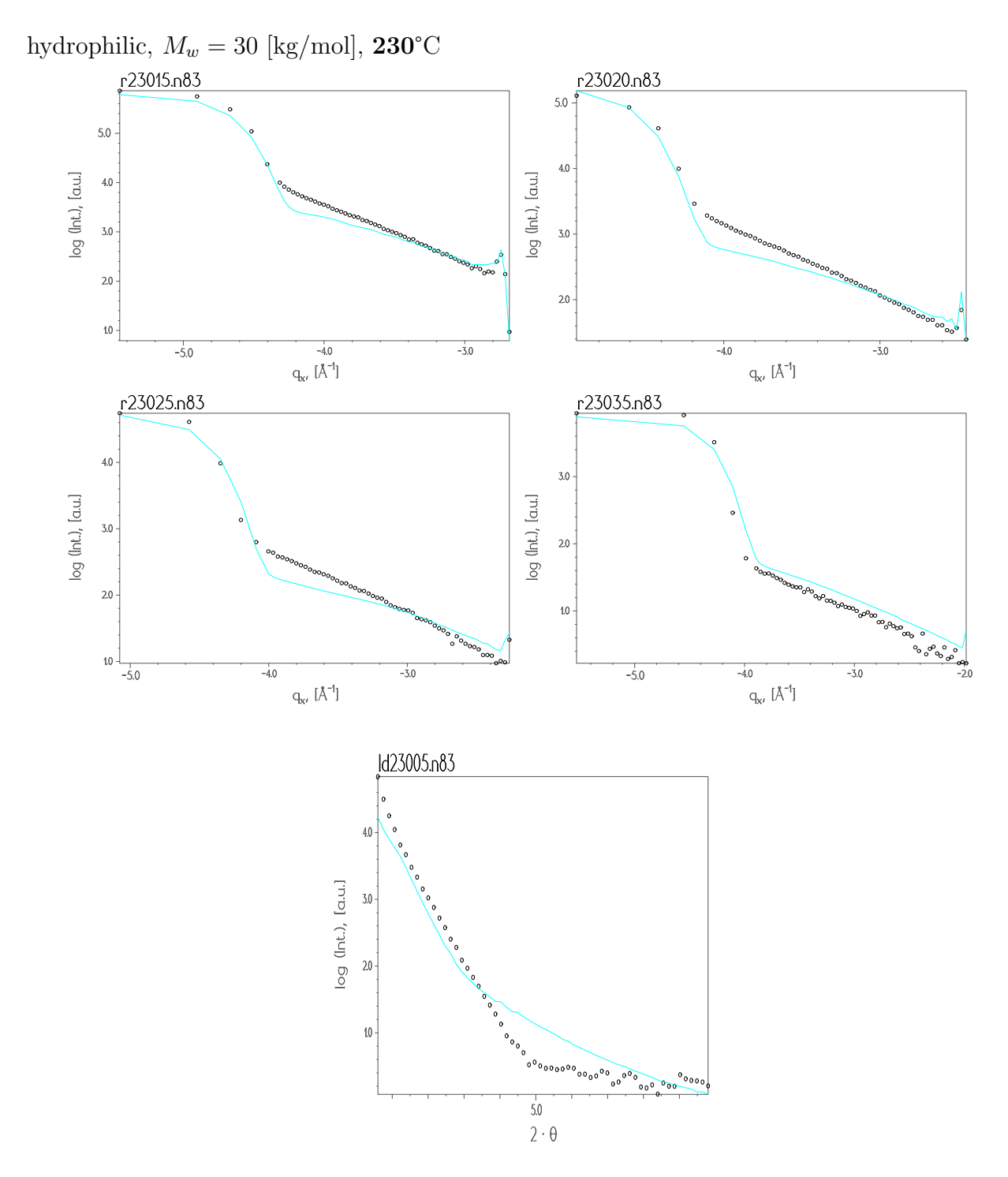


Figure A.59: Longitudinal and transverse scans of sample n83 at 230° C refined with the Liquid model. The curves with the symbols are the experimental data and the lines are the fits.

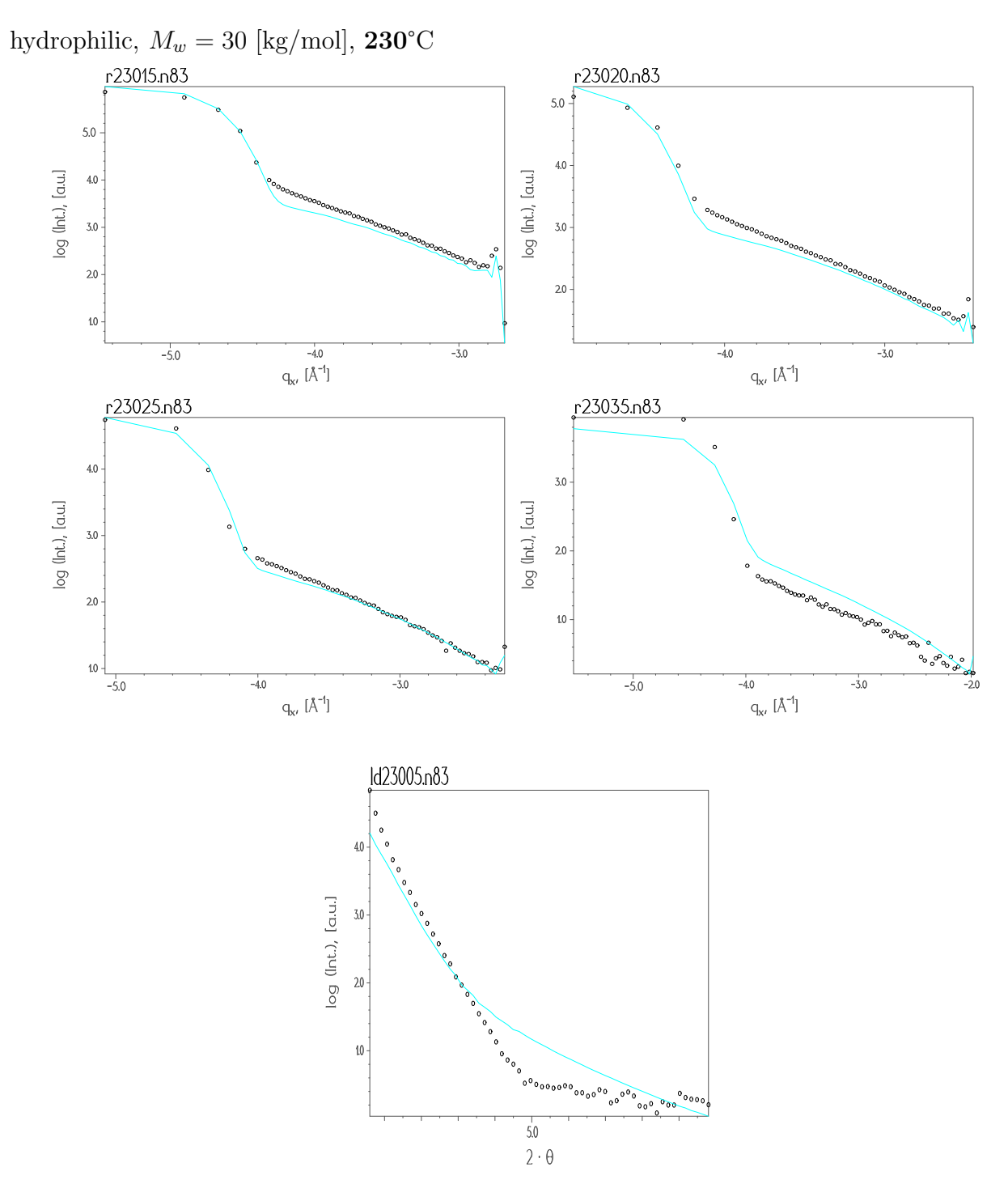


Figure A.60: Longitudinal and transverse scans of sample **n83** at **230°**C refined with the *Fractal model*. The curves with the symbols are the experimental data and the lines are the fits.

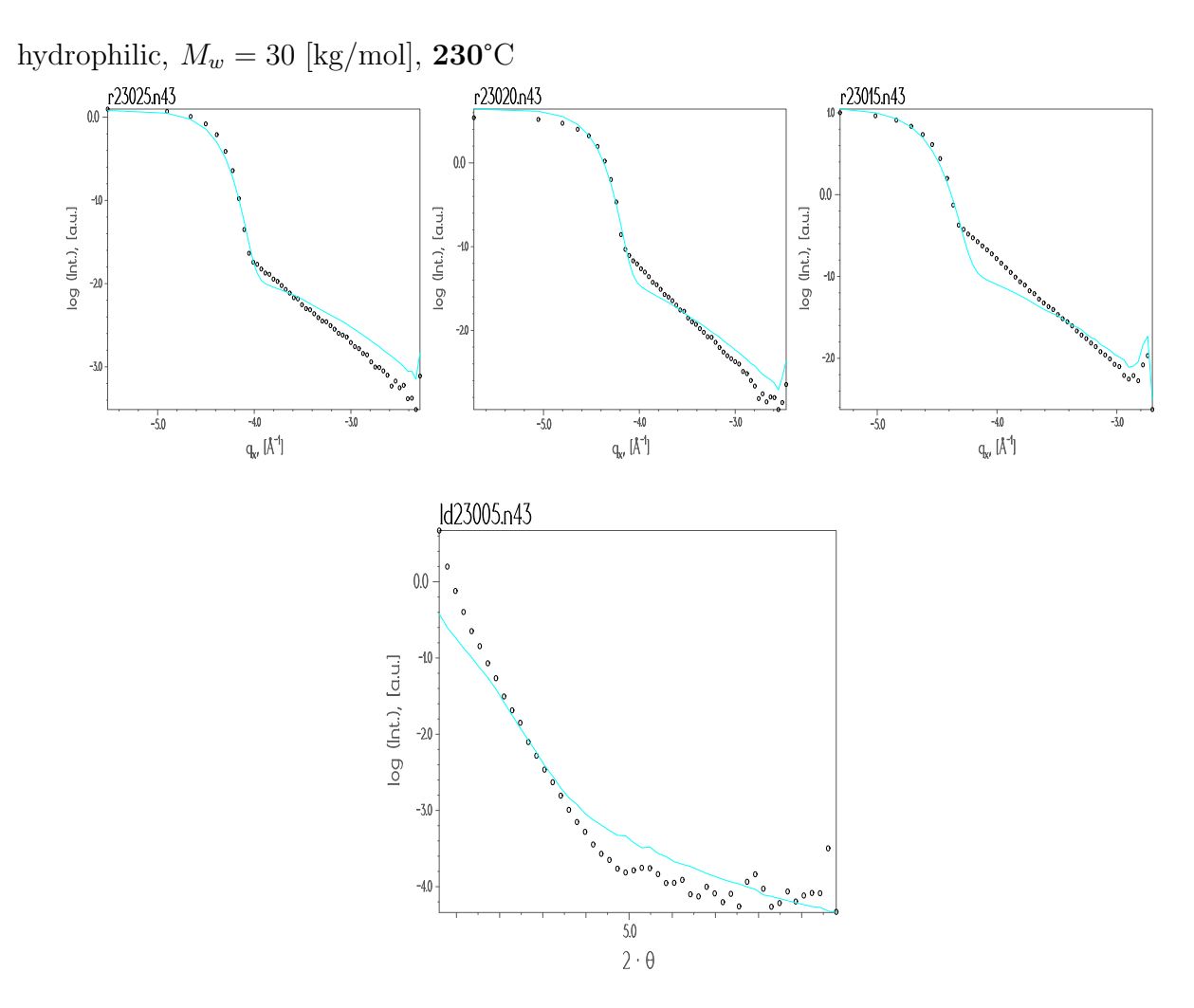


Figure A.61: Longitudinal and transverse scans of sample n43 at 230° C refined with the Liquid model. The curves with the symbols are the experimental data and the lines are the fits.

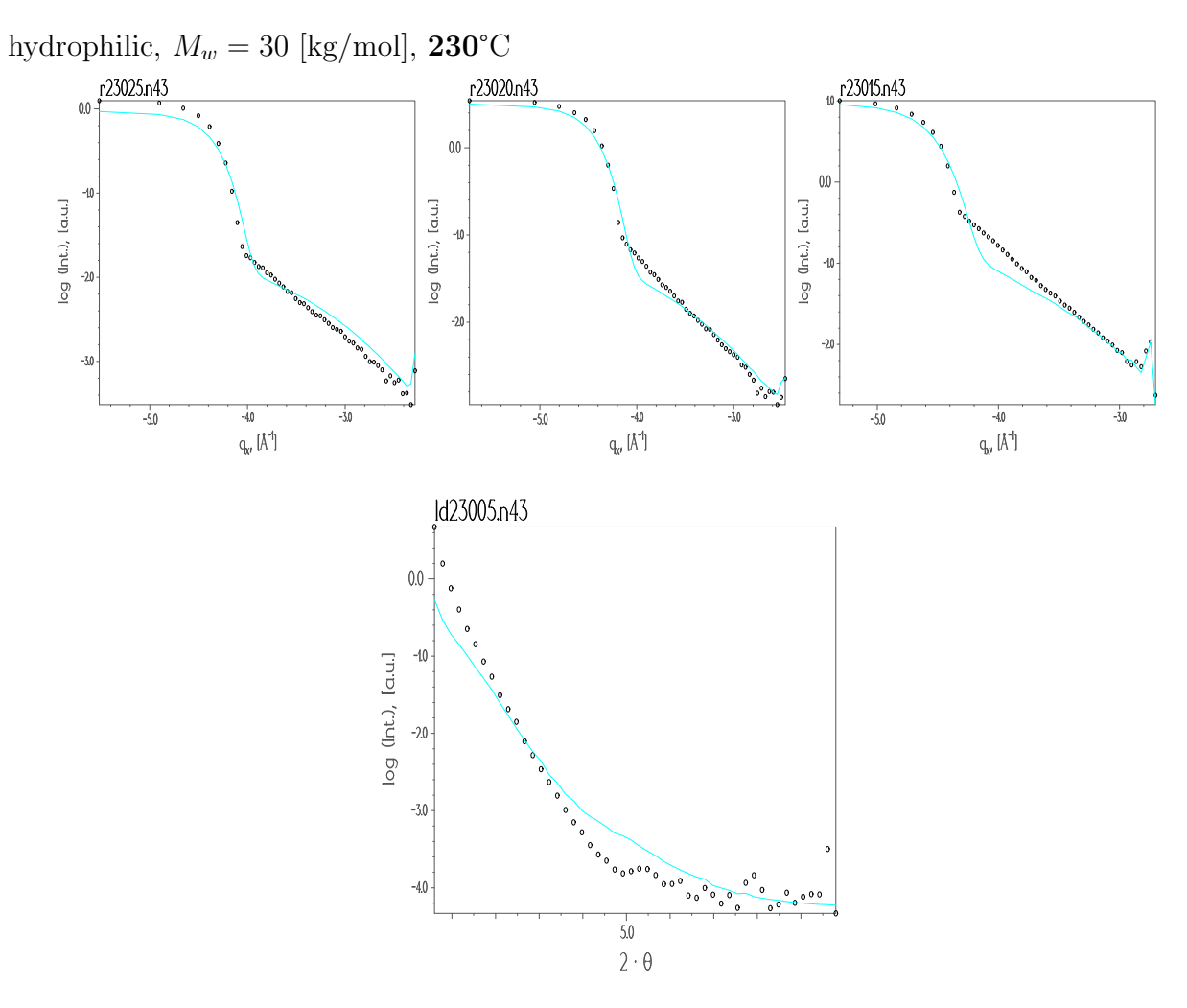


Figure A.62: Longitudinal and transverse scans of sample n43 at 230° C refined with the Fractal model. The curves with the symbols are the experimental data and the lines are the fits.

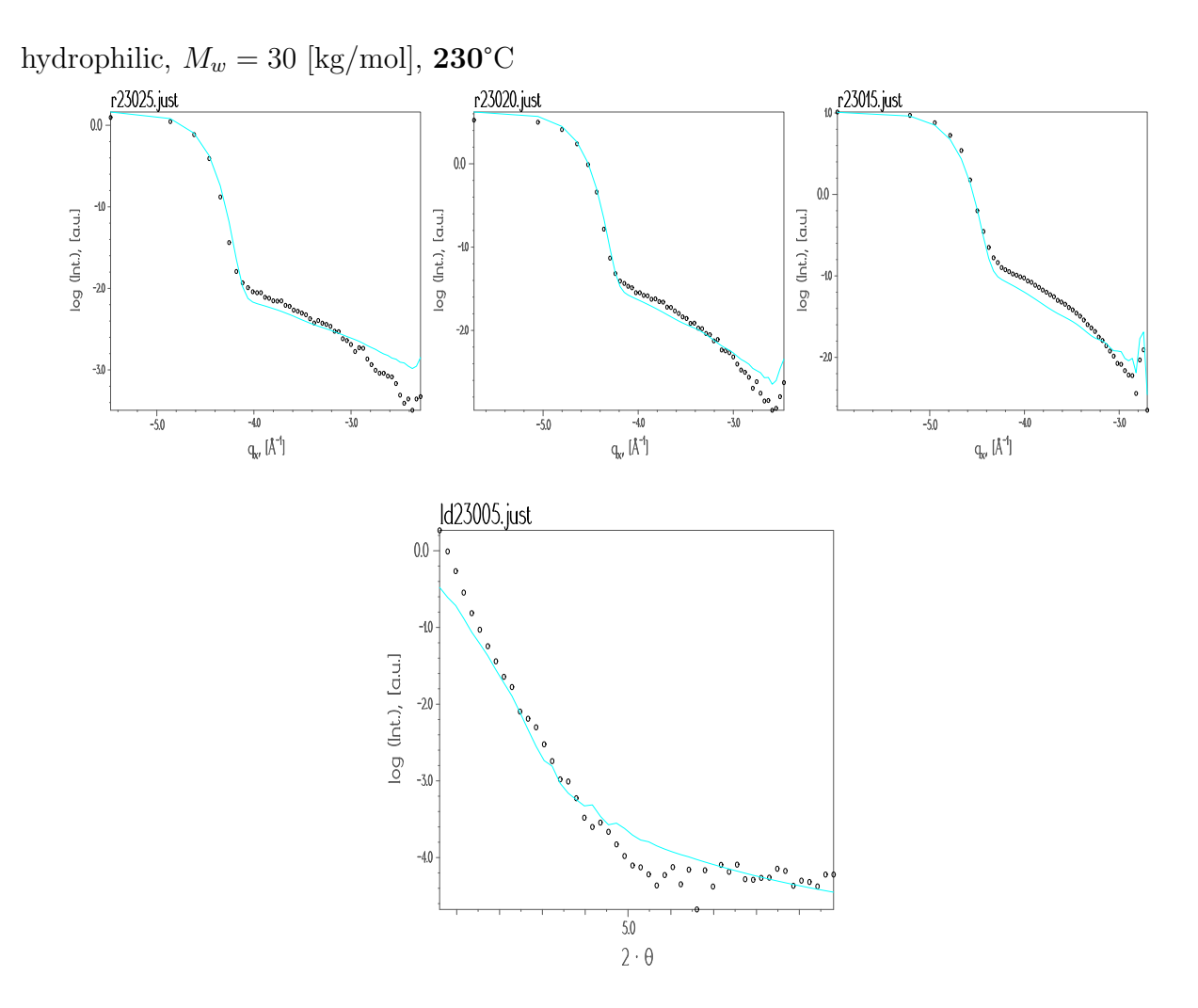


Figure A.63: Longitudinal and transverse scans of sample n23 at 230° C refined with the Liquid model. The curves with the symbols are the experimental data and the lines are the fits.

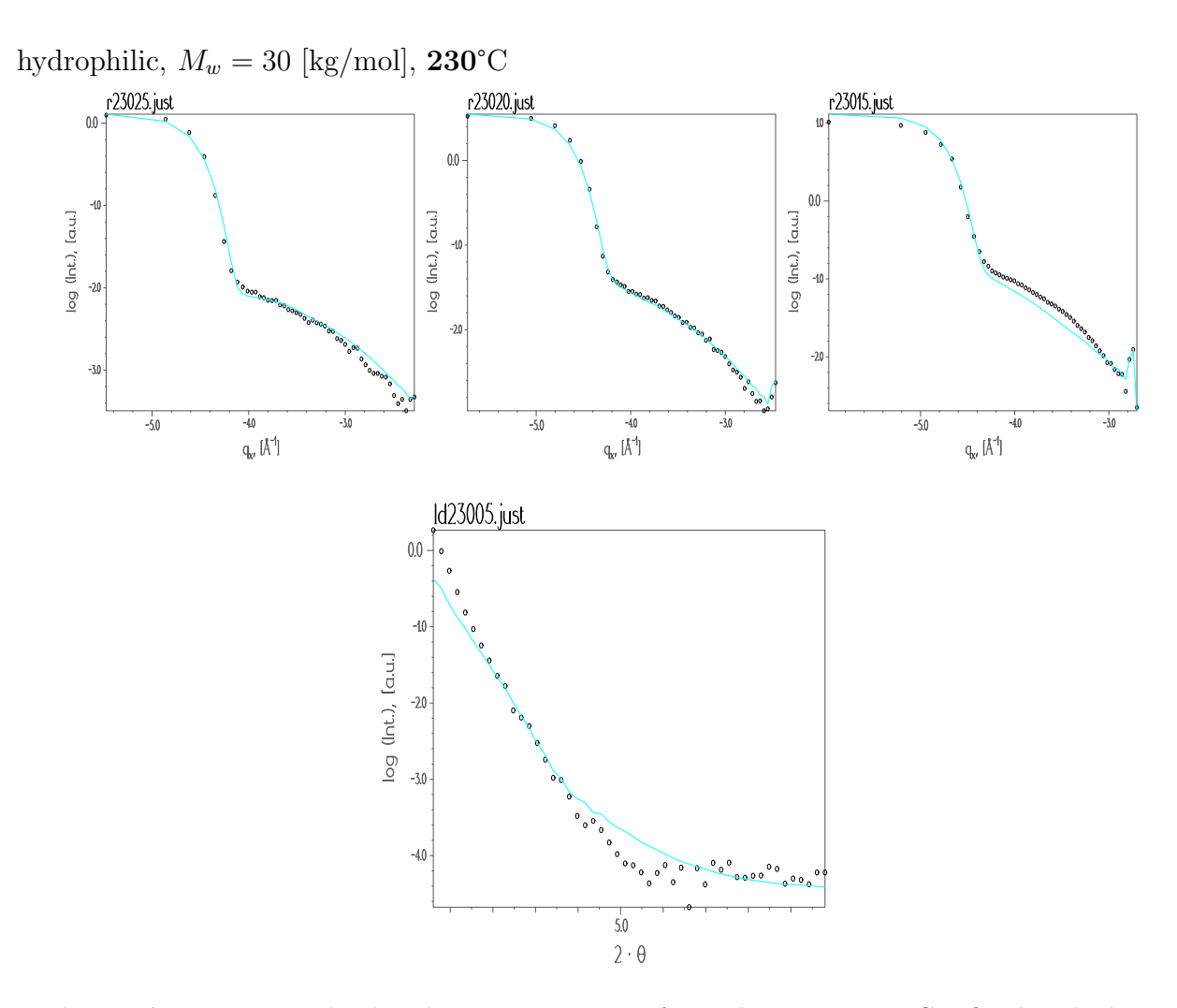


Figure A.64: Longitudinal and transverse scans of sample n23 at 230° C refined with the Fractal model. The curves with the symbols are the experimental data and the lines are the fits.

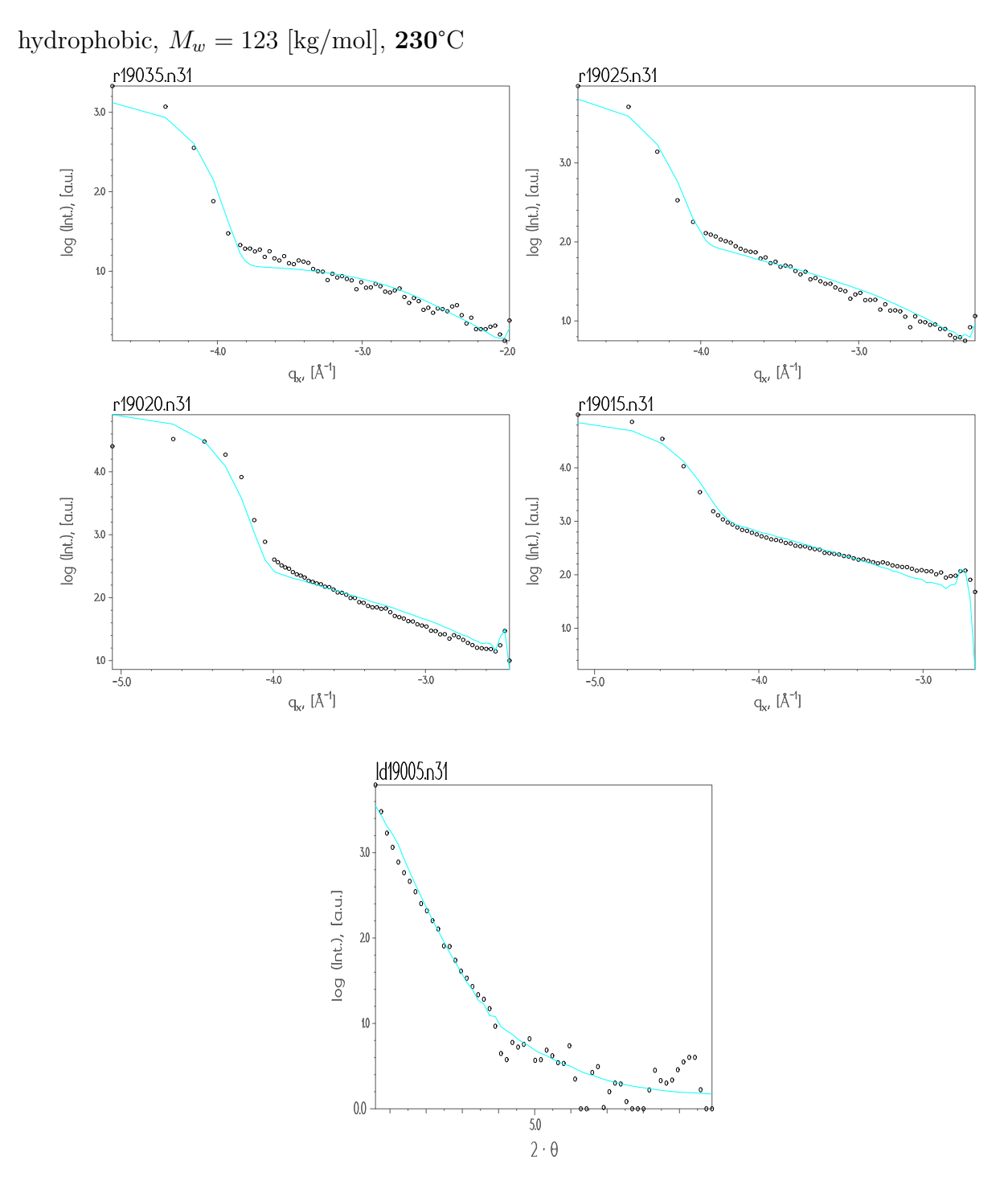


Figure A.65: Longitudinal and transverse scans of sample n31 at 190° C refined with the Liquid model. The curves with the symbols are the experimental data and the lines are the fits.

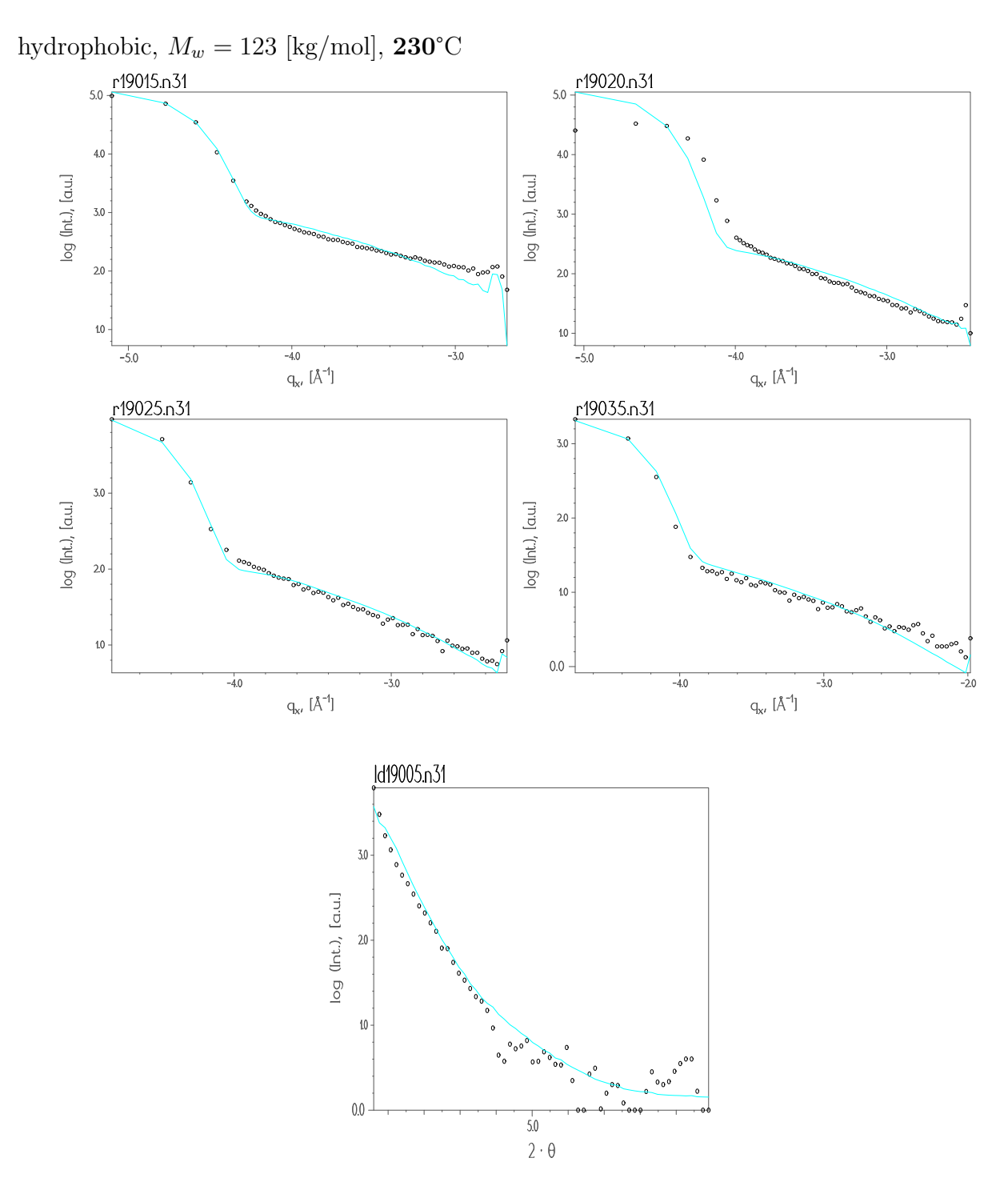


Figure A.66: Longitudinal and transverse scans of sample **n31** at **190**°C refined with the *Fractal model*. The curves with the symbols are the experimental data and the lines are the fits.

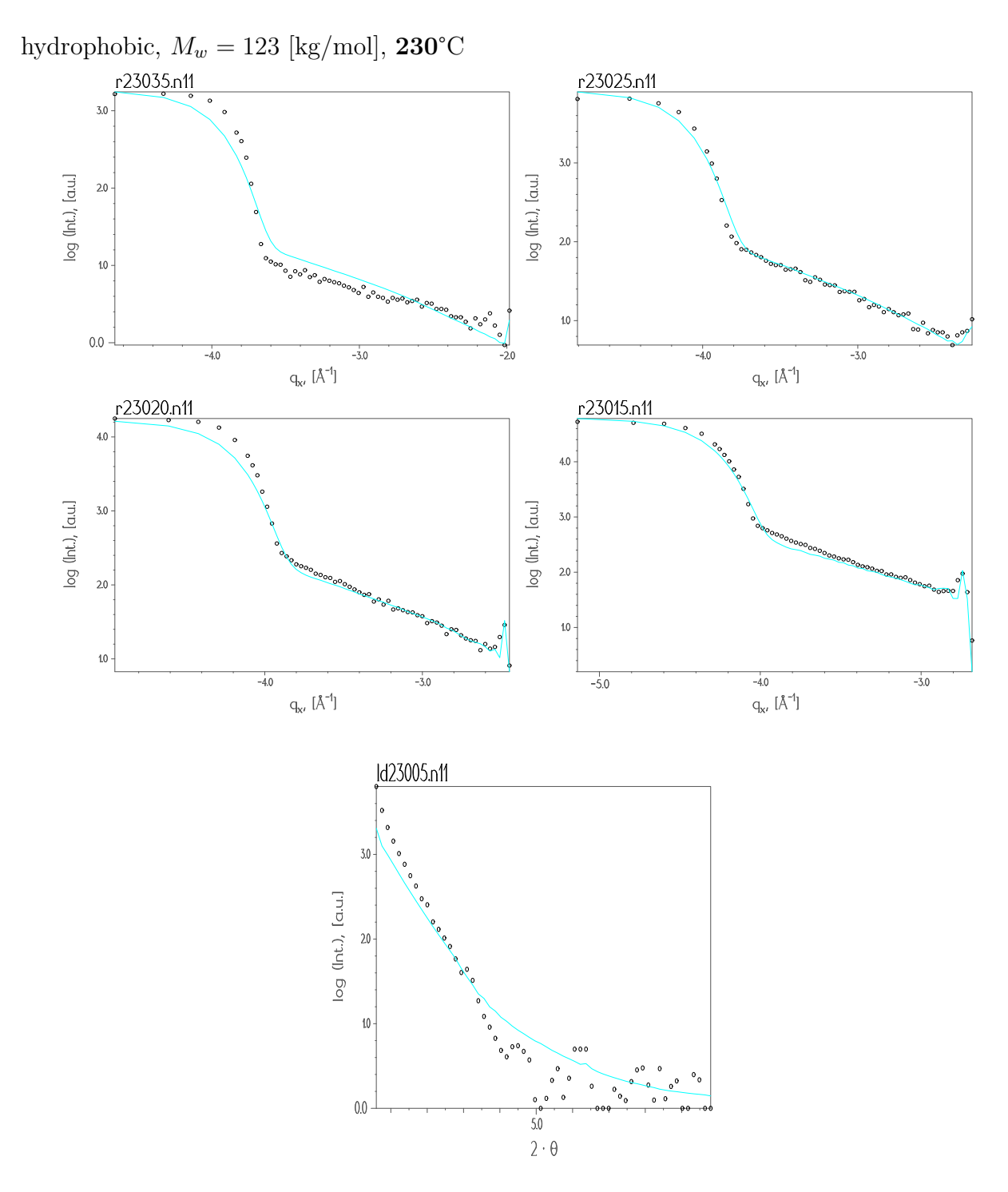


Figure A.67: Longitudinal and transverse scans of sample n11 at 230° C refined with the Liquid model. The curves with the symbols are the experimental data and the lines are the fits.

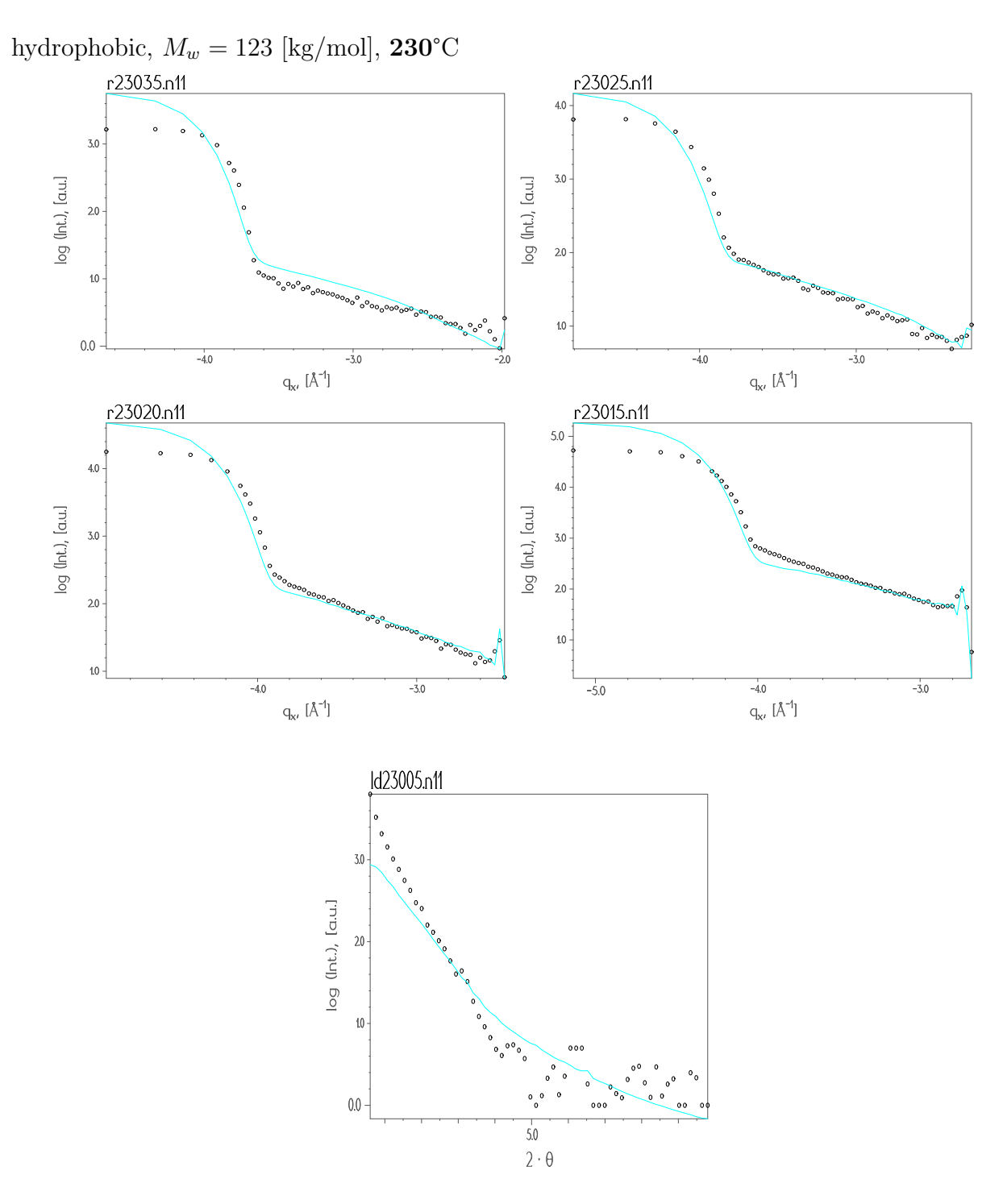


Figure A.68: Longitudinal and transverse scans of sample **n11** at **230**°C refined with the *Fractal model*. The curves with the symbols are the experimental data and the lines are the fits.

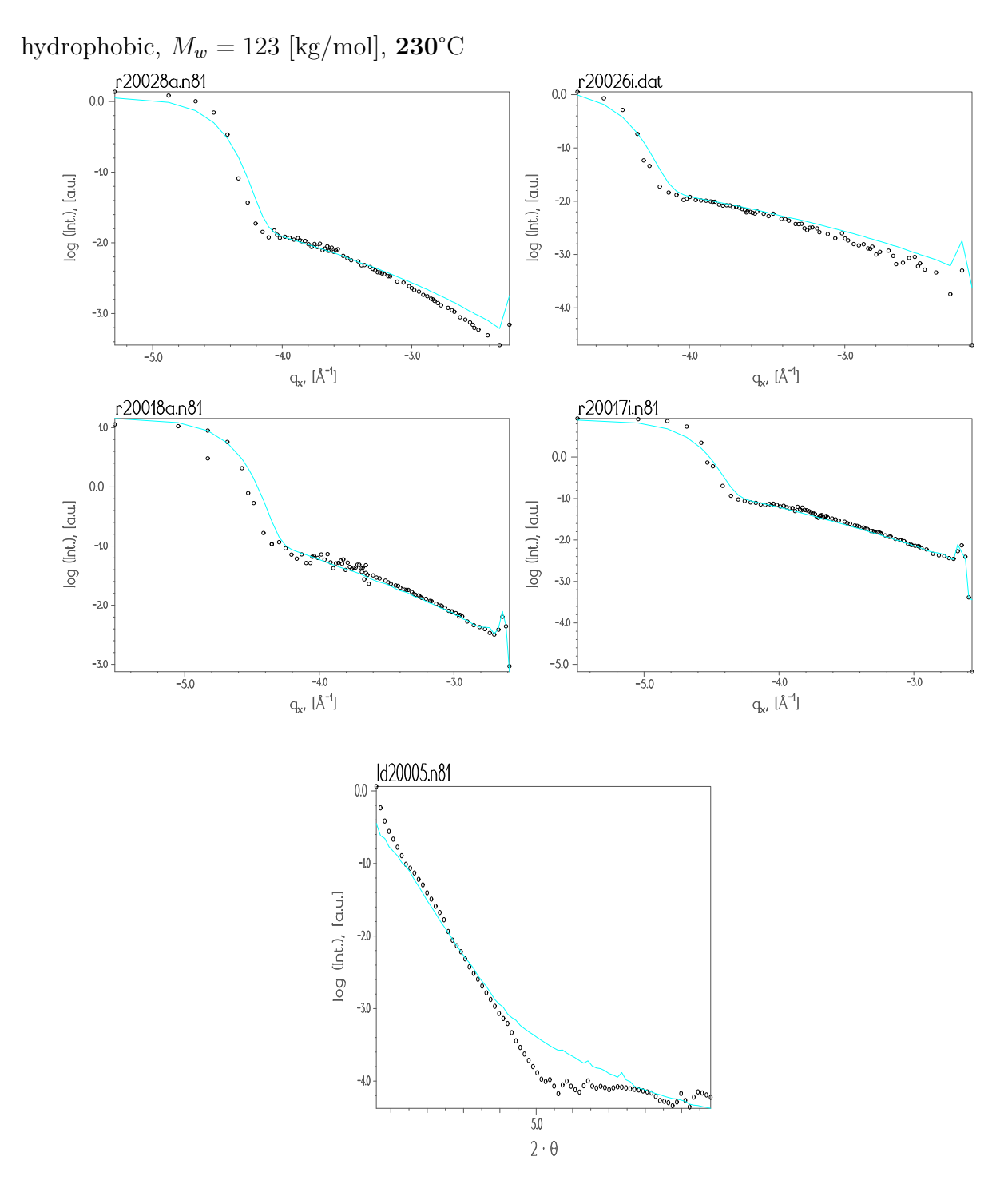


Figure A.69: Longitudinal and transverse scans of sample n81 at 200° C refined with the Liquid model. The curves with the symbols are the experimental data and the lines are the fits.

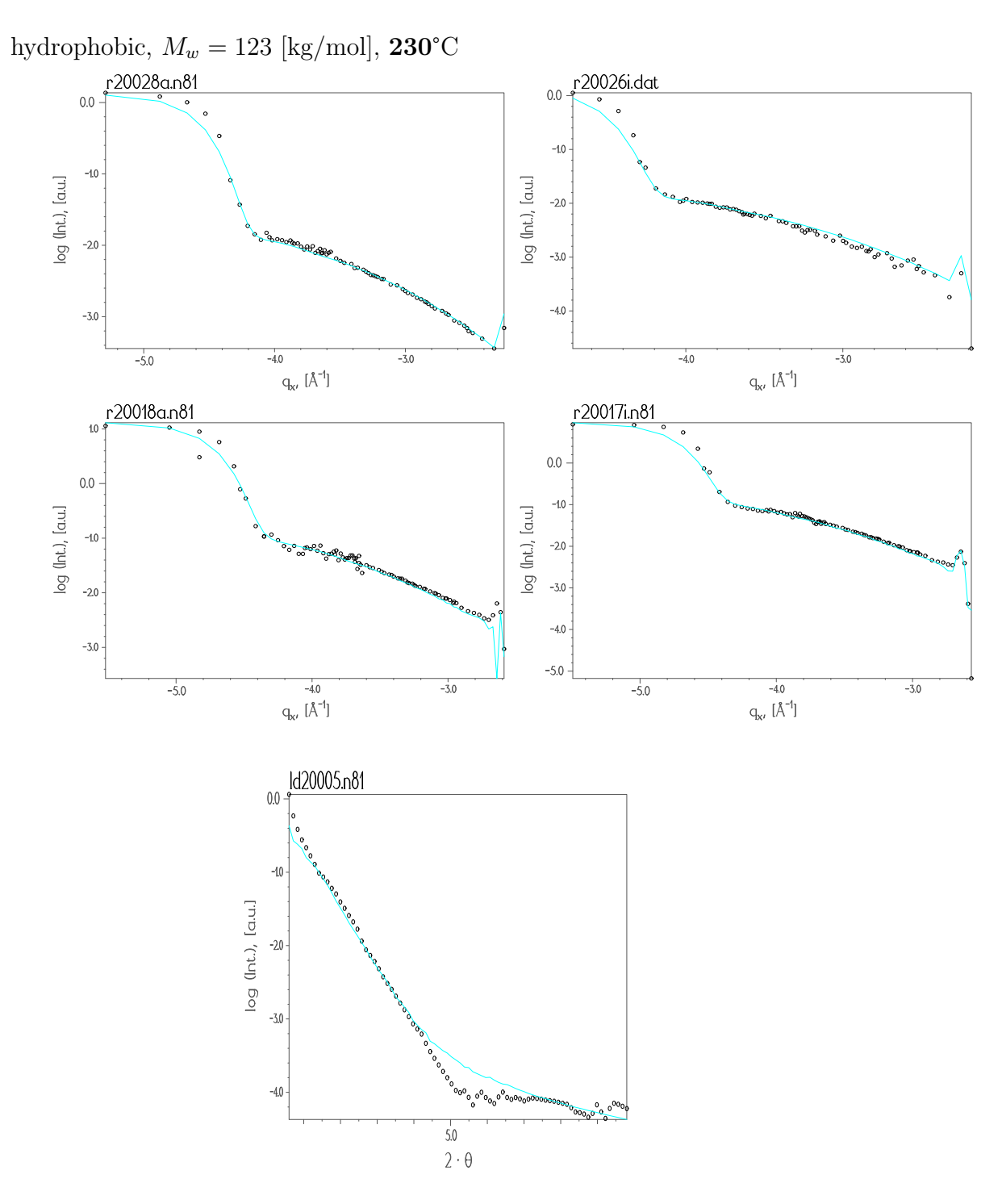


Figure A.70: Longitudinal and transverse scans of sample **n81** at **200**°C refined with the *Fractal model*. The curves with the symbols are the experimental data and the lines are the fits.

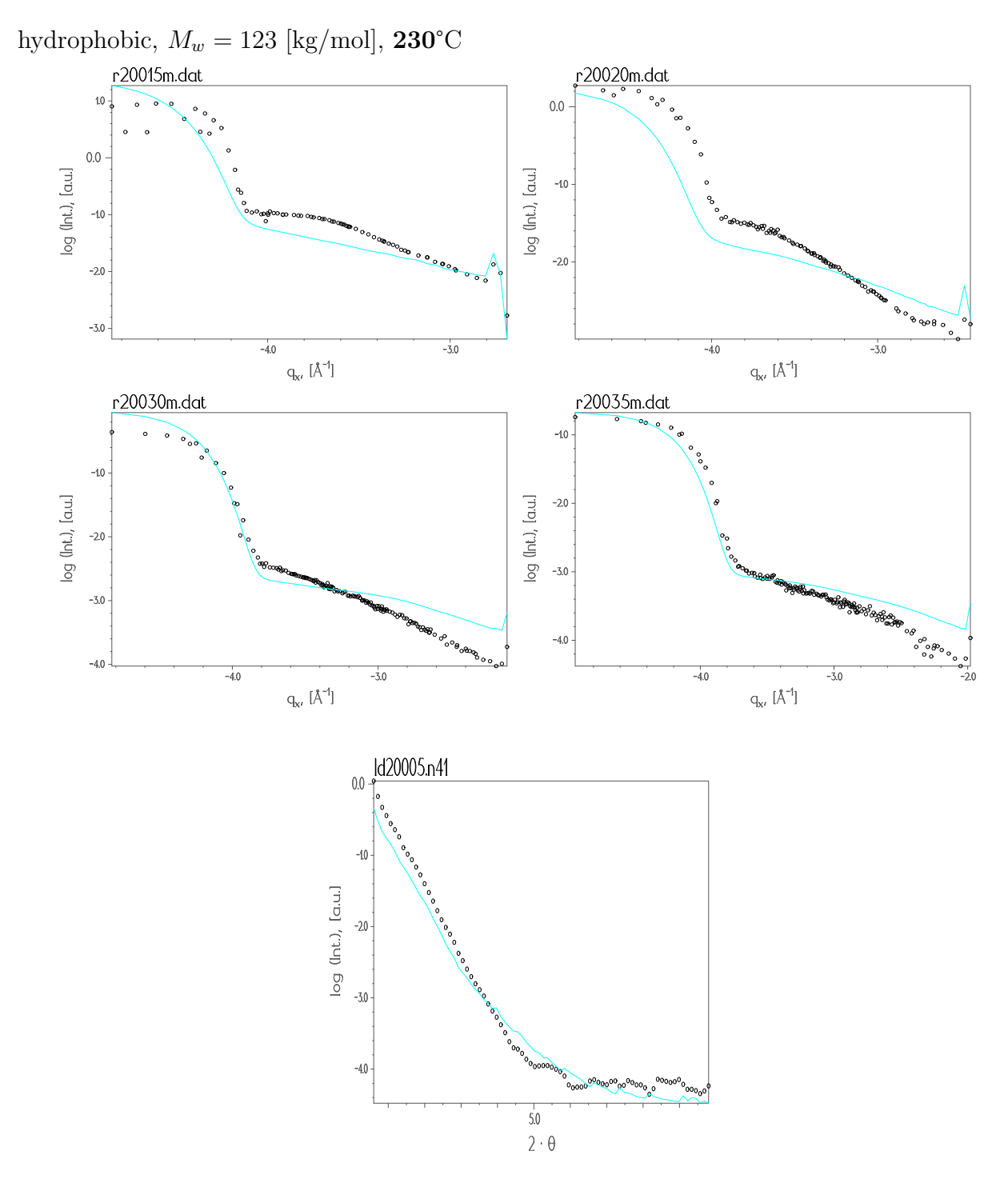


Figure A.71: Longitudinal and transverse scans of sample n41 at 200° C refined with the Liquid model. The curves with the symbols are the experimental data and the lines are the fits.

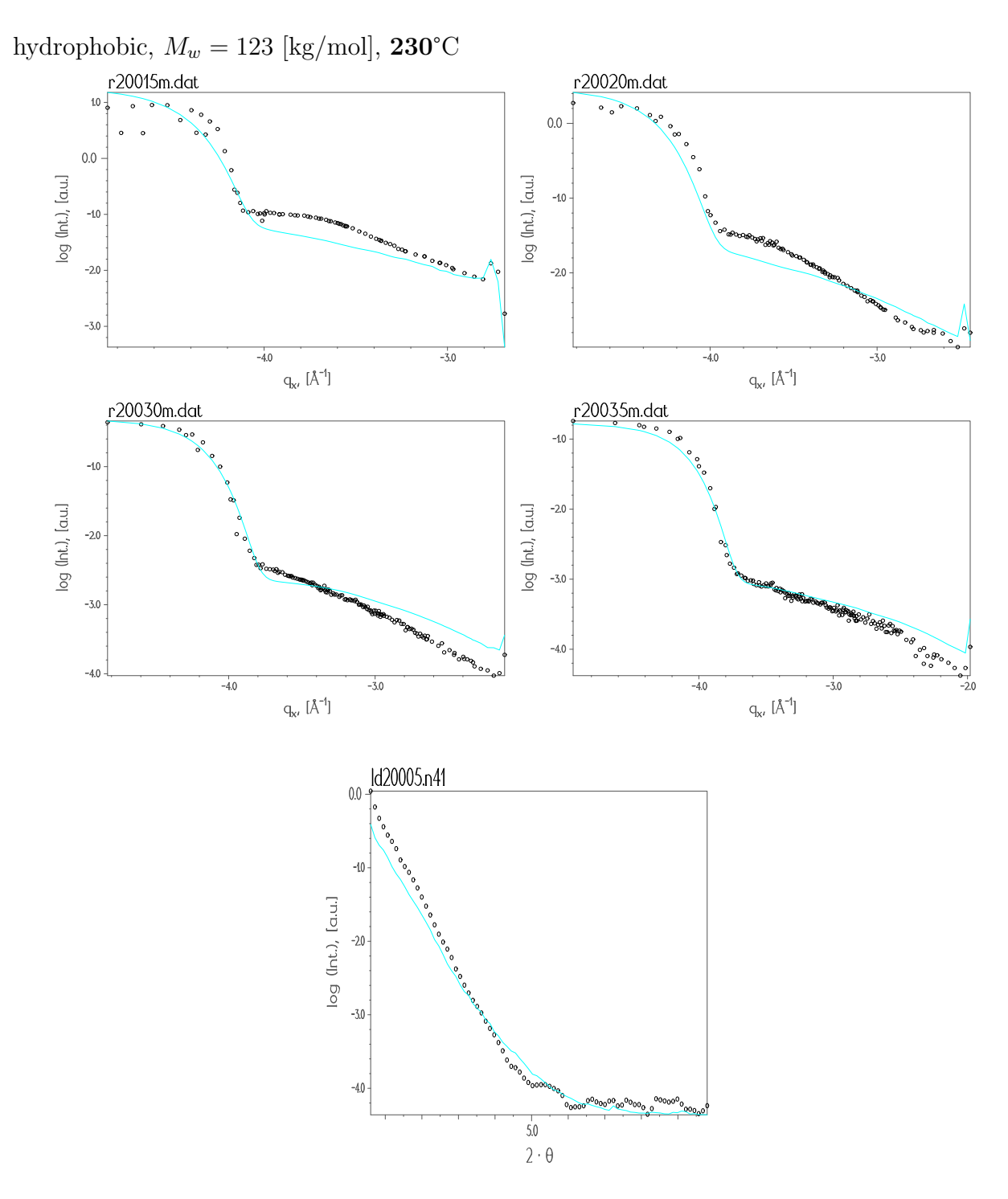


Figure A.72: Longitudinal and transverse scans of sample **n41** at **200**°C refined with the *Fractal model*. The curves with the symbols are the experimental data and the lines are the fits.

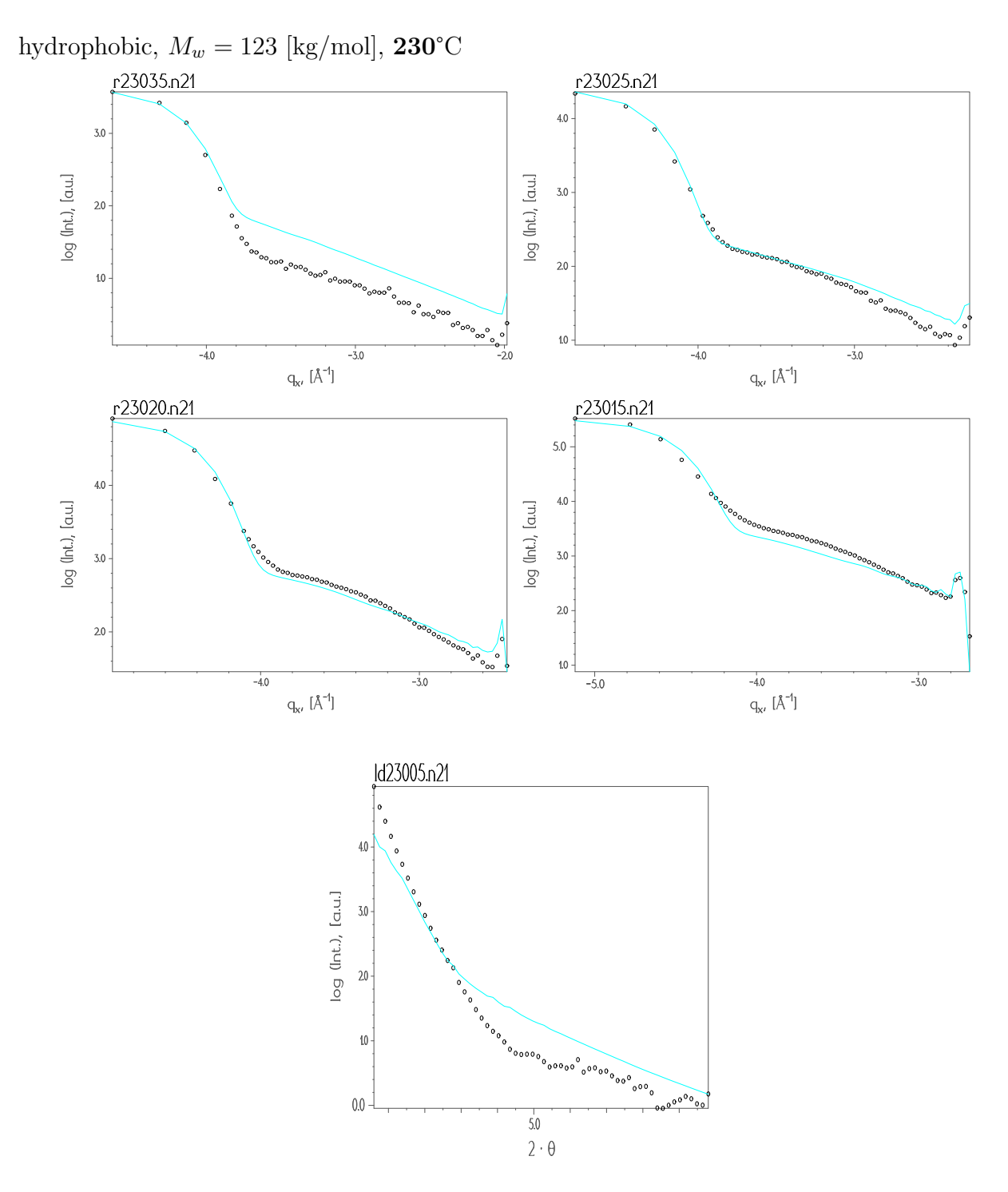


Figure A.73: Longitudinal and transverse scans of sample n21 at 230° C refined with the Liquid model. The curves with the symbols are the experimental data and the lines are the fits.

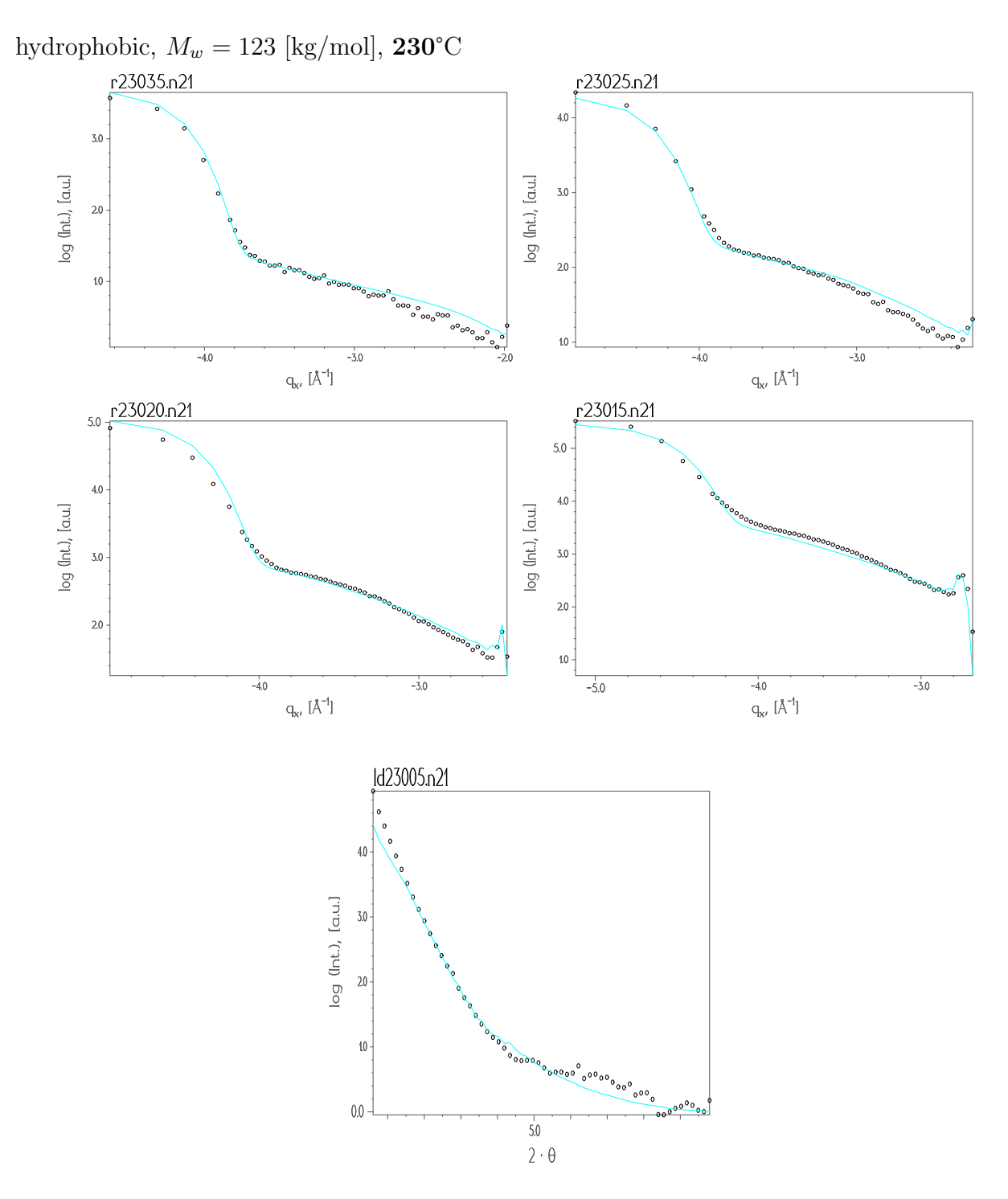


Figure A.74: Longitudinal and transverse scans of sample **n21** at **230**°C refined with the *Fractal model*. The curves with the symbols are the experimental data and the lines are the fits.

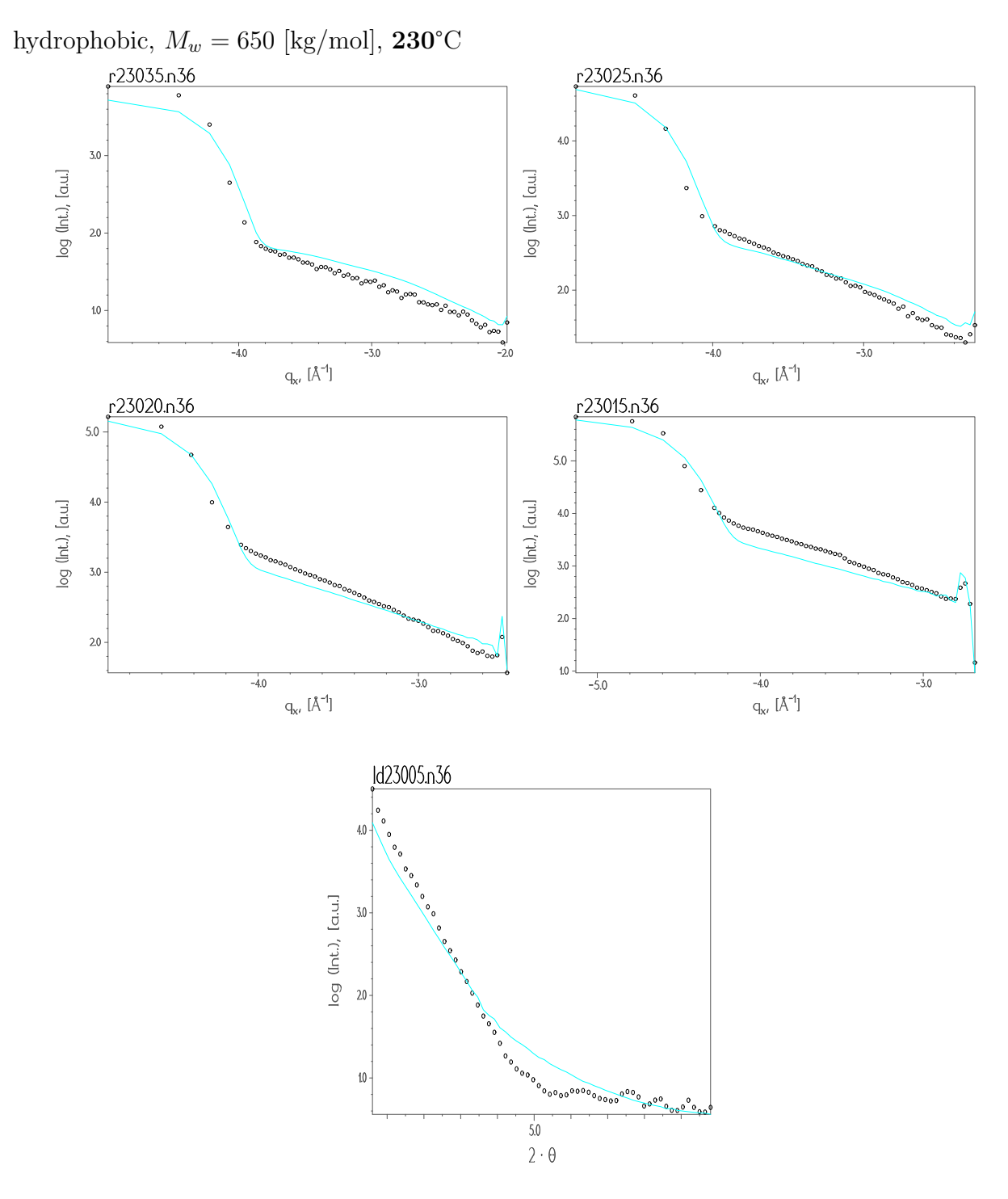


Figure A.75: Longitudinal and transverse scans of sample n36 at 230° C refined with the Liquid model. The curves with the symbols are the experimental data and the lines are the fits.

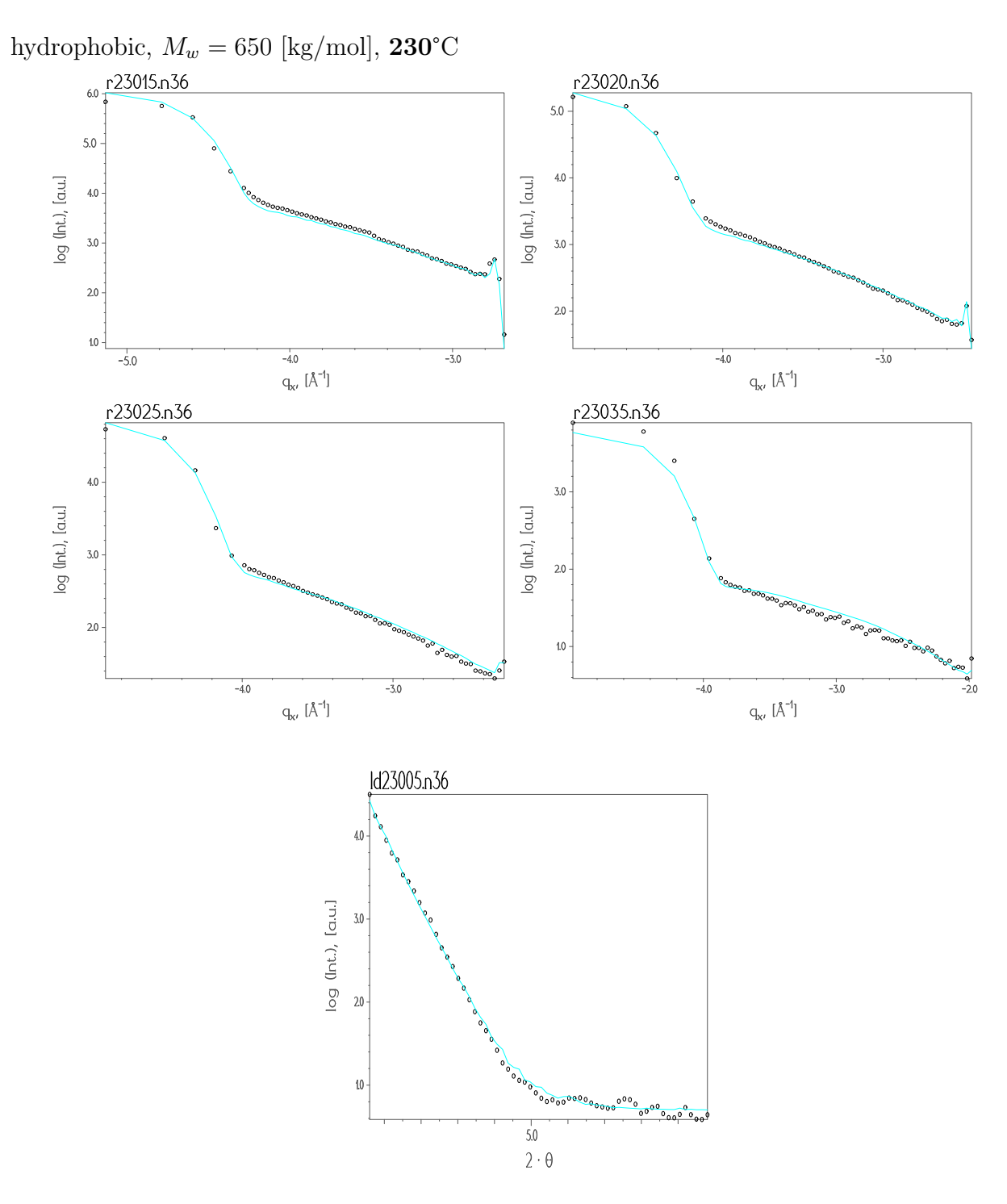


Figure A.76: Longitudinal and transverse scans of sample **n36** at **230**°C refined with the *Fractal model*. The curves with the symbols are the experimental data and the lines are the fits.

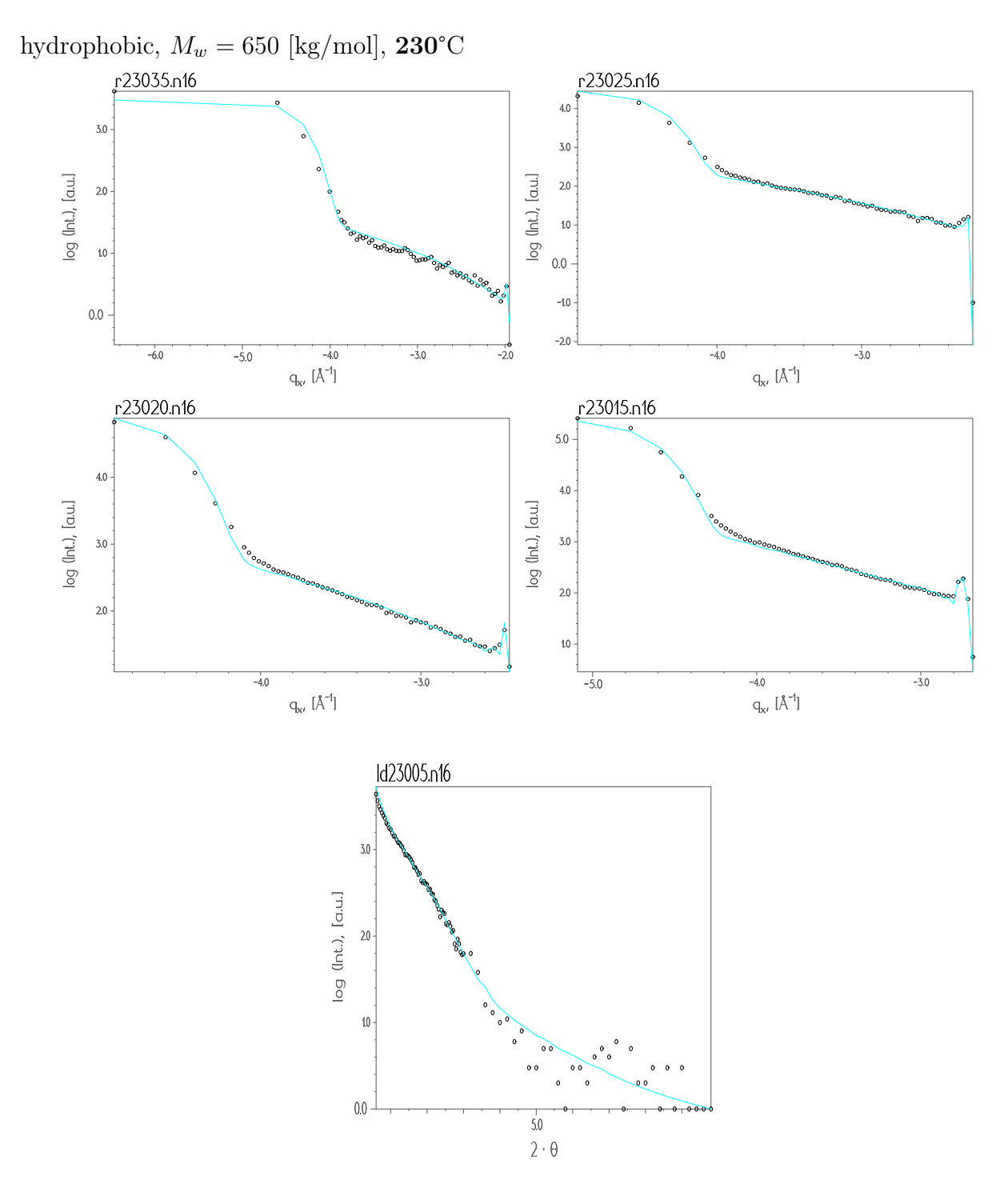


Figure A.77: Longitudinal and transverse scans of sample n16 at 230° C refined with the Liquid model. The curves with the symbols are the experimental data and the lines are the fits.

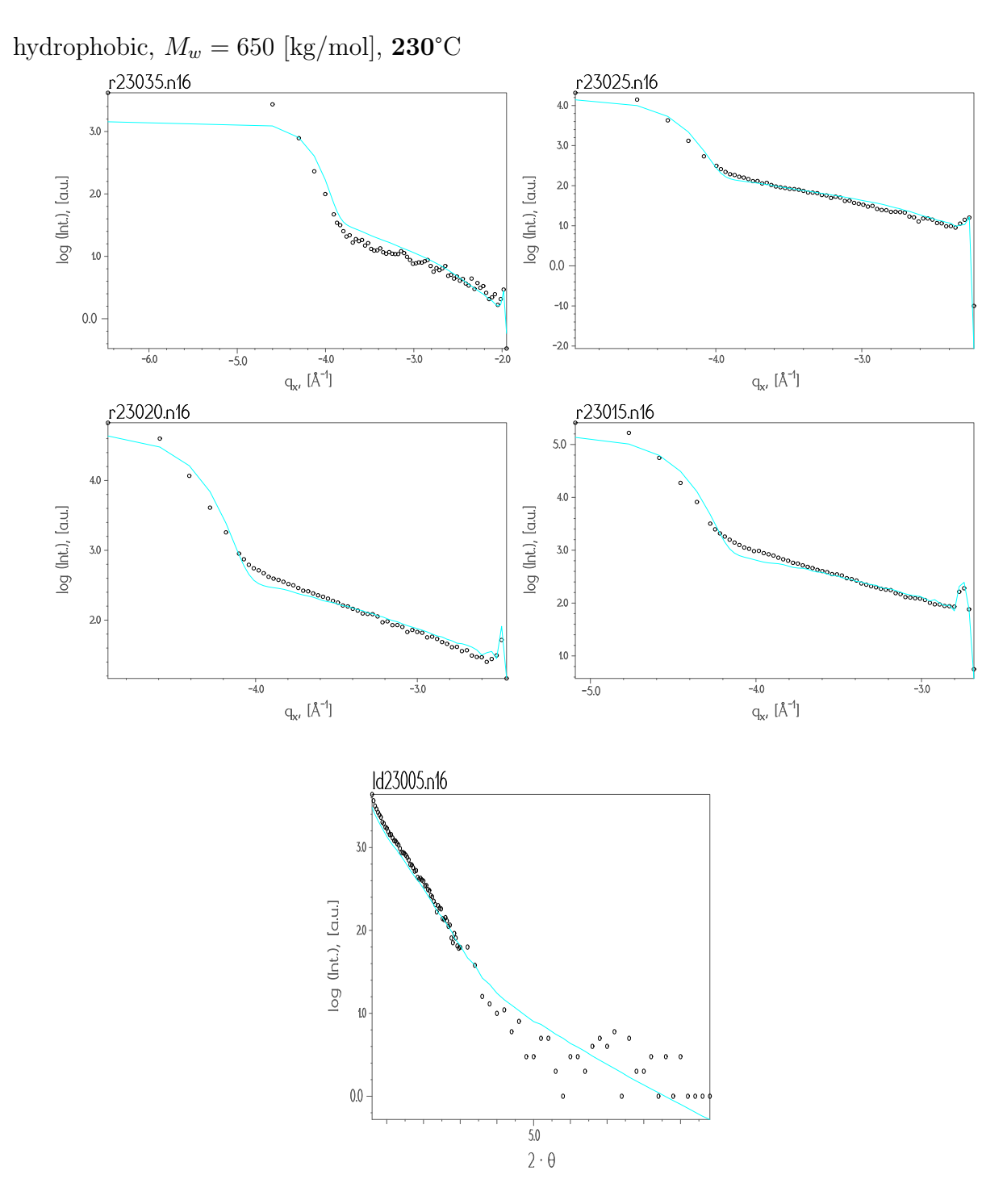


Figure A.78: Longitudinal and transverse scans of sample **n16** at **230**°C refined with the *Fractal model*. The curves with the symbols are the experimental data and the lines are the fits.

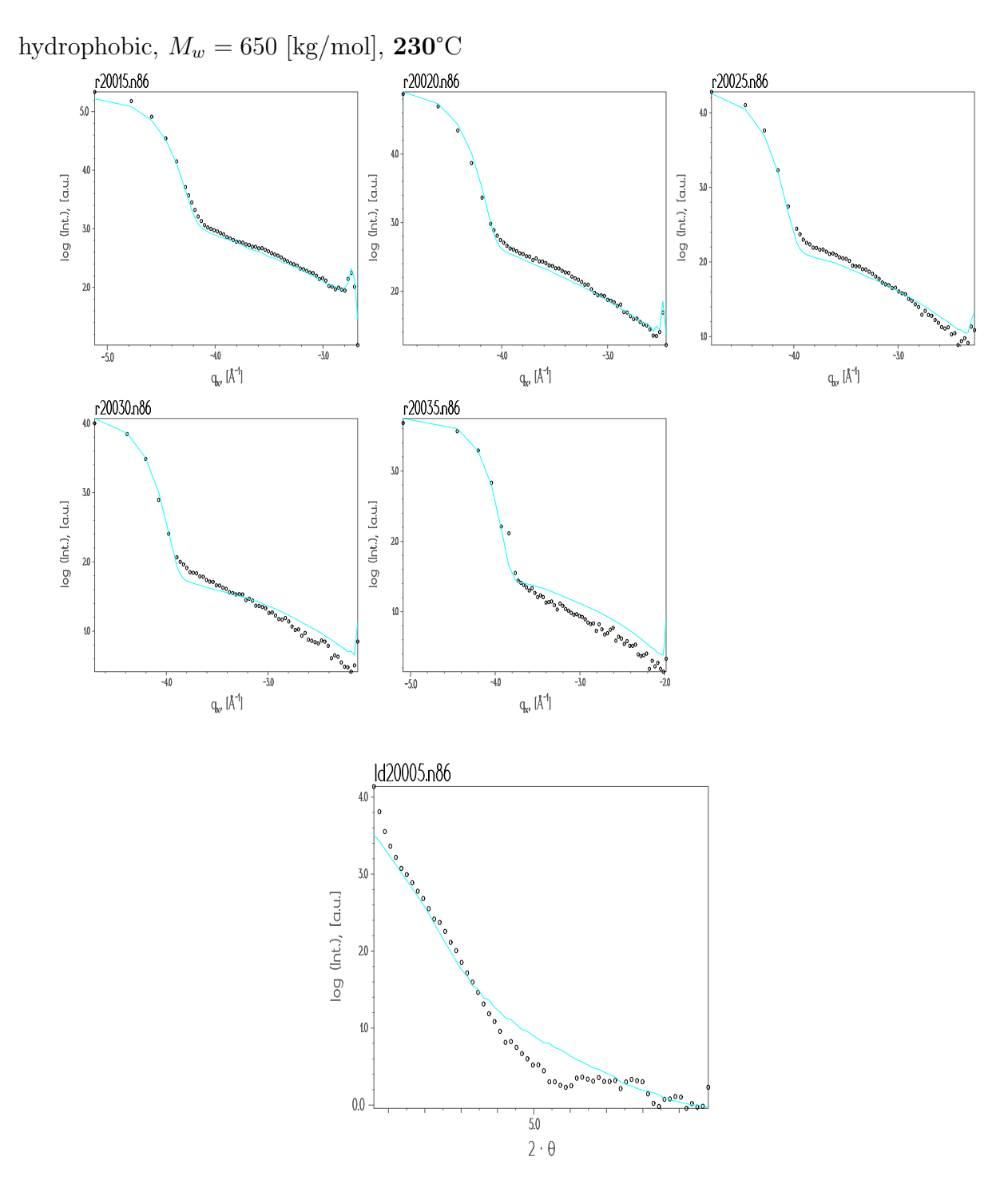


Figure A.79: Longitudinal and transverse scans of sample **n86** at **200°**C refined with the *Liquid model*. The curves with the symbols are the experimental data and the lines are the fits.

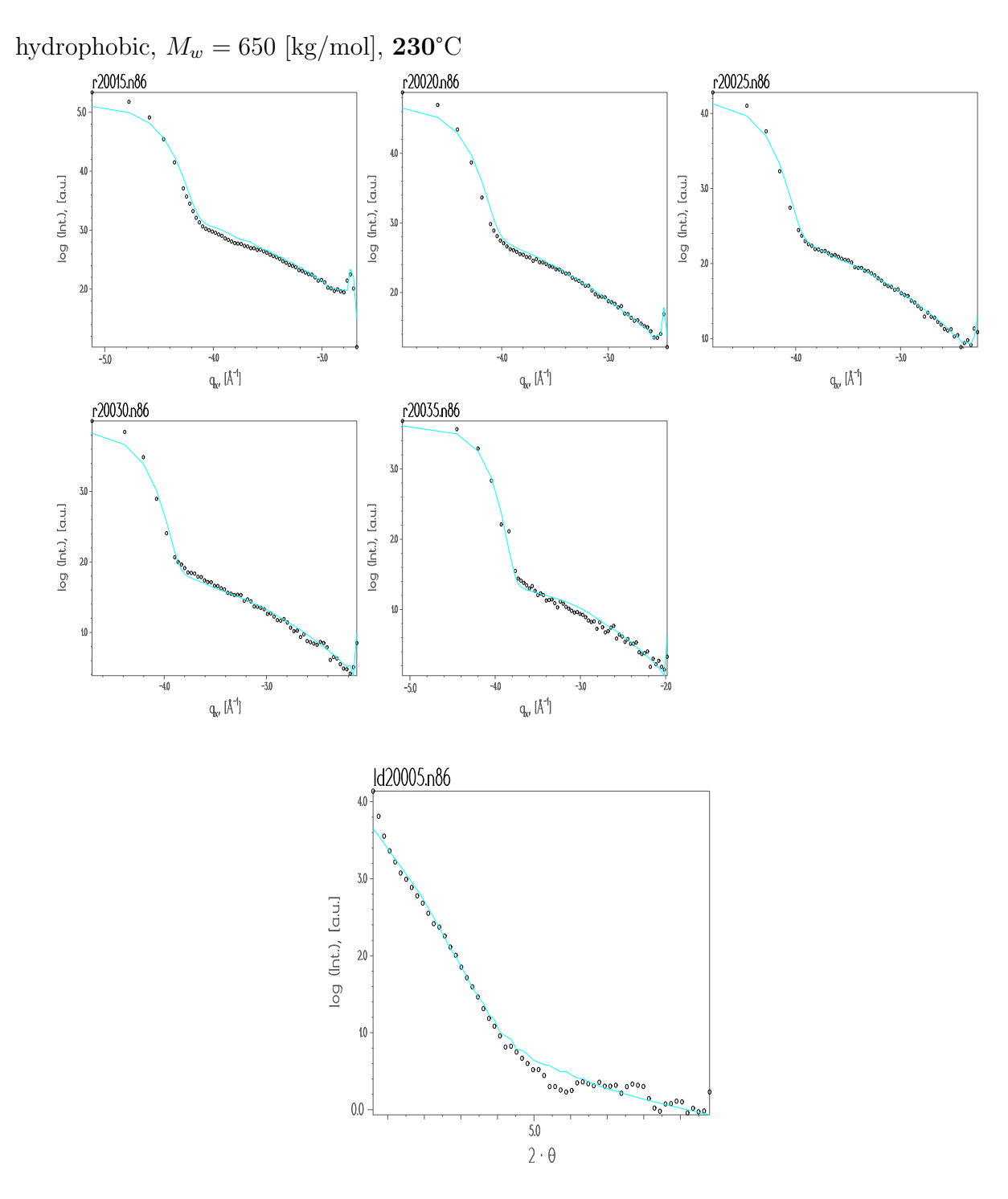


Figure A.80: Longitudinal and transverse scans of sample **n86** at **200°**C refined with the *Fractal model*. The curves with the symbols are the experimental data and the lines are the fits.

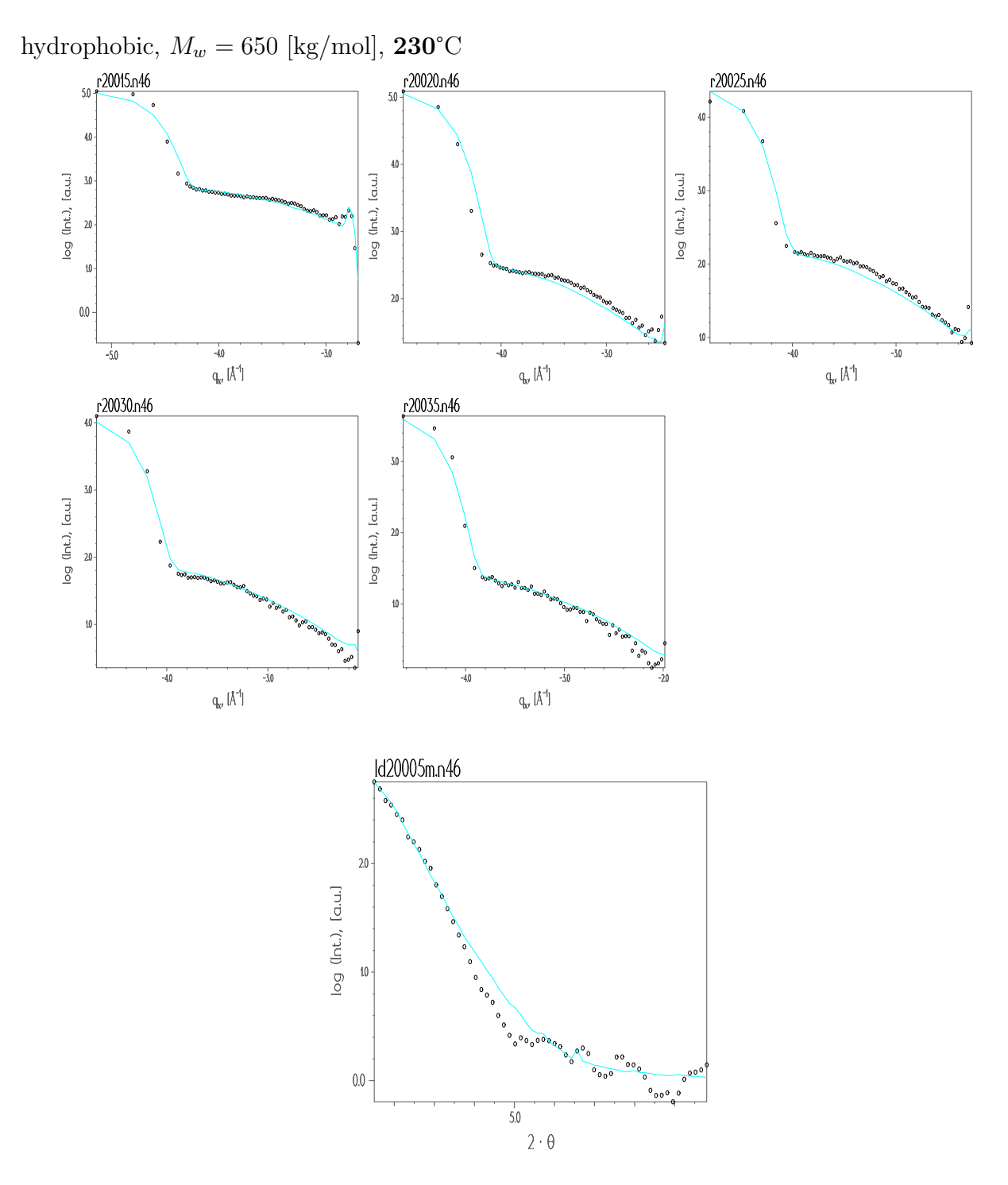


Figure A.81: Longitudinal and transverse scans of sample **n46** at **200**°C refined with the *Liquid model*. The curves with the symbols are the experimental data and the lines are the fits.

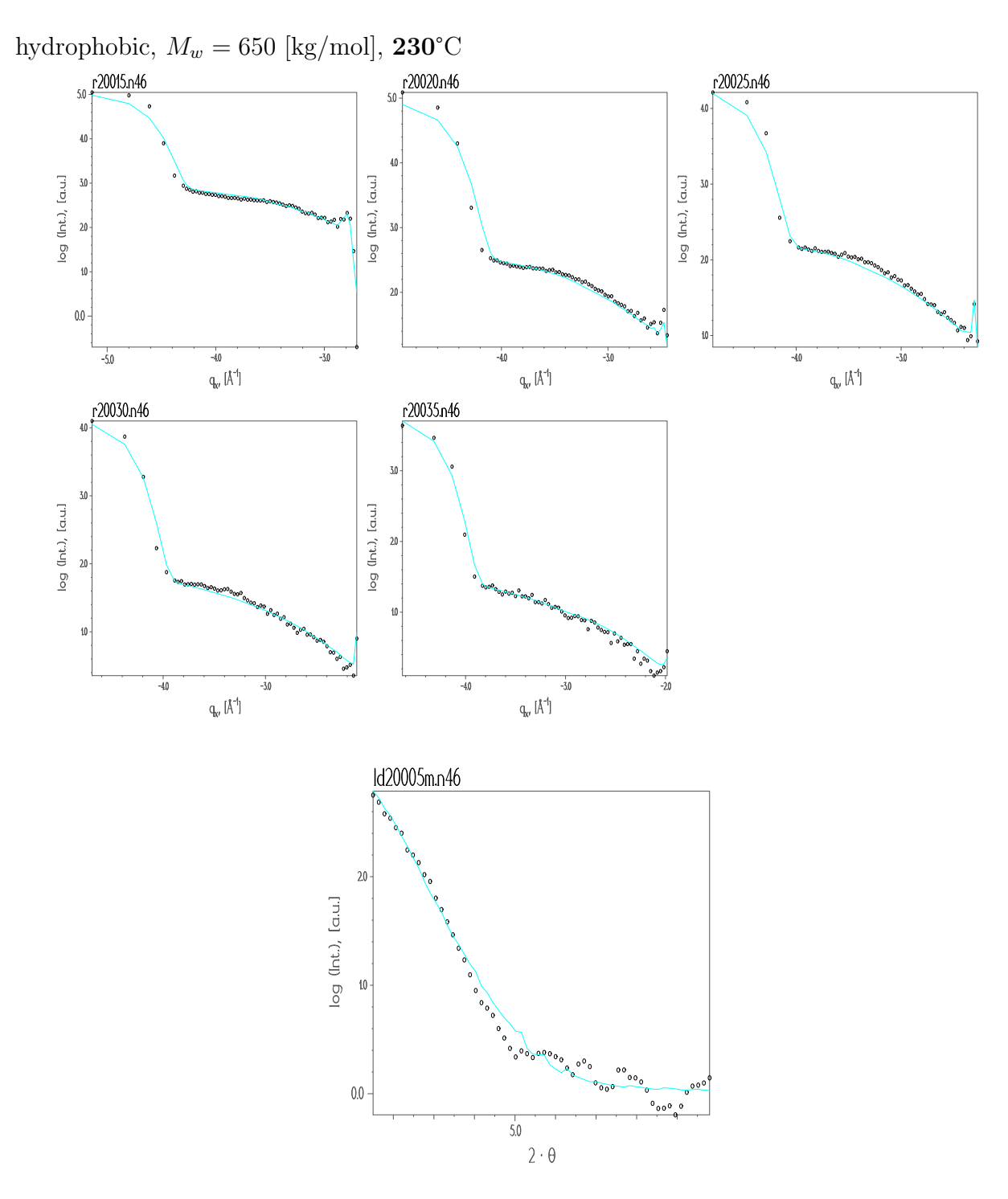


Figure A.82: Longitudinal and transverse scans of sample **n46** at **200**°C refined with the *Fractal model*. The curves with the symbols are the experimental data and the lines are the fits.

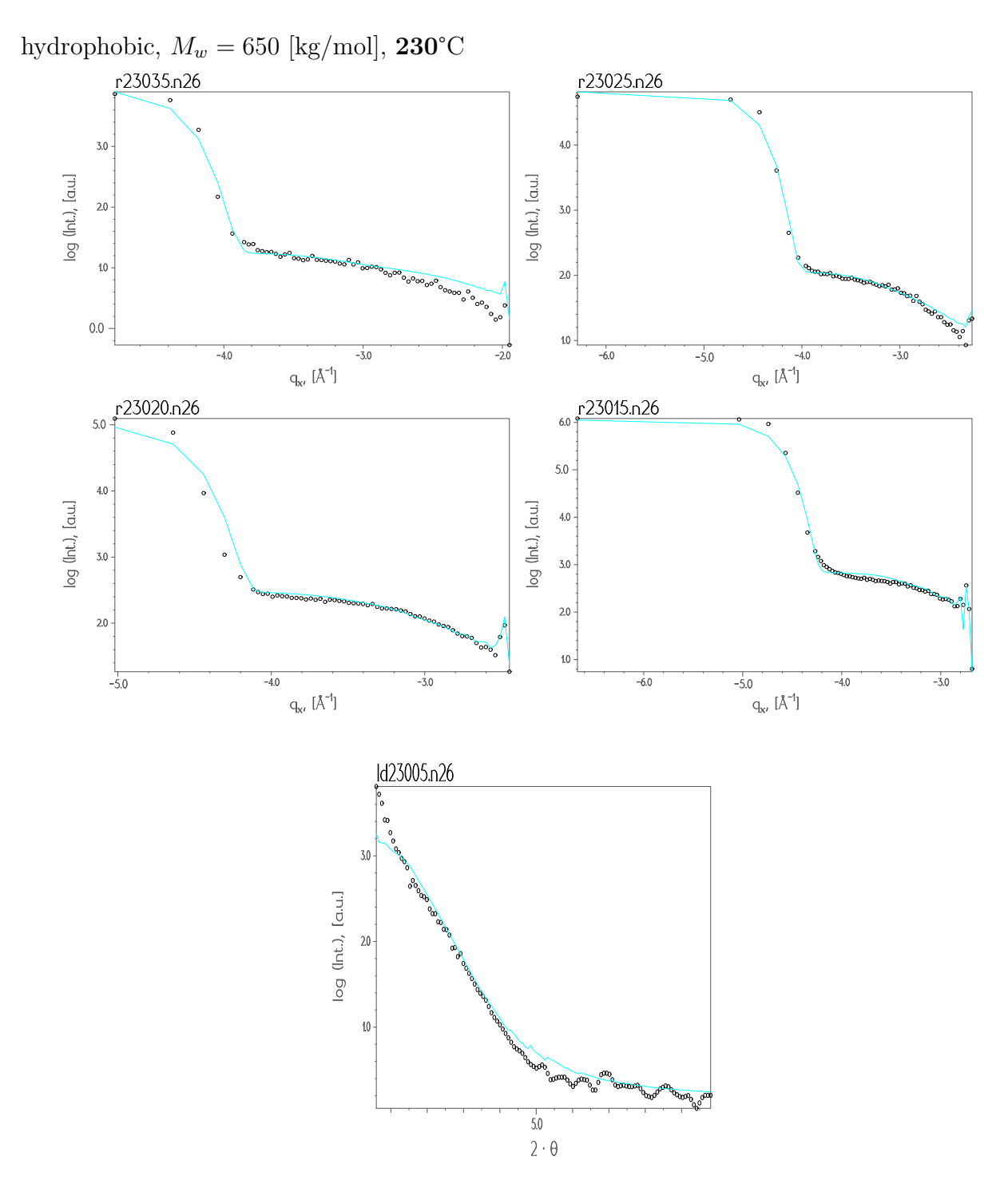


Figure A.83: Longitudinal and transverse scans of sample n26 at 230° C refined with the Liquid model. The curves with the symbols are the experimental data and the lines are the fits.

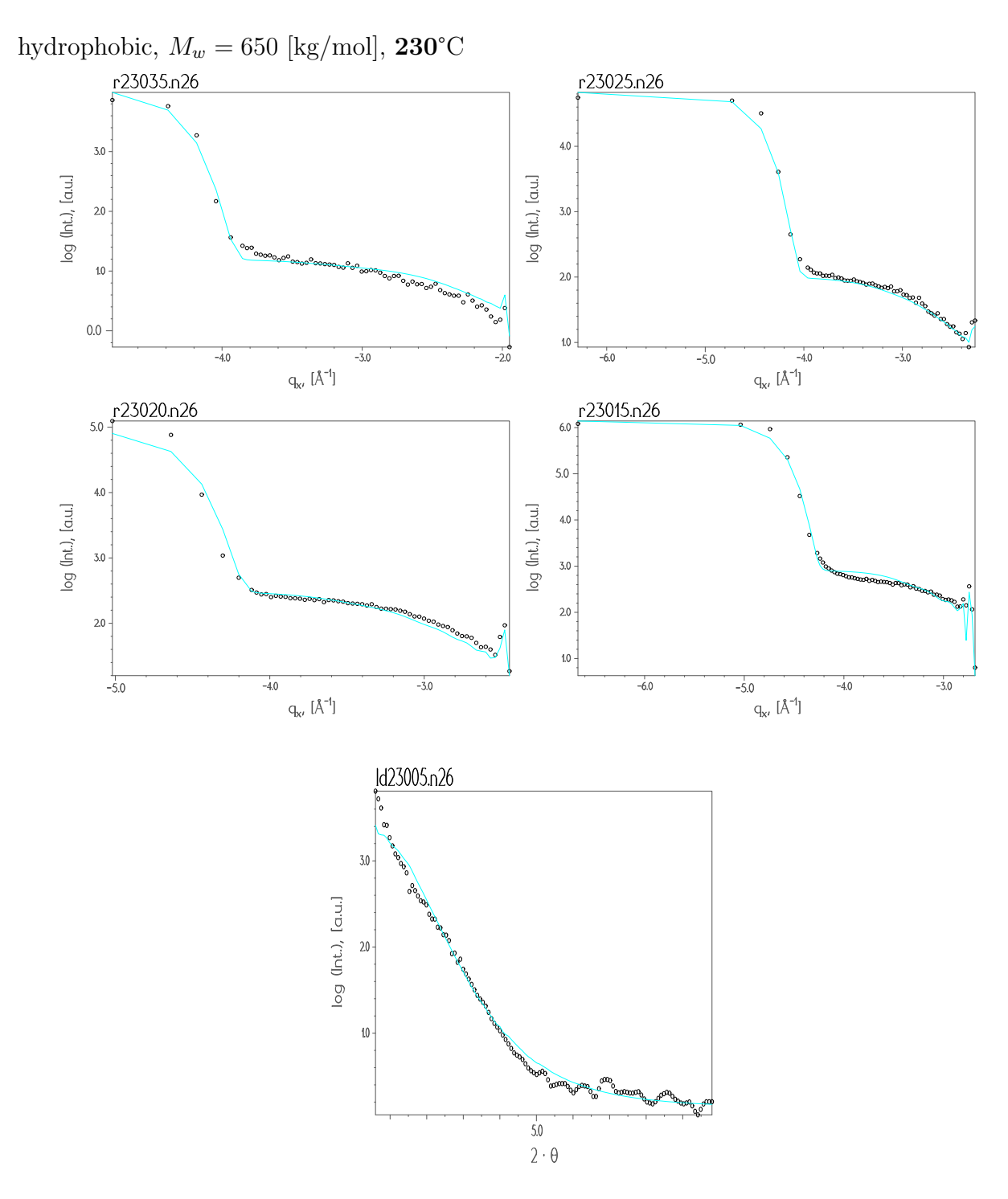


Figure A.84: Longitudinal and transverse scans of sample **n26** at **230**°C refined with the *Fractal model*. The curves with the symbols are the experimental data and the lines are the fits.

Sample	Correlation length	Hurst parameter	Correlation length	Hurst parameter
number	of the substrate,	of the substrate,	of the first layer,	of the first layer
	$\xi_{sub}\cdot 10^3, [{ m \AA}]$	h_{sub}	$\xi_{SiO_x} \cdot 10^3, [\text{Å}]$	h_{SiO_x}
n26	$0.90^{(f)}$	$0.40^{(f)}$	0.040 ± 0.002	0.416 ± 0.002
n46	$0.80^{(f)}$	$0.50^{(f)}$	0.3005 ± 0.0007	$0.20^{(f)}$
n86	$0.90^{(f)}$	0.3852 ± 0.0004	$0.10^{(f)}$	$0.20^{(f)}$
n16	0.7482 ± 0.0003	$0.70^{(f)}$	0.465 ± 0.001	$0.20^{(f)}$
n36	0.768 ± 0.002	$0.40^{(f)}$	0.3964 ± 0.0006	$0.20^{(f)}$
n21	0.9416 ± 0.0006	0.3365 ± 0.0002	0.9415 ± 0.0003	0.3365 ± 0.0003
n41	1.0150 ± 0.0007	0.418 ± 0.003	$0.10^{(f)}$	$0.20^{(f)}$
n81	0.9503 ± 0.0007	0.3853 ± 0.0004	0.900 ± 0.0001	$0.20^{(f)}$
n11	0.9348 ± 0.0001	0.3714 ± 0.0007	0.7392 ± 0.0006	$0.20^{(f)}$
n31	0.8820 ± 0.0001	$0.40^{(f)}$	0.273 ± 0.003	$0.30^{(f)}$
n23	$0.90^{(f)}$	0.4535 ± 0.0002	$0.09^{(f)}$	0.7256 ± 0.0003
n43	$0.90^{(f)}$	$0.40^{(f)}$	0.1002 ± 0.0006	$0.20^{(f)}$
n83	$0.80^{(f)}$	$0.40^{(f)}$	0.418 ± 0.002	$0.20^{(f)}$
n13	1.0135 ± 0.0007	0.5767 ± 0.0003	0.1394 ± 0.0002	$0.20^{(f)}$
n33	$0.80^{(f)}$	$0.40^{(f)}$	0.2713 ± 0.0003	$0.20^{(f)}$

Table A.12: Correlation length and Hurst parameter of the substrate and the first layer obtained after the refinement of diffuse scattering curves measured at 230°C (*Liquid model*).

Sample	Surface tension,	χ^2
number	$\eta, [N/m]$	
n26	0.01543 ± 0.00007	5.69
n46	0.01608 ± 0.00007	6.85
n86	0.01466 ± 0.00008	8.11
n16	0.01664 ± 0.00002	4.88
n36	0.01036 ± 0.00001	8.34
n21	0.01002 ± 0.00004	20.89
n41	0.01090 ± 0.0007	39.23
n81	0.0202 ± 0.0001	14.27
n11	0.0162 ± 0.0001	7.78
n31	0.0168 ± 0.0001	7.09
n23	0.01142 ± 0.00007	7.71
n43	0.0157 ± 0.0001	9.96
n83	0.01073 ± 0.0001	9.39
n13	0.01615 ± 0.00008	4.39
n33	0.01158 ± 0.00004	8.90

Table A.13: Surface tension at the polymer/air interface and χ^2 obtained from refinements of diffuse scattering curves measured at 230°C (*Liquid model*).

Sample	Correlation length	Hurst parameter	Correlation length	Hurst parameter
number	of the substrate,	of the substrate,	of the first layer,	of the first layer
	$\xi_{sub}\cdot 10^3,$ [Å]	h_{sub}	$\xi_{SiO_x} \cdot 10^3$, [Å]	h_{SiO_x}
n26	6.98 ± 0.03	0.35 ± 0.05	0.42 ± 0.08	0.86 ± 0.05
n46	0.9501 ± 0.0004	0.5604 ± 0.0003	0.1758 ± 0.0002	0.1706 ± 0.0001
n86	0.648 ± 0.002	0.492 ± 0.006	0.983 ± 0.002	0.226 ± 0.002
n16	0.684 ± 0.003	0.687 ± 0.003	0.559 ± 0.001	$0.20^{(f)}$
n36	0.3500 ± 0.0004	0.3258 ± 0.0002	0.04742 ± 0.00003	$0.20^{(f)}$
n21	0.8707 ± 0.0006	0.7539 ± 0.0003	0.9428 ± 0.003	$0.20^{(f)}$
n41	0.186 ± 0.008	0.584 ± 0.006	0.2043 ± 0.0002	$0.20^{(f)}$
n81	2.0641 ± 0.0006	0.5951 ± 0.0004	0.9352 ± 0.001	$0.20^{(f)}$
n11	0.6056 ± 0.0006	$0.20^{(f)}$	0.555 ± 0.001	$0.20^{(f)}$
n31	0.353 ± 0.004	$0.59^{(f)}$	0.5908 ± 0.0006	$0.20^{(f)}$
n23	4.0335 ± 0.0002	$0.20^{(f)}$	$0.10^{(f)}$	$0.20^{(f)}$
n43	1.11 ± 0.02	$0.20^{(f)}$	0.1986 ± 0.0004	$0.20^{(f)}$
n83	0.4554 ± 0.0006	$0.20^{(f)}$	2.8355 ± 0.0008	$0.20^{(f)}$
n13	0.9400 ± 0.004	$0.20^{(f)}$	$0.10^{(f)}$	$0.20^{(f)}$
n33	$0.20^{(f)}$	$0.20^{(f)}$	$0.10^{(f)}$	$0.10^{(f)}$

Table A.14: Correlation length and Hurst parameter of the substrate and the first layer obtained after the refinement of diffuse scattering curves measured at 230°C (*Fractal model*).

Sample	Correlation length	Hurst parameter of	Roughness of	
number	of the polym. film,	the polym. film,	the polym. film,	χ^2
	$\xi_{PS} \cdot 10^3, [\text{Å}]$	h_{PS}	$\sigma_{PS},~[{ m \AA}]$	
n26	2.77 ± 0.02	0.25 ± 0.03	7.85 ± 0.02	9.60
n46	1.0587 ± 0.0003	0.2586 ± 0.0001	6.984 ± 0.003	4.35
n86	3.475 ± 0.003	$0.20^{(f)}$	7.717 ± 0.003	3.60
n16	1.0914 ± 0.0007	$0.20^{(f)}$	7.388 ± 0.007	7.88
n36	4.8347 ± 0.0002	$0.20^{(f)}$	7.6154 ± 0.0003	1.53
n21	6.8273 ± 0.0003	$0.20^{(f)}$	10.375 ± 0.001	4.67
n41	4.919 ± 0.005	$0.20^{(f)}$	9.899 ± 0.002	20.60
n81	3.799 ± 0.001	0.2327 ± 0.0001	7.3491 ± 0.0008	7.51
n11	0.9202 ± 0.0003	$0.19^{(f)}$	6.7986 ± 0.0002	12.83
n31	2.040 ± 0.001	$0.20^{(f)}$	8.152 ± 0.001	7.81
n23	11.899 ± 0.0003	0.22418 ± 0.00003	10.002 ± 0.002	4.13
n43	17.073 ± 0.009	0.2006 ± 0.0004	10.002 ± 0.002	7.62
n83	6.6981 ± 0.0004	0.2347 ± 0.0001	9.1159 ± 0.0007	13.89
n13	6.8600 ± 0.002	$0.20^{(f)}$	7.001 ± 0.001	4.77
n33	3.063 ± 0.003	$0.20^{(f)}$	9.050 ± 0.002	9.45

Table A.15: Correlation length, Hurst parameter and roughness of the polymer film as well as χ^2 obtained from refinements of diffuse scattering curves measured at 230°C (*Fractal model*).

Samples n46, n41, n86 and n81 were measured at 200°C, sample n31 at 190°C.

A.2.2.2 Hydrophobic samples

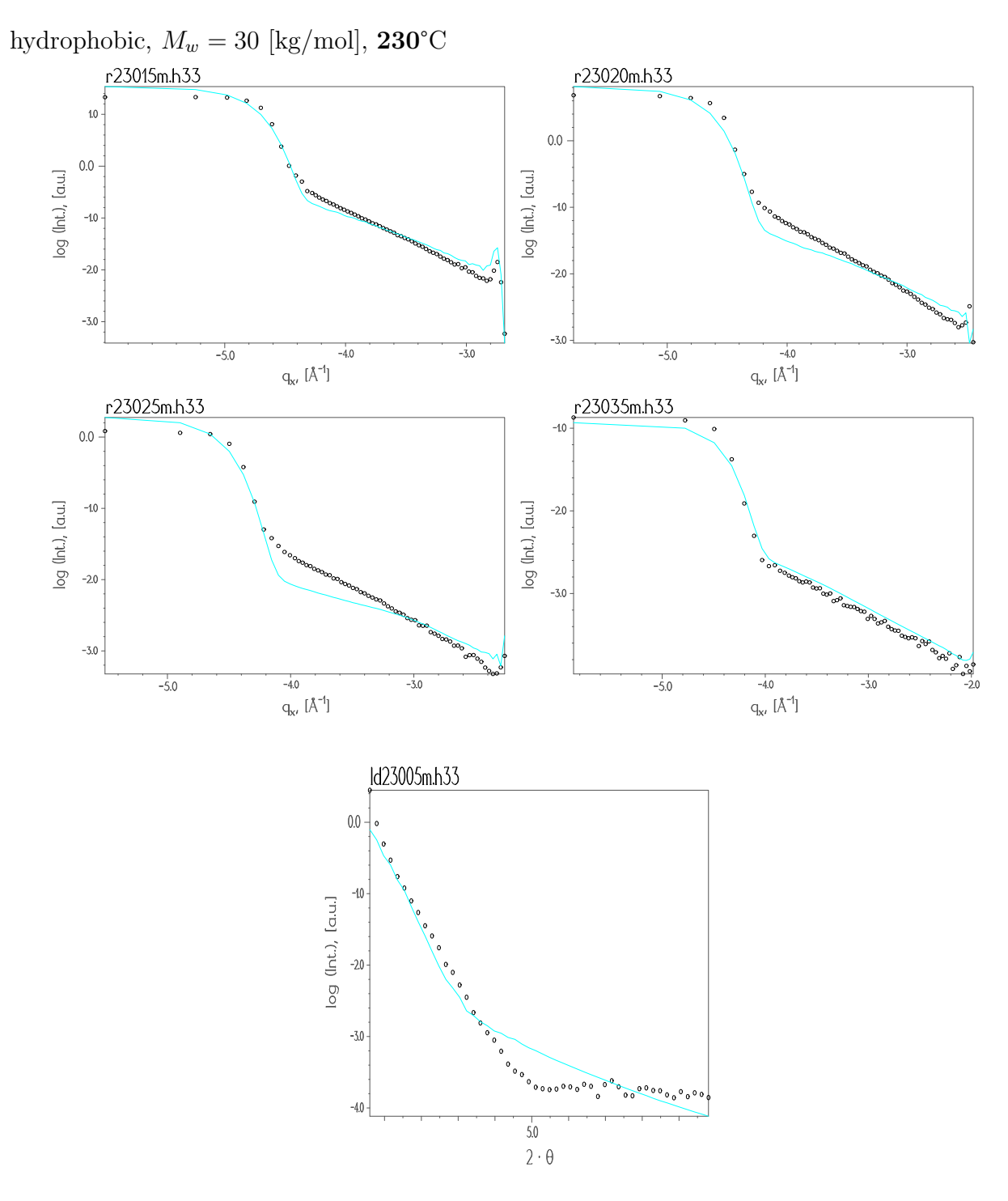


Figure A.85: Longitudinal and transverse scans of sample h33 at 230° C refined with the Liquid model. The curves with the symbols are the experimental data and the lines are the fits.

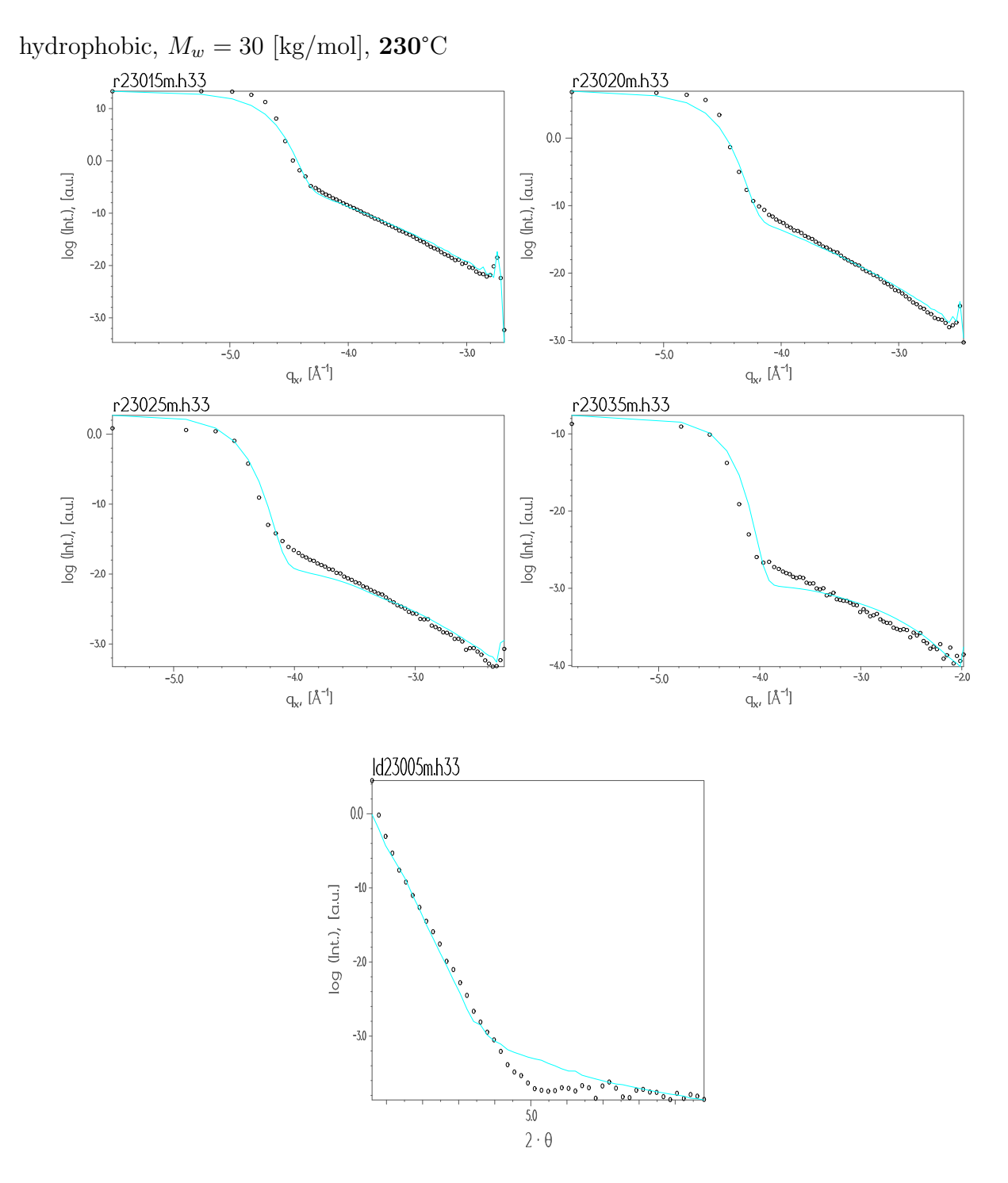


Figure A.86: Longitudinal and transverse scans of sample **h33** at **230**°C refined with the *Fractal model*. The curves with the symbols are the experimental data and the lines are the fits.

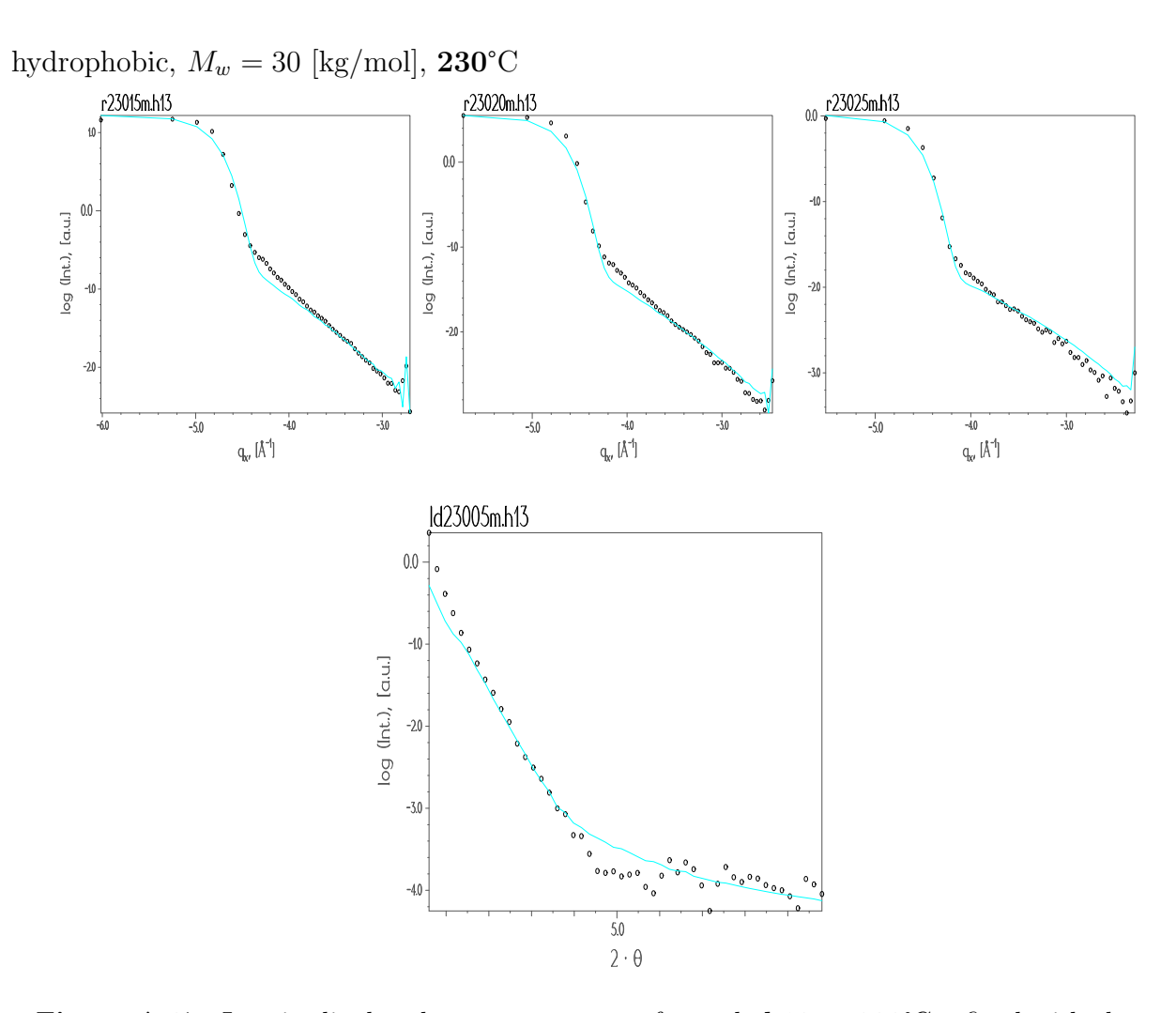


Figure A.87: Longitudinal and transverse scans of sample h13 at 230° C refined with the Liquid model. The curves with the symbols are the experimental data and the lines are the fits.

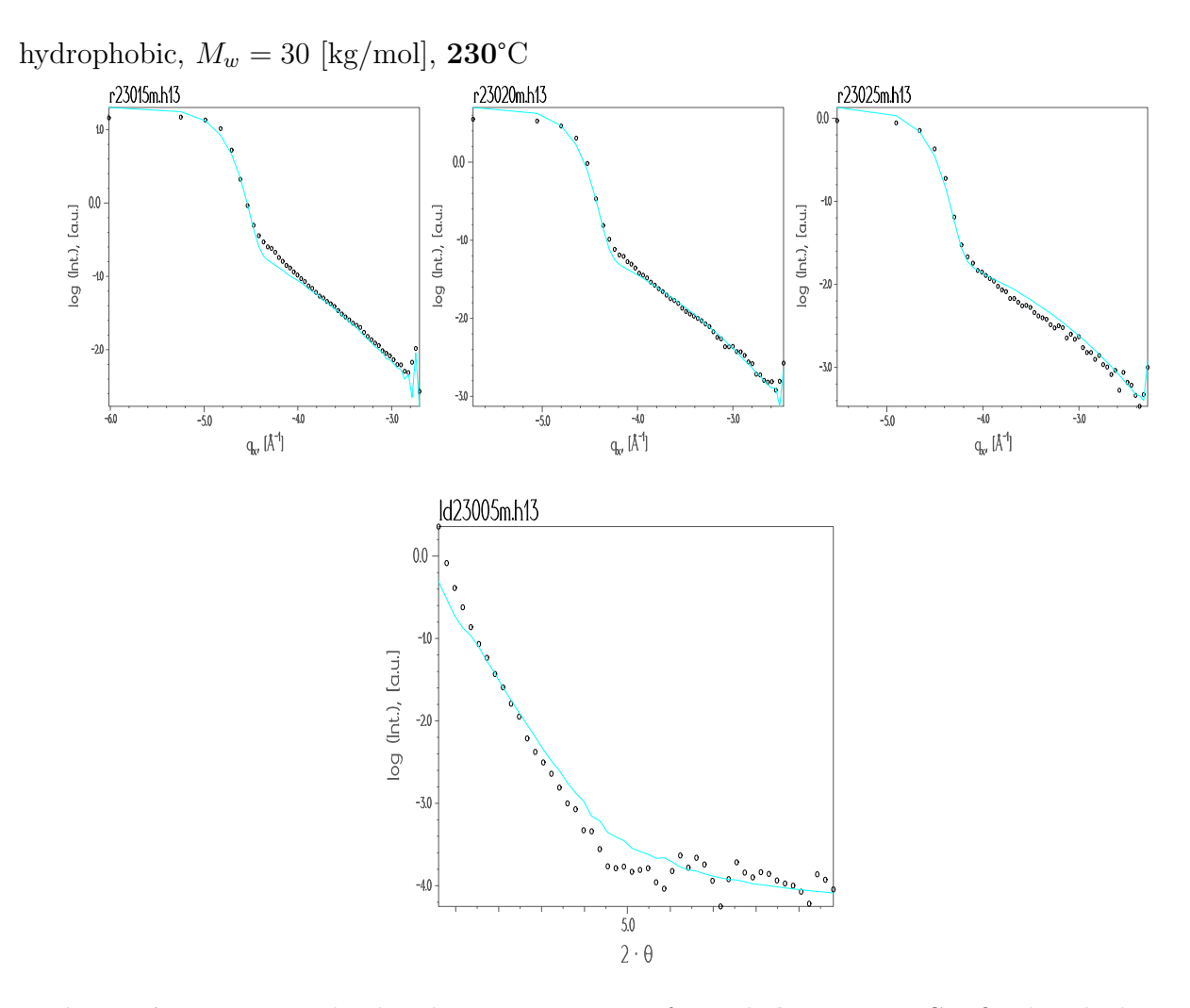


Figure A.88: Longitudinal and transverse scans of sample h13 at 230° C refined with the Fractal model. The curves with the symbols are the experimental data and the lines are the fits.

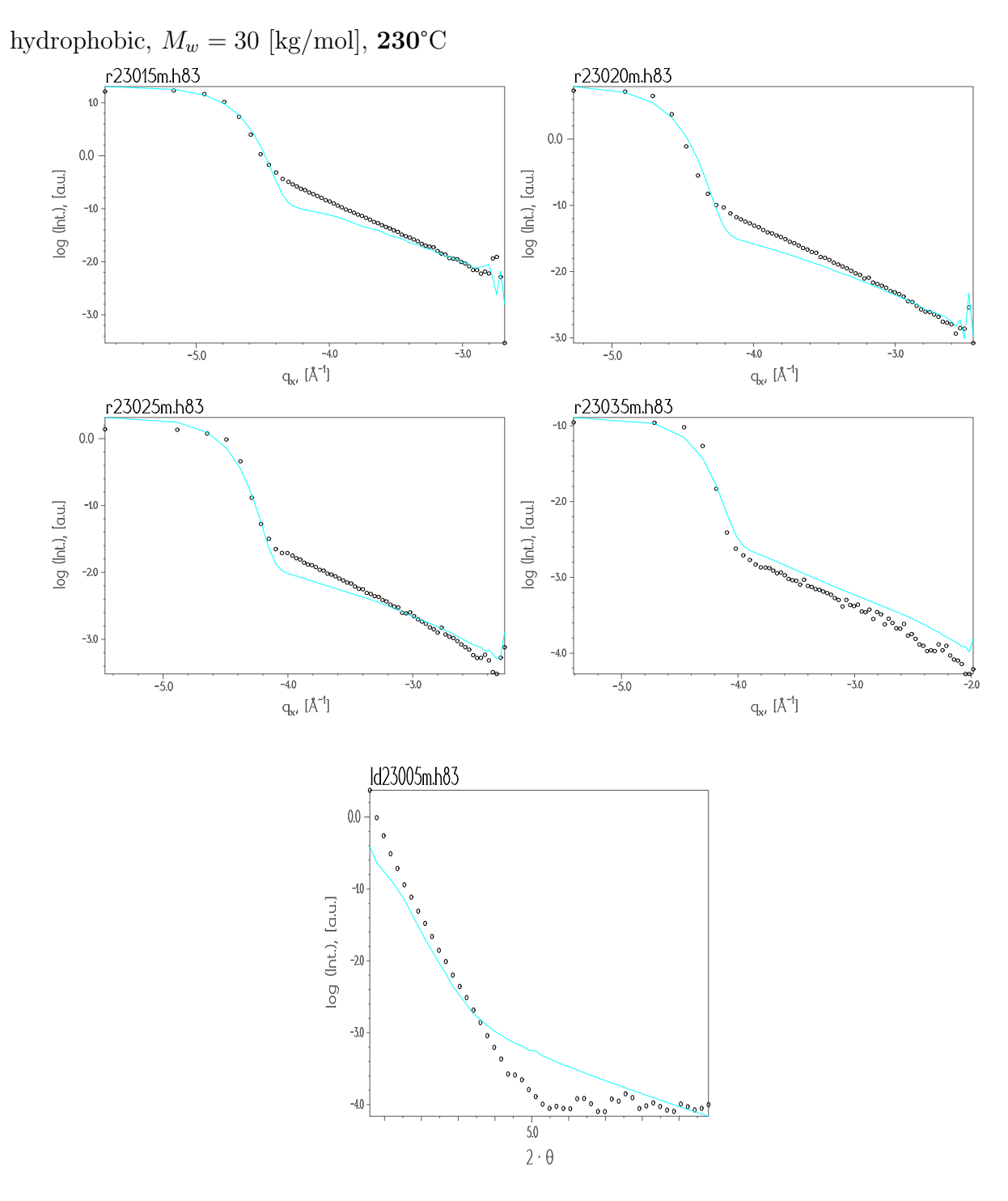


Figure A.89: Longitudinal and transverse scans of sample **h83** at **230**°C refined with the *Liquid model*. The curves with the symbols are the experimental data and the lines are the fits.

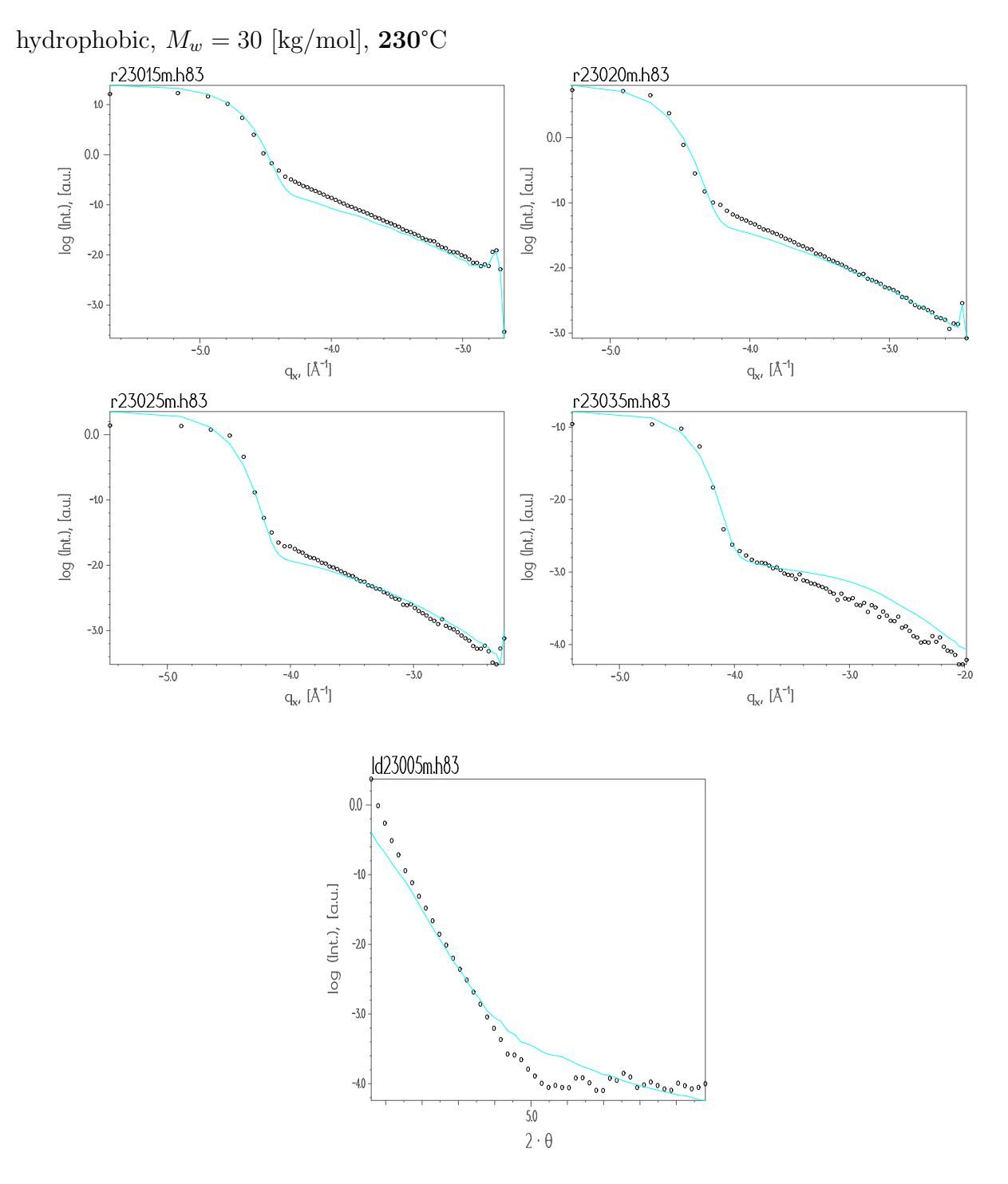


Figure A.90: Longitudinal and transverse scans of sample **h83** at **230°**C refined with the *Fractal model*. The curves with the symbols are the experimental data and the lines are the fits.

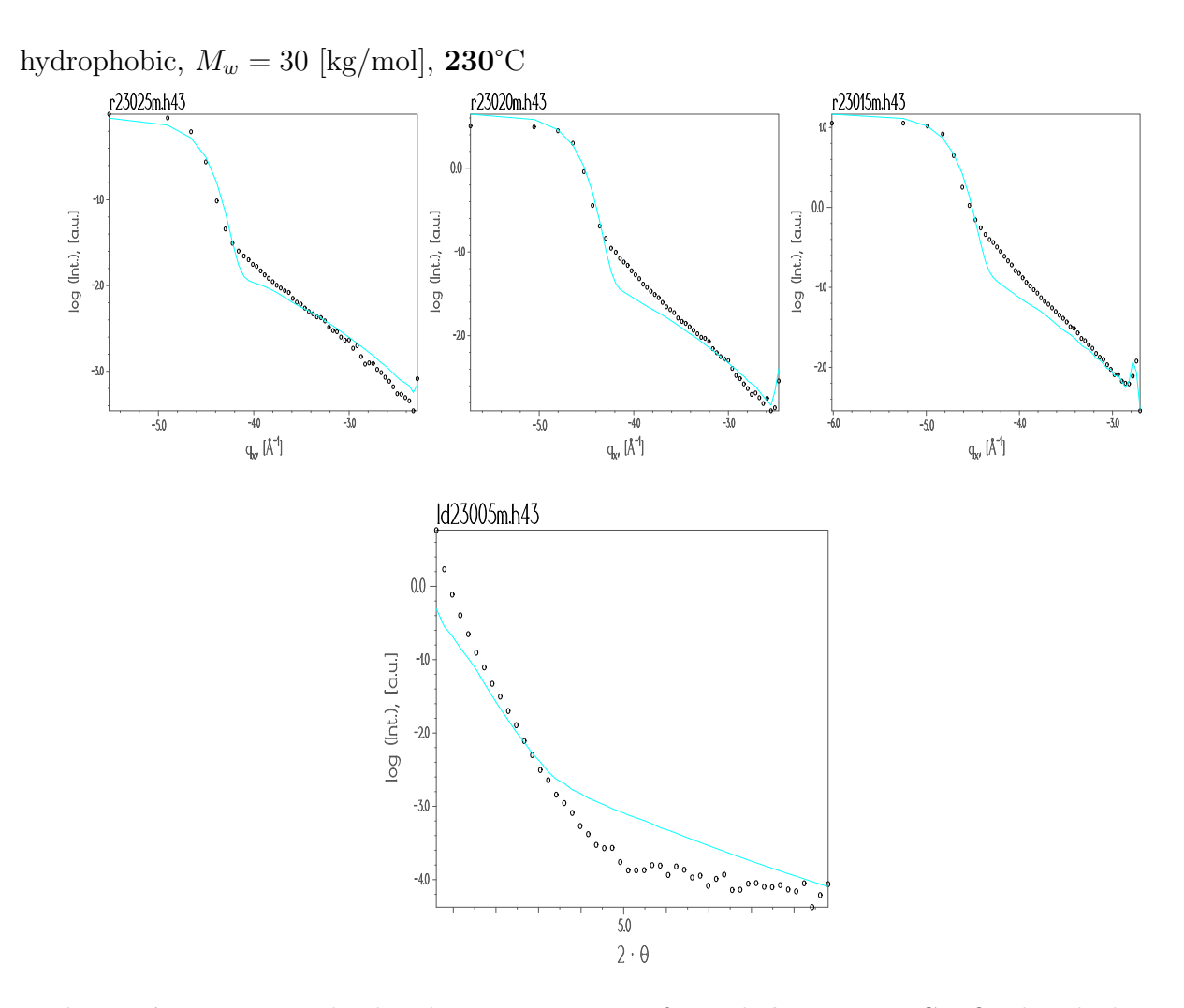


Figure A.91: Longitudinal and transverse scans of sample $\mathbf{h43}$ at $\mathbf{230}^{\circ}\mathrm{C}$ refined with the Liquid model. The curves with the symbols are the experimental data and the lines are the fits.

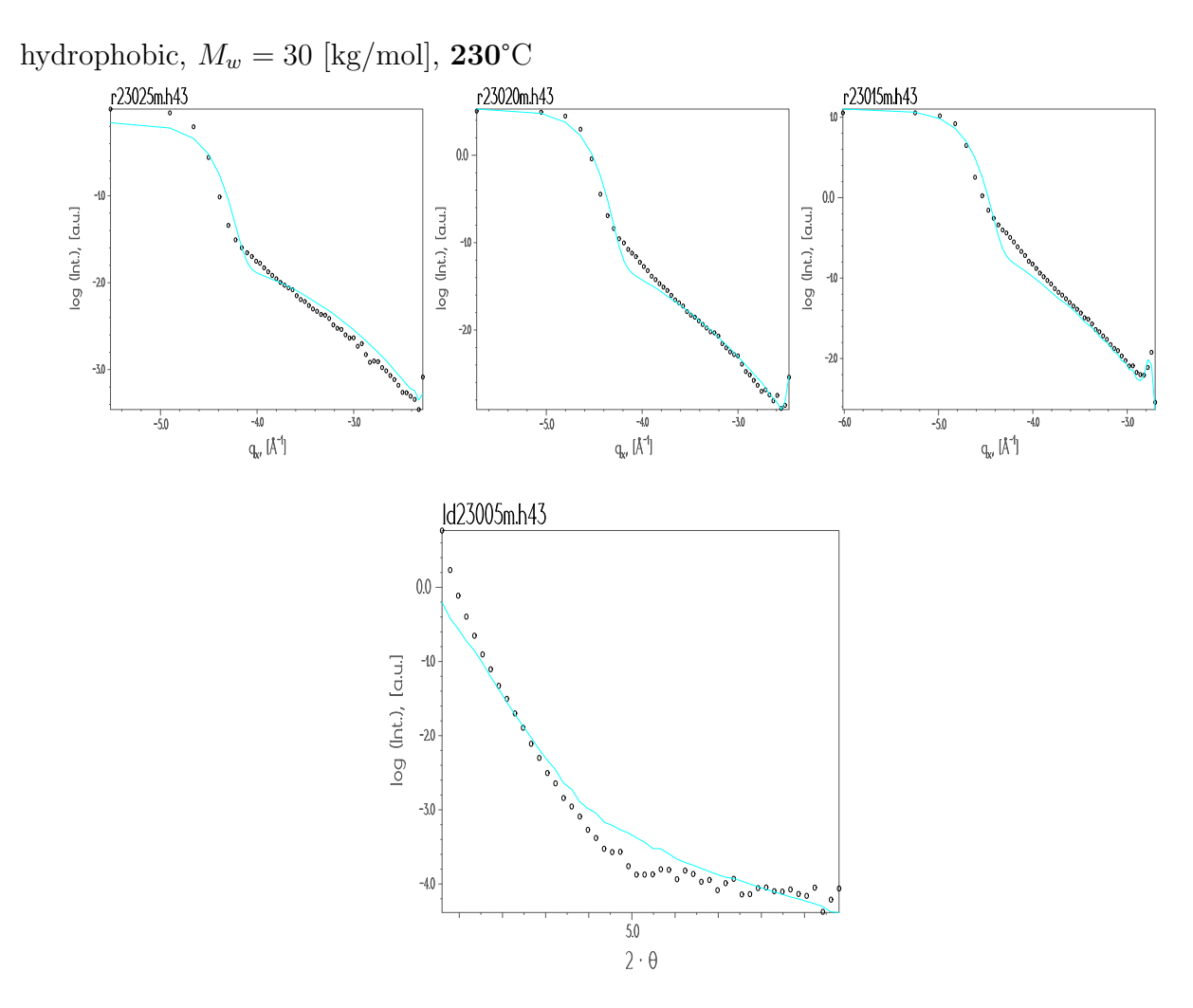


Figure A.92: Longitudinal and transverse scans of sample **h43** at **230°**C refined with the *Fractal model*. The curves with the symbols are the experimental data and the lines are the fits.

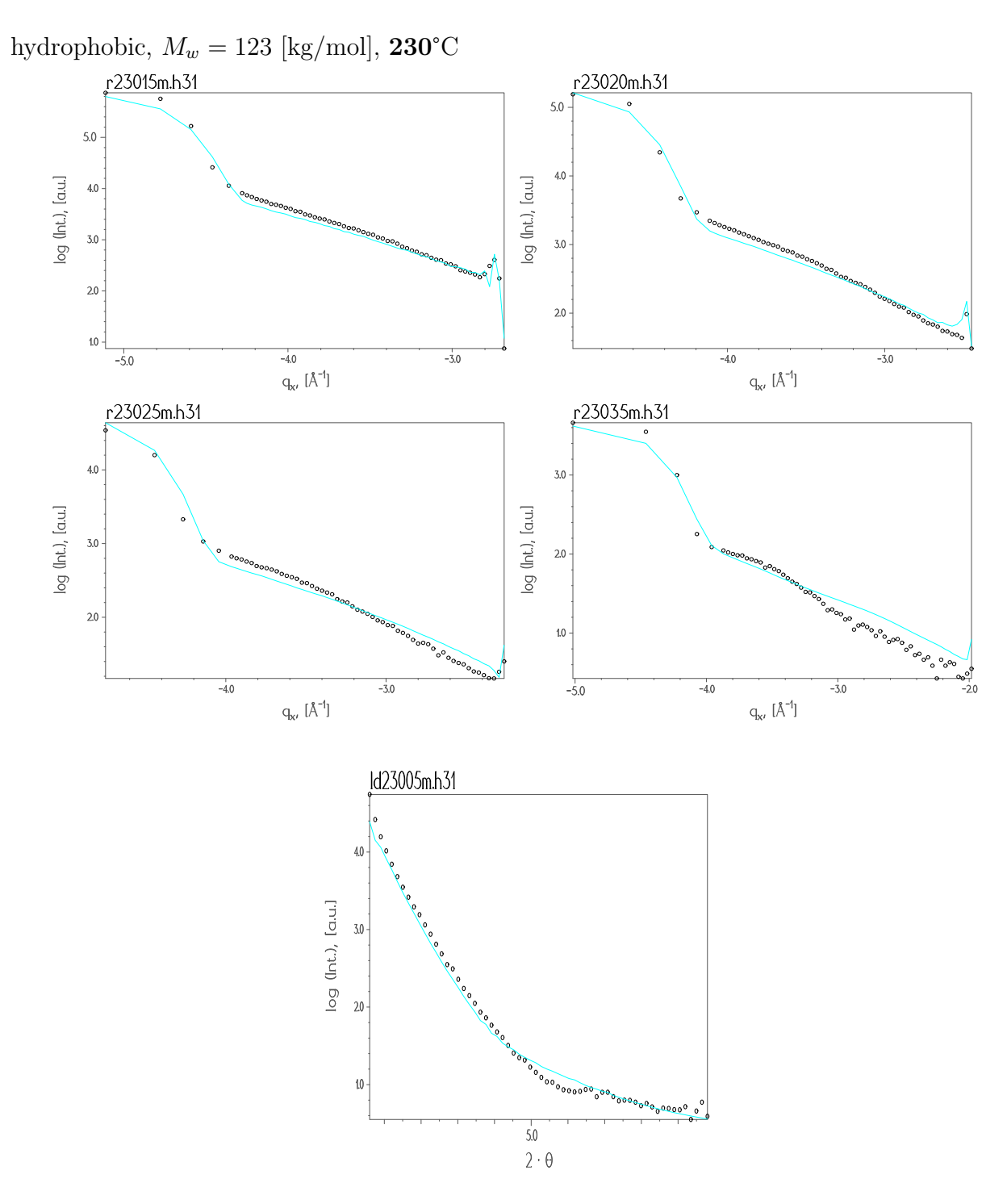


Figure A.93: Longitudinal and transverse scans of sample **h31** at **230**°C refined with the *Liquid model*. The curves with the symbols are the experimental data and the lines are the fits.

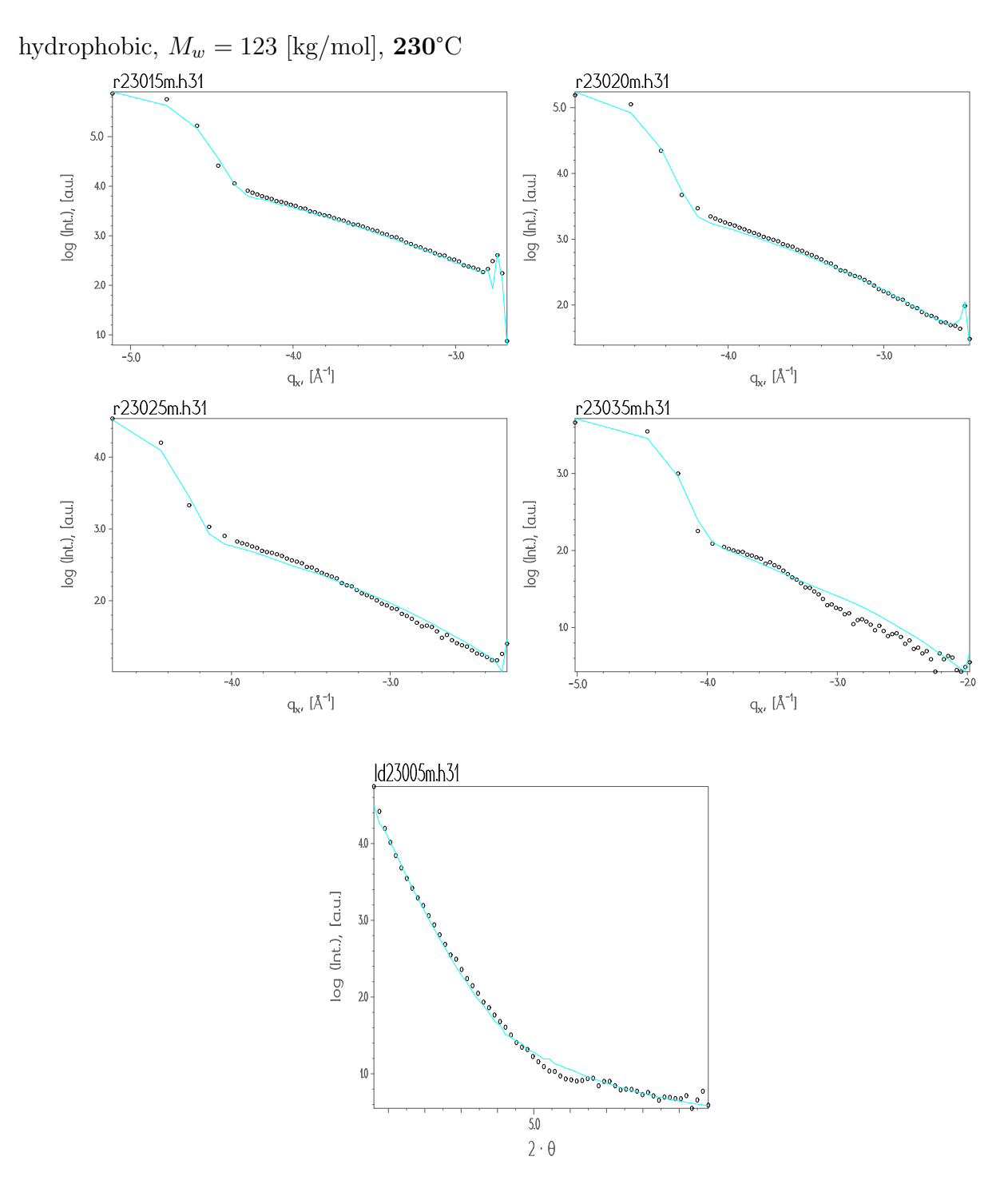


Figure A.94: Longitudinal and transverse scans of sample **h31** at **230**°C refined with the *Fractal model*. The curves with the symbols are the experimental data and the lines are the fits.

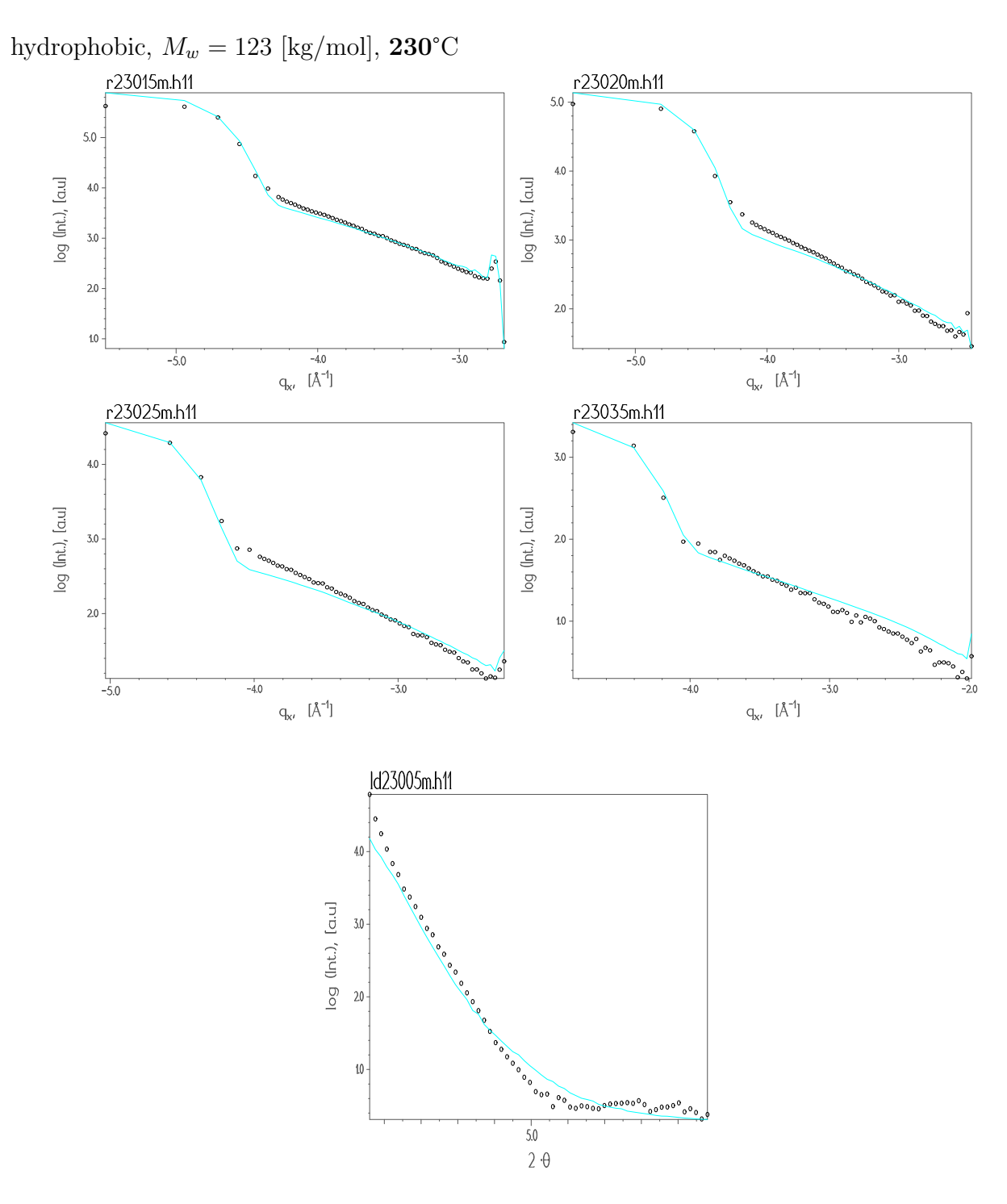


Figure A.95: Longitudinal and transverse scans of sample **h11** at **230**°C refined with the *Liquid model*. The curves with the symbols are the experimental data and the lines are the fits.

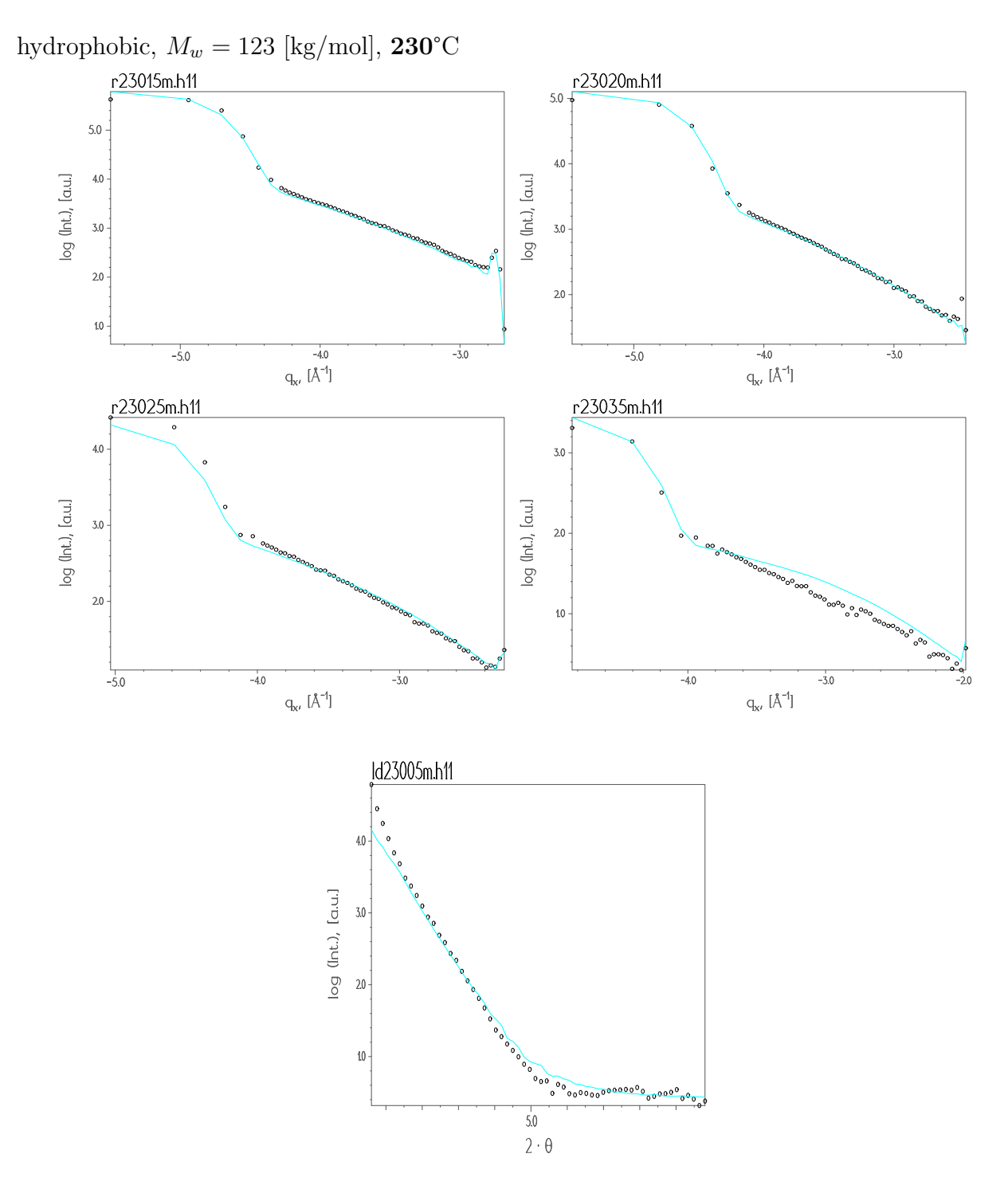


Figure A.96: Longitudinal and transverse scans of sample **h11** at **230**°C refined with the *Fractal model*. The curves with the symbols are the experimental data and the lines are the fits.

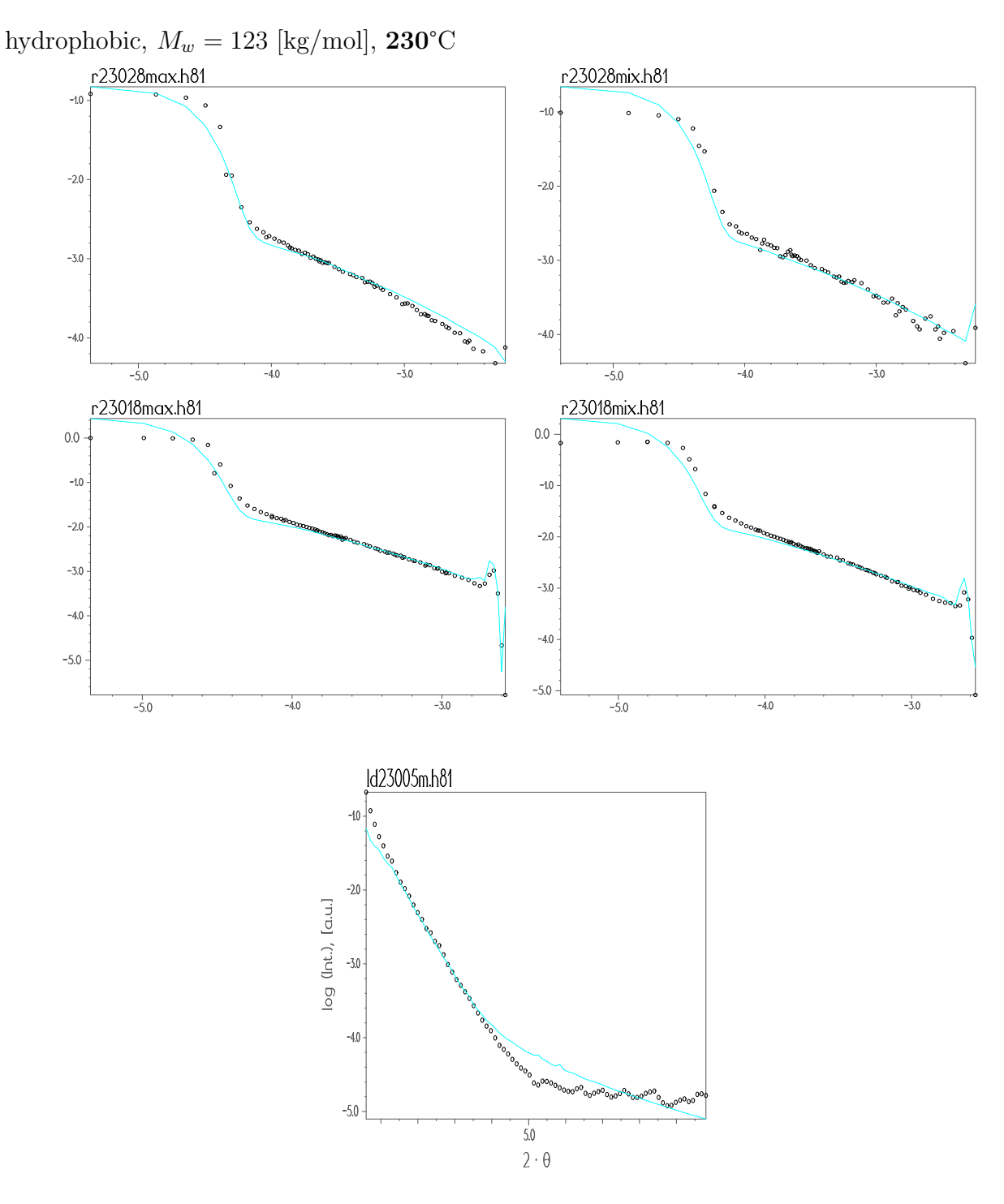


Figure A.97: Longitudinal and transverse scans of sample h81 at 230° C refined with the Liquid model. The curves with the symbols are the experimental data and the lines are the fits.

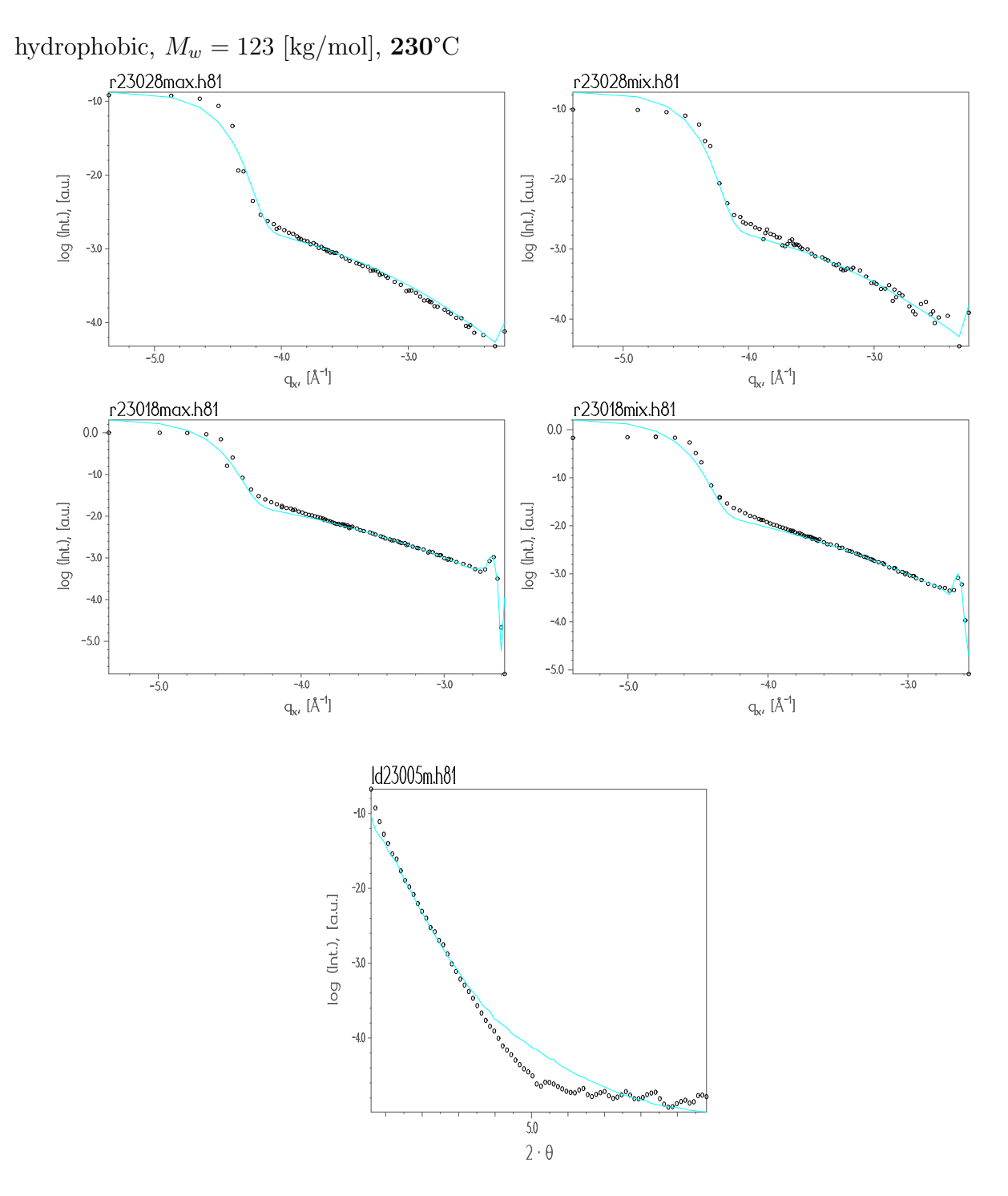


Figure A.98: Longitudinal and transverse scans of sample **h81** at **230**°C refined with the *Fractal model*. The curves with the symbols are the experimental data and the lines are the fits.

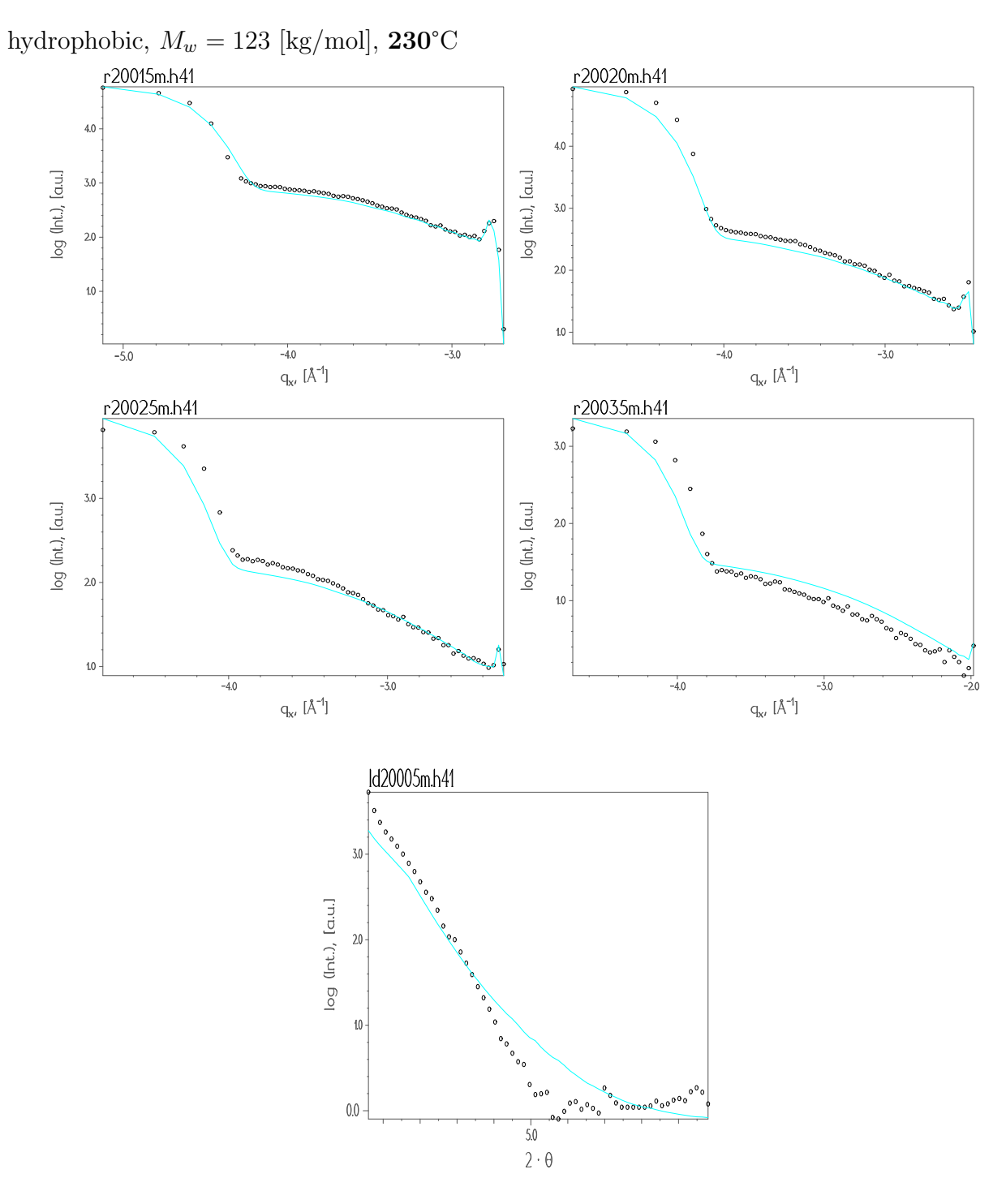


Figure A.99: Longitudinal and transverse scans of sample h41 at 200° C refined with the Liquid model. The curves with the symbols are the experimental data and the lines are the fits.

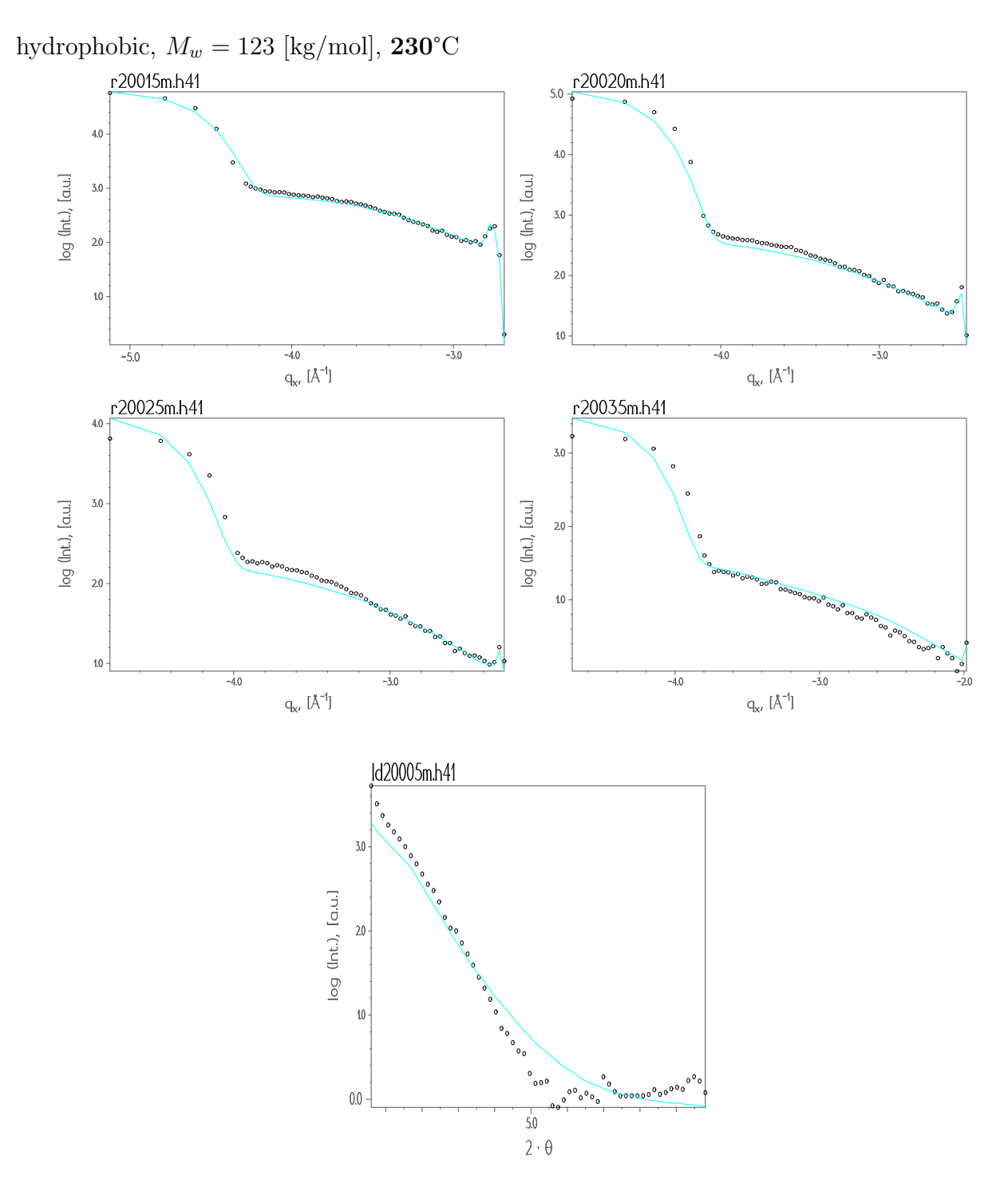


Figure A.100: Longitudinal and transverse scans of sample h41 at 200° C refined with the Fractal model. The curves with the symbols are the experimental data and the lines are the fits.

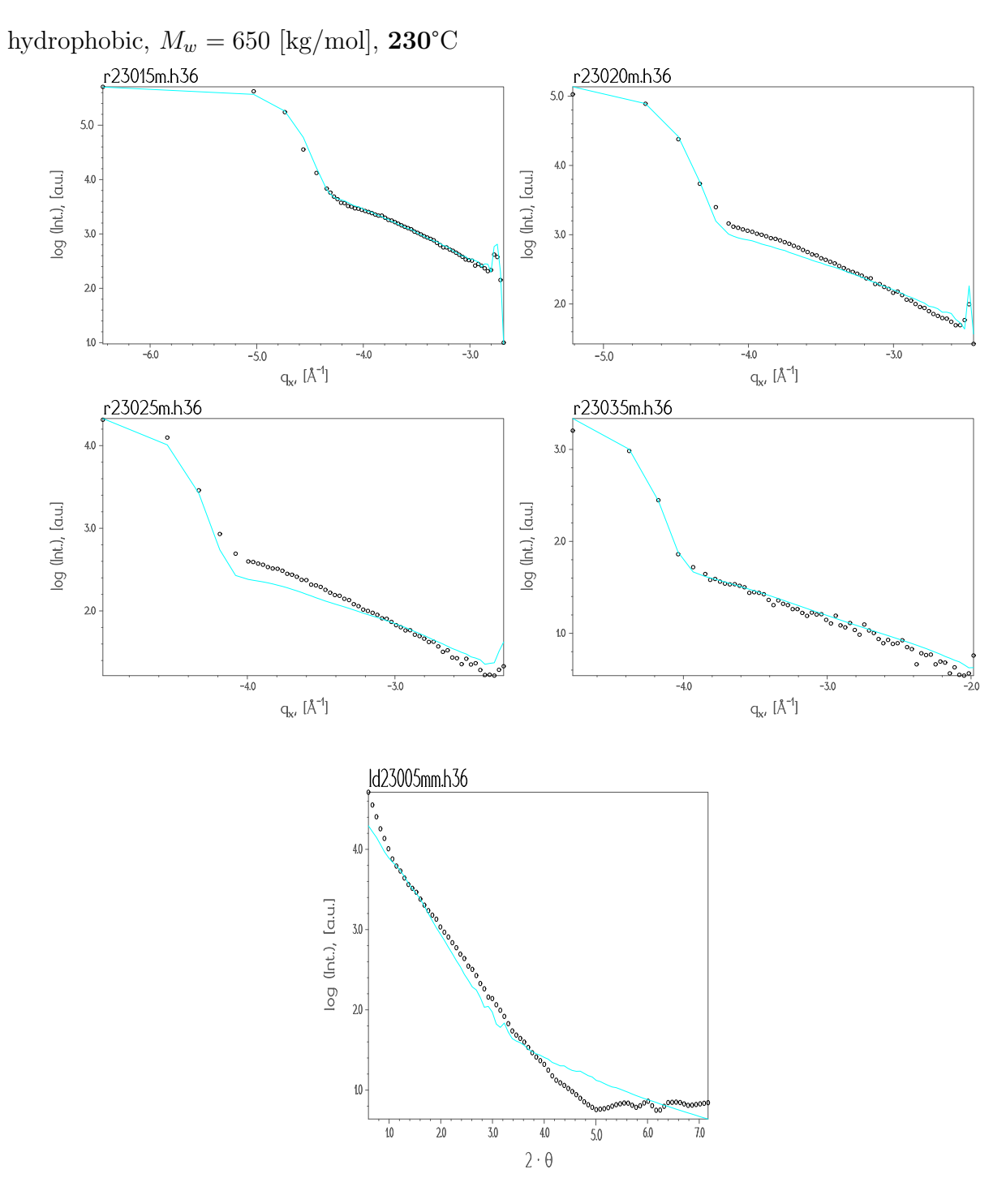


Figure A.101: Longitudinal and transverse scans of sample **h36** at **230°**C refined with the *Liquid model*. The curves with the symbols are the experimental data and the lines are the fits.

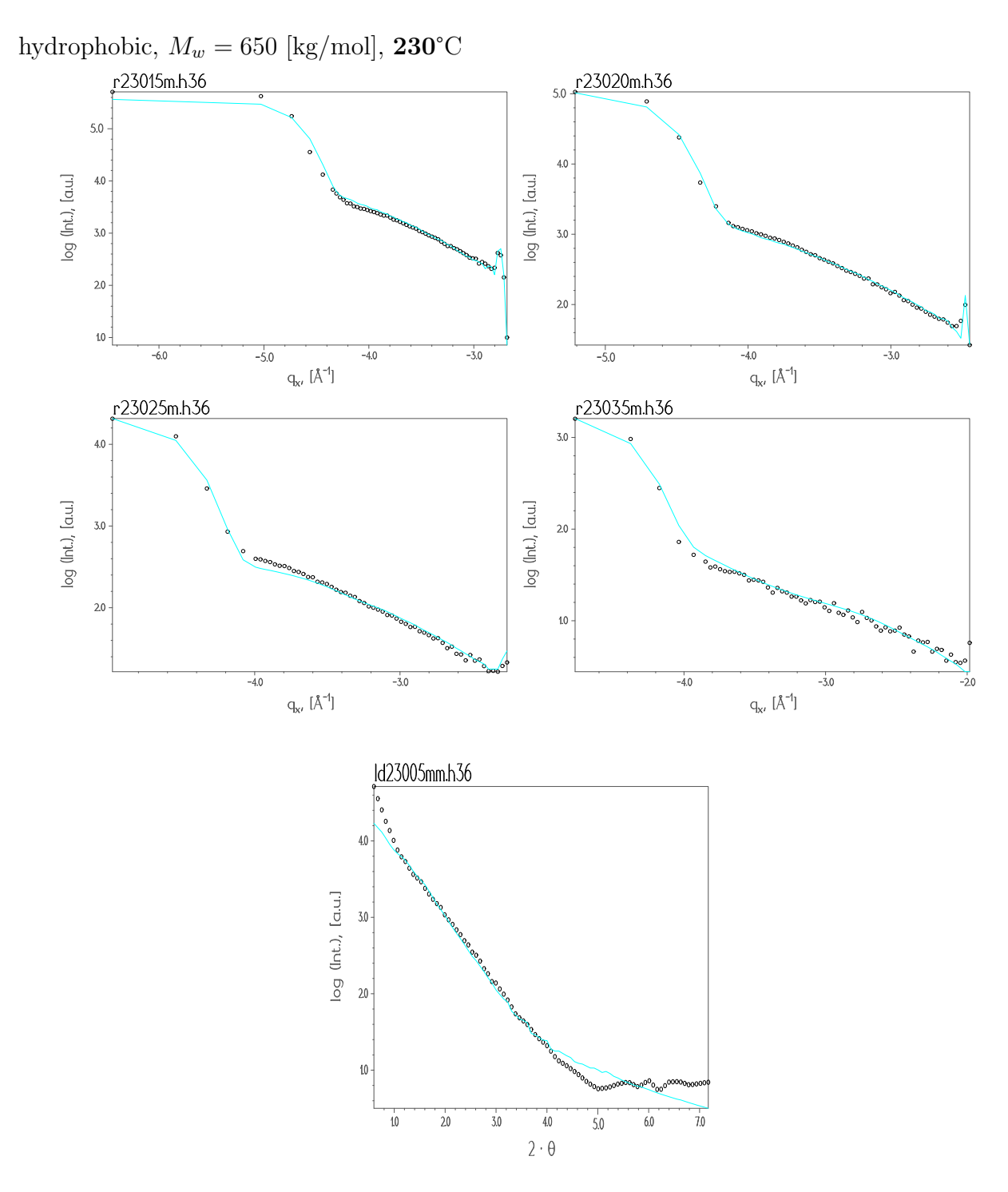


Figure A.102: Longitudinal and transverse scans of sample **h36** at **230**°C refined with the *Fractal model*. The curves with the symbols are the experimental data and the lines are the fits.

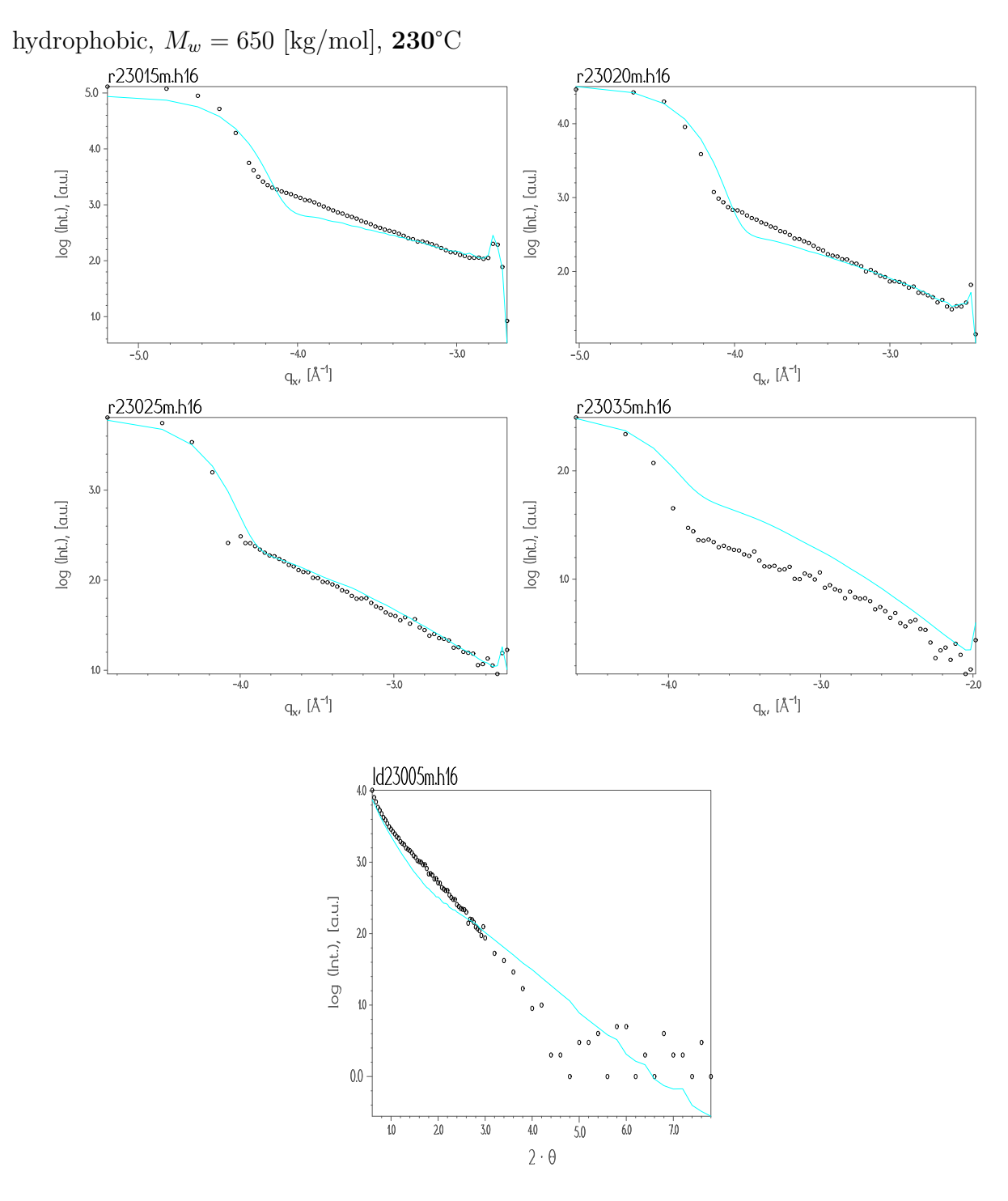


Figure A.103: Longitudinal and transverse scans of sample h16 at 230° C refined with the Liquid model. The curves with the symbols are the experimental data and the lines are the fits.

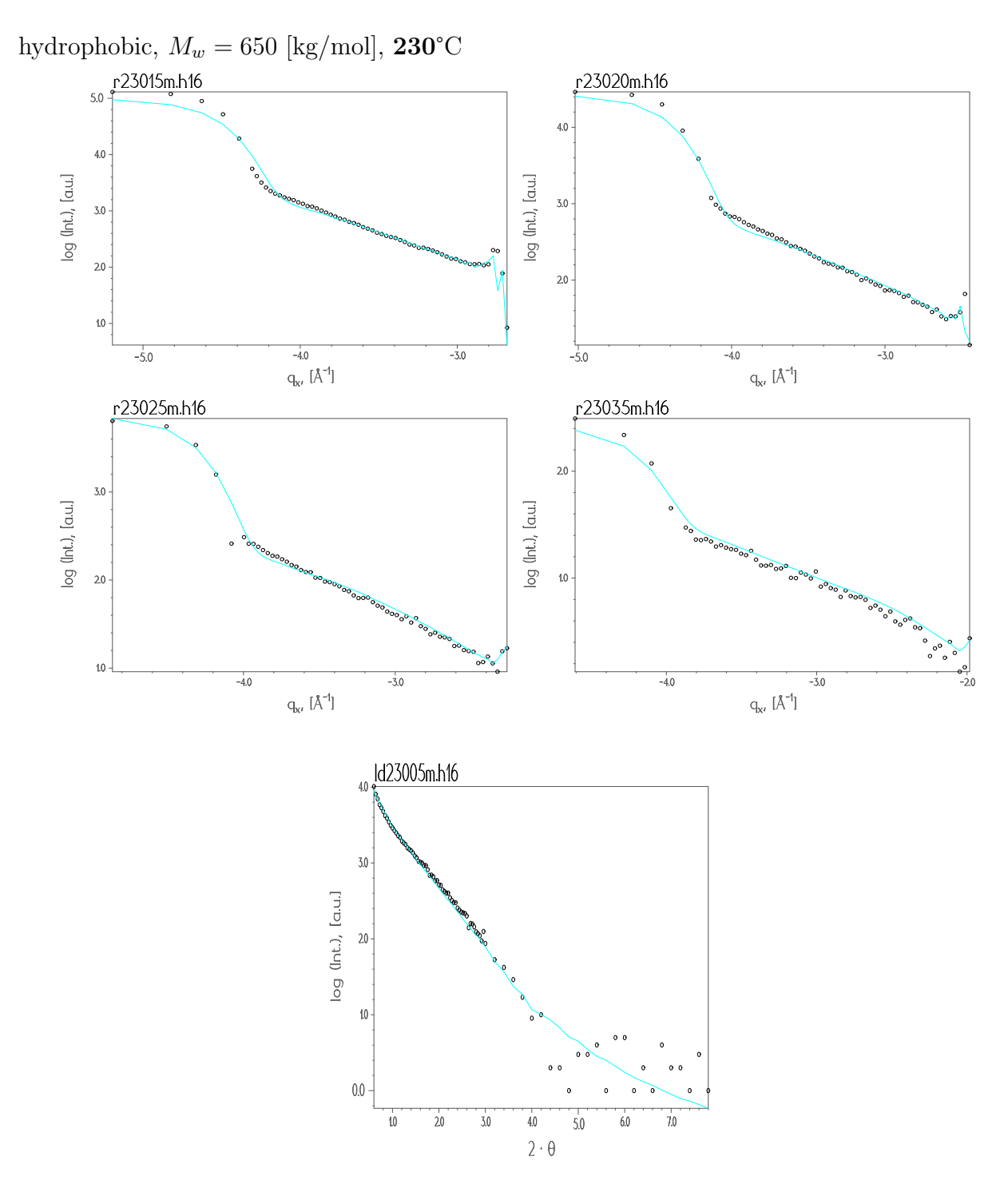


Figure A.104: Longitudinal and transverse scans of sample h16 at 230° C refined with the Fractal model. The curves with the symbols are the experimental data and the lines are the fits.

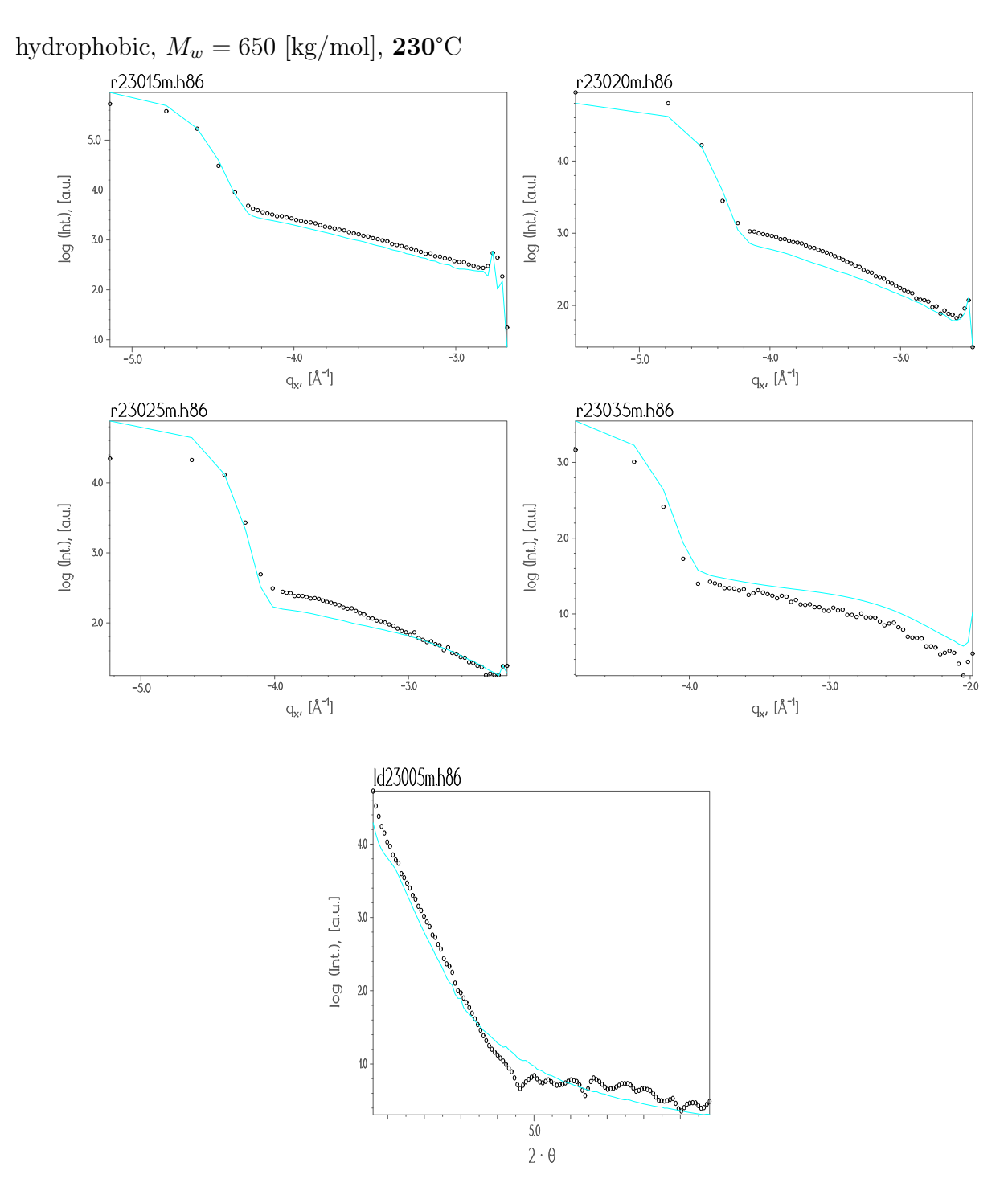


Figure A.105: Longitudinal and transverse scans of sample h86 at 230° C refined with the Liquid model. The curves with the symbols are the experimental data and the lines are the fits.

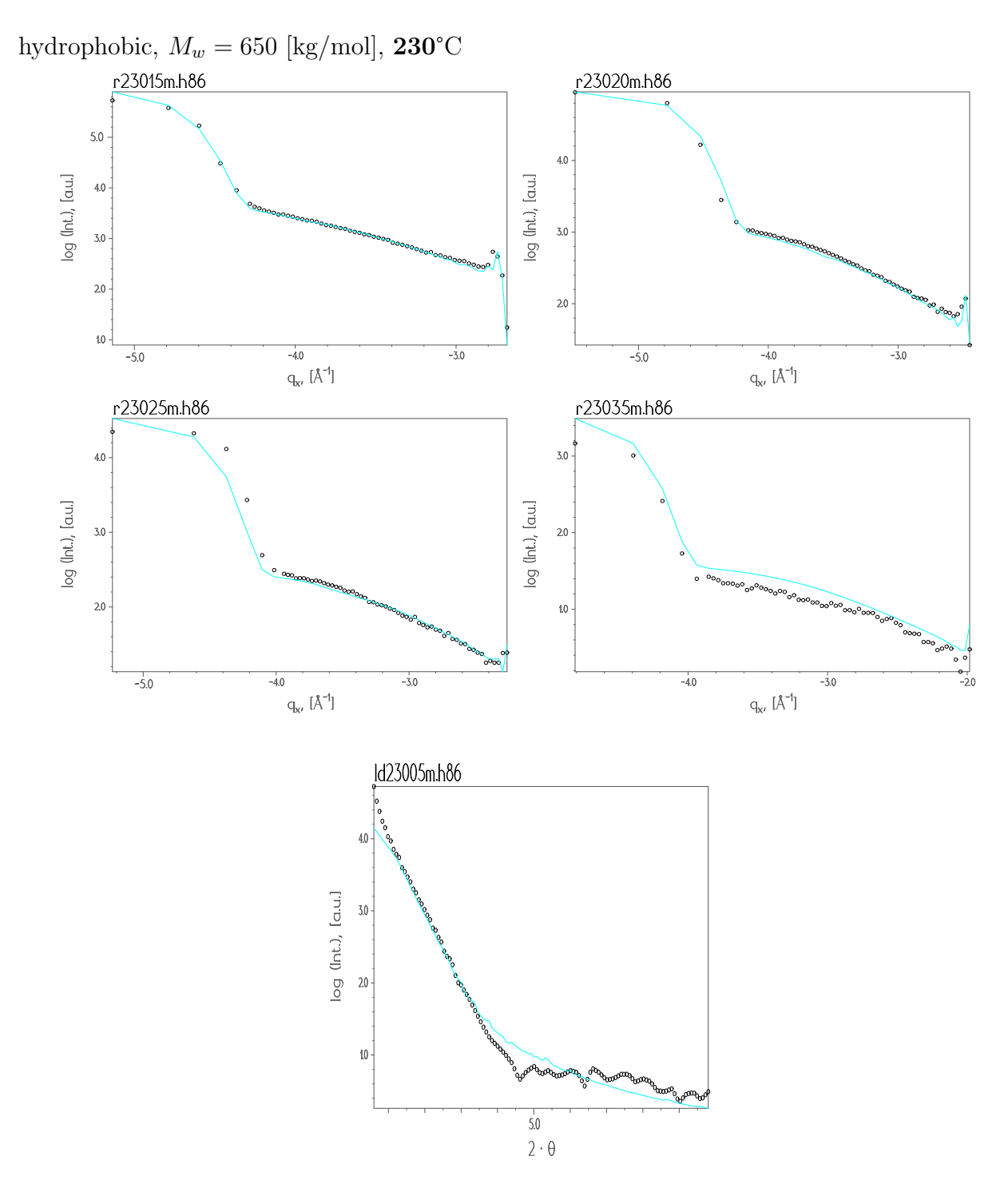


Figure A.106: Longitudinal and transverse scans of sample **h86** at **230**°C refined with the *Fractal model*. The curves with the symbols are the experimental data and the lines are the fits.

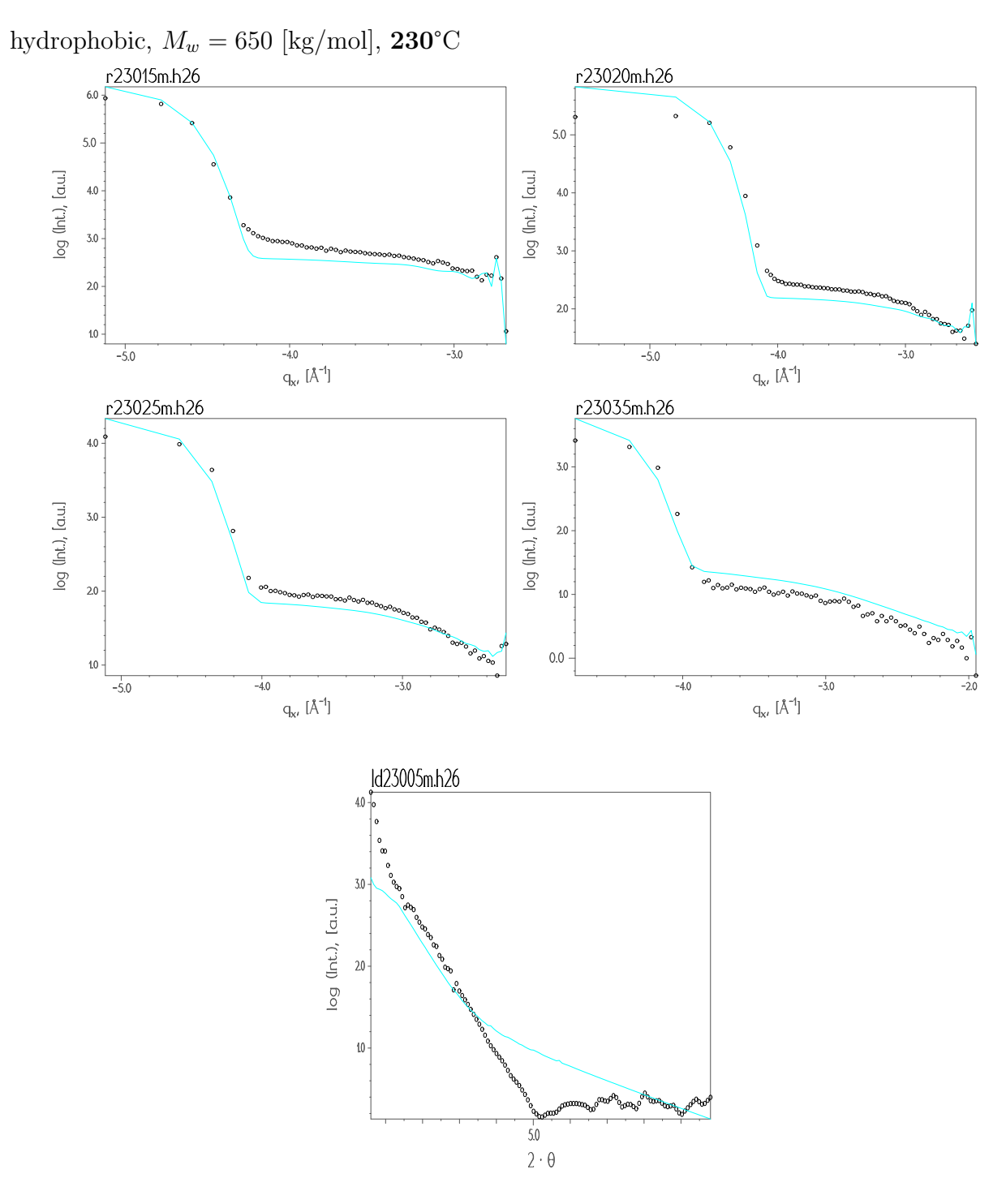


Figure A.107: Longitudinal and transverse scans of sample h26 at 230° C refined with the Liquid model. The curves with the symbols are the experimental data and the lines are the fits.

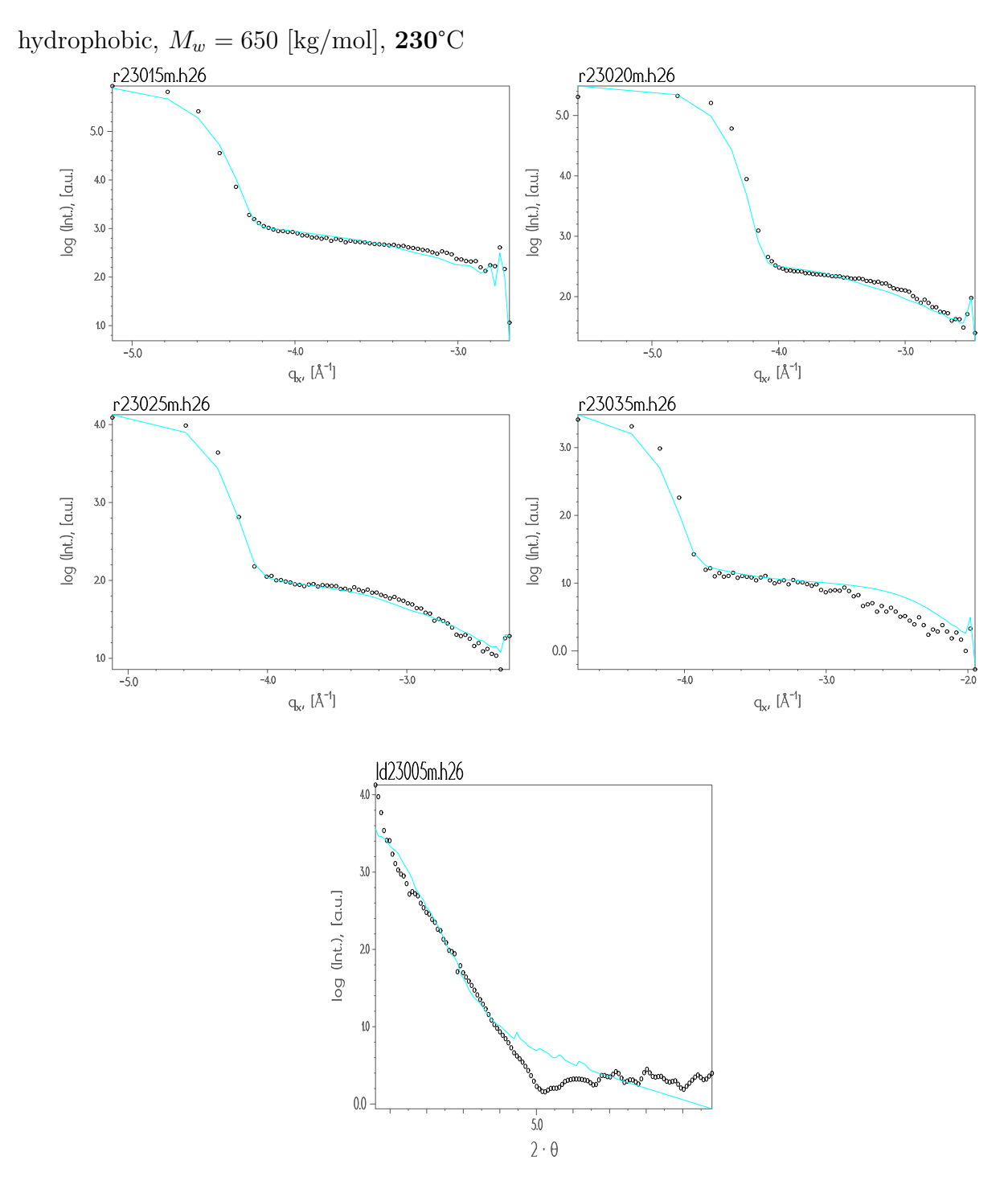


Figure A.108: Longitudinal and transverse scans of sample **h26** at **230**°C refined with the *Fractal model*. The curves with the symbols are the experimental data and the lines are the fits.

Sample	Correlation length	Hurst parameter	Correlation length	Hurst parameter
number	of the substrate,	of the substrate,	of the first layer,	of the first layer
	$\xi_{sub} \cdot 10^3$,[Å]	h_{sub}	$\xi_{SiO_x} \cdot 10^3$, [Å]	h_{SiO_x}
h26	0.567 ± 0.003	$0.20^{(f)}$	$0.60^{(f)}$	0.442 ± 0.003
h46	_	_	_	_
h86	0.4833 ± 0.0004	0.7920 ± 0.0002	0.1658 ± 0.0009	$0.25^{(f)}$
h16	2.02 ± 0.03	0.6716 ± 0.0007	0.6887 ± 0.0005	0.1969 ± 0.0005
h36	$0.10^{(f)}$	0.7921 ± 0.0001	0.826 ± 0.002	$0.25^{(f)}$
h21	_	_	_	_
h41	0.899 ± 0.003	$0.30^{(f)}$	0.7945 ± 0.0004	0.3423 ± 0.0002
h81	1.2827 ± 0.002	$0.20^{(f)}$	1.107 ± 0.002	$0.20^{(f)}$
h11	0.9295 ± 0.0003	$0.20^{(f)}$	$0.1.0^{(f)}$	$0.20^{(f)}$
h31	$1.0^{(f)}$	$0.20^{(f)}$	1.0423 ± 0.0006	$0.20^{(f)}$
h23	_	_	-	_
h43	$0.19^{(f)}$	0.577 ± 0.007	$0.40^{(f)}$	$0.20^{(f)}$
h83	$0.15^{(f)}$	$0.50^{(f)}$	$0.70^{(f)}$	$0.20^{(f)}$
h13	$0.10^{(f)}$	0.5767 ± 0.008	$0.10^{(f)}$	$0.20^{(f)}$
h33	0.8224 ± 0.0006	0.2319 ± 0.0008	$0.48^{(f)}$	$0.20^{(f)}$

Table A.16: Correlation length and Hurst parameter of the substrate and the first layer obtained after the refinement of diffuse scattering curves measured at 230°C (*Liquid model*).

Sample	Surface tension,	χ^2
_	,	X
number	$\eta, [N/m]$	
h26	0.0098 ± 0.0001	25.90
h46	_	_
h86	0.01179 ± 0.00004	10.72
h16	0.0062 ± 0.0001	16.55
h36	0.0114 ± 0.0005	4.88
h21	_	_
h41	0.0161 ± 0.0001	9.07
h81	0.0178 ± 0.0001	11.88
h11	0.01413 ± 0.00001	4.76
h31	0.01795 ± 0.0001	5.02
h23	_	_
h43	0.01415 ± 0.0002	13.89
h83	0.0140 ± 0.0002	15.17
h13	0.0157 ± 0.0003	3.94
h33	0.01032 ± 0.00005	9.83

Table A.17: Surface tension at the polymer/air interface and χ^2 obtained from refinements of diffuse scattering curves measured at 230°C (*Liquid model*).

Sample	Correlation length	Hurst parameter	Correlation length	Hurst parameter
number	of the substrate,	of the substrate,	of the first layer,	of the first layer
	$\xi_{sub}\cdot 10^3,$ [Å]	h_{sub}	$\xi_{SiO_x} \cdot 10^3, [\text{Å}]$	h_{SiO_x}
h26	0.196 ± 0.004	0.604 ± 0.004	0.354 ± 0.002	0.787 ± 0.002
h46				_
h86	0.693 ± 0.0003	$0.28^{(f)}$	0.0560 ± 0.0001	$0.20^{(f)}$
h16	7.157 ± 0.008	0.677 ± 0.008	0.021 ± 0.004	0.271 ± 0.005
h36	6.95 ± 0.03	0.30 ± 0.03	0.98 ± 0.02	0.49 ± 0.05
h21				_
h41	1.55 ± 0.03	0.46 ± 0.04	0.840 ± 0.006	0.216 ± 0.008
h81	0.825 ± 0.001	0.206 ± 0.004	0.861 ± 0.005	$0.20^{(f)}$
h11	$0.10^{(f)}$	$0.20^{(f)}$	$0.060^{(f)}$	$0.20^{(f)}$
h31	9.832 ± 0.001	$0.20^{(f)}$	4.233 ± 0.006	$0.20^{(f)}$
h23	_	_	_	_
h43	$0.10^{(f)}$	$0.20^{(f)}$	$0.10^{(f)}$	$0.20^{(f)}$
h83	0.090 ± 0.001	$0.20^{(f)}$	$0.10^{(f)}$	$0.20^{(f)}$
h13	$0.10^{(f)}$	$0.20^{(f)}$	$0.10^{(f)}$	$0.20^{(f)}$
h33	0.0988 ± 0.0001	0.1567 ± 0.0003	0.1008 ± 0.0003	0.2081 ± 0.0002

Table A.18: Correlation length and Hurst parameter of the substrate and the first layer obtained after the refinement of diffuse scattering curves measured at 230°C (*Fractal model*).

Sample	Correlation length	Hurst parameter of	Roughness of	
number	of the polym. film,	the polym. film,	the polym. film,	χ^2
	$\xi_{PS} \cdot 10^3, [\text{Å}]$	h_{PS}	$\sigma_{PS},~ [{ m \AA}]$	
h26	0.431 ± 0.002	$0.20^{(f)}$	$7.00^{(f)}$	9.75
h46	_	_	_	-
h86	1.691 ± 0.003	$0.20^{(f)}$	$8.2^{(f)}$	6.19
h16	20.045 ± 0.007	$0.20^{(f)}$	$10.60^{(f)}$	5.37
h36	4.97 ± 0.03	$0.20^{(f)}$	$9.00^{(f)}$	2.85
h21	_	_	_	_
h41	1.02 ± 0.02	0.287 ± 0.007	6.88 ± 0.01	5.78
h81	7.073 ± 0.007	0.20 ± 0.0001	8.769 ± 0.005	9.34
h11	12.8645 ± 0.0008	$0.20^{(f)}$	7.9298 ± 0.0004	3.49
h31	8.796 ± 0.002	$0.20^{(f)}$	8.5266 ± 0.0006	2.18
h23	_	_	_	_
h43	12.870 ± 0.003	0.2123 ± 0.0002	9.124 ± 0.002	5.90
h83	5.189 ± 0.002	$0.20^{(f)}$	7.927 ± 0.001	8.49
h13	9.81 ± 0.01	$0.20^{(f)}$	8.015 ± 0.004	3.89
h33	19.5109 ± 0.0005	0.1361 ± 0.0001	9.9987 ± 0.0002	4.54

Table A.19: Correlation length, Hurst parameter and roughness of the polymer film as well as χ^2 obtained from refinements of diffuse scattering curves measured at 230°C (*Fractal model*).

Sample h41 was measured at 200°C.

Appendix B

Lists

B.1 List of tables

3.1	Analytic continuations
4.1	List of the studied samples
4.2	Layer 1 parameters
4.3	Correlation functions and refined parameters
4.4	Cut-off positions from capillary wave theory
4.5	Averages of correlation lengths and Hurst parameters
4.6	Effective thicknesses
4.7	Refinement results of the reflectivity data
5.1	Physical properties of CCl ₄
5.2	Characteristics of the diblock copolymer
A.1	Dispersion, roughness and thickness of the first layer
A.2	Dispersion, roughness and thickness of the polymer film
A.3	The thickness of the polymer films at different temperatures
A.4	Correlation length and Hurst parameter of the substrate and the
	first layer (Liquid model, 150°C, n -samples)
A.5	Surface tension at the polymer/air interface and χ^2
	(Liquid model, 150°C, n-samples)
A.6	Correlation length and Hurst parameter of the substrate and the
	first layer (Fractal model, 150°C, n-samples)
A.7	Correlation length, Hurst parameter, roughness of the polymer film
	and χ^2 (Fractal model, 150°C, n -samples)
A.8	Correlation length and Hurst parameter of the substrate and the
	first layer (Liquid model, 150°C, h-samples)
A.9	Surface tension at the polymer/air interface and χ^2
	(Liquid model, 150°C, h-samples)
A.10	Correlation length and Hurst parameter of the substrate and the
	first layer (Fractal model, 150°C, h -samples)

A.11	Correlation length, Hurst parameter, roughness of the polymer film
	and χ^2 (Fractal model, 150°C, h-samples)
A.12	Correlation length and Hurst parameter of the substrate and the
	first layer (Liquid model, 230°C, n -samples)
A.13	Surface tension at the polymer/air interface and χ^2
	(Liquid model, 230°C, n-samples)
A.14	Correlation length and Hurst parameter of the substrate and the
	first layer (Fractal model, 230°C, n-samples)
A.15	Correlation length, Hurst parameter, roughness of the polymer film
	and χ^2 (Fractal model, 230°C, n-samples)
A.16	Correlation length and Hurst parameter of the substrate and the
	first layer (Liquid model, 230°C, h -samples)
A.17	Surface tension at the polymer/air interface and χ^2
	(Liquid model, 230°C, h-samples)
A.18	Correlation length and Hurst parameter of the substrate and the
	first layer (Fractal model, 230°C, h-samples)
A.19	Correlation length, Hurst parameter, roughness of the polymer film
	and χ^2 (Fractal model, 230°C, h-samples)
B.1	List of tables
B.2	List of figures

Table B.1: List of tables.

B.2 List of figures

2.1	Effects of correlation lengths and Hurst parameter
2.2	Scheme of the surface force balance
3.1	Scattering geometry (polymer films)
3.2	Intensities vs. α_i
3.3	Multiple layer system
3.4	Two layers with refractive indices n_2 and n_3 .
3.5	Scattering geometry (confined liquids)
3.6	I_{diff} vs. q_x
4.1	Scheme of the beamline W1
4.2	Photo of the polymer sample cell
4.3	Photos of the sample heaters
4.4	Scans in reciprocal space
4.5	Monomer of polystyrene
4.6	Reflectivities at 50°C
4.7.	Reflectivity of sample n26
4.8	Structure factor of samples h36 und h81
4.9	Longitudinal diffuse scattering of sample h36
4.10	Roughness of the polymer films vs. temperature
4.11	Reflectivities showing modifications
4.12	Transverse scans at 50°C and 230°C
4.13	Transverse scans at 150°C
4.14	Correlation lengths at 50°C
4.15	Temperature behaviour
4.16	Reflectivities of HF–etched Si wafers
4.17	Δ -profiles of HF-etched Si wafers

5.1	Scheme of the confined liquids sample cell
5.2	Photo of the confined liquids wafers
5.3	Photo of the beamline D4.1
5.4	Scheme of the diffractometer
5.5	Sketch of the goniometer
5.6	Scheme of the vacuum system
5.7	Reflectivities of CCl ₄
5.8	Scheme of the confined liquid wafers
5.9	Structure of CCl ₄
5.10	Liquid structure factor of Octamethylcyclotetrasiloxane
5.11	Type of monomers
5.12	Reflectivity of PEO-b-PBh
5.13	Reflectivities of confined CCl ₄
5.14	Microscope photo of SI wafers and Octamethylcyclotetrasiloxane
5.15	Out-of-plane scan of confined CCl ₄
5.16	Reflectivities of confined PEO-b-PB (I)
5.17	Reflectivities of confined PEO-b-PB (II)
A.1 - A.30	Longitudinal and transverse scans of n -samples at
	150°C (Liquid and Fractal models)
A.31 - A.54	Longitudinal and transverse scans of h-samples at
	150°C (Liquid and Fractal models)
A.55 - A.84	Longitudinal and transverse scans of n -samples at
	230°C (Liquid and Fractal models)
A.85 - A.108	Longitudinal and transverse scans of h-samples at
	230°C (Liquid and Fractal models)

Table B.2: List of figures.

Danksagung

Ich danke Herrn Prof. Dr. Th. Brückel für die Bereitstellung des Themas dieser Arbeit und die Möglichkeit, die Arbeit in seiner Arbeitsgruppe durchführen zu können. Mein ganz besonderer Dank gilt Herrn Dr. Oliver Seeck für Anleitung und Hilfestellung bei den Experimenten und unzählige Diskussionen, die wesentlich zum Gelingen dieser Arbeit beigetragen haben.

Für technische Hilfe bei der Anfertigung der Experimentiereinrichtungen und beim Aufbau der Experimente danke ich den Ingenieuren Herrn Küssel, FZ Jülich, sowie Herrn Rüdiger Nowak und Frau Anita Ehnes, HASYLAB.

Für die Präparation der Polymer-Dünnschichtproben möchte ich mich bei Frau Dr. Hyunjung Kim, Argonne National Laboratory, sehr herzlich bedanken. Weiterhin danke ich Frau Dr. Denitza Lambreva, Universität Amsterdam, für die Präparation der confined polymer Proben.

Allen Mitgliedern der Arbeitsgruppen in Jülich und am HASYLAB, mit denen ich während meiner Zeit in Kontakt stand, sei hiermit für das freundliche Arbeitsklima gedankt.

Nicht zuletzt gilt mein Dank meinem Mann für die fortwährende Unterstützung und Ermutigung.

Hiermit versichere ich, daß ich die vorliegende Dissertation se be und keine anderen als die angegebenen Quellen und Hilfsm kenntlich gemacht habe.	
Hasloh im März 2005 (Mi	lena Lippmann)

CURRICULUM VITAE

Milena Lippmann

Personal Date

Birthday 02.08.1972

Birth name Milena Dimitrova Mihaylova

Place of birth Kazanlak, Bulgaria

Nationality Bulgarian Sex Female Marital status Married

Adress Großer Dorn 21, 25474 Hasloh

Email lippmann@desy.de

Languages Bulgarian, English, German, Russian

Education

1985 – 1990 Secondary mathematical school, Kazanlak, Bulgaria

1990 – 1996 – Sofia university Sv. Kliment Ohridski, physics faculty

Subject: solid state physics

Master thesis: Microscopic, diffraction and calorimetric investigations of polypropylene and polyethylene–co–vinyl acetate blends.

Scientific work

1996 – 1999 Research associate at Sofia university, faculty of physics, department of general physics, laboratory of X–ray diffraction

1999 – 2000 Research associate within the scope of an UNESCO course at the academy of science of the Czech republic, institute of macromolecular chemistry, laboratory of neutron and X–ray diffraction, Prague, Czechia

2001 Ph.D. thesis: Structure, phase transitions and mechanical properties of polypropylene and polyethylene—co—vinyl acetate blends (not approved in Germany)

2000 – 2003 Research associate at the Forschungszentrum Jülich, Institut für Festkörperforschung – Streumethoden Ph.D. thesis: The microstructure of confined and thin polymer films

 $\underline{\text{Others}}$

Since 2004 Maternity

Hasloh, May 2005

Milena Lippmann

Publications

- Mihaylova, M., Kresteva, M., Krestev, V. & Nedkov, E. X-ray investigation of poly(propylene-co-ethylene) and poly(ethylene-co-vinyl acetate) blends irradiated with fast electrons. Rad. Phys. Chem. **56** (1999), 581 – 589.
- Misheva, M., Mihaylova, M., Jourelov, N., Kresteva, M. & Nedkov, E. Positron annihilation lifetime spectroscopy study of irradiated poly(propylene-co-ethylene)/poly(ethylene-co-vinyl acetate) blends. Rad. Phys. Chem. 58 (2000), 39 – 47.
- Mihaylova, M., Krestev, V., Kresteva, M., Amzil, A. & Berlinova, I. Amphiphilic graft copolymers with polyoxyethylene side chains: supermolecular structure in solid state. I. WAXS studies. *Eur. Pol. J.* **37** (2001), 233 239.
- Mihaylova, M., Nedkov, T., Krestev, V. & Kresteva, M.
 Supermolecular structure of poly(propylene-co-ethylene)/poly(ethylene-co-vinyl acetate) blends irradiated with fast electrons. SEM, SAXS and DSC studies.
 Eur. Pol. J. 37 (2001), 2177 2187.
- Baldrian, J., Horuy, M., Steinhart, M., Sikora, A., Mihaylova, M., Amenitsch, H. & Bernstoff, S.
 Cocrystallization behaviour of low-molecular-weight PEO fractions in polymer blends. Material structure in chemistry, biology, physics and technology 8 (2001), 67.
- Knaapila, M., Lyons, B., Kisko, K., Foreman, J., Vainio, U., Mihaylova, M., Seeck, O.H., Palsson, L.-O., Serimaa, R., Torkkeli, M. & Monkmann, A.P.
 X-ray diffraction studies of multiple orientation in poly(9,9-bis-(2-ethylhexyl) fluorene-2,7-diyl) thin films.
 J. Phys. Chem. B 107 (2003), 12425 12430.